MICROCOPY RESOLUTION TEST CHART

AD-A165 886

THE EFFECT OF ABERRATIONS AND APODISATION ON THE PERFORMANCE OF COHERENT IMAGING SYSTEMS

J.P. Mills

University of Rochester
Office of Research and Project Administration
Rochester, New York   14627

February 1986

Final Report

DTIC
ELECTE
MAR 2 4 1986
S
D

Approved for public release; distribution unlimited.

AIR FORCE WEAPONS LABORATORY
Air Force Systems Command
Kirtland Air Force Base, NM   87117-6008

86

This final report was prepared by the University of Rochester, Rochester, New York, under Contract F29601-84-K-0014, Job Order 317J1413 with the Air Force Weapons Laboratory, Kirtland Air Force Base, New Mexico. Major J. C. Mann (ARDC) was the Laboratory Project Officer-in-Charge.

When Government drawings, specifications, or other data are used for any purpose other than in connection with a definitely Government-related procurement, the United States Government incurs no responsibility or any obligation whatsoever. The fact that the Government may have formulated or in any way supplied the drawings, specifications, or other data, is not to be regarded by cation, or otherwise in any manner construed, as licensing the holder, any other person or corporation; or as conveying any rights or permission to manufacture, use, or sell any patented invention that may in any way be related thereto.

This report has been authored by a contractor of the United States Government. Accordingly, the United States Government retains a nonexclusive, royalty-free license to publish or reproduce the material contained herein, or allow others to do so, for the United States Government purposes.

This report has been reviewed by the Public Affairs Office and is releasable to the National Technical Information Service (NTIS). At NTIS, it will be available to the general public, including foreign nations.

If your address has changed, if you wish to be removed from our mailing list, or if your organization no longer employs the addressee, please notify AFWL/ARDC, Kirtland AFB, NM 87117 to help us maintain a current mailing list.

This technical report has been reviewed and is approved for publication.
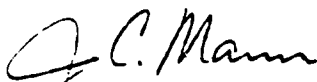
J. C. MANN
Major, USAF
Project Officer

LEROY F. WILSON
Chief, Excimer Lasers Branch

FOR THE COMMANDER
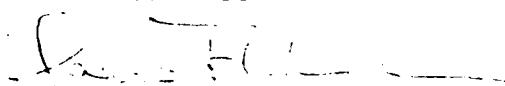
HARRO ACKERMAN
Lt Colonel, USAF
Chief, Laser Science & Technology

DO NOT RETURN COPIES OF THIS REPORT UNLESS CONTRACTUAL OBLIGATIONS OR NOTICE ON A SPECIFIC DOCUMENT REQUIRES THAT IT BE RETURNED.

AD-A165 886

REPORT DOCUMENTATION PAGE

1a. REPORT SECURITY CLASSIFICATION	1b. RESTRICTIVE MARKINGS
Unclassified	

2a. SECURITY CLASSIFICATION AUTHORITY	3. DISTRIBUTION/AVAILABILITY OF REPORT
	Approved for public release; distribution
2b. DECLASSIFICATION/DOWNGRADING SCHEDULE	unlimited..

4. PERFORMING ORGANIZATION REPORT NUMBER(S)	5. MONITORING ORGANIZATION REPORT NUMBER(S)
	AFWL-TR-85-80

6a. NAME OF PERFORMING ORGANIZATION	6b. OFFICE SYMBOL (If applicable)	7a. NAME OF MONITORING ORGANIZATION
University of Rochester		Air Force Weapons Laboratory

6c. ADDRESS (City, State and ZIP Code)	7b. ADDRESS (City, State and ZIP Code)
Office of Research and Project Administration Rochester, New York 14627	Kirtland Air Force Base, NM 87117

8a. NAME OF FUNDING/SPONSORING ORGANIZATION	8b. OFFICE SYMBOL (If applicable)	9. PROCUREMENT INSTRUMENT IDENTIFICATION NUMBER
		F29601-84-K-0014

8c. ADDRESS (City, State and ZIP Code)	10. SOURCE OF FUNDING NOS.			
	PROGRAM ELEMENT NO.	PROJECT NO.	TASK NO.	WORK UNIT NO.
	63605F	317J	14	13

11. TITLE (Include Security Classification)
THE EFFECT OF ABERRATIONS AND APODISATION ON THE PERFORMANCE OF COHERENT IMAGING SYSTEMS

12. PERSONAL AUTHOR(S)
Mills, J. P.

13a. TYPE OF REPORT	13b. TIME COVERED	14. DATE OF REPORT (Yr., Mo., Day)	15. PAGE COUNT
Final Report	FROM 3 Nov 83 TO 30 Sep 84	1986 ~~January~~ February	210

16. SUPPLEMENTARY NOTATION
Submitted in partial fulfillment of the requirements for the degree Doctor of Philosophy, Institute of Optics, University of Rochester.

17. COSATI CODES			18. SUBJECT TERMS (Continue on reverse if necessary and identify by block number)
FIELD	GROUP	SUB. GR.	Apodisation, Conerent Imaging, Imaging, Aberrations
20	06		

19. ABSTRACT (Continue on reverse if necessary and identify by block number)

The effect of aberrations on coherent imaging systems and the utility of apodisation in improving the performance of such systems was theoretically and experimentally investigated. The imaging performance of these systems was evaluated in terms of the images of certain simple objects—a point, two closely-spaced points, an edge, and a slit. Apodisation is defined as the deliberate modification of the amplitude transmittance of the exit pupil of the optical system. The effects on the imaging performance for various amounts of defocus, astigmatism, coma, and spherical aberration were determined for both unapodised and apodised systems. It is well known that for an aberration-free system, apodisation is effective in moderating the deleterious effects of the coherent imaging process. Since all real optical systems have aberrations, this dissertation addressed the more general case of apodisation in aberrated coherent imaging systems. It was found that apodisation was effective in improving the performance of these aberrated systems, i.e., ringing in the image of (over)

20. DISTRIBUTION/AVAILABILITY OF ABSTRACT	21. ABSTRACT SECURITY CLASSIFICATION
UNCLASSIFIED/UNLIMITED ☐ SAME AS RPT ☐ DTIC USERS ☒	Unclassified

22a. NAME OF RESPONSIBLE INDIVIDUAL	22b. TELEPHONE NUMBER (Include Area Code)	22c. OFFICE SYMBOL
Maj Mann	(505) 844-1769	AR-1

DD FORM 1473, 83 APR   EDITION OF 1 JAN 73 IS OBSOLETE.

19. ABSTRACT (Continued)

an edge or a slit was greatly reduced and the mensuration error in the image of two points was almost eliminated. The performance of an unaberrated system was seen to be a special case. Experiments have been conducted which verified the theoretical model which was used to make extensive theoretical predictions.

ACKNOWLEDGEMENTS

Although the work described in this thesis is primarily my own, I could not have done it without the help of many individuals and institutions. I gratefully acknowledge their contributions.

I thank my wife, Patricia. Not only has she displayed great understanding of the demanding situation we found ourselves in, but she was a material help in the accomplishment of this project. She taught me how to use computers and helped me write some of the programs, and did most of the typing and figures of my dissertation. I thank her also for her constant encouragement.

My advisor, Provost Brian J. Thompson, provided guidance and advice which was invaluable. I was given three years by the Air Force to complete my studies and that would have been impossible without his assistance and encouragement. Provost Thompson has also provided a close and vital model of excellence.

I am indebted to the U.S. Air Force for allowing me the opportunity to study optics. I am particularly grateful to Dr. Ray Wick and his organization, the Air Force Weapons Laboratory for supporting my research.

I thank Mr. Charles Betz, Mr. Tom Armading, and Ms. Eileen Williams of the University of Rochester Computing Center for supporting my computer needs and providing the quality word processing and graphics necessary for the completion of this work.

I have formed a close working relationship with Prof. Michael Morris and his research group. They have treated me like one of their own; their material and personal support is deeply appreciated.

TABLE OF CONTENTS

LIST OF FIGURES

LIST OF TABLES

CHAPTER 1 INTRODUCTION

This dissertation describes a systematic study of coherent optical imaging systems which had optical aberrations and in which apodisation was employed to improve their performance. Apodisation has proven to be an extreme important method of improving the performance of incoherent optical systems, including those with aberrations. However, until this thesis, the benefit of applying apodisation to aberrated coherent optical systems had not been established. Since all optical systems have at least some residual aberrations, this study was well motivated.

In this thesis, the utility of apodisation in improving the performance of aberrated coherent optical imaging systems was investigated both theoretically and experimentally. The emphasis was on describing the optical system performance when (1) aberrations were present and (2) when apodisation was added to an already aberrated system. Based on the previous research concerning unaberrated systems, it was hoped that apodisation would improve the performance of aberrated systems as well. It will be shown in the following chapters that this was indeed the case. Among other effects, apodisation used in an aberrated coherent imaging systems was found to be effective in (1) reducing the ringing in the image of an edge or a slit and (2) decreasing the error in the measured positions of the peaks in the image of two closely-spaced points. This behavior of an apodised coherent system had previously been reported when the system was free from aberrations. The analogous behavior when the system was aberrated is a new result.

Apodisation is a deliberate modification of the amplitude transmittance of an optical system. As an illustrative example, consider a centered, circularly-symmetric aberration-free, unapodised, coherent optical system. The amplitude transmittance

$A(x,y)$ of the exit pupil of such a system can be described by the function

$$A\left(x,y\right) = circ\left(\frac{r}{a}\right) , \tag{1.1}$$

where $r^2 = x^2 + y^2$, x and y are coordinates of the exit pupil, a is the radius of the exit pupil, and *circ* represents a function which has a value $A(x,y) = 1$ for $r \leq a$ and $A(x,y) = 0$ for $r > a$. The modulus of the amplitude distribution in the image of a point source through this simple system (the modulus of the amplitude impulse response) is displayed in Fig. 1.1a. When squared, it yields the Airy diffraction pattern or the irradiance impulse response which is shown in Fig. 1.1c. If now for example, $A(x,y)$ is modified by a Gaussian apodising function, the amplitude transmittance becomes

$$A\left(x,y\right) = circ\left(\frac{r}{a}\right)e^{-\left(\frac{r}{\beta}\right)^2} , \tag{1.2}$$

where β is the characteristic width of the Gaussian. The Gaussian is of course only one of an infinite number of possible apodising functions. The modulus of the amplitude impulse response for this system with $\beta = .58$ is shown in Fig. 1.1b. There are two immediately noticeable effects when comparing Figs. 1.1a and 1.1b. First, the peak irradiance has been significantly decreased by the apodisation; and second, the outer rings evident in Fig. 1.1a have been totally suppressed in Fig. 1.1b. It is apparent that the term apodisation is appropriate since it is derived from the Greek: a - meaning without, and pod - meaning foot. The apodisation has indeed removed the "feet" of the amplitude impulse response. This change has important implications in the analysis of coherent optical systems.

While incoherent optical systems are not within the scope of this study, it is useful to compare them to coherent optical systems. Such a comparison emphasizes the important characteristics of coherent systems. Image forming systems have traditionally
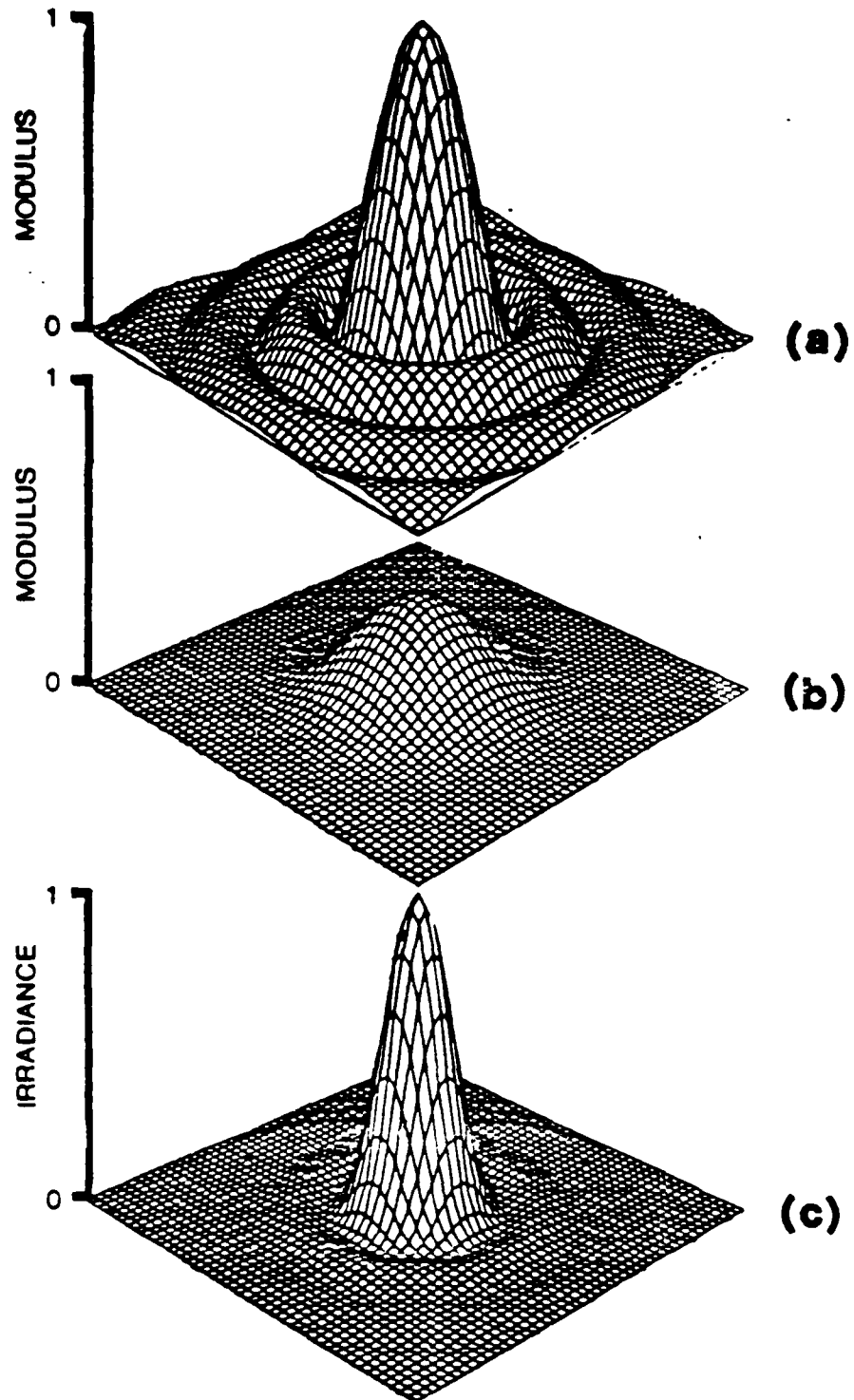
Fig. 1.1 The modulus of the amplitude impulse response through an optical system with
(a) a uniformly transmitting aperture and (b) a Gaussian apodiser in the aperture.
The irradiance impulse response with the uniform aperture is shown in (c). The
vertical scales are in relative units, with (a) and (b) having the same scale. The
other axes of each plot have units of relative distance and the scaling is the same.

been incoherent because the object to be imaged was usually either self-luminous or incoherently illuminated. Incoherent systems have the convenient property that they are linear in irradiance, which is, of course, the detected quantity. On the other hand, when an object is illuminated coherently the system is linear in complex field amplitude and hence nonlinear in irradiance. Partially coherent systems are also not linear in irradiance but are linear in the mutual intensity function, or for the non-quasi-monochromatic case, in the mutual coherence function.

Another important difference between coherent and incoherent systems is the form of their impulse response functions. This difference is also illustrated in the plots of Fig.1.1. The incoherent impulse response (Fig.1.1c) is in terms of irradiance while the coherent impulse response (Fig.1.1a) is in terms of amplitude. These figures graphically illustrate the fundamental difference; i.e. the incoherent impulse response is by definition real and positive, while this is not necessarily true for the coherent impulse response. Thus, the convolution associated with the imaging process is performed with a fundamentally different impulse response. This difference leads to the deleterious effects which often arise in coherent imaging.

One such effect occurs in the image of an edge. The form of the image of an edge through an optical system is dependent on whether the illumination is coherent or incoherent. This is shown in Fig.1.2, where the irradiance of the coherent and incoherent images of an edge are plotted relative to the geometrical image of that edge.

These curves were generated by calculating

$$I\left(v\right) = \left| \frac{1}{2} + \frac{1}{\pi} \int_0^v \frac{\sin y}{y} dy \right|^2 \tag{1.3}$$

for the coherent image of an edge and
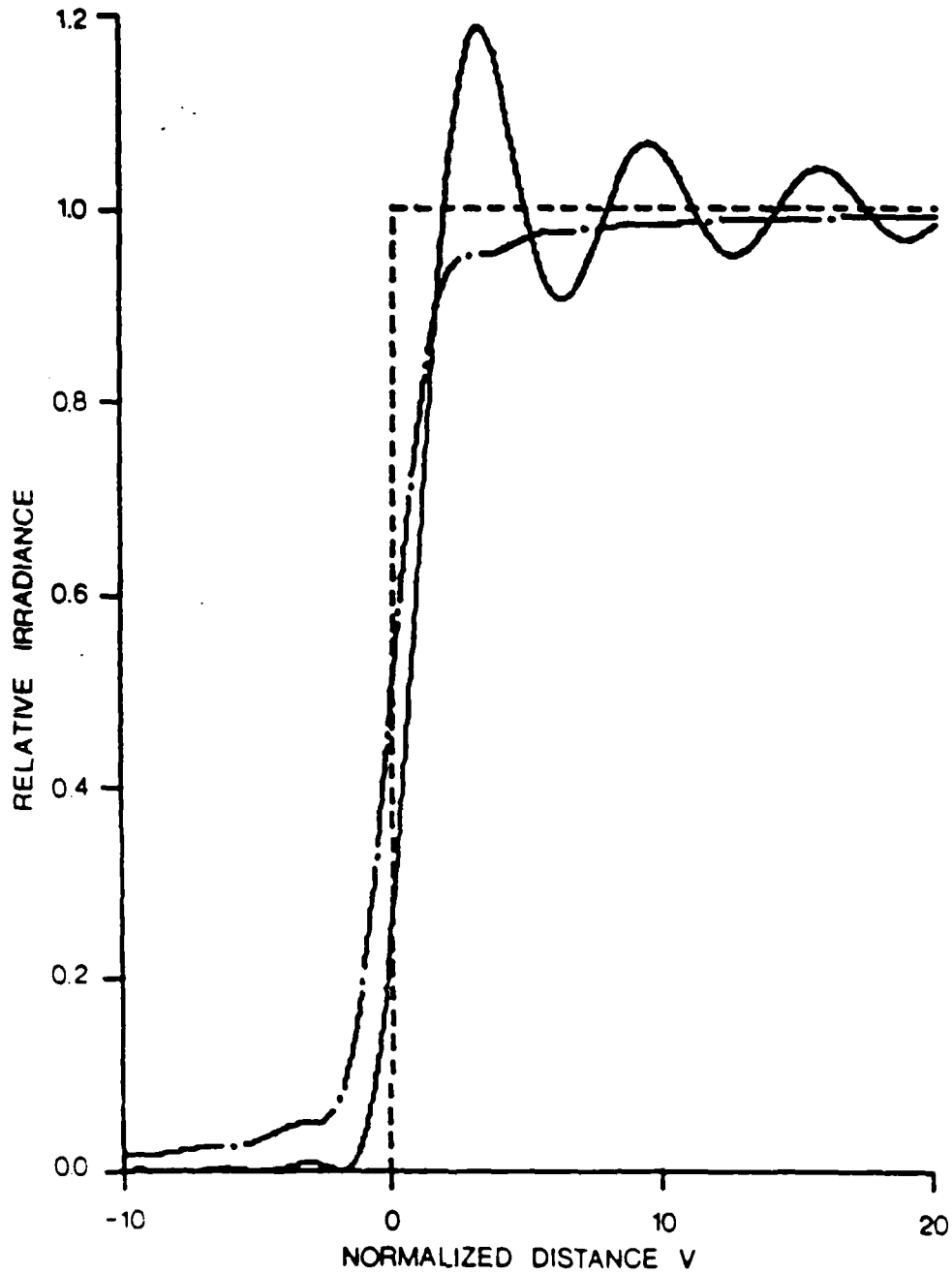
Fig 1 2 The coherent and incoherent images of an edge are plotted relative to the geometrical image of the edge (_____ coherent, ___ ___ ___ incoherent, _ _ _ _ _ geometrical)

$$I\left(v\right) = \frac{1}{2} + \frac{1}{\pi}\int_{o}^{2v}\frac{\sin y}{y}dy + \frac{1}{2\pi v}\left(\cos 2v - 1\right) \tag{1.4}$$

for the incoherent image of the same edge. The quantity v is the canonical distance coordinate

$$v = \frac{2\pi a}{\lambda d}y, \tag{1.5}$$

where a is the exit pupil radius, λ is the mean wavelength of the illumination, d is the distance from the exit pupil to the image plane, and y is the image plane coordinate perpendicular to the edge image. The coherent image exhibits a pronounced ringing which is a direct result of the negative regions of the amplitude impulse response. Also, the position of the coherently imaged edge (the half peak-irradiance point) is shifted to the right relative to the incoherent image. Such defects in imaging are not limited to edge images, but also occur in images of other simple objects such as two points or a slit, as well as in more complicated images.

The shift of the edge in the coherent case, relative to the incoherent case is due to the nonlinearity of the coherent imaging process. The nonlinearity arises when the field amplitude in the image plane is multiplied by its complex conjugate to give the image irradiance distribution. Thompson[1] has suggested that the analysis of coherent images should be in terms of the square root of the irradiance. Such a comparison for the case just considered is shown in Fig. 1.3, where the amount of edge ringing on the illuminated side of the edge image is reduced and there is no shift in the position of the edge. There is, however, an effective increase in the amount of ringing on the dark side of the imaged edge.

This study was concerned exclusively with coherent optical systems. Incoherent and partially coherent optical systems were not investigated, although occasionally the
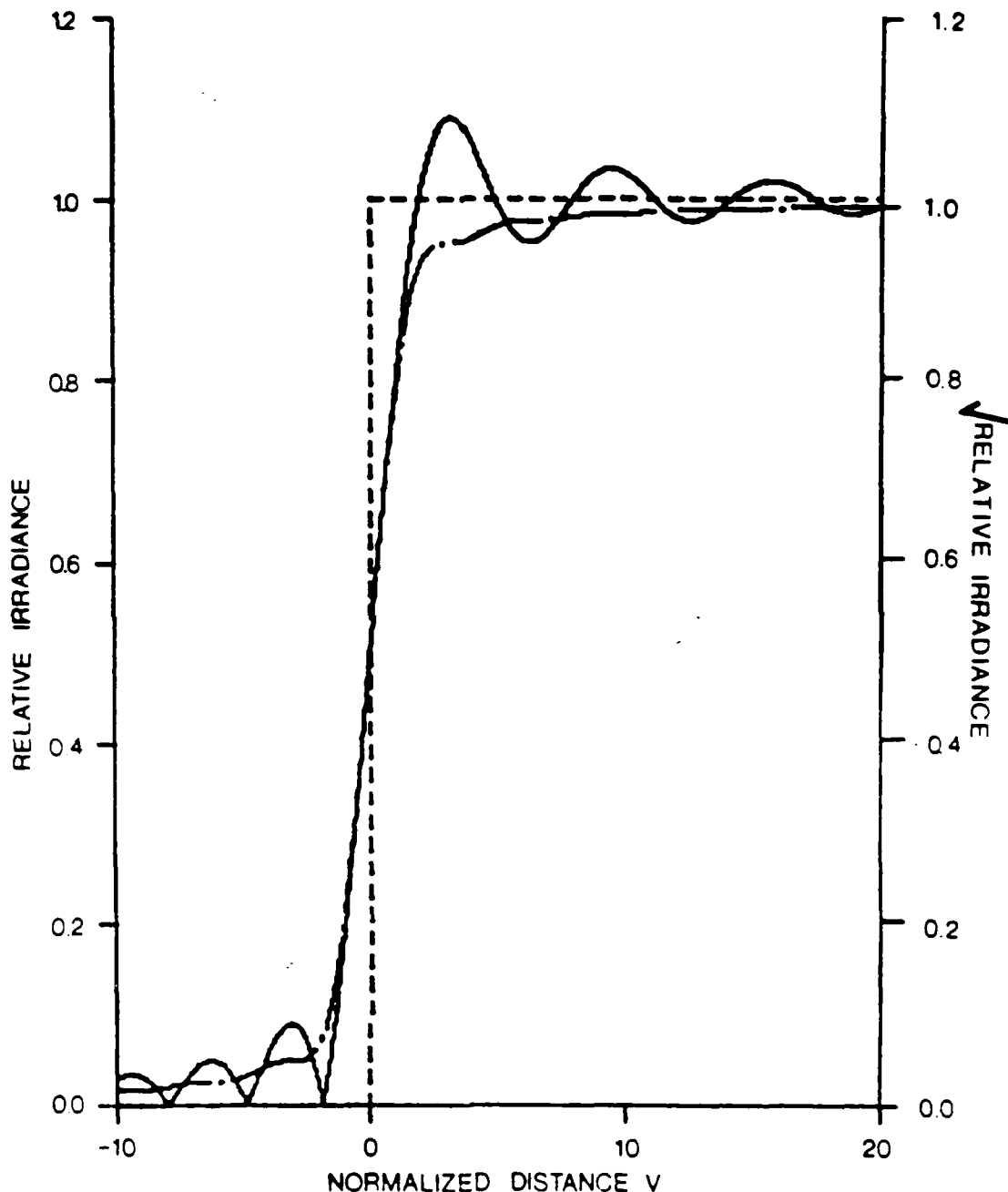
Fig 1.3 The irradiance of the incoherent image of an edge and the square root of the irradiance of the coherent image of an edge are plotted relative to the geometrical image of the edge (_____ coherent, ____ ____ ____ incoherent, _ _ _ _ _ geometrical). The left ordinate refers to the incoherent image while the right one refers to the coherent image.

calculated results were compared to the equivalent incoherent case. The partially coherent case contains, as limits of coherence, both the incoherent and coherent cases. The effects studied here, e.g. edge ringing, are the most pronounced when the illumination is fully coherent. Thus, the limitation to coherent systems was a worst case analysis. For that reason only coherent optical systems were considered.

The use of apodisation to improve the performance of optical systems has been the subject of a large number of studies. Most of these have considered only incoherent illumination. The original application of apodisation was to increase the resolution of spectroscopic instruments. As expected, in recent years the number of studies of apodisation in coherent systems has increased. In these studies, however, the optical system was always assumed to be free of aberrations. The researchers who have considered the use of apodisation in improving the performance of an aberrated system have limited themselves to incoherent systems. There have only been a few studies concerning the effects of aberration on the performance of coherent optical systems. There apparently have been no studies analyzing the effect of apodisation on the performance of aberrated coherent optical systems.

The research described in this dissertation partially fills that void. That is, the performance of coherent imaging systems was theoretically and experimentally analyzed under the conditions: (1) no aberrations or apodisation, (2) third-order aberrations but no apodisation, and (3) both aberrations and apodisation.

In Chapter 2, the basic equations needed to analyze coherent imaging and beam propagation systems are developed and previous research relating to this problem is reviewed. Chapter 3 is devoted entirely to an analysis of the amplitude impulse response, which is central to the study of all optical systems. In Chapter 4, theoretical results under differing conditions of aberrations and apodisation in coherent imaging systems are

presented and analyzed. The experimental methods and results are fully described in
Chapter 5. Finally, conclusions are presented in Chapter 6.

CHAPTER 2 OPTICAL IMAGING SYSTEMS - ANALYSIS

The concepts to be studied in this disertation are amenable to analysis using simple optical system models. In the first section of this chapter, these simple models are described and the formulae for their analysis are developed from the Rayleigh-Sommerfeld theory. Next, the diffraction theory of aberrations is outlined with particular emphasis on the use of Zernike polynomials. Then, the previous research relating to this problem is described Finally, the rationale for using a Guassian apodiser rather than some other is given.

2.1 THEORETICAL BASIS FOR THE ANALYSIS OF COHERENT IMAGING SYSTEMS

2.1.1 Beam Propagation Formulae

The optical systems considered in this thesis will be modeled and analyzed using standard physical optics techniques. One of the basic tools in this field is the beam propagation equation. This equation takes two forms, Fresnel or Fraunhofer,

Exit Pupil Plane   **Observation Plane**
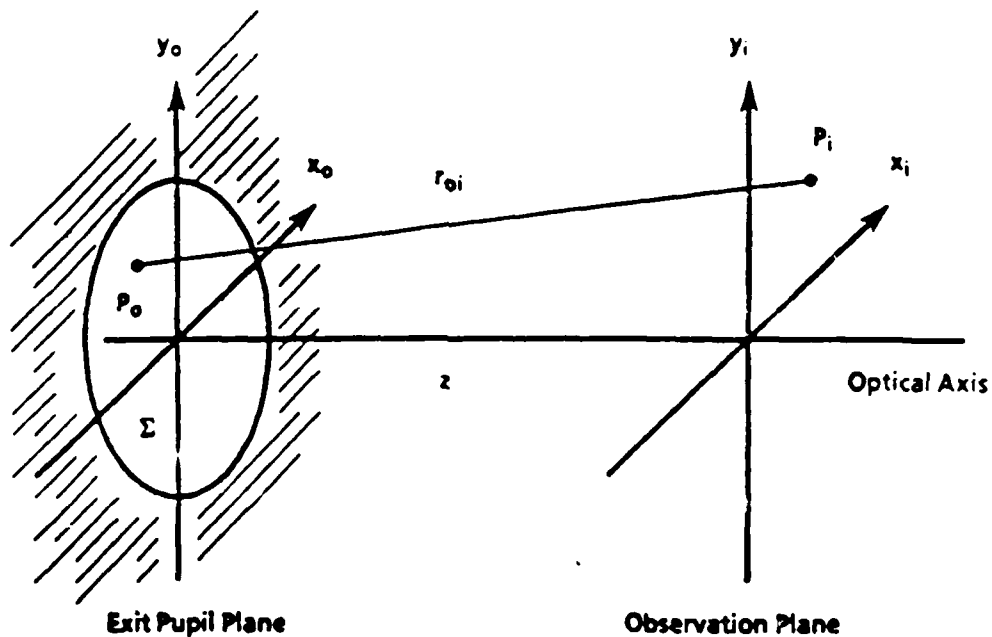
Fig.2.1 The diffraction geometry used in the derivation of the beam propagation formulae.

10

depending on the distance of propagation. It approximately describes the optical field in an observation plane (see Fig.2.1), given that the optical field is precisely known in the plane of the exit pupil. The two planes are separated by the axial distance z; and a general point P_o in the exit pupil plane is separated from a general point P_i in the observation plane by the distance r_{oi}.

The optical field at the observation point P_i can be described by the Rayleigh-Sommerfeld diffraction formula* (an application of the Huygens-Fresnel principle[2])

$$U_i\left(P_i\right) = -\frac{1}{i\lambda} \int \int_{\Sigma} U_o\left(P_o\right) \frac{e^{i\frac{2\pi}{\lambda}r_{oi}}}{r_{oi}} \cos\left(\bar{n}, \bar{r}_{oi}\right) ds, \qquad (2.1)$$

where the integration is over the exit pupil Σ and it has been assumed that $r_{oi} \gg \lambda$. The cosine term is the obliquity factor,

where $\bar{n}$ is a unit vector normal to the exit pupil plane pointing away from P_i and $\bar{r}_{oi}$ is the vector joining the two points P_o and P_i and pointing towards P_i.

Following the treatment in the text by Goodman[2], some initial approximations can be made to make (2.1) more amenable to calculation. First, the limits of integration are made infinite with the understanding that, in accordance with the Kirchoff boundary conditions, the field in the plane of the exit pupil $U_o(x_o, y_o)$ will be zero outside the exit pupil Σ. Futhermore, it is assumed that the distance z between the exit pupil and the observation plane is much greater than the maximum linear dimension in the exit pupil. Additionally, it is assumed that in the plane of observation only a finite region about the optical axis is of interest, and that the distance z is much greater than the maximum linear dimension of this region. With these assumptions the obliquity factor is readily

---

*Throughout this thesis, quantities like $U_o(P_i)$ and $U_o(P_o)$ which are complex-valued are printed in bold-face type.

approximated by

$$\cos\left(\bar{n},\overline{r_{oi}}\right) \simeq -1, \tag{2.2}$$

where the accuracy is within 5 percent[2] if the angle $(\bar{n},\bar{r}_{oi})$ does not exceed $18°$.

Similarly, the quantity r_{oi} in the denominator of (2.1) will not differ significantly from z, allowing (2.1) to be rewritten as*

$$U_i\left(P_i\right) = \frac{1}{i\lambda z}\int\int_{-\infty}^{\infty}U_o\left(x_o,y_o\right)e^{i\frac{2\pi}{\lambda}r_{oi}}dx_o dy_o. \tag{2.3}$$

The quantity r_{oi} in the exponent cannot be replaced with z because any error between r_{oi} and z would be multiplied by the very large number $2\pi/\lambda$ with the product easily exceeding 2π radians.

However, a further simplification can be made by applying the Fresnel approximation. The distance r_{oi} is given exactly by

$$r_{oi} = \left[z^2 + \left(x_i-x_o\right)^2 + \left(y_i-y_o\right)^2\right]^{\frac{1}{2}}. \tag{2.4}$$

Using the binomial expansion of the square root, (2.4) can be written approximately as

$$r_{oi} \simeq z\left[1 + \frac{1}{2}\left(\frac{x_i-x_o}{z}\right)^2 - \frac{1}{2}\left(\frac{y_i-y_o}{z}\right)^2\right]. \tag{2.5}$$

Substituting (2.5) into (2.3), performing the squaring operations of (2.5), and rearranging terms results in the Fresnel propagation formula

$$U_i\left(x_i,y_i\right) = \frac{e^{i\frac{2\pi}{\lambda}z}}{i\lambda z}e^{i\frac{\pi}{\lambda z}\left(x_i^2+y_i^2\right)}\int\int_{-\infty}^{\infty}U_o\left(x_o,y_o\right)e^{i\frac{\pi}{\lambda z}\left(x_o^2+y_o^2\right)}e^{-\frac{i2\pi}{\lambda z}\left(x_o x_i + y_o y_i\right)}dx_o dy_o \tag{2.6}$$

This is a basic formula which relates the optical field amplitude in the exit pupil plane $U_o(x_o,y_o)$ to the optical field amplitude in the observation plane $U_i(x_i,y_i)$.

*In this thesis a double integral with infinite limits on both integrals is represented as in (2.3).

The quantity $U_o(x_o,y_o)$ contains all of the information about the exit pupil, including aberrations and apodisation. That is

$$U_o\left(x_o,y_o\right) = U_{in}\left(x_o,y_o\right)A\left(x_o,y_o\right)e^{i\frac{2\pi}{\lambda}\Phi\left(x_o,y_o\right)}B\left(x_o,y_o\right), \tag{2.7}$$

where $U_{in}(x_o,y_o)$ is the wavefront incident on the exit pupil, $A(x_o,y_o)$ represents the amplitude transmittance of the exit pupil, $\Phi(x_o,y_o)$ represents the phase aberrations associated with the exit pupil, and $B(x_o,y_o)$ represents the finite extent of the exit pupil $A(x_o,y_o)$ is the term which describes the apodiser. In general, $A(x_o,y_o)$ could be complex; but in this study only real apodisations will be considered.

It is instructive to note that, aside from multiplicative amplitude and phase factors in (2.6) that are independent of (x_o,y_o), the function $U_i(x_i,y_i)$ may be found from a Fourier transform of

$$U_o\left(x_o,y_o\right)\exp\left[i\left(\pi/\lambda z\right)\left(x_o^2+y_o^2\right)\right], \tag{2.8}$$

where the transform must be evaluated at the spatial frequencies $f_x = x_i/\lambda z$ and $f_y = y_i/\lambda z$ to assure the correct spatial scaling in the observation plane.

In the near-field analysis of an optical system, (2.6) is used directly. The field amplitude in the exit pupil, $U_o(x_o,y_o)$ is, as stated previously, limited in spatial extent by that exit pupil and contains the incident field amplitude, the attentuation by the apodiser and any aberrations which may be part of the illuminating wavefront. The field amplitude at each point in the observation plane can then be determined by performing the indicated integration.

For a far-field analysis, (2.6) simplifies further. If, in addition to the assumptions made in the Fresnel propagation case, the stronger (Fraunhofer) assumption

$$z \gg \frac{\pi}{\lambda}\left(x_o^2 + y_o^2\right)_{max} \tag{2.9}$$

is adopted, then the quadratic phase factor inside the integral is approximately unity. In this case, the observed field amplitude can be found directly as a Fourier transform of the field amplitude of the exit pupil. Thus, in the region of Fraunhofer diffraction,

$$U_i\left(x_i,y_i\right) = \frac{e^{i\frac{2\pi}{\lambda}z}}{i\lambda z}e^{i\frac{\pi}{\lambda z}\left(x_i^2+y_i^2\right)}\int\int_{-\infty}^{\infty}U_0\left(x_0,y_0\right)e^{-\frac{i2\pi}{\lambda z}\left(x_0x_i+y_0y_i\right)}dx_0dy_0.\qquad(2.10)$$

Aside from the multiplicative factors preceding the integral, this equation states that $U_i(x_i,y_i)$ is the Fourier transform of the exit pupil distribution $U_0(x_0,y_0)$, evaluated at the spatial frequencies $f_x = x_i/\lambda z$ and $f_y = y_i/\lambda z$.

The analysis of the focussed beam propagation system is likewise simplified by the presence of the focussing lens. A perfect lens only changes the curvature of the incident wavefront, i.e., the field just after the lens, $U_0'(x_0,y_0)$, is given by

$$U_0'\left(x_0,y_0\right)=U_{in}\left(x_0,y_0\right)A\left(x_0,y_0\right)e^{i\frac{2\pi}{\lambda}\Phi\left(x_0,y_0\right)}B\left(x_0,y_0\right)e^{-\frac{i\pi}{\lambda f}\left(x_0^2+y_0^2\right)}=U_0\left(x_0,y_0\right)e^{-\frac{i\pi}{\lambda f}\left(x_0^2+y_0^2\right)},$$

where $U_{in}(x_0,y_0)$ is the field just before the lens and f is the focal length of the lens, assuming that the lens is in the exit pupil.

If the observation plane is a distance f away from the exit pupil, then the quadratic phase factors inside the integral of (2.6) cancel. In this case, the integral is again an exact Fourier transform of the exit pupil function:

$$U\left(x_i,y_i\right) = \frac{e^{i\frac{2\pi}{\lambda}f}}{i\lambda f}e^{i\frac{\pi}{\lambda f}\left(x_i^2+y_i^2\right)}\int\int_{-\infty}^{\infty}U_0\left(x_0,y_0\right)e^{-\frac{i2\pi}{\lambda f}\left(x_0x_i+y_0y_i\right)}dx_0dy_0\qquad(2.11)$$

2.1.2 Imaging Systems

The analysis of imaging systems will be based on the techniques of Fourier transforms. These methods were developed primarily by Duffieux[3,4], partly in

collaboration with Lansraux[4]. The following development follows closely that of Born
and Wolf[5], Section 9.5.1.
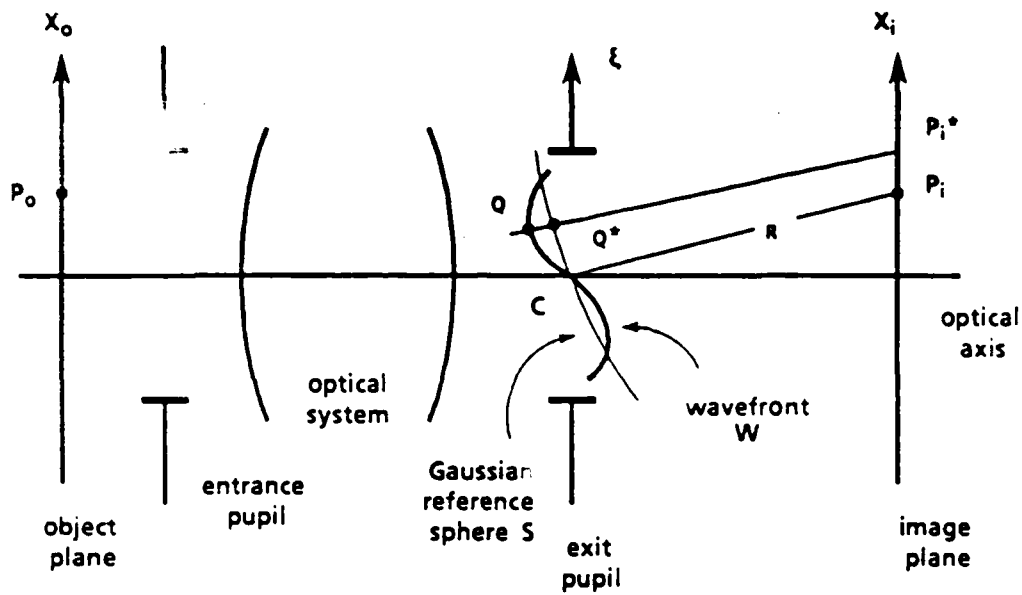
Fig.2.2 The geometry of a centered optical system which gives rise to an aberrated
wavefront W. The aberration function Φ is in terms of the distance QQ* between
W and the reference sphere S.

Consider the centered optical system sketched in Fig.2.2. Points in the image plane
and in the plane of the exit pupil are specified by Cartesian coordinates (x_i, y_i) and (ξ, η),
respectively. The y_o, y_i, and η axes while not shown in Fig.2.2 are perpendicular to the
optical axis and to the x_o, x_i, and ξ axes, respectively. Points in the object plane are
specified by scale normalized coordinates (x_o, y_o) such that, if P_o at (X_o, Y_o) is a typical
object point and M is the lateral magnification, then $x_o = MX_o$ and $y_o = MY_o$ so that the
object point and its image have the same coordinate values.

The imaging properties of the optical system are specified by the transmission
function K $(x_o, y_o; x_i, y_i)$, defined as the complex amplitude, per unit area of the object
plane, at the point (x_i, y_i) in the image plane, due to a disturbance of unit amplitude and
zero phase at the object point (x_o, y_o). The imaging process is then described by

$$U_i\left(x_i, y_i\right) = \int\int_{-\infty}^{\bullet} U_o\left(x_o, y_o\right) K\left(x_o, y_o; x_i, y_i\right) dx_o\, dy_o \; . \tag{2.12}$$

where $U_o(x_o, y_o)$ represents the complex disturbance in the object plane and $U_i(x_i, y_i)$ is the resultant optical field amplitude at the point (x_i, y_i) in the image plane.

The transmission function K $(x_o, y_o; x_i, y_i)$ depends on the physical properties of the optical system. This dependence can be derived by determining the image of a point object of unit amplitude and zero phase at the point $x_o = x_o'$, $y_o = y_o'$. In this case, the object is described by

$$U_o\left(x_o, y_o\right) = \delta\left(x_o - x_o'\right)\delta\left(y_o - y_o'\right) \; , \tag{2.13}$$

where δ is the Dirac delta function. Then (2.12) reduces to

$$U_i\left(x_i, y_i\right) = K\left(x_o', y_o'; x_i, y_i\right) \; ; \tag{2.14}$$

that is, the transmission function K is equal to the disturbance in the image plane due to the point source (2.13) in the object plane.

The Gaussian reference sphere S is centered on the image point $x_i' = x_o'$, $y_i' = y_o'$ (shown as P_i in Fig.2.2). Let R be the radius of the reference sphere and let

$$H\left(x_o', y_o'; \xi, \eta\right) = \frac{i}{\lambda} G\left(x_o', y_o'; \xi, \eta\right)\frac{e^{-ikR}}{R} \tag{2.15}$$

be the disturbance at a typical point (ξ, η) on this sphere due to the point source (2.13). Apart from an additive factor $\pi/2$, the phase of G is then the aberration function Φ and the amplitude of G is a measure of the non-uniformity in the amplitude of the image-forming wave. The factor i/λ on the right side of (2.15) was introduced to simplify later formulae.

Using the Rayleigh-Sommerfeld diffraction formula (2.1), the optical field in the image plane is (small angles of diffraction assumed)

$$U_i\left(x_i, y_i\right) = \frac{1}{i\lambda} \int \int H\left(x_o', y_o'; \xi, \eta\right) \frac{e^{i\frac{2\pi}{\lambda}s}}{s} d\xi\, d\eta \quad , \tag{2.16}$$

where s is the distance from the point (ξ, η) on the reference sphere to the point (x_i, y_i) in the image plane; and the integral extends over that portion of the reference sphere which approximately fills the exit pupil.

The distance s is given exactly by

$$s = \left\{ R^2 + \left[\left(x_i - x_o'\right) - \xi\right]^2 + \left[\left(y_i - y_o'\right) - \eta\right]^2 \right\}^{1/2} \tag{2.17}$$

and approximately by

$$s \simeq R - \left(x_i - x_o'\right)\frac{\xi}{R} - \left(y_i - y_o'\right)\frac{\eta}{R} \quad , \tag{2.18}$$

where the binomial expansion has been applied to (2.17), all but the first three terms have been dropped, and the terms which are quadradic in object or image plane coordinate have been discarded as being much smaller than R.

Then, the combination of (2.14)-(2.18) results in

$$K\left(x_o, y_o; x_i, y_i\right) = \frac{1}{\lambda^2 R^2} \int \int_{-\infty}^{\infty} G\left(x_o, y_o; \xi, \eta\right) e^{\frac{-i2\pi}{\lambda R}\left[\left(x_i - x_o\right)\xi + \left(y_i - y_o\right)\eta\right]} d\xi\, d\eta \quad , \tag{2.19}$$

where G is taken to be equal to zero at points ξ, η outside the opening in the exit pupil. This is the required relation between the transmission function K and the pupil function G of the system. Since K may be regarded as the disturbance in the image of a point source, it can now be identified also as the amplitude impulse response of the optical system. From (2.19) it can be seen that this amplitude impulse response is proportional to

the Fourier transform of the pupil function G, where the transform must be evaluated at the spatial frequencies $f_x = (x_i - x_o)/\lambda R$ and $f_y = (y_i - y_o)/\lambda R$.

In a well-corrected circularly symmetric system, K approximates, apart from a constant factor, the amplitude of the Airy diffraction pattern. Since this study involves the performance of optical systems which are not very well-corrected, the form of K will depart, sometimes significantly, from the Airy pattern. However, considered as a function of (x_o, y_o), the transmission function varies slowly as this point explores the object surface. More precisely, the working field may be divided into regions, where each region is large compared to the finest detail that the system can resolve; and with the property that in each such region Γ, K is to a good approximation, a function of the displacement vector from the image point, but not of the image point itself. In such cases,

$$K\left(x_o, y_o ; x_i, y_i\right) = K_\Gamma\left(x_i - x_o, y_i - y_o\right).$$ (2.20)

A region Γ with this property is said to be an isoplanatic region of the system. This study will only consider objects that are so small as to fall within such an isoplanatic region. In this case, (2.12) and (2.19) may be replaced by

$$U_i\left(x_i, y_i\right) = \int\int_{-\infty}^{\infty} U_o\left(x_o, y_o\right) K\left(x_i - x_o, y_i - y_o\right) dx_o dy_o$$ (2.21)

and

$$K\left(x_i - x_o, y_i - y_o\right) = \frac{1}{\lambda^2 R^2} \int\int_{-\infty}^{\infty} G\left(\xi, \eta\right) e^{\frac{-i2\pi}{\lambda R}\left[\left(x_i - x_o\right)\xi + \left(y_i - y_o\right)\eta\right]} d\xi d\eta ,$$ (2.22)

where the function G is now independent of the object point.

If $U_o(x_o,y_o)$, $U_i(x_i,y_i)$, and K are represented as the Fourier integrals

$$U_o\left(x_o,y_o\right)=\int\int_{-\infty}^{\infty}u_o\left(f,g\right)e^{-i2\pi\left(fx_o+gy_o\right)}dfdg ,\qquad(2.23a)$$

$$U_i\left(x_i,y_i\right)=\int\int_{-\infty}^{\infty}u_i\left(f,g\right)e^{-i2\pi\left(fx_i+gy_i\right)}dfdg ,\qquad(2.23b)$$

$$K\left(x,y\right)=\int\int_{-\infty}^{\infty}k\left(f,g\right)e^{-i2\pi\left(fx+gy\right)}dfdg ,\qquad(2.23c)$$

then, by the Fourier inversion formula

$$u_o\left(f,g\right)=\int\int_{-\infty}^{\infty}U_o\left(x_o,y_o\right)e^{i2\pi\left(fx_o+gy_o\right)}dx_o dy_o ,\qquad(2.24a)$$

$$u_i\left(f,g\right)=\int\int_{-\infty}^{\infty}U_i\left(x_i,y_i\right)e^{i2\pi\left(fx_i+gy_i\right)}dx_i dy_i ,\qquad(2.24b)$$

$$k\left(f,g\right)=\int\int_{-\infty}^{\infty}K\left(x,y\right)e^{i2\pi\left(fx+gy\right)}dxdy \qquad(2.24c)$$

Equation (2.21) represents the imaging process as a convolution Substituting (2.24a-c) into the Fourier inverse of (2.21) and applying the convolution theorem² results in

$$u_i\left(f,g\right)=u_o\left(f,g\right)k\left(f,g\right).\qquad(2.25)$$

This equation implies that if the optical fields in the object and image planes are each considered as a superposition of spatial frequencies f and g, then each component

of spatial frequency in the image plane depends only on the corresponding component in the object plane, and the ratio of components is k. A comparison of (2.23c) and (2.22) reveals that

$$k\left(\frac{\xi}{\lambda R}, \frac{\eta}{\lambda R}\right) = G\left(\xi\eta\right),$$ (2.26)

so that the frequency response function $k(f,g)$ is equal to the value of the pupil function G at the point

$$\xi = \lambda R f \text{ and } \eta = \lambda R g.$$ (2.27)

The calculation of the image of any appropriately small object can now be accomplished by Fourier transform techniques. That is,

$$U_i\left(x_i, y_i\right) = F\left\{k\left(f,g\right)F^{-1}\left\{U_o\left(x_o, y_o\right)\right\}\right\},$$ (2.28)

where $F\{\}$ and $F^{-1}\{\}$ indicate the direct and inverse Fourier transforms, respectively, of the bracketed terms. The inverse Fourier transform must be evaluated at the spatial frequencies $f = \xi/\lambda R$ and $g = \eta/\lambda R$ and the direct Fourier transform must be evaluated at the spatial frequencies $f = (x_i - x_o)/\lambda R$ and $g = (y_i - y_o)/\lambda R$. This powerful tool, (2.28), will be used extensively in the analysis of aberrated imaging systems in this thesis.

2.1.3 Measures of Performance

2.1.3.1 Two-Point Resolution

The performance of an optical system is measured using criteria that are dependent upon the intended use of the system. In the telescope, for example, the resolution of two closely-spaced point objects is important. Lord Rayleigh[6] developed the first resolution criterion, which now bears his name. Using Airy's[7] result concerning the image of a point source through a circular aperture, Lord Rayleigh stated that two

point sources are just resolved if the maximum of one irradiance pattern coincides with the first minimum of the other. As Barakat[8] has pointed out, the Rayleigh criterion is based on the tacit assumption that the two point sources are mutually incoherent. It is necessary of course that they also be of equal irradiance. Born and Wolf[5] extended Rayleigh's criterion by stating that resolution is obtained when the irradiance, midway between the geometrical images is 19% less than the maximum irradiance in the image of the two points.

An alternate criterion, suggested by Sparrow[9], states that the two point sources are just resolved if the second derivative of their image irradiance vanishes at a point midway between the Gaussian image points. The Sparrow criterion is more readily amenable to quantitative calculations and has often been used in assessing systems. It is also well suited to analyzing resolution in coherent systems. The Sparrow criterion will be used in this study.

The spatial coherence of the illumination from two point sources can dramatically affect the resolution of their images. This is illustrated in Fig.2.3, where Grimes and Thompson[10] have calculated the irradiance distribution in the image of two point objects for various values of γ, the complex degree of coherence between the two point sources. The geometrical separation of the points,which is just greater than the Rayleigh limit, is indicated by the two vertical dashed lines. The two points are well resolved in the incoherent limit, the resolution decreasing with increasing γ until when $\gamma = 0.6$ the curve is essentially flat midway between the Gaussian image points (the Sparrow resolution limit). For greater values of γ, the two points are unresolved. Rojak[11] has calculated the limit of resolution using the Sparrow criterion for values of γ from the coherent limit to the incoherent limit.
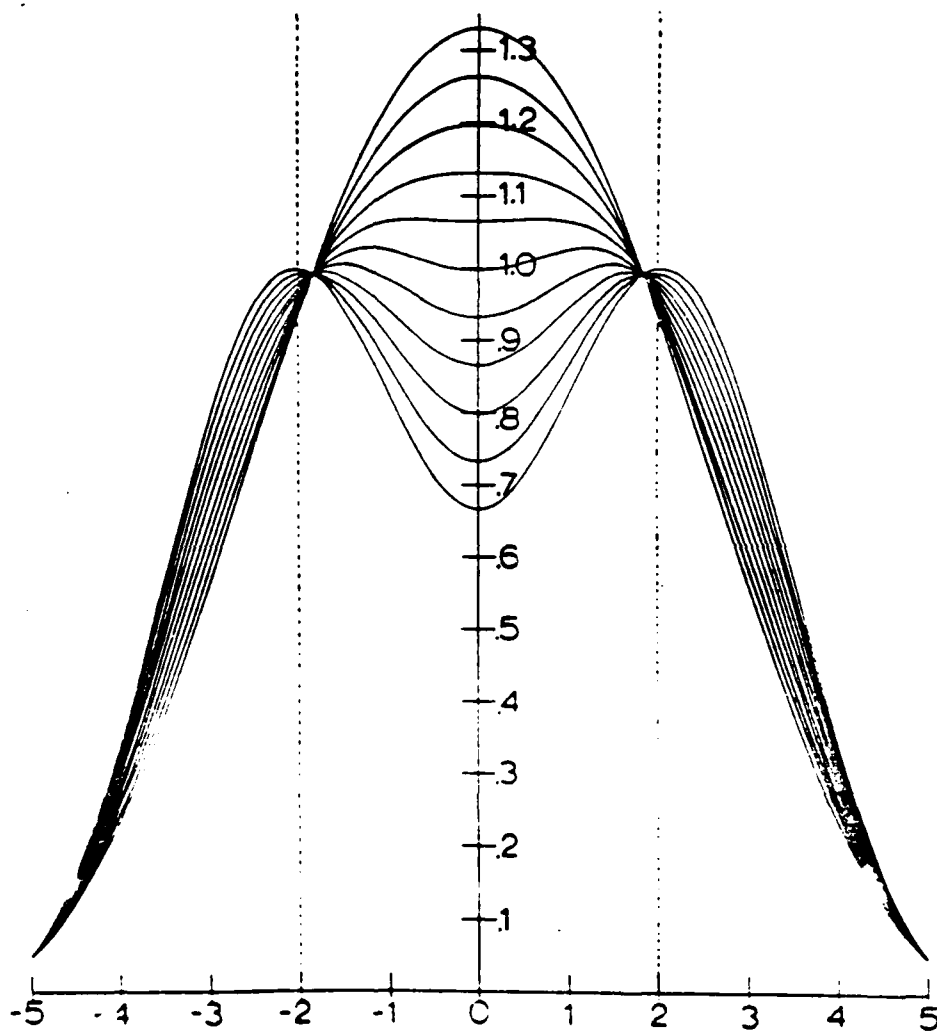
Fig 2 3 The image irradiance distribution for various values of γ from γ = 0 to γ = 1.0
(from bottom to top in the center of the graph) in steps of 0.1 (after Grimes and
Thompson[10]).

.2.1.3.2 Mensuration Error

It is apparent from Fig.2.3 that the separation of the two points when measured in the image plane depends on the degree of coherence. The difference between the expected separation based on geometrical considerations and the measured separation is termed the mensuration error. This mensuration error for a fixed degree of coherence depends also on the separation of the point sources in the object plane[10]. In the analysis of the image of two point sources, the only measurable quantity is the separation of the two peaks in the resultant irradiance distribution, a separation that would normally be considered to be the real separation of the object points. Hence, the mensuration error is a very important measure of performance in some optical imaging systems.

2.1.3.3 Edge Ringing, Shift, and Acutance

It is important in other systems to accurately image an edge object. Two major effects encountered are edge-ringing and edge-shifting. These effects have been investigated by, among others, Hopkins[12], Steel[13], Canals-Frau and Rosseau[14], Kinzly[15], Skinner[16,17], Considine[18], and Thompson[19]. These effects are illustrated in Fig.1 2 where the theoretical irradiance distribution of the image of an edge object by a one-dimensional ideal lens is shown for both coherent and incoherent illumination. It is also apparent from this figure that the slope of the irradiance near the edge is different for the two cases. The slope of the edge irradiance is termed the acutance and is greater for a coherent image than for an incoherent image of the same edge with the same optical system. When quantified, these effects can also be measures of performance of the imaging system.

2.1.3.4 Slit Ringing and Width

The use of bar targets for measuring resolution of optical systems is perhaps the most common and rapid method of evaluating an optical system. The OTF of an

incoherent system can quickly be estimated, using an object consisting of many sets of bar targets, each having a different fundamental spatial frequency. Although the OTF is not applicable to coherent systems, it is interesting to compare the image of a slit (or a bar) in the coherent and incoherent limits. When coherently illuminated, the edges of the slit will exhibit edge-ringing and edge-shifting. As an illustration of this problem, the coherent image of a slit is displayed in Fig.2.4. Under coherent illumination the slit appears to be narrower than under incoherent illumination. The opposite situation would occur for a coherently imaged bar; the bar would appear to be wider. The size of the bar (or slit) can be used as a measure of the performance of the system. The normalized distance v used in this figure was defined in Chapter 1.

A more meaningful depiction of the coherent image of an edge might be a plot of the square root of the irradiance. This follows the suggestion made by Thompson[1]. Fig. 2.5 is such a plot. The advantage of this approach is the removal of the nonlinearity in the coherent imaging process. One result is that there is no edge shift; another is that the edge ringing is reduced.

2.1.3.5 Strehl Ratio, Encircled Energy, Second Moment, and Near-field Fluctuations

In the case of laser systems, the important parameters of the focussed beam are the Strehl ratio, encircled energy, and second moment of the irradiance distribution. The Strehl ratio is formed by the ratio of the peak irradiance in a particular plane of the focal region of an aberrated beam to the peak irradiance in the focal region of an unaberrated beam. The encircled energy is the total energy within a given circle in a plane normal to the beam. The second moment refers to the variance of the irradiance distribution of the beam. Each of these can be used as a measurement of performance. In the near field of
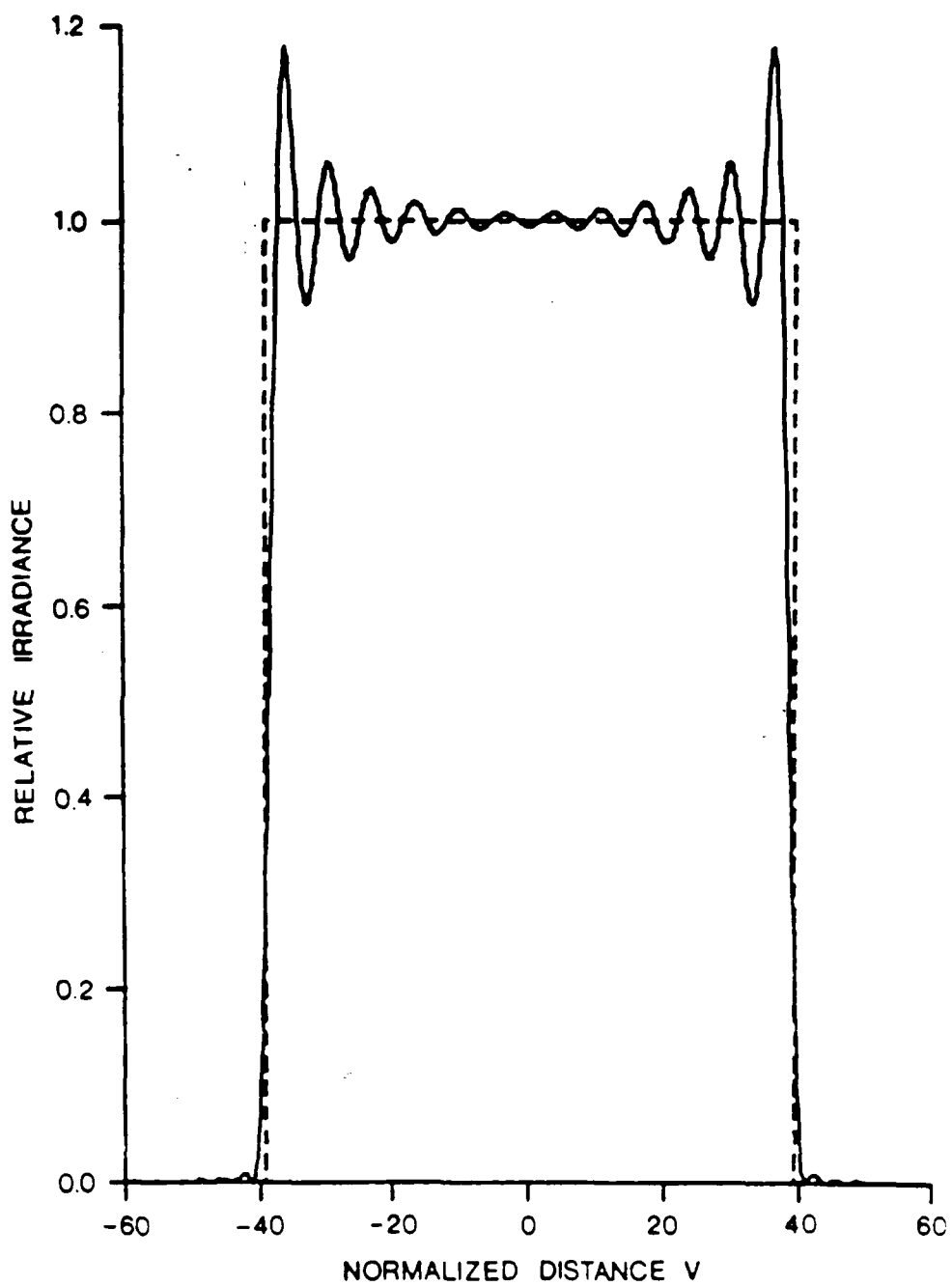
Fig.2.4 The coherent image of a slit (solid curve) through an unaberrated and unapodised optical system having a circular exit pupii. The geometricai image of the slit is shown as a dashed curve.
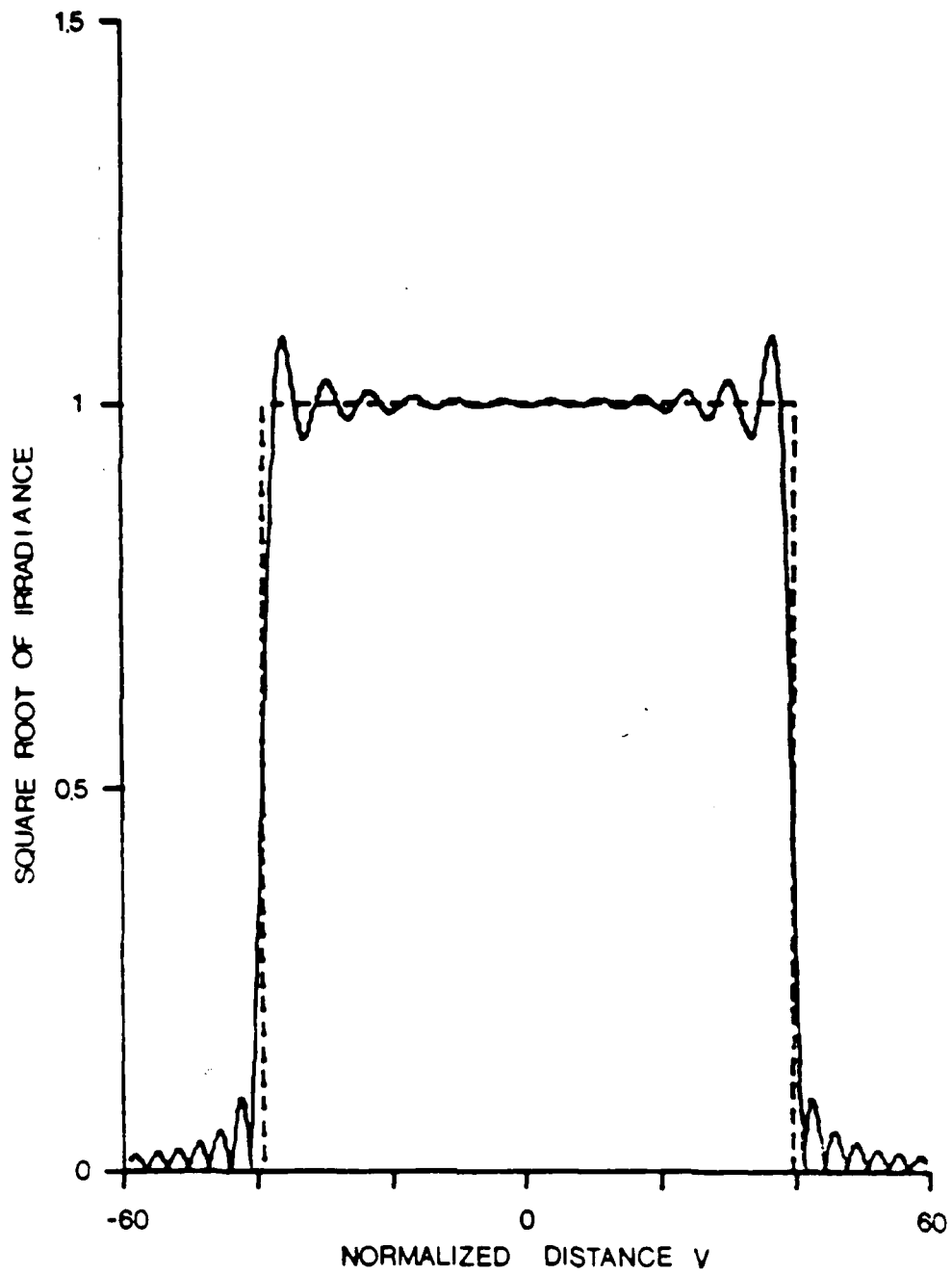
Fig 2.5 The solid line is a plot of the square root of the irradiance distribution of the image of a slit through a circularly symmetric, unaberrated, unapodised coherent optical system. The dashed line is the geometrical image of that same edge.

the beam propagation system, the irradiance distribution can have significant fluctuations that arise from diffraction caused by the apertures in the system. These fluctuations can degrade the far field performance of the system by distorting reflecting surfaces as pointed out by Avizonis, et al[20]. The fluctuations could also damage components of the final amplifier stages in systems such as a high peak power pulsed laser. Thus, the amount of the near-field fluctuations can be an important limitation of performance in these systems.

2.2 THE DIFFRACTION THEORY OF ABERRATIONS

Both the geometrical- and diffraction-based theories of aberrations are covered comprehensively in the text by Born and Wolf[5]. Those parts of their treatment which are pertinent to this study will be briefly reviewed.

Consider again the centered optical system shown in Fig.2.2 with a monochromatic point source P_o in the object plane. The Gaussian image point P_i in the image plane is the center of the Gaussian reference sphere S which intersects the exit pupil at the on-axis point C. A real wavefront W arising from the point source P_o will in general not coincide with the reference sphere but will deviate from it, perhaps as shown in Fig.2.2. The real wavefront is drawn intersecting the reference sphere at the axial point C.

At an arbitrary point Q on W a line perpendicular to W represents an optical ray, or wave normal. In general, this wave normal will intersect the image plane at a point P^* which is different from P_i. The separation of these two points $P_i P_i^*$ is the wave normal aberration while the deformation of W relative to S along the ray QQ^* is the wavefront aberration. The deformation of W in the region of the exit pupil will be described by the aberration function Φ. Assuming that the refractive index of the image space is unity, Φ (taken as positive in Fig.2.2) represents the distance QQ^* along the wave normal.

In this study, the aberration function will be expressed in terms of both the Zernike polynomials and the Siedel expansion. The Zernike polynomials are a complete set of polynomials which are orthogonal over a unit circle. They were introduced by Zernike[21] in his famous paper on the phase contrast microscope and have been used extensively by many researchers since then.

The circle polynomials of Zernike are polynomials $V_n{}^m(x,y)$ in the real variables x and y. In terms of the polar coordinates, $x = \zeta \sin\theta$ and $y = \zeta \cos\theta$, they are expressed as

$$V_n^m\left(\zeta\sin\theta, \zeta\cos\theta\right) = R_n^m\left(\zeta\right)e^{im\theta}.$$ (2.29)

where $m \geq 0$ or $m > 0$ and $n \geq 0$ are integers, $n \geq |m|$, and $n-|m|$ is even. These polynomials satisfy the orthonormal relation

$$\int\int_{x^2+y^2 \leq 1} V_n^{m*}\left(x,y\right) V_n^m\left(x,y\right) dx dy = \frac{\pi}{n+1}\delta_{mm}\delta_{nn},$$ (2.30)

where δ_{ij} is the Kronecker delta function and the asterisk denotes the complex conjugate. The radial functions $R_n{}^m(\rho)$ are polynominals in ζ containing powers in ζ^n, ζ^{n-2}, ..., $\zeta^{|m|}$.

Instead of the complex polynomials $V_n{}^m$, one may use the real polynomials

$$\Phi_n^m = \frac{1}{2}\left[V_n^m + V_n^{-m}\right] = R_n^m\left(\rho\right) \cos m\theta$$ (2.31a)

and

$$\Phi_n^{-m} = \frac{1}{2i}\left[V_n^m - V_n^{-m}\right] = R_n^m\left(\rho\right) \sin m\theta.$$ (2.31b)

The wavefront can then be expressed as

$$\Phi(\rho,\theta) = \sum_{n=o}^{k} \sum_{m=o}^{n} R_n^m (C_{nm} \cos m\theta + D_{nm} \sin m\theta),$$ (2.32)

where C_{nm} and D_{nm} are the coefficients denoting the amount of a particular aberration present.

In this study the polynomial $R_n{}^m(\rho)\cos m\phi$ is sufficient to describe the aberrations because the system is assumed to be symmetrical about the meridional plane ($\phi = 0$). Table 2.1 lists the primary wavefront aberrations as well as lower order wavefront deformations. The first column of the table lists the third order and lower wavefront aberrations. The second and third columns list the corresponding n and m values used in the equations (2.29) through (2.32). The fourth column lists the specific functional form of each of these aberrations in terms of the Zernike polynomials of (2.32). The fifth column lists these same aberration terms where a conversion from the variables ρ and θ to the variables x and y have been accomplished. In this case the wavefront is expressed as

$$\Phi(x,y) = \sum_{i=o}^{k} \sum_{j=o}^{i} B_{ij} x^j y^{i-j} , \qquad (2.32)$$

where B_{ij} is the coefficient controlling the amount of a particular aberration which is present. In the last column, the aberration s are expressed as terms from the expansion

$$\Phi(\rho,\theta) = \sum_{n=o}^{k} \sum_{l=o}^{n} \rho^n (a_{nl}\cos^l\theta + b_{nl}\sin^l\theta), \qquad (2.33)$$

where the coefficients a_{nl} and b_{nl} are commonly called the Seidel coefficients. The difference between this expansion and the Zernike expansion of (2.32) is that the wavefront is expressed in terms of powers of $\cos\theta$ and $\sin\theta$ while in the Zernike expansion the wavefront is expressed in terms of multiples of the polar angle θ.

The entries for x-tilt, y-tilt, and piston are relevant for interferometric measurement and interpretation of wavefronts. Piston is a term referring to amounts of uniform phase across the exit pupil.

Aberration	n	m	Zernike	Monomial	Seidel
Third order spherical	4	2	$6\rho^4 - 6\rho^2 + 1$	$1-6y^2-6x^2+6y^4+12x^2y^2+6x^4$	ρ^4
Third order coma along x axis	3	1	$(3\rho^3-2\rho)\sin\theta$	$-2x + 3xy^2 + 3x^3$	$\rho^3\cos\theta$
Third order coma along y axis	3	2	$(3\rho^3-2\rho)\cos\theta$	$-2y + 3y^3 + 3x^2y$	
Astigmatism with axis at ±45°	2	0	$\rho^2\sin2\theta$	$2xy$	$\rho^2\cos2\theta$
Astigmatism with axis at 0° or 90°	2	2	$\rho^2\cos2\theta$	y^2-x^2	
Focus Shift	2	1	$2\rho^2-1$	$-1 + 2y^2 + 2x^2$	ρ^2
x Tilt	1	0	$\rho\sin\theta$	x	$\rho\sin\theta$
y Tilt	1	1	$\rho\cos\theta$	y	$\rho\cos\theta$
Piston	0	0	1	1	1

Table 2.1

Various representations of the first and third order wavefront aberrations[72].

2.3 PREVIOUS RESEARCH - APODISATION TO IMPROVE SYSTEM PERFORMANCE

The technique of suppressing the sidelobes in the irradiance distribution of the far-field diffraction pattern of a finite aperture was the original definition of apodisation. Mor... ...dly defined now, apodisation refers to any method which changes the performance of an optical system by modifying the amplitude and phase transmittance of the exit pupil. It has been shown by many researchers that apodisation can indeed improve the imaging properties of an optical system. Most of the work has assumed an aberration-free system, but recently there has been some interest in aberrated systems as well. However, there are apparently no studies concerning the use of apodisation to improve the performance of aberrated coherent optical systems.

2.3.1 Studies of Systems without Aberrations

2.3.1.1 Incoherent Optical Systems

In retrospect, the most common apodisation seen in optical systems is the central obscuration. Lord Rayleigh[22] was the first to point out that a circular stop in the center of a circular aperture causes the central maximum of the Airy pattern to become narrower and also increases the depth of focus. Straubel[23] appears to have been the first to study effects of an apodiser other than the central obscuration. Most studies since then have attempted to optimize some aspect of performance of an optical system by finding an appropriate apodising filter. Toraldo di Francia[24] originated the concept of superresolution over a limited field. This occurs when the diffraction pattern is forced to assume a series of zeroes, the first one being such that the central core is narrower than that for the uniform pupil, while the remaining zeroes are spaced around the core in such a way that a dark zone of limited extent and exhibiting low secondary lobes is

produced. Luneberg[25] used the calculus of variations to determine the pupil function given a prespecified distribution of image irradiance. In two comprehensive review articles, Wolf[26](1951) and later Jacquinot and Roizen-Dossier[27](1964) described the previous work. Since then, many workers (see for example references 28-31) have contr... ... to this field. Barakat[8,32,33] has been especially productive, solving three of the four apodisation problems originally posed by Luneberg[25].

2.3.1.2 Partially Coherent Optical Systems

Studies using partially coherent illumination are motivated by the physical fact that real systems are seldom either fully coherent or fully incoherent. McKechnie[34] has shown that, by obstucting the central part of the condenser, the resolution of a microscope may be improved. In a similar study, Nayyar and Verma[35] have calculated the limit of resolution (a modified Rayleigh criterion) for opaque annular and π-phase semi-transparent annular apertures of two partially coherent point objects. Other studies concerning two point objects, using different forms of apodisation, were conducted by Magiera and Pietraszkiewicz[36], Nayyar and Verma[37], and Mehta[38,39]. Kintner and Sillitto[40] have found a general condition for apodisers which insure suppression of edge-ringing. Som and Biswas[41] have studied the performance, in partially coherent light, of apodisers which were optimized for use in coherent illumination.

2.3.1.3 Coherent Optical Systems

The most noticeable defect in the coherent image of an edge object is the phenomena of edge-ringing. The use of apodisers to suppress edge-ringing has been shown to be successful by Araki and Asakura[42,43], K.P. Rao,et al[44,45], Smith[46], Leaver and Smith[47], and Thompson and Krisl[48]. However, it is noted in several of these studies that as edge ringing is suppressed the amount of edge shift is increased. The work of Araki

and Asakura[43] is particularly interesting because they have found an optimum apodiser which suppresses edge-ringing but introduces a minimum amount of additional edge shift. In related studies, Leaver[49] has investigated the image of a line object and Rao et al[50] have studied the images of trapazoidal objects.

The improvement of the two-point resolution of a coherent optical system has been approached from several viewpoints. Barakat[8] found apodisers which improved the two-point resolution according to the Sparrow criterion. Thompson[51] has investigated the diffraction by annular apertures which have central regions that are semi-transparent and which add a uniform phase. Such apertures will result in an improved two-point resolution. Wilkins[52] has solved the apodisation problem of determining the diffraction pattern which has a specified Sparrow limit of resolution and the maximum possible Strehl ratio. Clements and Wilkins[53] have solved the similar problem of maximizing the encircled energy with a specified Rayleigh resolution limit.

The work of Wilkins and Clements[52,53] applies not only to image forming systems but also to beam propagation systems. In a related study, Hazra[54] also has found a class of optimum apodisers which will maximize the encircled energy. Rao et al[55] have investigated the effect of a specific type of apodiser on several measures of far-field performance.

The performance of apodisers in the near field has been studied by Hadley[56] as well as Thompson and Krisl[48] These workers have shown that apodisation can decrease the peaks of the Fresnel diffraction pattern which arise from apertures within the beam propagation system with very little transmission loss.

The paper by Thompson and Krisl[48] presents a compact overview of the subject of apodisation as applied to coherent imaging and beam propagation systems. The problem of reducing the oscillations of the near field pattern in an aberration-free

system is solved. A comparison of five apodisers relative to several far-field performance parameters is also presented.

2.3.2 Studies of Systems with Aberrations

Most studies of systems with aberrations have assumed incoherent illumination, while only a few have considered the use of partially-coherent illumination. There have apparently been no studies specifically concerning the use of apodisation to improve the performance of aberrated coherent imaging systems. Some work has been done by considering the Gaussian nature of laser beams in aberrated beam propagation systems.

2.3.2.1 Incoherent Optical Systems

The majority of the work aimed at using apodisation to improve the performance of aberrated imaging systems has occurred in the last few years. However, Tsujiuchi's[57] review in 1963, discussed the derivation of optimum amplitude and phase filters to partially correct for defocusing and spherical aberration in systems with circular pupils.

A group at the University of Laval, has been studying the effect of apodisers in the presence of aberration. Biswas and Boivin[58] investigated optimum apodisers which were obtained by maximizing the encircled energy in circular, aberration-free systems. Then, they theoretically investigated the performance of these apodisers in the presence of primary and secondary spherical aberrations. Analytic expressions for various important properties of the diffracted field in the presence of apodisers and spherical aberration were presented, including amplitude point spread function, irradiance distribution, fractional encircled energy, Strehl ratio, and the two-point resolution. The authors found that the use of these filters in circular aberrated systems also increased the encircled energy. These same authors also investigated the influence of primary astigmatism on the performance of these optimum apodisers[59]

Attacking the problem directly, Hazra et al[60] found optimum apodisers which maximize encircled energy in the presence of spherical aberration and defocus. To make the filter manufacturing process easier, they designed optimum ladder-step apodisers having a finite number of uniformly transmitting zones, each with a different transmittance. They illustrat.. .me method with an example of an optimum 8-step apodiser used with different amounts of defocus, primary, and secondary spherical aberrations. They calculated the image irradiance distribution, encircled energy, and Strehl ratio. They predict that the performance of the system as measured by the encircled energy will be improved.

The problem was approached in a slightly different manner by Yzuel and Calvo[61]. They optimized the Strehl ratio by varying the amplitude and phase of filters, in the circular pupil of an aberrated optical system. The optimization process was halted when the Strehl ratio exceeded 0.8. The point spread function, MTF, and the irradiance distribution along the axis were then computed. This method was shown, theoretically, to improve both the Strehl ratio and the MTF. Mints and Prilepskii[62] also chose to maximize the Strehl ratio using phase and amplitude filters. They considered a system having third-order spherical aberration and found an apodisation which theoretically improved the Strehl ratio.

A Polish group searched for apodisers which minimized the second moment of the irradiance distribution. Magiera et al[63] did this, n the presence of four orders of spherical aberration by varying the coefficients of a polynomial describing the transmittance of the apodiser. This group, in a separate paper[64], then examined the effects of their optimum filter on the second moment of the image irradiance distribution in the presence of three orders of spherical aberrations. They showed

numerical results indicating the predicted improvement in performance. They also compared their filter to an optimum Bessel filter which was derived by Asakura and Ueno[65] for the aberration-free case.

2.3.2.2 ?:· ⸱ Coherent Optical Systems

Using the polynomial filter previously mentioned, Magiera and Pluta[66] derived formulae for the amplitude impulse response, second moment of the point spread function, the two-point irradiance distribution in partially coherent light, the point image contrast, and the equations which must be satisfied by the Sparrow and Rayleigh resolution criteria in the presence of third, fifth, and seventh order spherical aberrations.

Gupta and Singh[67] have investigated the influence of primary astigmatism on the irradiance distribution in the Fraunhofer diffraction patterns formed by an optical system with a circular aperture under partially coherent illumination when the mutual coherence function contains a spatially non-stationary quadratic phase term. Results are presented which illustrate the degrading effects of various amounts of astigmatism and the extent of improvement obtained when using a apodising filter

2.3.2.3 Coherent Optical Systems

Although there have been no studies specifically addressing apodisation in aberrated coherent imaging systems, portions of several of the studies previously outlined have some relevance to the proposed research. In several cases[57,58,66], the amplitude impulse response was calculated. However, these studies did not address the imaging properties of the aberrated and apodised systems. Magiera and Pluta[66] derived a formula for the two-point irradiance distribution in partially-coherent light. Taking the fully coherent limit, the formula presented will provide a useful comparison for one of

the results of the Chapter IV. Barakat[68] has calculated and plotted the images of edges, discs, and bars in the presence of defocus, coma, and spherical aberration. In aberrated beam propagation systems, the effect of a truncated Gaussian apodisation has been investigated by several researchers. Holmes et al[69] have considered the effect of Gaussian as well as sinusoidal phase aberrations on Gaussian beams in the near and far fields of an annular system. Lowenthal[70,71] has examined the far-field diffraction patterns for Gaussian beams with spherical aberrations; and has developed an aberration tolerance criterion for Gaussian beams. For these systems the apodisation was due to the inherent nature of the laser beam

2.3.3 Previous Research Conclusions

An extensive amount of work has been done using apodisation to improve the performance of aberrated optical systems. Some authors have used filters obtained in aberration-free studies while others have derived optimal filters assuming known amounts of fixed aberration. Generally, such apodisers have improved performance, but in a few cases they have actually degraded performance

To summarize the published research, most of the researchers who have studied the effects of apodisation on aberrated systems have assumed the use of incoherent illumination. Those who studied coherent systems have mostly concentrated on the image of a single point source. They have been interested in measures of performance such as the irradiance point spread function, encircled energy, and Strehl ratio. Only a few have considered the image of two point objects in partially coherent light. The issue of generalized imaging in apodised and aberrated coherent imaging systems has not been addressed.

2.4 THE GAUSSIAN APODISER

The Gaussian apodiser is the only type of apodiser considered in this research. Only one type of apodiser was used because most of the apodisers which were found to be optimum for various other applications differ little from each other or from a Gaussian. Additionally, the Gaussian was chosen because it has some intuitively pleasing effects when used in a coherent optical imaging system.

The first consideration when chosing an apodiser is that it produce an amplitude impulse response which is real and positive[48]. Many of the deleterious effects seen in coherent imaging (edge ringing for example) occur because the amplitude impulse response has negative regions. By contrast, an incoherent system has an impulse response which is everywhere real and positive. This realization leads to the conclusion that it would be appropriate to make the amplitude impulse response for the coherent case also real and positive. The amplitude impulse response of a coherent imaging system is proportional to the Fourier transform of the exit pupil. The Fourier transform of a Gaussian function is itself a Gaussian function. So a Gaussian apodiser in the exit pupil will produce an amplitude impulse response which is real and positive. This is not strictly true because the Gaussian will always be truncated by the finite aperture of the exit pupil. However, if the Gaussian is truncated far from its center, this statement will be approximately true.

Some of the apodisation functions suggested for use in conerent optical systems are shown in Fig. 2.6, where the amplitude transmittance is plotted versus the radius of the aperture. The radius of each function has been scaled so that the truncation point corresponds to a, the radius of the aperture being apodised. With the exception of the Lukosz limit, the functions are all very similar.
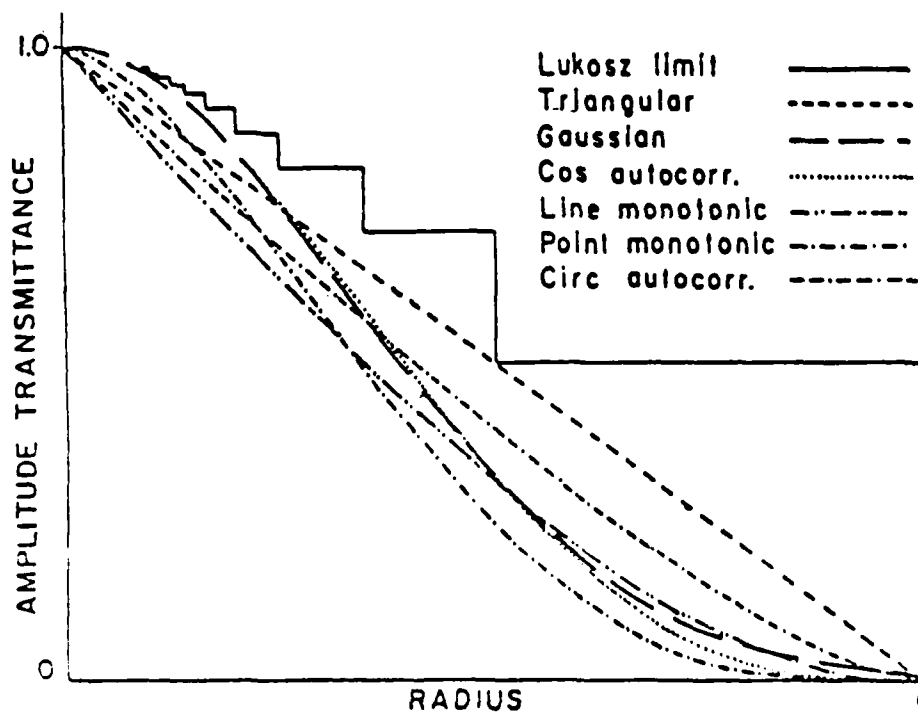
Fig.2.6 A comparison[82] of apodisation functions suggested for coherent optical imaging
systems. All functions were truncated at a radius of a. Also snown is the Lukosz
limit, a theoretical upper limit on apodisation functions.

An important consideration when a real and positive amplitude impulse response is desired was presented in a strict mathematical sense by Boas and Kac[84] and later independently from a signal-processing point of view by Lukosz[85]. They showed that there is an upper limit on the value of a space-limited function if the function is to have an everywhere positive Fourier transform. This limit is shown in Fig. 2.6.

The Gaussian was chosen for use in this research because, as well as producing a real and positive amplitude impulse response and not differing significantly from many of the apodisers which have been found useful, it has some nice effects on the system. One effect is that the transform of a Gaussian is a Gaussian. Also, when a Gaussian is used, the imaging system has some similarities to a laser propagation system. Both effects aid the intuitive process when thinking about the effects of the apodiser on the system

CHAPTER 3   THE AMPLITUDE IMPULSE RESPONSE - THEORY

3.1 INTRODUCTION

The amplitude impulse response, as pointed out in the last chapter, is central to
the analysis of optical imaging systems. In such systems, the image amplitude can be
found by performing a convolution of the geometric image with the amplitude impulse
response.

The amplitude impulse response has been calculated for a simple system having
various combinations of aberrations and apodisations. The physical situation is depicted
in Fig. 3.1. A unit-amplitude plane-polarized coherent plane wavefront is incident on a
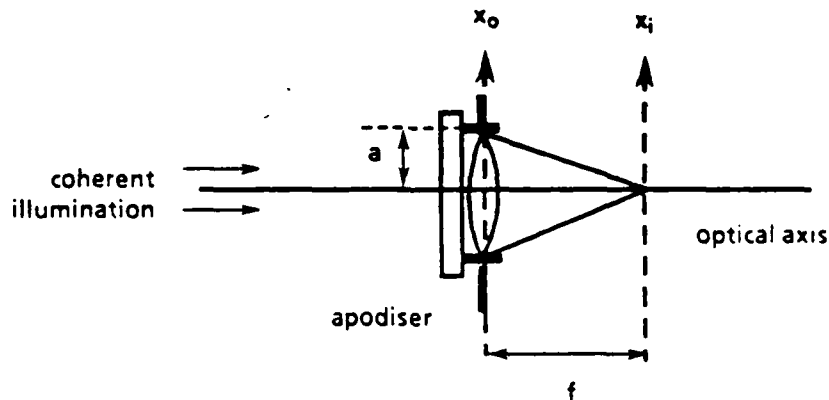
Fig.3.1   The diffraction geometry used in calculated the amplitude. impulse response.

test lens of radius a and focal length f. This is equivalent to an imaging system with a
point object at infinity. The y_0 and y_i axes which are perpendicular to both the x_0 and x_i
axes respectively and to the optical axis are not shown. The lens in general has
aberrations and an apodiser could be adjacent to the lens. The (x_0,y_0) plane is chosen to
be coincident with the lens.

In this case, (2.11) is used directly as

$$U_i\left(x_i,y_i\right) = \frac{e^{i\frac{2\pi}{\lambda}f}}{i\lambda f}e^{i\frac{\pi}{\lambda f}\left(x_i^2+y_i^2\right)}\int\int_{-\infty}^{\infty}U_o\left(x_o,y_o\right)e^{-\frac{i2\pi}{\lambda f}\left(x_o x_i + y_o y_i\right)}dx_o dy_o.$$ (3.1)

The field amplitude within the exit pupil is described by (2.7). Combining (2.7) and (2.11) yields

$$U_i\left(x_i,y_i\right) = F\left\{A\left(x_o,y_o\right)e^{i\frac{2\pi}{\lambda}\Phi\left(x_o,y_o\right)}B\left(x_o,y_o\right)\right\},$$ (3.2)

where the notation $F\{\ \}$ refers to the Fourier transform of the quantity within the brackets, the spatial frequencies of the transform are $f_x = x_i/\lambda f$ and $f_y = y_i/\lambda f$, and the terms in front of the integral have been dropped. The term $U_{in}(x_o,y_o)$ in (2.7), is the amplitude of the input wavefront, which in this case equals one.

The aberration term $\Phi\left(x_o,y_o\right)$ in the exponent of (3.2) can be expressed in terms of the Seidel coefficients by describing the aberrated wavefront with the expression

$$\Phi\left(\rho,\theta\right) = \sum_{n=0}^{k}\sum_{l=0}^{n}\rho^n\left(a_{nl}\cos^l\theta + b_{nl}\sin^l\theta\right),$$ (2.32)

where the coefficients a_{nl} and b_{nl} have units of wavelength and ρ has been normalized to unity at the edge of the aperture. This is the form of the aberration function assumed when referring to the amount of aberration present in a particular system.

When calculations are performed however, the monomial form of the Zernike polynomial

$$\Phi\left(x,y\right) = \sum_{i=0}^{k}\sum_{j=0}^{i}B_{ij}x^j y^{i-j}$$ (2.33)

is used instead. This is because the Fourier transform operation indicated in (3.2) is performed on the computer as a discrete fast Fourier transform on a regular rectangular array

The apodisation used throughout this dissertation is in terms of the real amplitude transmittance. It has the form

$$A\left(r\right) = e^{-3r^2}$$

<div align="right">(3.3a)</div>

$$r^2 = x_i^2 + y_i^2,$$

<div align="right">(3.3b)</div>

where the constant in the exponent was chosen so that the value of A(r) at the edge of the aperture, r = 1, was equal to 0.050 (see Fig. 3.2). Thus there was very little amplitude in the transmitted wavefront at the edge of the aperture. This should allow the separation of the effects of the aberrations from the effects of the hard aperture.

A VAX-11/750 computer was used to compute (3.2) using a program written in FORTRAN-77. The Fourier transform was accomplished by using a fast-Fourier transform[73] subroutine from the IMSL[74] package. This program, labeled PSF.FOR, is documented in Appendix 1.

The quantity $U_i(x_i,y_i)$ is, in general, complex. Consequently, the output of the program is in terms of real and imaginary coefficients. That is,

$$U_i\left(x_i,y_i\right) = a\left(x_i,y_i\right) + ib\left(x_i,y_i\right) = m\left(x_i,y_i\right)e^{ip\left(x_i,y_i\right)},$$

<div align="right">(3.4)</div>

where $a(x_i,y_i)$ and $b(x_i,y_i)$ are the just mentioned coefficients and $m(x_i,y_i)$ and $p(x_i,y_i)$ are the modulus and phase, respectively, of $U(x_i,y_i)$.

Coherently illuminated systems are linear in complex amplitude. However, if measurements are to be made in an experiment, it is the irradiance $I_i(x_i,y_i)$ which is
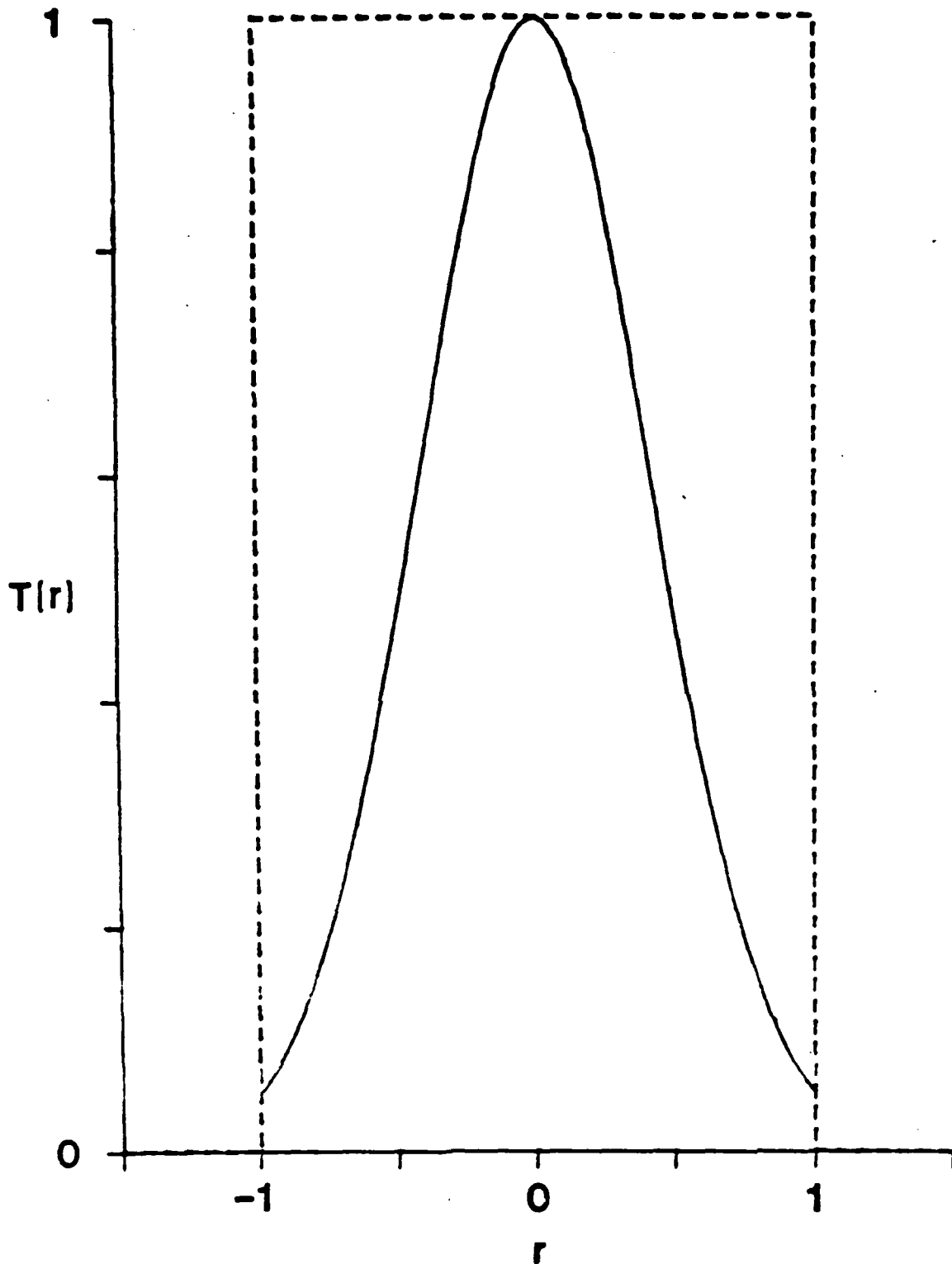
Fig.3.2 The amplitude transmittance of the Gaussian filter used in this study (solid line) is shown relative to the unapodised amplitude transmittance of the exit pupil (dashed line).

usually measured . The irradiance is related to the complex amplitude by

$$I_i\left(x_i,y_i\right) \propto U_i\left(x_i,y_i\right)U_i^*\left(x_i,y_i\right) = \left| U_i\left(x_i,y_i\right) \right|^2, \tag{3.5}$$

where the asterisk denotes the complex conjugate.

3.2 COMPARISONS WITH KNOWN RESULTS

A typical output of this program is displayed in Fig. 3.3. The system, in this case was unaberrated and unapodised and the pupil function was a circular aperture. The distance coordinates used in Fig. 3.3 , as well as in many other figures in the thesis, are the canonical distance coordinates u and v. They are canonical in the sense that the pattern displayed in these figures is independent of the exit pupil size, the wavelength of illumination, and the distance from the exit pupil to the image plane. Specifically, these new coordinates are defined by

$$u = \frac{2\pi a}{\lambda d_i}x_i \quad and \quad v = \frac{2\pi a}{\lambda d_i}y_i , \tag{3.6}$$

where a is the radius of the exit pupil, λ is the wavelength of the illumination, d_i is the distance from the exit pupil to the image plane, and x_i and y_i are the real coordinates in the image plane.

A coherent optical system is linear in field amplitude, which is a complex quantity. So unlike an incoherent system, the phase in the optical field is critically important in determining the final image irradiance distribution. For this reason, the phase has been calculated for the unaberrated case in Fig. 3.3 and for many of the aberrated cases considered later in this chapter.

The phase distribution in the amplitude impulse response of an unaberrated system (see Fig. 3.3b) is uniform everywhere except along concentric circles where the phase jumps discontinuously by an amount equal to π radians. These jumps occur at the same spatial locations as do the zero values in the modulus distribution of Fig. 3.3a. This implies that every other ring in the amplitude impulse response is composed of negative

46
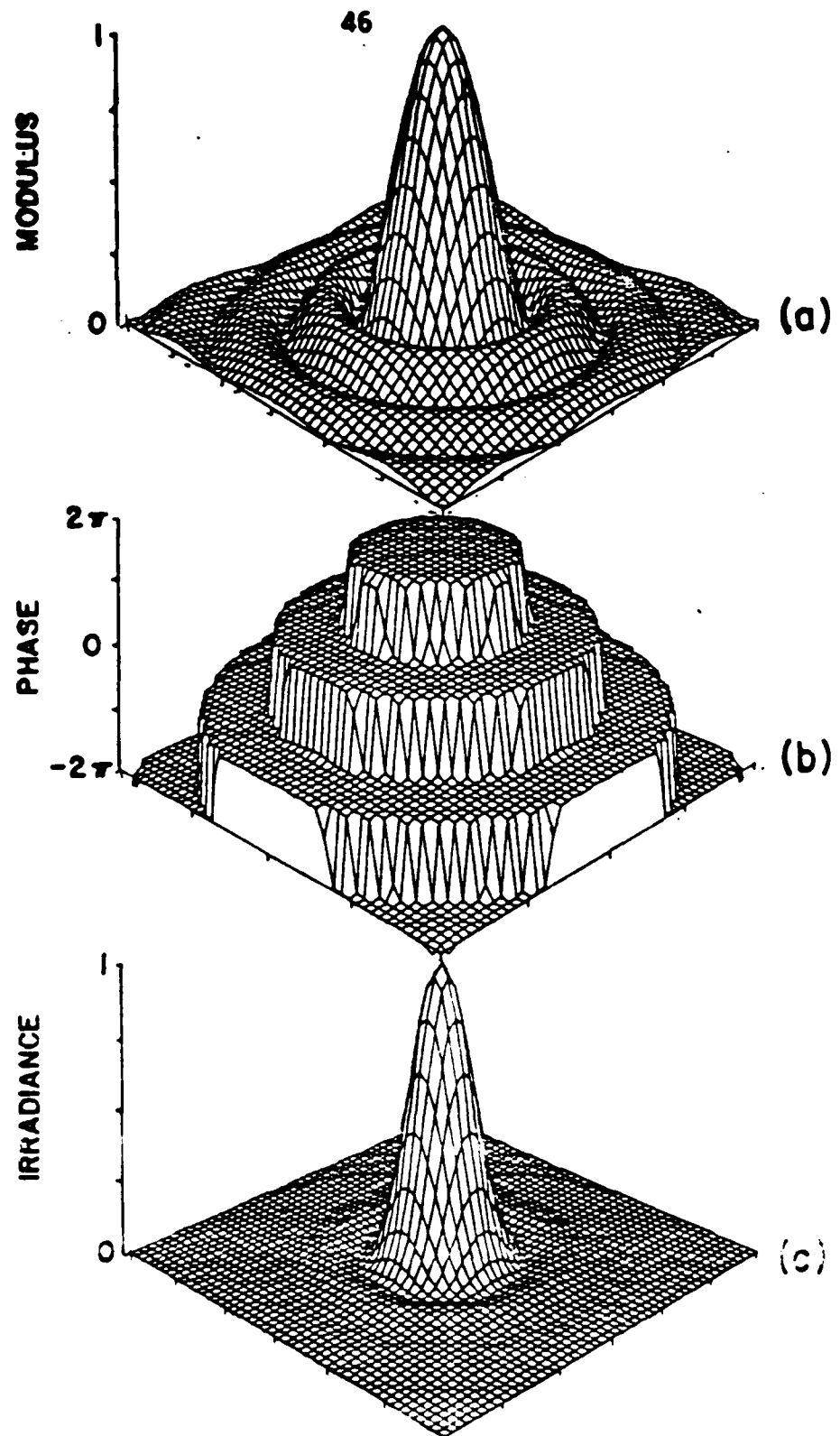
Fig 3.3 The impulse response of an unaberrated, unapodised, circularly symmetric optical system in terms of (a) modulus, (b) phase, and (c) irradiance. The unlabeled axes are canonical distance coordinates. All plots have the same distance scales.

values. It is these negative regions which cause the ringing phenomena seen in the image of an edge (see Fig. 1.2). Thus the knowledge of the phase distribution in the amplitude impulse response is very important in determining the behavior of the system.

The irradiance distrib   of this impulse response is shown in Fig. 3.3c. It is obtained by squaring the modulus distribution. Since the optical system in this case is unaberrated and has a circular exit pupil, it is expected that the irradiance distribution would approximate an Airy[7] pattern. A careful comparison of Fig. 3.3c with a theoretical Airy distribution reveals the error between the two patterns to be less than 1%. This error arises mainly from the problem of inadequately representing a circular aperture with a rectangular array of samples. Nevertheless, this agreement is quite close and thus lends credibility to the theoretical development and the computer program used to realize that development.

The program gains additional credibility when the irradiance patterns in the presence of simple aberrations are compared to similar results in the literature. Fig. 3.4 displays the theoretical irradiance impulse responses for two optical systems with different amounts of aberrations. The impulse response in Fig. 3.4a is from an optical system having 0.48 waves of coma; i.e., $\Phi(\rho,\theta) = 0.48\lambda\rho^3\cos\theta$. The quantity λ refers to the wavelength of the coherent illumination. The ring structure has been distorted by the presence of the aberration such that the ring has been flattened on one side of the central lobe and heightened on the opposite side. In Fig. 3.4b the aberration in the system is 0.16 waves of astigmatism ($\Phi(\rho,\theta) = 0.16\lambda\rho^2\cos^2\theta$). These particular aberration values were chosen because another author (Nijboer [75,76]) has calculated similar results using these values. Nijboer's results are reproduced in Fig. 3.5 where the plots show the irradiance distribution for (a) 0.48 wave of coma and (b) 0.16 waves of astigmatism.
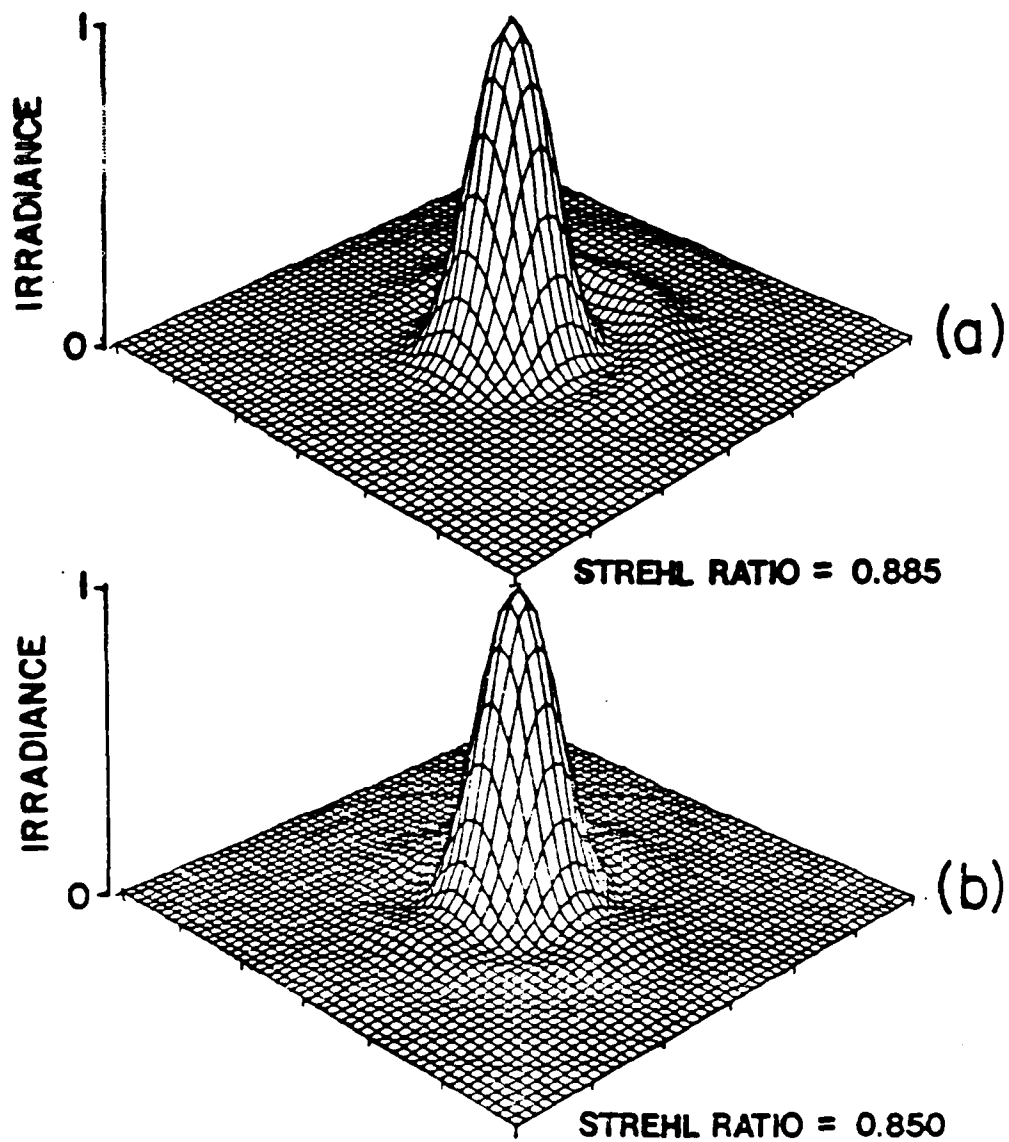
Fig.3.4 The irradiance impulse response through a coherent, unapodised, circularly symmetric optical system having (a) 0.48 waves of coma, and (b) 0.16 waves of astigmatism. The unlabeled axes are canonical distance coordinates. Both plots have the same distance scales.
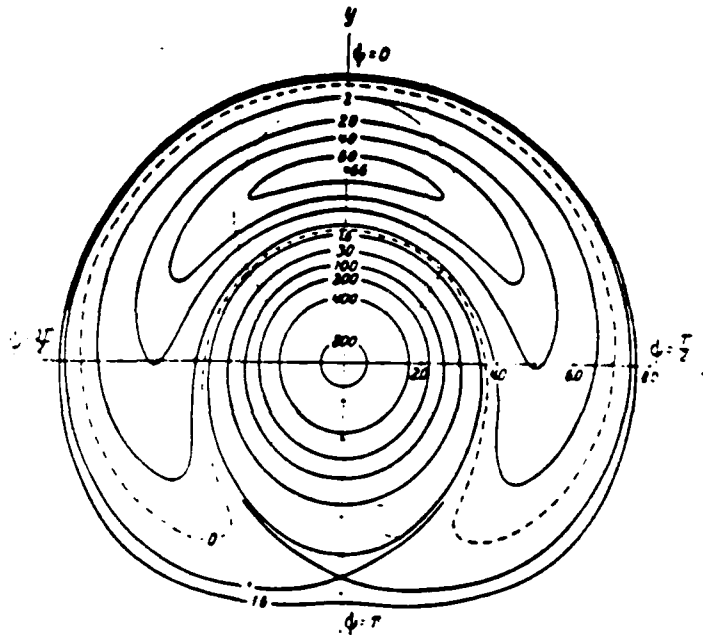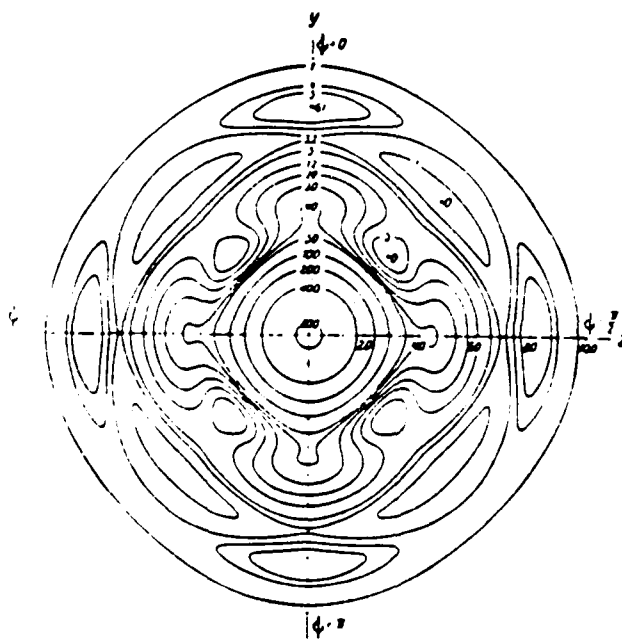
STREHL RATIO = 0.879

STREHL RATIO = 0.840

Fig 3.5 Irradiance contours in the images of point sources through an optical system
having (a) 0.48 waves of coma and (b) 0.16 waves of astigmatism. These plots are
from Nijboer[75,76]

These plots display the irradiance impulse responses in terms of the contours of equal irradiance. The presentation formats for Figs. 3.4 and 3.5 differ but the qualitative agreement is good. The comatic patterns both show a disappearance of the first ring on one side of the central lobe and an enhancement of that ring the opposite side; and the astigmatic patterns both show a distinct four-lobed character in the first ring. As a quantitative measure, the Strehl ratio was computed for the two cases and compared to Nijboer's results. The Strehl ratio for each plot of the two figures is shown beside the plot. The agreement here is very good.

Similar comparisons were made for other amounts of aberrations. In each case the qualitative agreement between the model developed here and the data published by other authors was quite good. The quantitative agreement was typically on the order of 1%.

3.3 THE EFFECT OF ABERRATIONS ON THE IMPULSE RESPONSE

3.3.1 Defocus

The aberration of defocus has the functional form $\Phi(\rho,\theta) = a_{21}\rho^2$, where the coefficient a_{21} is the amount of aberration. The subscripted numbers 2 and 1 come from columns 2 and 3 respectively of Table 2.1. Defocus is the simplest type of aberration in that the real wavefront differs from the spherical reference wavefront only in its radius of curvature. A calculation of the amplitude impulse response for the case when $a_{21} = 0.5\ \lambda$ yields the results shown in Fig. 3.6. In this figure the top two plots show the modulus and phase of the amplitude impulse when the exit pupil of the optical system has a uniform transmittance, i.e., there is no apodisation. For ready comparison, the amplitude impulse response (modulus and phase) for the same system with a Gaussian apodiser is shown in the bottom two plots of this same figure.
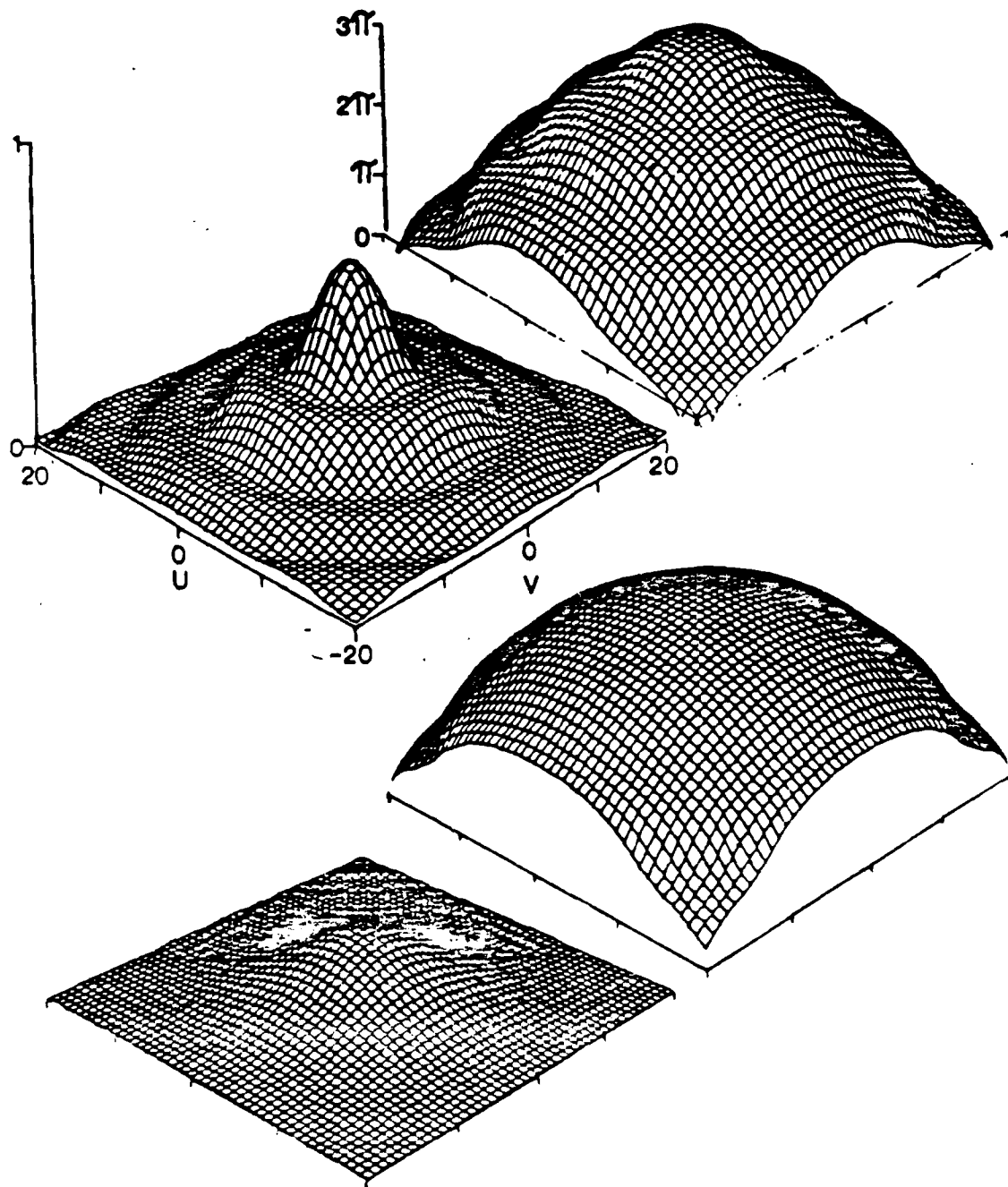
Fig.3.6 The amplitude impulse response (modulus and phase) in the presence of 0.5λ defocus and for the case of an unapodised and Gaussian apodised aperture. The top two plots are for the unapodised case while the bottom two are for the case of a Gaussian apodiser. The vertical scales for the modulus plots (left hand column) and the phase plots (right hand column) are indicated by the top two plots. This same scaling is used in Figs 3.9, 3.12, and 3.15.

The modulus and phase of the unapodised amplitude impulse response (top two plots) should be compared to the analogous plots of Fig. 3.3 where there are no aberrations in the system. The peak value of the modulus in the aberrated case has decreased relative to the unaberrated case. The zero values in the modulus pattern for the unaberrated case have evolved to relative minimums which do not go to zero. The phase of the aberrated amplitude impulse response (upper right plot of Fig. 3.6) no longer has the discontinuities evident in the unaberrated case.

When the apodiser described by (3.3) and plotted in Fig. 3.2 is applied to this aberrated system, the modulus of the amplitude impulse response (lower left plot of Fig. 3 6) is considerably smoothed, as is the phase. The phase varies by less than π radians over the region of the modulus plot where the modulus is greater than 10% of its peak value. So this amplitude impulse response does not change sign until the absolute value of the amplitude is quite small. Thus the impulse response is almost real and positive.

This has important implications for the imaging performance of this optical system. For instance, the ringing in the coherent image of an edge is caused by the negative regions of the impulse response. In this case the apodiser has smoothed the amplitude impulse response such that it has very little amplitude in the regions where there are negative values of amplitude. It can be expected then, that the image of an edge through this system would be free from ringing. The results in the next chapter confirm this expectation

The amplitude impulse response, both unapodised and apodised, for other values of defocus are shown in Fig. 3.7. Here the amount of aberration is different for each column of plots, varying from 0.1 λ on the left to 1.0 λ on the right. From these plots we can see the evolution of the modulus and phase as more defocus is added to the system.

AMPLITUDE IMPULSE RESPONSE
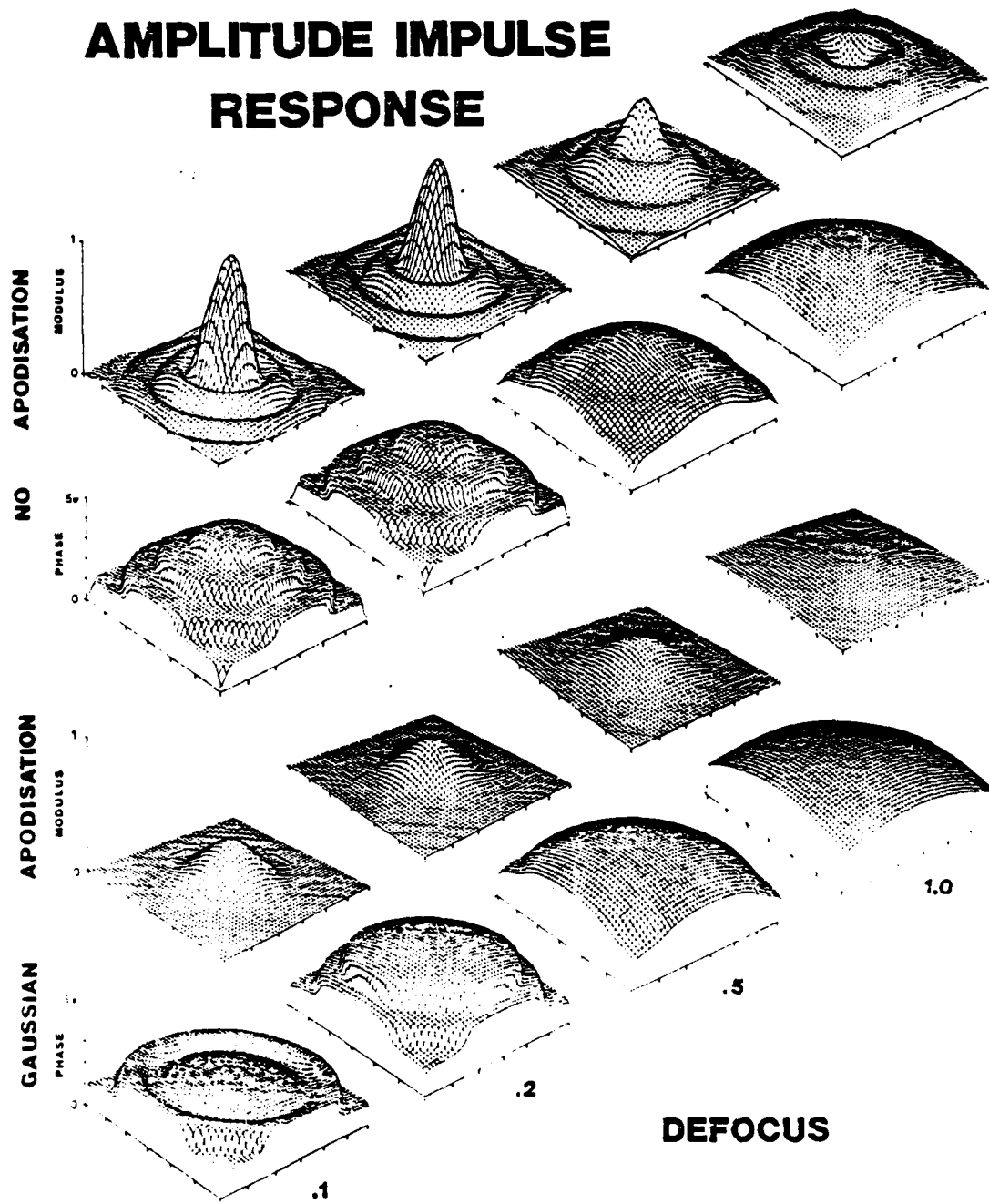
Fig.3.7 The amplitude impulse response (modulus and phase) with varying amounts of defocus for the case of an unapodised and Gaussian apodised exit pupil. The amount of aberration for each column is indicated at the bottom of that column.

54
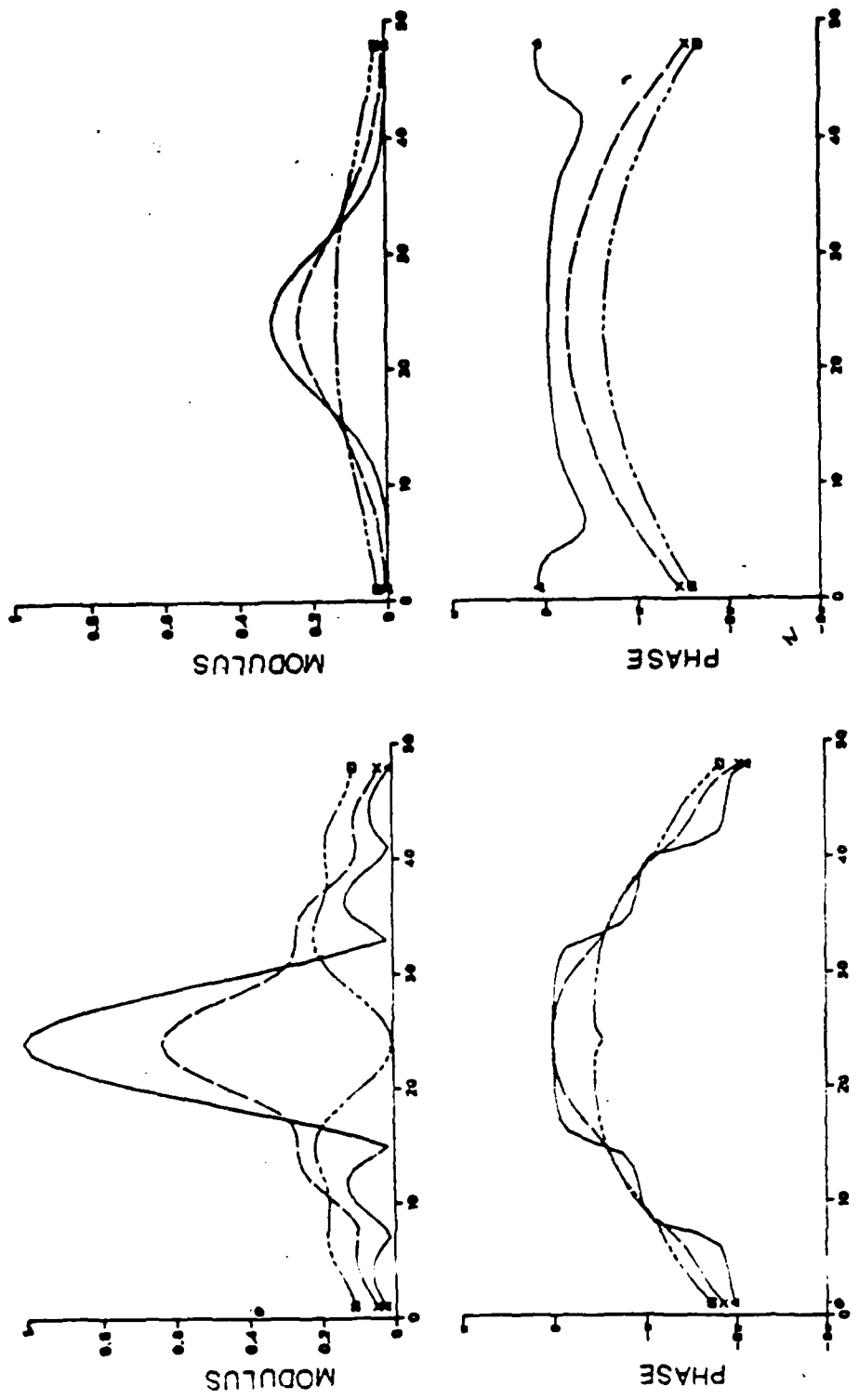
Fig. 3.8 Central slices through the plots of modulus and phase in the presence of varying amounts of defocus and for the unapodised as well as Gaussian apodised cases (———— 0.1λ, ———— 0.5λ, —·—·—· 1.0λ).

The modulus and phase along slices through the center of some of these impulse responses are shown in Fig. 3.8. The relationship of phase to modulus is clearly seen in this figure.

Apodisation, in each case of the last three figures, smoothes both the modulus and phase. In each case, the amplitude impulse response becomes almost real and positive when the apodiser is applied. There are, however, limits to this process. As the amount of aberration increases the apodiser becomes less effective in making the amplitude impulse response almost real and positive. For the case of one wave of defocus, it appears that the phase changes by more than π radians over the region where the modulus is still relatively large.

3.3.2 Spherical Aberration

The aberration of spherical has the functional form $\Phi(\rho,\theta) = a_{42}\rho^4$. Spherical is a radially symmetric aberration. Due to its *fourth power dependence on the radial* distance parameter ρ, spherical aberration describes a wavefront having the largest deviation from the spherical reference wavefront of any of the aberrations considered here. A calculation of the impulse response (modulus and phase when $a_{42} = 0.5 \lambda$ is shown in Fig. 3.9. The top two plots (the unapodised case) should be compared to the unaberrated impulse response of Fig. 3.3. The presence of spherical aberration causes a decrease in the value of the central peak (Strehl ratio) and an increase in the energy in the side lobes, particularly the first side lobe. The position of the ring of minimum values between the central lobe and the first side lobe remains unchanged.

The impulse response when an apodiser is used is shown in the bottom two plots of Fig. 3.9. The apodiser used is the one described by (3.3) and plotted in Fig. 3.2. As in the case of defocus, the use of the apodiser has resulted in a much smoother impulse response. An examination of the phase distribution shows that the phase is nearly
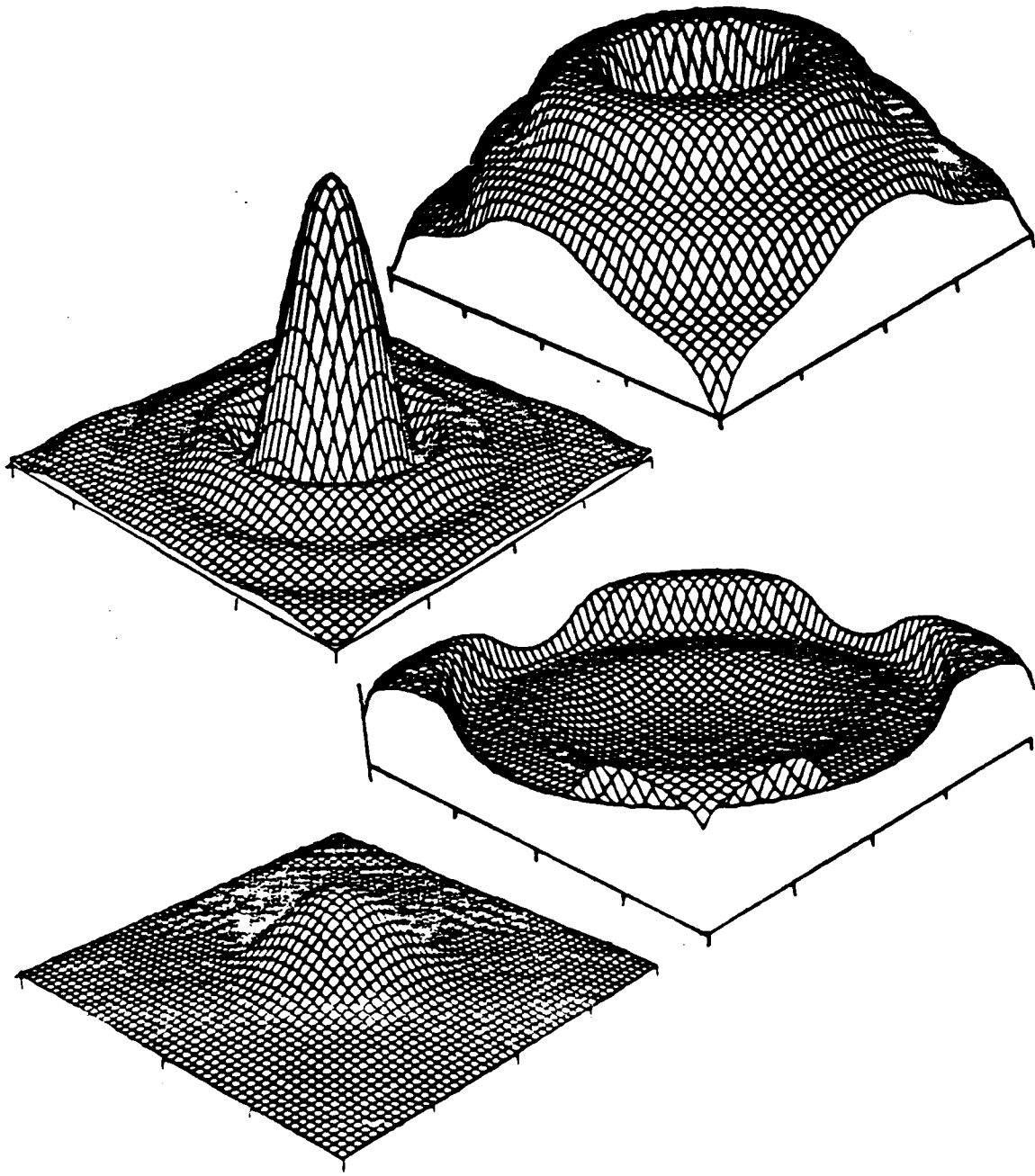
Fig.3.9 The amplitude impulse response (modulus and phase) in the presence of 0.5λ
spherical aberration and for the case of an unapodised and Gaussian apodised
aperture. The top two plots are for the unapodised case while the bottom two
are for the case of a Gaussian apodiser. See Fig. 3.6 for the scaling.

AMPLITUDE IMPULSE RESPONSE
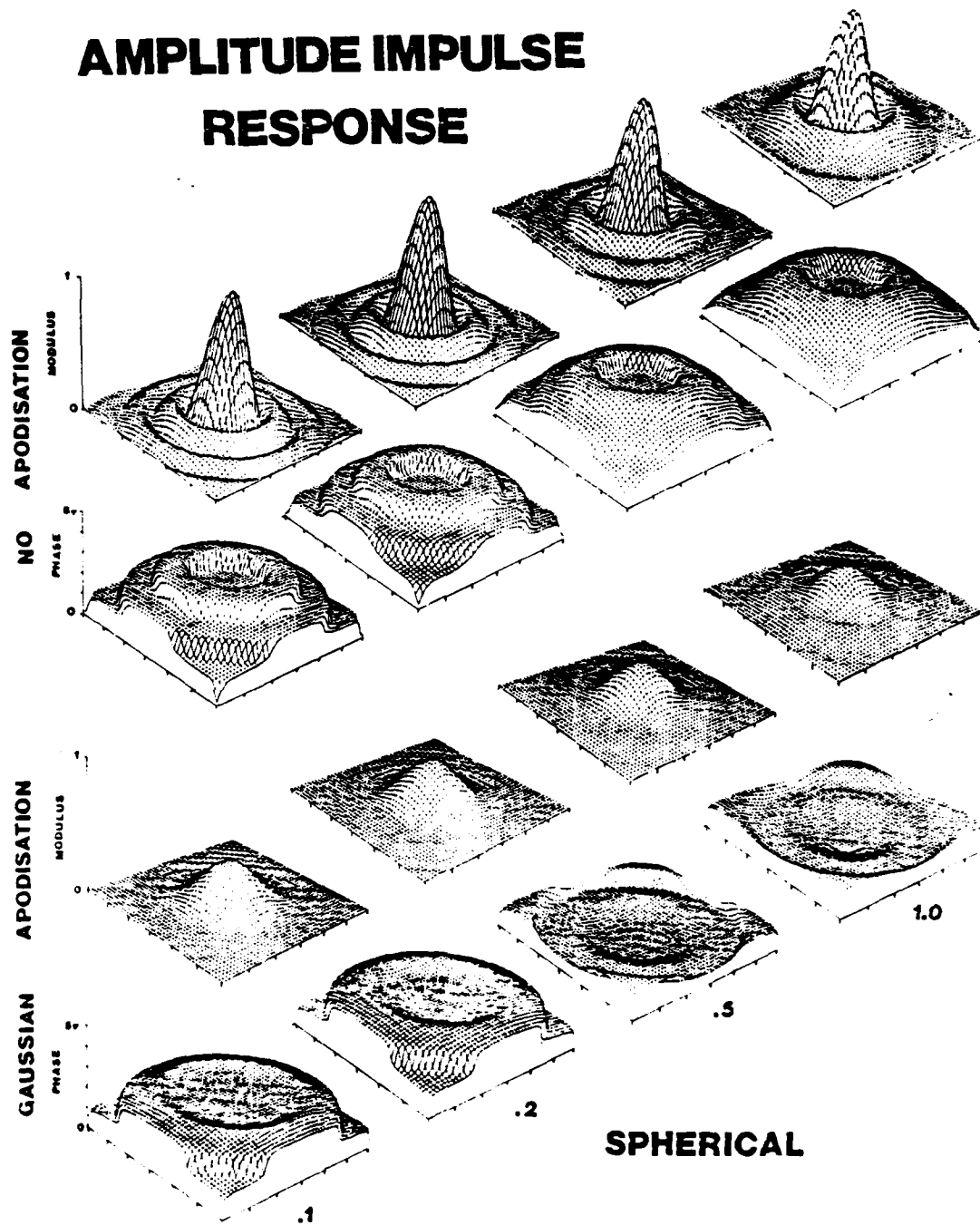
Fig.3.10   The amplitude impulse response (modulus and phase) with varying amounts
of spherical aberration for the case of an unapodised and Gaussian apodised
exit pupil. The amount of aberration for each column is indicated at the
bottom of that column.
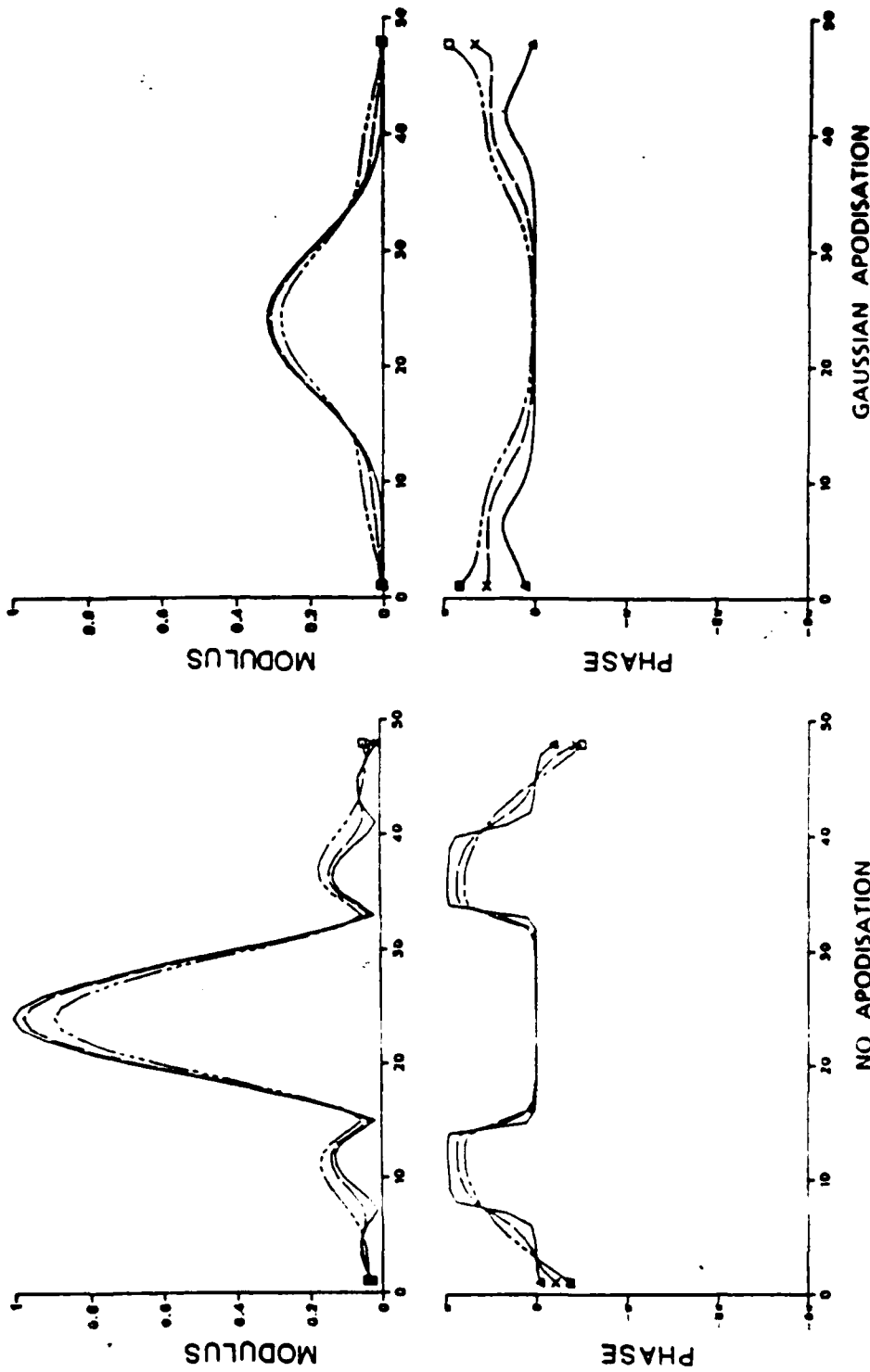
Fig.3.11 Central slices through the plots of modulus and phase in the presence of varying amounts of spherical and for the unapodised as well as Gaussian apodised cases (———— 0.1λ, — — — — 0.5λ, — · — · — 1.0λ).

uniform over the region of the impulse response having significant amounts of energy. This impulse response can also be described as being almost real and positive.

The evolution of the unapodised and apodised amplitude impulse responses as more spherical aberration is added to the system is shown in Fig. 3.10. Central slices through some of these plots are shown in Fig. 3.11. The same general phenomena seen in the case of defocus are seen here as well. The use of the apodiser results in an impulse response which is free from side lobes in the modulus pattern and which has a relatively flat phase over the region where there is a significant amount of energy.

Again there are limits to this process. When the amount of spherical aberration is about one wave, the impulse response has significant amounts of energy in regions where the phase has changed by $\lambda/2$. So the apodiser is not totally effective, although the apodised impulse response is still much smoother than the unapodised one.

3.3.3 Coma

The aberration of coma can be described by $\Phi(\rho,\theta) = a_{31}\rho^3\cos\theta$. Coma is the first aberration considered for which the wavefront in the exit pupil depends on the polar angle θ as well as the radial distance ρ. This aberration therefore produces an unsymmetrical amplitude impulse response as seen in Fig. 3.12. The use of the apodiser in this case appears to be less effective than in the previous cases, because the first side lobe is still evident in the modulus of the apodised impulse response (lower left plot of Fig. 3.12). Also, there is a π phase change in the region of this first side lobe.

The evolution of these impulse responses with increasing amounts of aberration is shown in Fig. 3.13. Central slices of some of these data are shown in Fig. 3.14. The slices are along the axis showing the minimum amount of symmetry. The same general conclusions that were drawn for the cases of defocus and spherical aberration can be drawn for this case as well. First, the apodiser is effective in transforming the aberrated
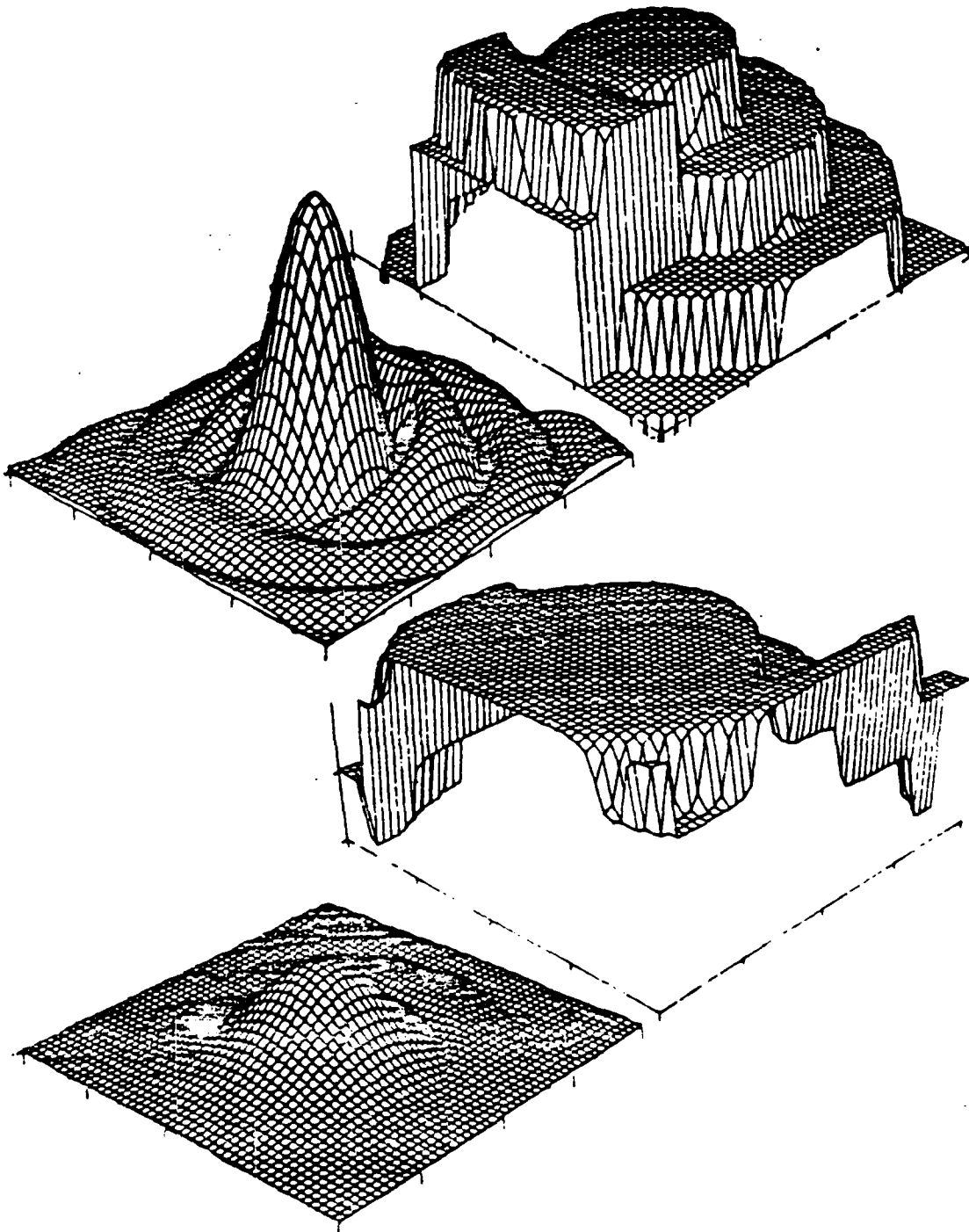
Fig. 3.12   The amplitude impulse response (modulus and phase) in the presence of -0.5λ
y-axis coma and for the case of an unapodised and Gaussian apodised
aperture. The top two plots are for the unapodised case while the bottom
two are for the case of a Gaussian apodiser. See Fig. 3.6 for scaling.

AMPLITUDE IMPULSE RESPONSE
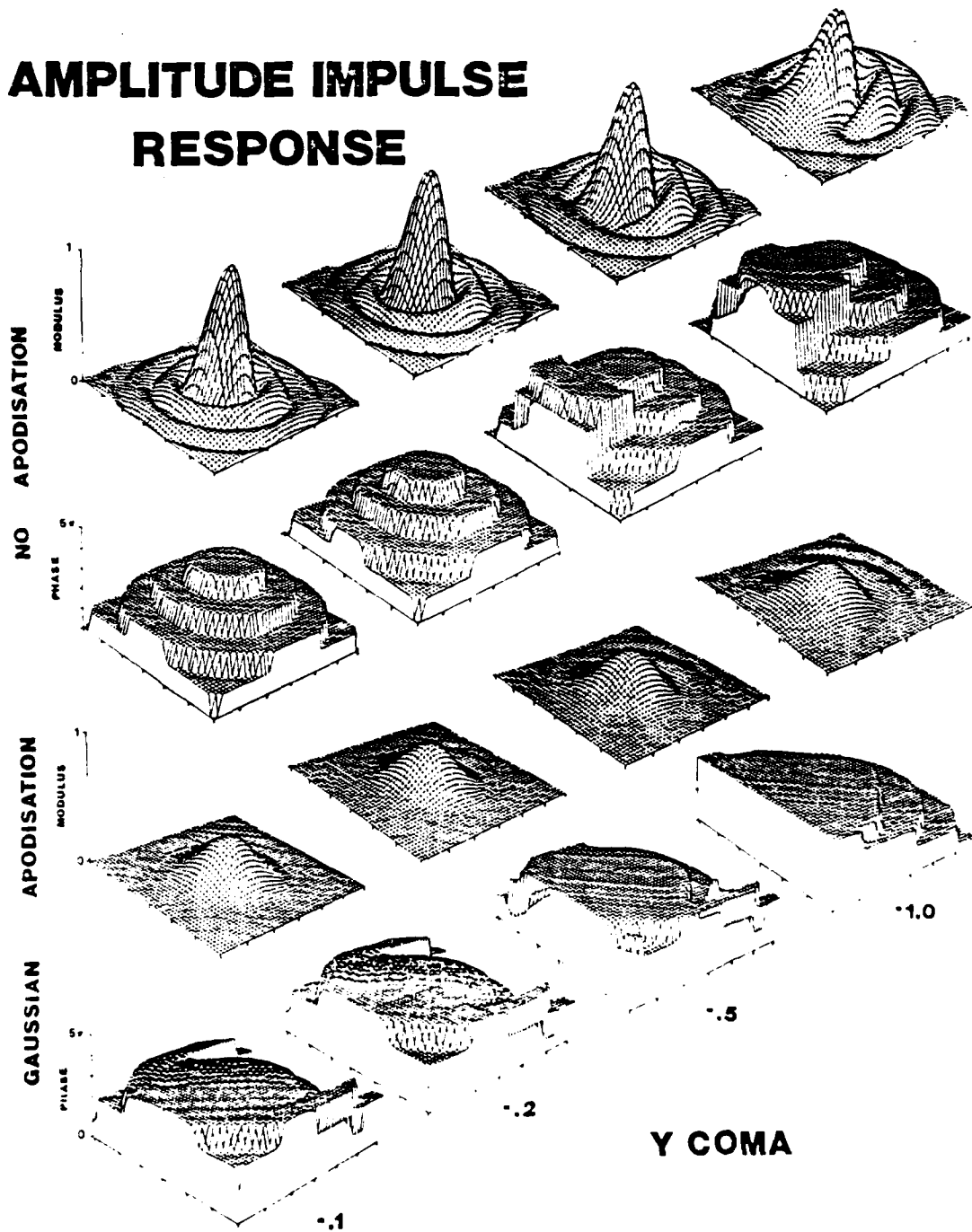
Fig.3.13 The amplitude impulse response (modulus and phase) with varying amounts of y coma for the case of an unapodised and Gaussian apodised exit pupil. The amount of aberration for each column is indicated at the bottom of that column.

62
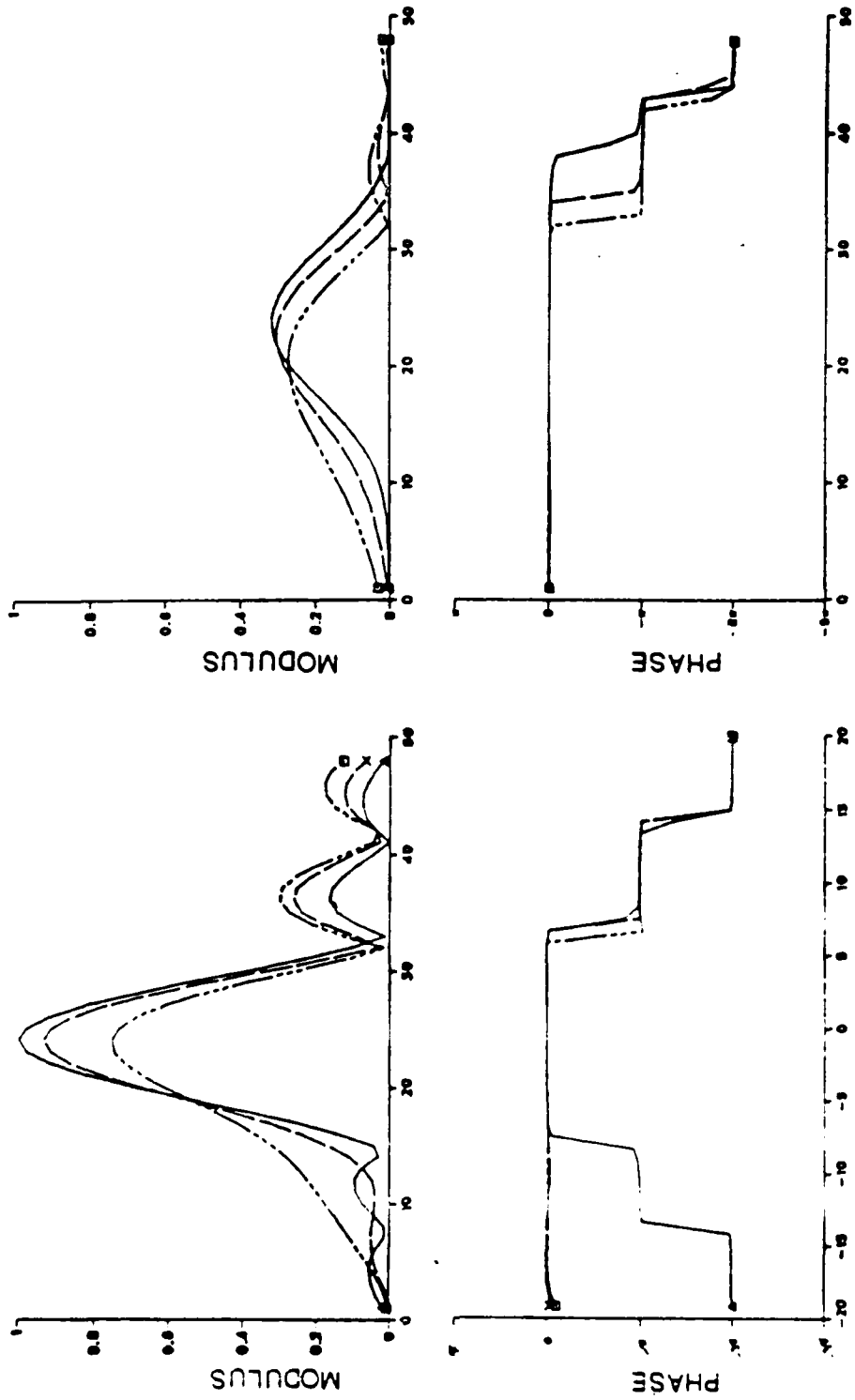
Fig 3 14 Central slices through the plots of modulus and phase in the presence of varying amounts of y-axis coma and for the unapodised as well as Gaussian apodised cases (—— 0.1λ, —— 0.5λ, —·—·— 1.0λ).

impulse response into a much smoother function. Second, there are limits to the effectiveness of the apodiser. The limit in this case appears at a lower value of aberration than in the other cases. For as little as half a wavelength there is a π phase change in a region of the impulse response where t⁻ ⁻⁻dulus shows a side lobe.

3.3.4 Astigmatism

The aberration of astigmatism is described by $\Phi(\rho,\theta) = a_{20}\rho^2\cos^2\theta$. Like coma, astigmatism is an unsymmetric aberration. The appearance of the unapodised and apodised impulse responses when $a_{20} = 0.5\lambda$ is shown in Fig. 3.15. Both phase plots show a saddle shape which is characteristic of astigmatism. Astigmatism results in a wavefront which has different radii of curvature along two orthogonal directions in the plane of the exit pupil. This behavior is evident also in the focal plane as seen in Fig. 3.15.

The effect of apodisation is to smooth both the amplitude and phase of the impulse response. This behavior holds as the amount of aberration is increased from 0.1 λ to 1.0 λ, as seen in Figs. 3.16 and 3.17. The general shapes of functions in Fig. 3.17 differ little from the analogous plot for the case of defocus (Fig. 3.8). This is because, in one dimension, astigmatism results in a wavefront which is spherical but having a radius of curvature different from the reference wavefront.

The same conclusions as before can be drawn. That is, the apodiser smooths the aberrated impulse response for a limited amount of aberration. The limit in this case appears to be about one wavelength.
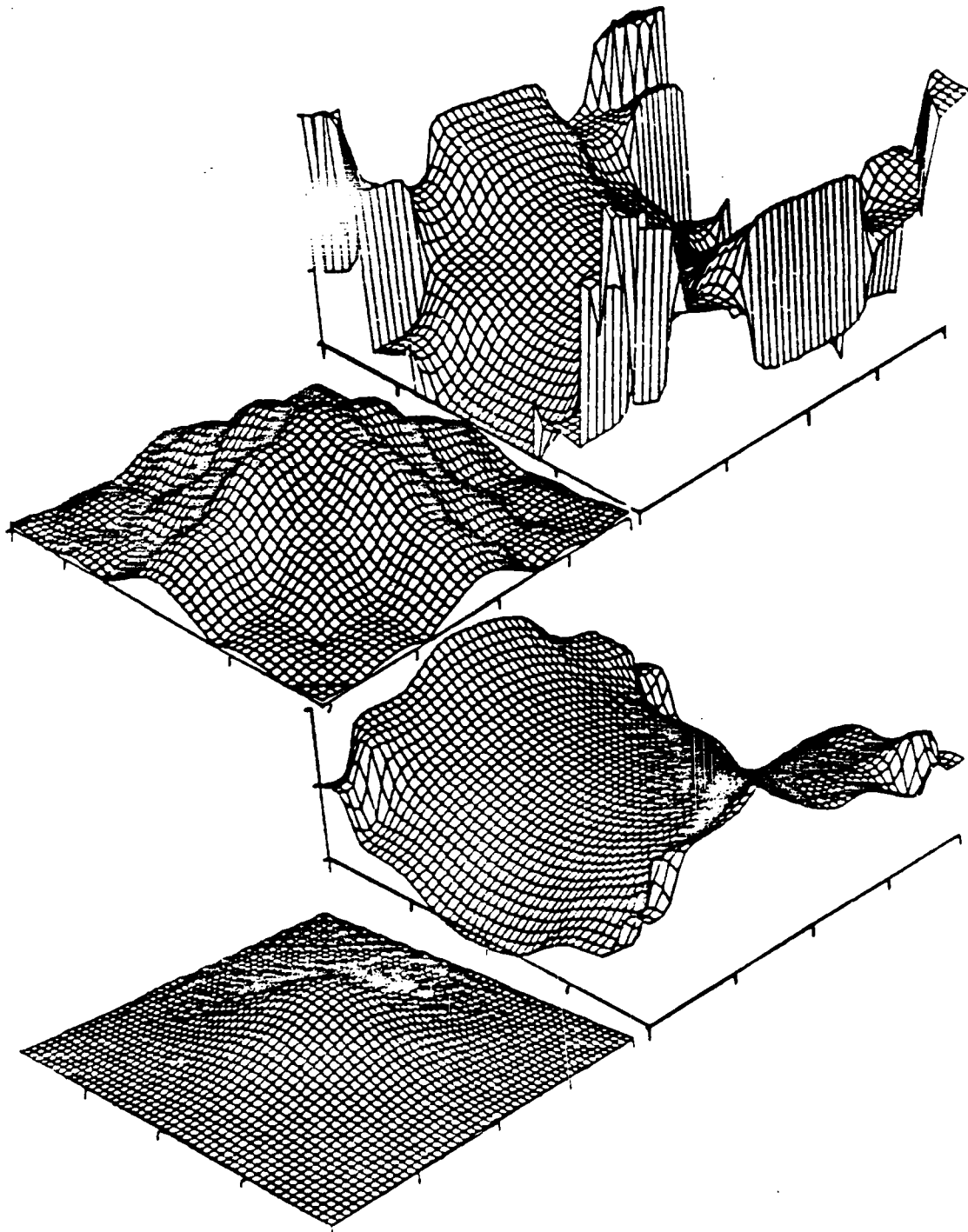
Fig.3.15 The amplitude impulse response (modulus and phase) in the presence of 0.5λ 0° astigmatism and for the case of an unapodised and Gaussian apodised aperture. The top two plots are for the unapodised case while the bottom two are for the case of a Gaussian apodiser. See Fig. 3.6 for scaling.

AMPLITUDE IMPULSE
RESPONSE
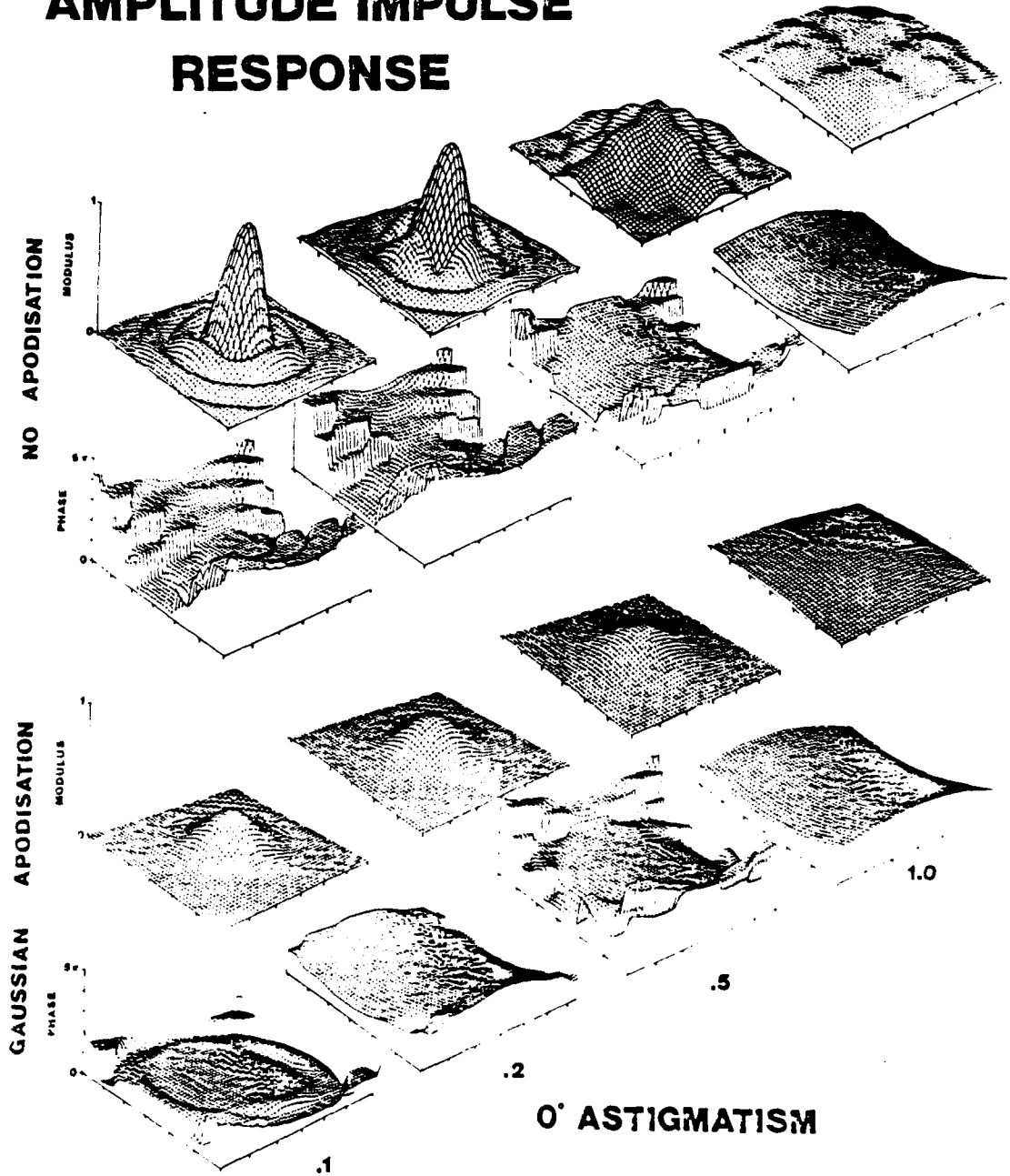
Fig.3.16   The amplitude impulse response (modulus and phase) with varying amounts
of 0° astigmatism for the case of an unapodised and Gaussian apodised exit
pupil. The amount of aberration for each column is indicated at the bottom
of that column.
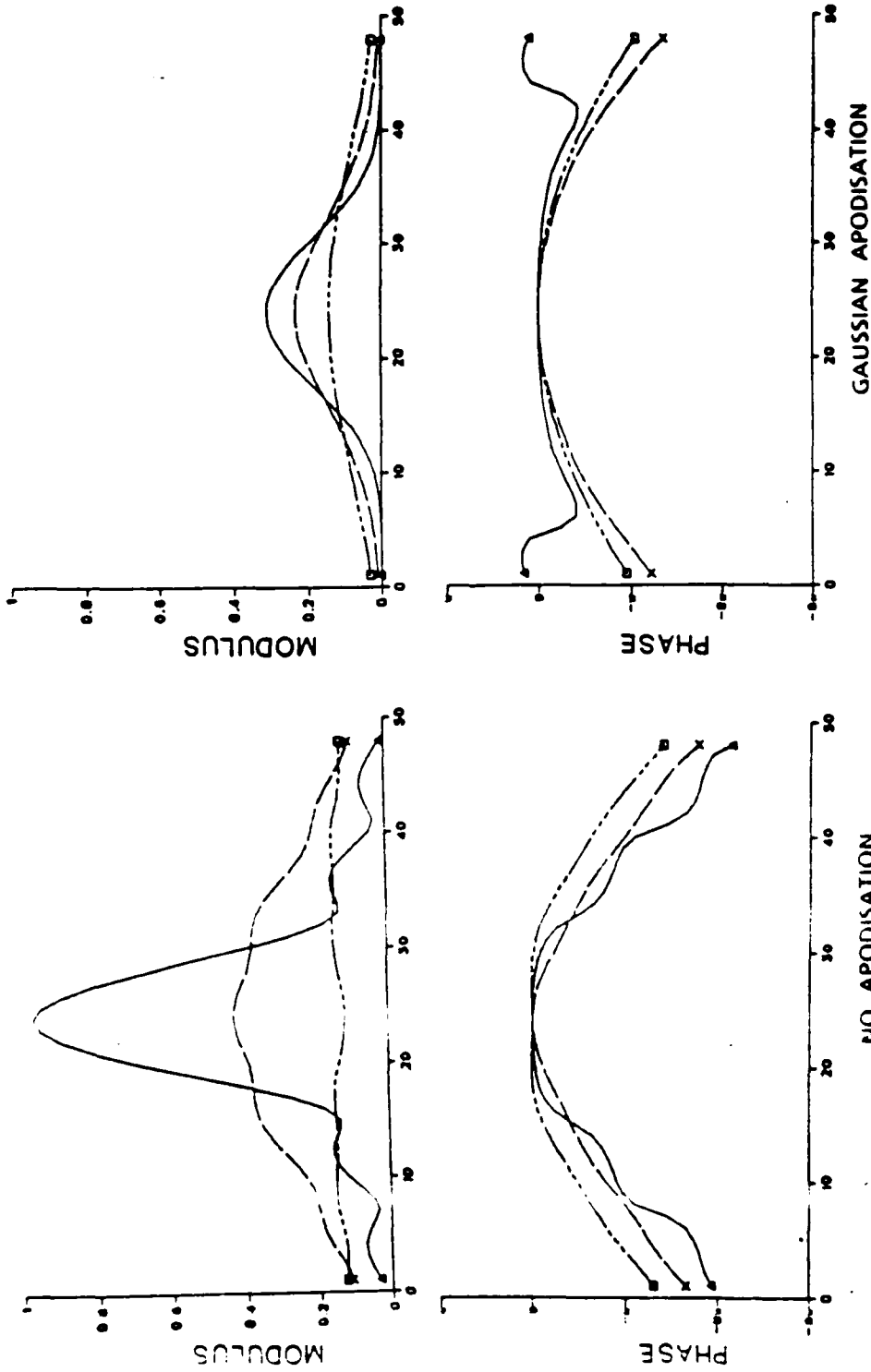
Fig 3 17   Central slices through the plots of modulus and phase in the presence of varying amounts of 0° astigmatism and for the unapodised as well as Gaussian apodised cases (—— 0.1λ, — — — 0.5λ, ——— 1.0λ).

3.3.5 On-axis Calculations

A common feature in all of the impulse data is that the addition of aberrations to an unaberrated optical system always results in a decrease in the peak value of the central lobe of the modulus. This behavior is plotted in Fig. 3.18 for various values of the four aberrations and the two cases of apodisation. The peak values have been normalized to unity for the unaberrated system. From this plot, it can be seen that the peak value of modulus occurs when there are no aberrations. The addition of any amount of the four aberrations to an unaberrated system results in a decrease in the peak value. Notice that in the case of defocus, the central peak completely disappears for $\Phi = 1.0$ wave. This is a so-called fringe of defocus.

Figure 3.19 shows the behavior of the central value of irradiance as the same aberrations were added. Fig. 3.19 can be obtained by squaring each value in Fig. 3.18. When the irradiance is used as is Fig. 3.19, the plots could also be labeled as the Strehl ratio. Note that the use of the apodiser immediately decreases the Strehl ratio by a factor of 10 for the unaberrated case.

The last figure in this chapter, Fig. 3.20, shows the behavior of the phase at the central peak of the impulse response as a function of the amount of aberration (Φ) and apodisation present. For most of the aberrations the phase is relatively unchanged as aberrations are added. For the case of defocus, however, there is a π phase jump in the unapodised case. The location of this jump corresponds to the location of the zero in the modulus of the unaberrated impulse response. This is consistent with the earlier observation that zeros in the modulus distribution of an unaberrated amplitude impulse response are accompanied by π phase jumps.
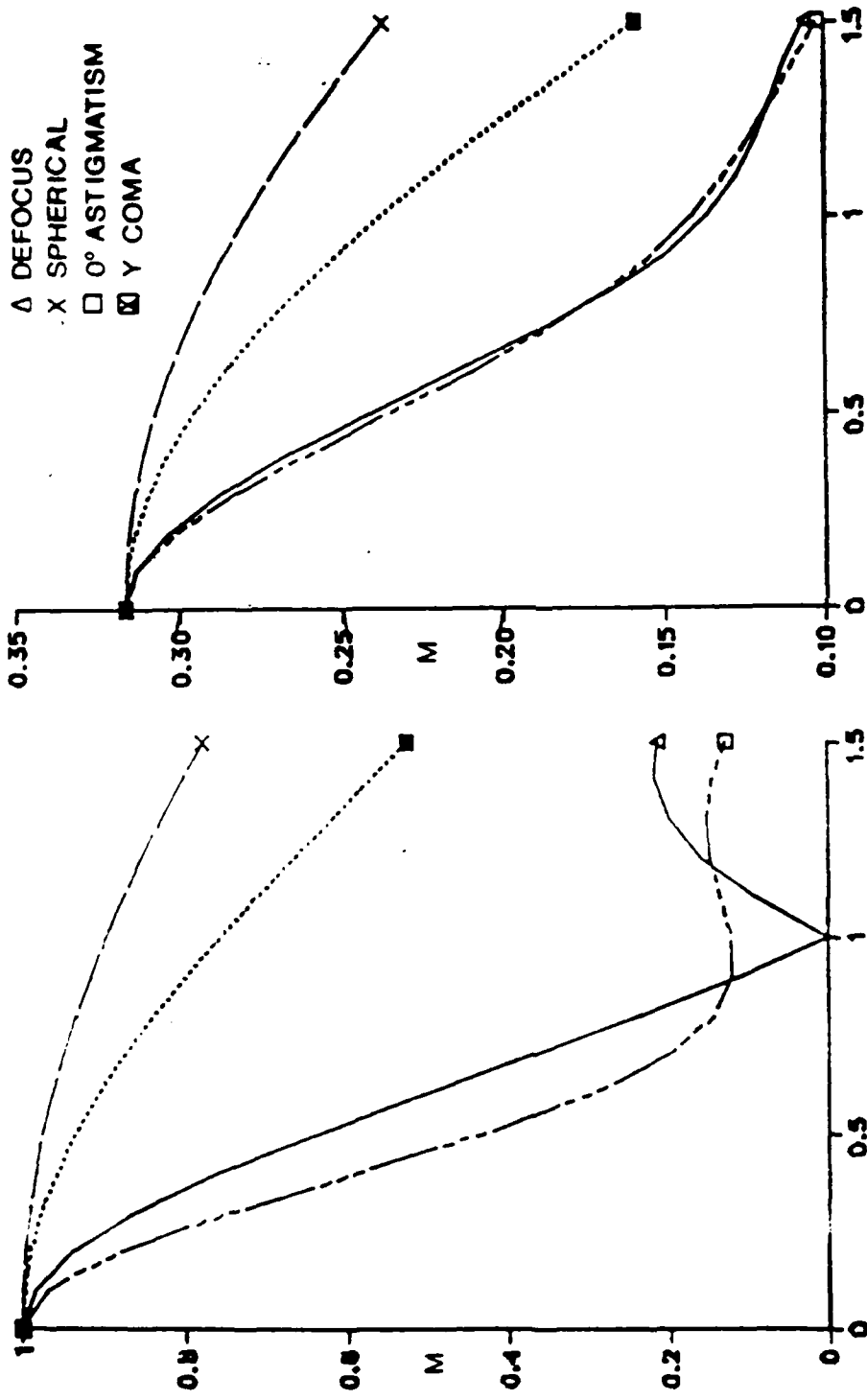
Fig. 3.18 The central value of the modulus as a function of the type and amount of aberration for cases of unapodised and Gaussian apodised apertures. For each plot, the abscissa is the amount of aberration (Φ) in waves and the ordinate is the peak value of the modulus (M).
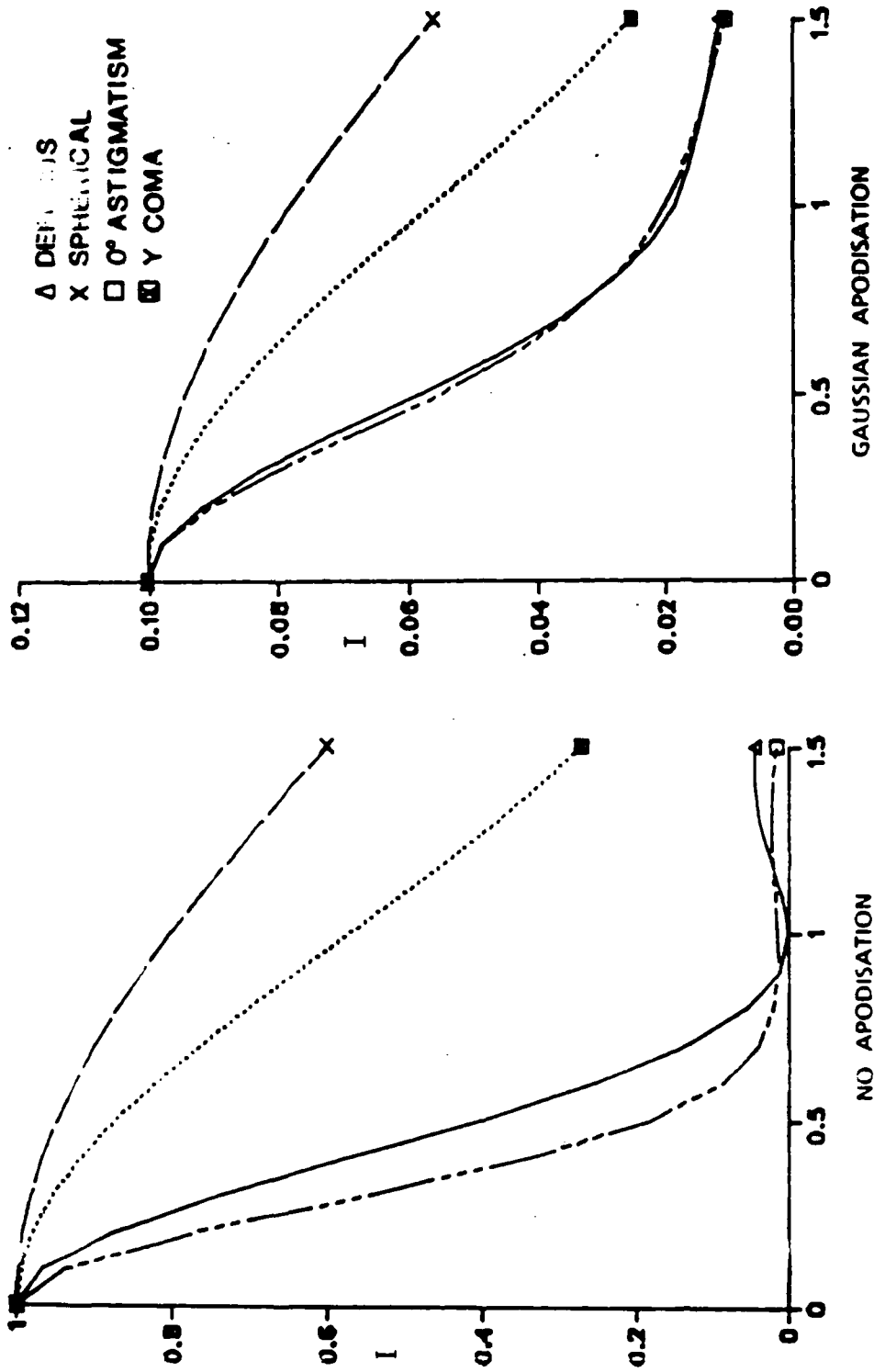
Fig 3.19 The central value of the phase as a function of the type and amount of aberration for cases of unapodised and Gaussian apodised apertures. For each plot, the abscissa is the amount of aberration (Φ) in waves and the ordinate is the peak value of the irradiance (I)
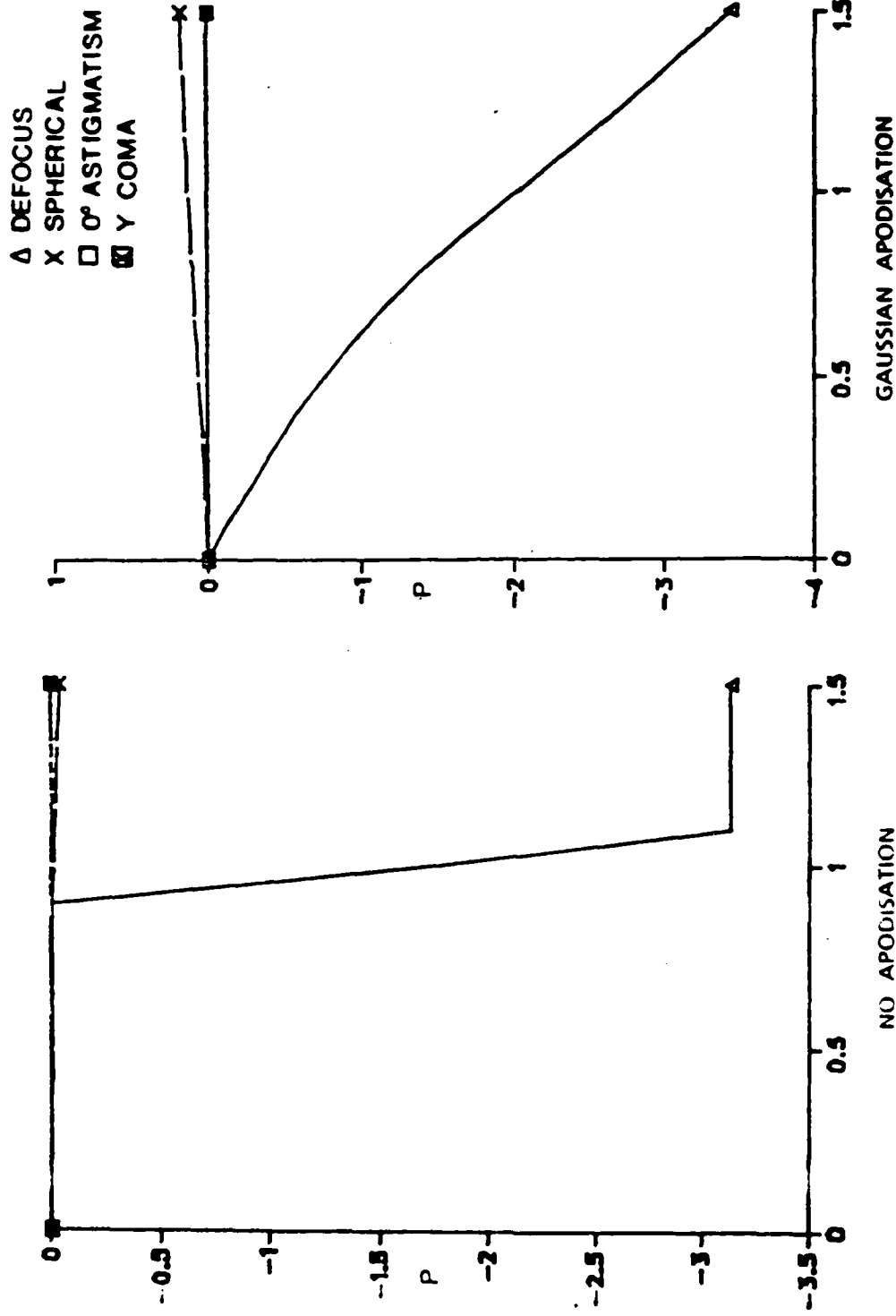
Fig 3.20 The central value of the irradiance as a function of the type and amount of aberration for cases of unapodised and Gaussian apodised apertures. For each plot, the abscissa is the amount of aberration (θ) in waves and the ordinate is the value of the phase (P) in radians at the peak of the modulus.

3.4 Impulse Response Conclusions

In this chapter the form of the impulse response has been determined for various amounts of defocus, spherical, coma, and astigmatism and for two cases of apodisation. The two cases were no apodisation and the Gaussian apodiser described by (3.3). Since coherent optical systems are linear in the complex field amplitude, the impulse response was displayed in terms of both its modulus and phase.

It was seen that, in the absence of the apodiser, the addition of an aberration significantly modified the form of the impulse response. However, when the apodiser was in place, the form of the impulse response did not vary much as an aberration was increased; the modulus, for the most part, smoothly fell from its peak value to zero and the phase was relatively flat over the region where there was a significant amount of modulus.

The apodiser was effective in removing the "feet" of the aberrated impulse response within certain limits. Those limits were approximately 1.0 wave for defocus, spherical, and astigmatism and 0.5 waves for coma. The implication is that within these limits the apodiser will improve certain aspects of the performance in a coherent imaging system; e.g., removing the edge ringing. Even beyond these limits the performance should be improved; for example, the edge ringing should be greatly diminished if not eliminated.

CHAPTER 4 IMAGING SYSTEMS ANALYSIS - THEORY

The effect of apodisation on the performance of aberrated coherent optical systems has been theoretically investigated. The objects considered in this analysis were an edge, a slit, and two closely spaced points; and the performance of the optical system was measured against criteria which were specific for each of these test objects. The performance predictions detailed below are based on the theory described in Chapter 2. Experimental verification of key parts of the theory are contained in Chapter 5.

The optical system was modeled as shown in Fig. 2.2 which, for convenience, is reproduced here and labeled as Fig. 4.1. Under the conditions detailed in Section 2.1.2,
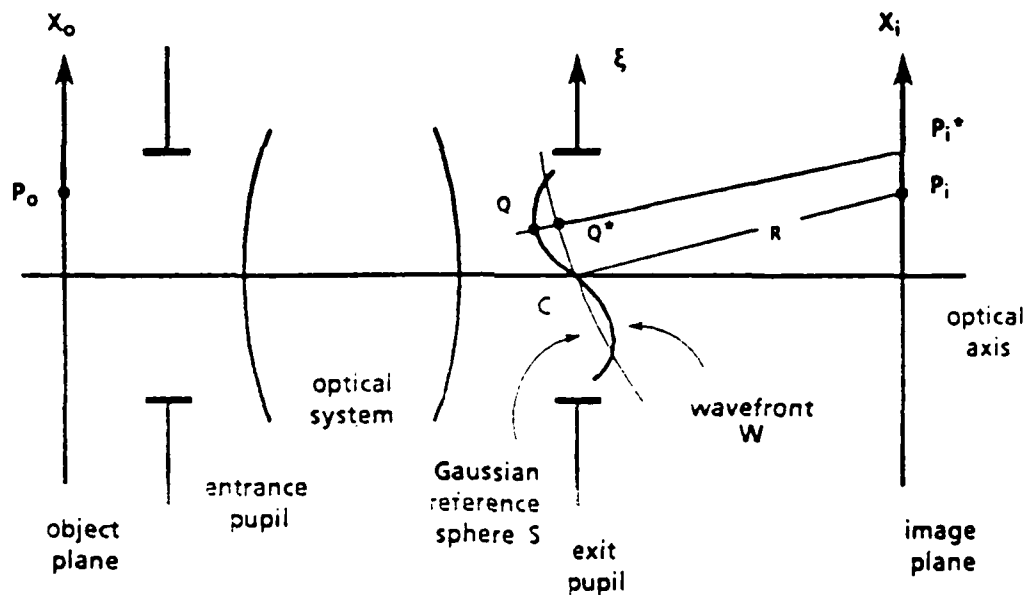
Fig.4 1 The geometry of a centered optical system which gives rise to an aberrated wavefront W. The aberration function ϕ is in terms of the distance QQ* between W and the reference sphere S.

the optical field in the image plane $U_i(x_i, y_i)$ is related to the optical field in the object plane $U_o(x_o, y_o)$ by the (2.28):

$$U_i\left(x_i, y_i\right) = F\left\{ k\left(f, g\right) F^{-1}\left\{ U_o\left(x_o, y_o\right)\right\}\right\},\qquad (2.28)$$

where $F\{\ \}$ and $F^{-1}\{\ \}$ represent, respectively, the forward and inverse Fourier transforms

of the quantities within the brackets and k(f,g) is the scaled exit pupil transmittance. Equation (2.28) will be the basis for the predicted results within this chapter.

The results are plotted in terms of both the image irradiance and the square root of image irradiance. As stated before, the square root of irradiance is a good measure of an image because the nonlinearity of the detection process is removed. However the usual presentation seen in the literature is in terms of the irradiance. Thus, both scales are used in this chapter.

4.1 EDGE OBJECTS

An edge in the object (x_o, y_o) plane can be described by

$$e\left(x_o, y_o\right) = step\left(-y_o\right) = \begin{cases} 1 & if \ y_o \le 0 \\ 0 & otherwise \end{cases}, \tag{4.1}$$

where the edge has been aligned to be coincident with the x_o axis.

The inverse Fourier transform of (4.1) is given by[77]

$$F^{-1}\left\{e\left(x_o, y_o\right)\right\} = \frac{1}{2}\left|\delta\left(g\right) + \frac{1}{i\pi g}\right|\delta\left(f\right), \tag{4.2}$$

where δ is the Dirac delta function and f and g are the spatial frequency coordinates in the plane of the exit pupil:

$$f = \frac{\xi}{\lambda f_o} \quad and \quad g = \frac{\eta}{\lambda f_o} \tag{4.3}$$

The coordinates (ξ, η) refer to the space coordinates in the exit pupil plane and f_o is the distance from the object plane to the entrance pupil.

Combining (4.1) - (4.3) into (2.28) results in the optical field

$$U_i\left(x_i, y_i\right) = F\left\{\frac{1}{2}\kappa\left(\eta\right)\left|\delta\left(\frac{\eta}{\lambda f_o}\right) - \frac{\lambda f_o}{i\pi\eta}\right|\right\}, \tag{4.4}$$

where the problem has been reduced to one dimension because of the $\delta(f)$ term in (4.2).

The term $k(\eta)$ describes the exit pupil transmittance in a manner analogous to (2.7); i.e.,

$$k\left(\eta\right)=A\left(\eta\right)e^{i\frac{2\pi}{\lambda}\phi\left(\eta\right)}B\left(\eta\right),\qquad(4.5)$$

where $A(\eta)$ and $\phi(\eta)$ represent the amplitude and phase transmittance, respectively, of the exit pupil along the line $\xi = 0$ and $B(\eta)$ represents the finite extent of the exit pupil along that same line.

The calculation of (4.4) for various values of aberration and apodisation was accomplished using the University of Rochester Computer Center's DEC 10 computer. The program controlling these calculations was written in FORTRAN and employed a FFT routine from the IMSL[74] library. A documented copy of the program, labeled EDGE.FOR, is in Appendix 1. The program is a simple modification of the program PSF.FOR which was used in Chapter 3. The output of the program is in terms of the irradiance of the image which is proportional to the product of (4.4) times its complex conjugate. The square root of the irradiance is also a program output.

Typical results from this program are depicted in Figs. 4.2 through 4.4. These figures display both the irradiance and the square root of the irradiance of a perpendicular slice through the image of an edge when the optical system has various amounts (0.0, 0.5, and 1.0 waves) of defocus, y-axis coma, or spherical aberration. Separate plots of the effects of astigmatism are not shown because in one dimension astigmatism has the same functional form as defocus. The top plots in each figure are for an unapodised optical system, while the bottom plots are for a system with a Gaussian apodiser having an amplitude transmittance of

$$A\left(\eta\right)=e^{-3\eta^{2}}\qquad(4.6)$$

In each plot, the ordinate is in terms of the relative irradiance (or square root of irradiance) and the abscissa is in terms of the normalized distance v. For reference, the

NORMALIZED DISTANCE V
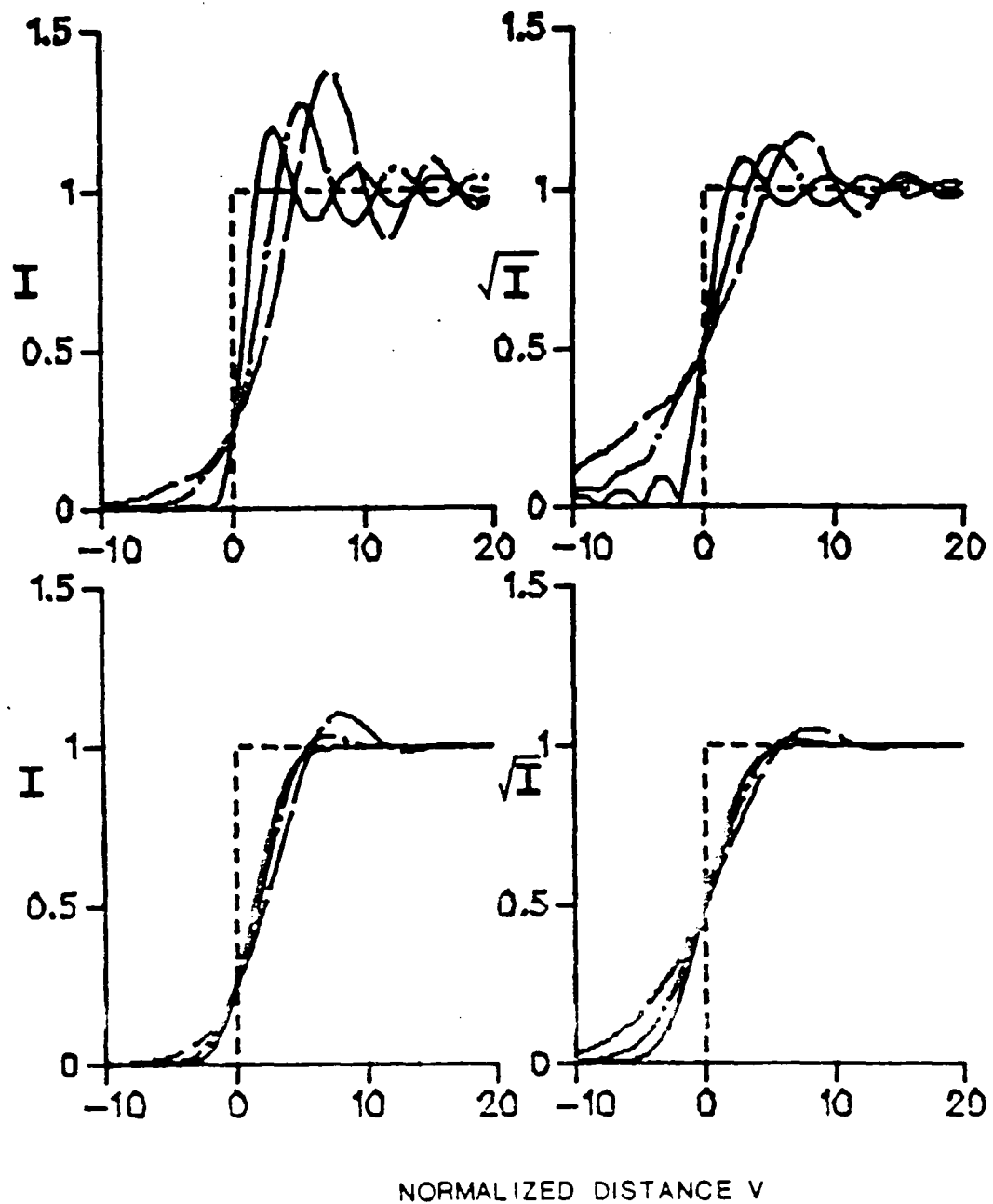
Fig.4.2 The coherent image of an edge through an optical system having 0.0, 0.5, and 1.0 waves of defocus. The top plots are for an unapodised optical system while the bottom plots are for a system having a Gaussian apodiser. The ordinates of the two plots on the left are in terms of image irradiance (I) while the ordinates for the others are in terms of the square root of image irradiance ($\sqrt{I}$). Legend: _____ unaberrated. ___ ___ ___ 0.5 waves. ___ _ ___ _ ___ 1.0 wave

NORMALIZED DISTANCE V
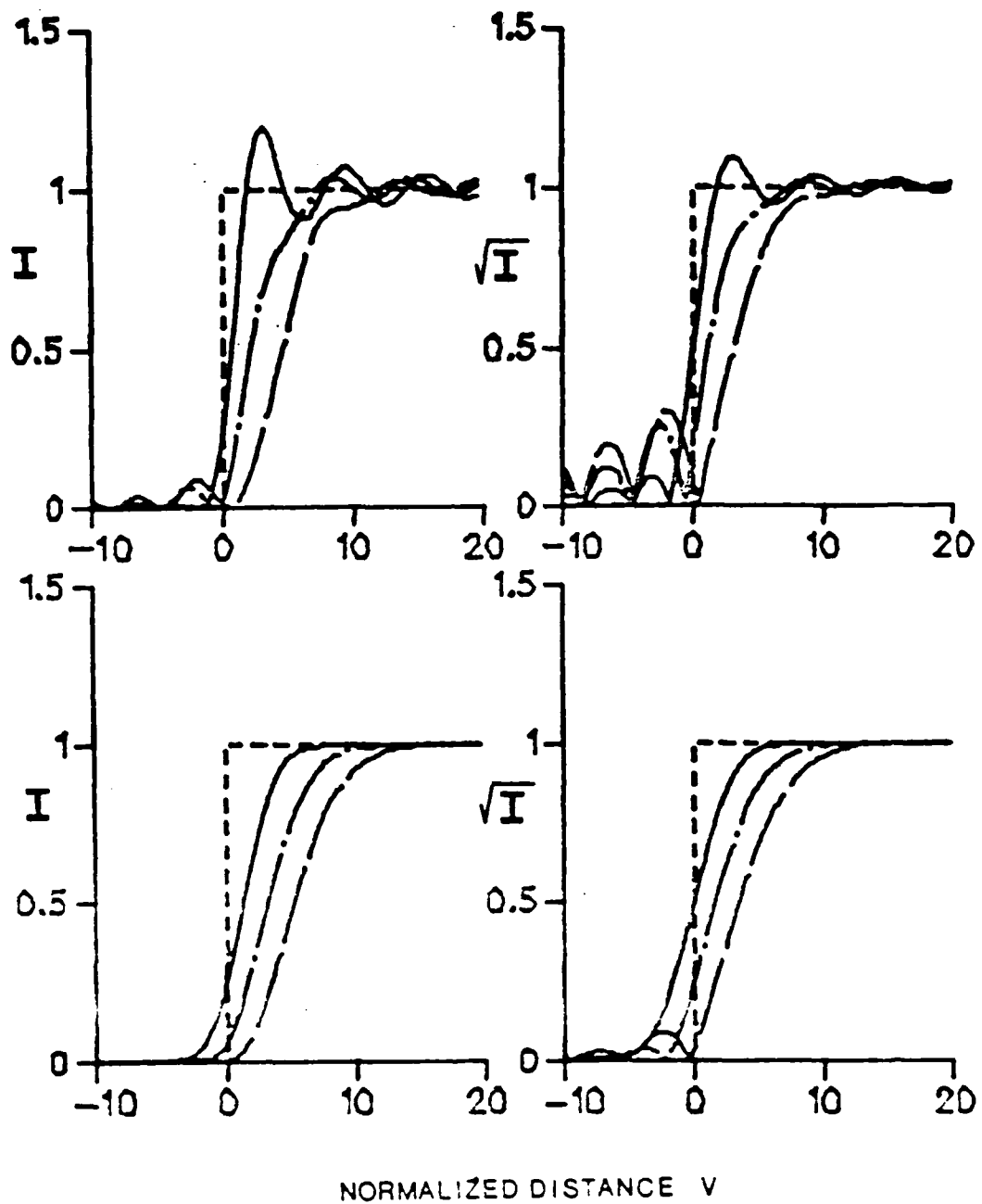
Fig.4.3 The coherent image of an edge through an optical system having 0.0, 0.5, and 1.0 waves of y-axis coma. The top plots are for an unapodised optical system while the bottom plots are for a system having a Gaussian apodiser The ordinates of the two plots on the left are in terms of image irradiance (I) while the ordinates for the others are in terms of the square root of image irradiance($\sqrt{I}$). Legend: _____ unaberrated, ___ ___ ___ 0.5 waves, ___ _ .. _ ___ 1.0 wave

NORMALIZED DISTANCE V
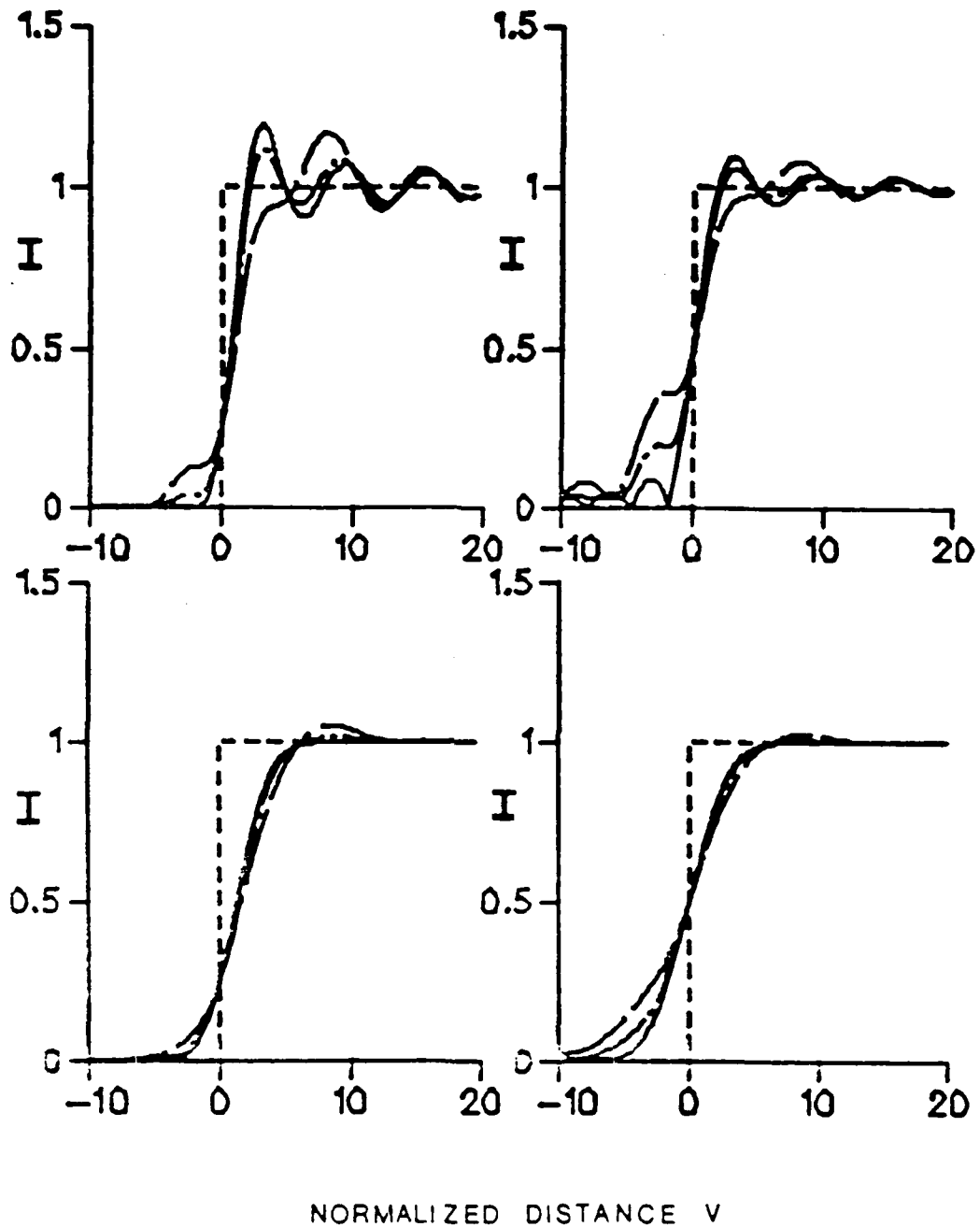
Fig.4.4 The coherent image of an edge through an optical system having 0.0, 0.5, and 1.0 waves of spherical. The top plots are for an unapodised optical system while the bottom plots are for a system having a Gaussian apodiser. The ordinates of the two plots on the left are in terms of image irradiance (I) while the ordinates for the others are in terms of the square root of image irradiance ($\sqrt{I}$). Legend:
_____ unaberrated, ____ ____ ____ 0.5 waves, ____ _.._ ____ 1.0 wave.

MICROCOPY RESOLUTION TEST CHART

position of the geometrically imaged edge is included on each plot as a line of short dashes.

For the apodiser used here, the amplitude transmittance has a value of 0.05 at a distance from the center of $\eta = 1.0$. The hard aperture also has a radius of $\eta = 1.0$. Because the Gaussian apodiser is truncated at a very low value, the discontinuity in transmittance at the edge of the aperture is almost removed. A plot of the apodiser described by (4.6) is shown in Fig. 3.3.

The measures of importance when evaluating coherent edge images are edge-ringing, edge-shifting, and acutance.

4.1.1 Edge Ringing

Edge ringing is the periodic deviation of the edge image from the geometrically ideal edge image. This phenomena is most pronounced in the top plots of Fig. 4.2. It can be quantified[42] in terms of the ratio of the maximum positive deviation to the geometric expected value of unity. This ratio for various values of the three aberrations considered is shown in Fig. 4.5 (a-c). From these plots it is clear that the use of apodisation will reduce the edge-ringing effect, especially for the case of coma shown. This behavior of an apodised system is well known in the case of aberration-free systems. It is now apparent that apodisation will reduce edge ringing even in the presence of aberrations. This result is not surprising because the impulse response of the system has been significantly smoothed, as seen in Chapter 3. Essentially, the apodiser acts as a weighting function in the exit pupil. It deemphasizes, by attenuation, the regions of the exit pupil near the edge of the aperture. It is in these same regions when aberrations are present, that the phase of the wavefront deviates most from the ideal shape of the spherical reference sphere. The effect of using the square root of the image irradiance is
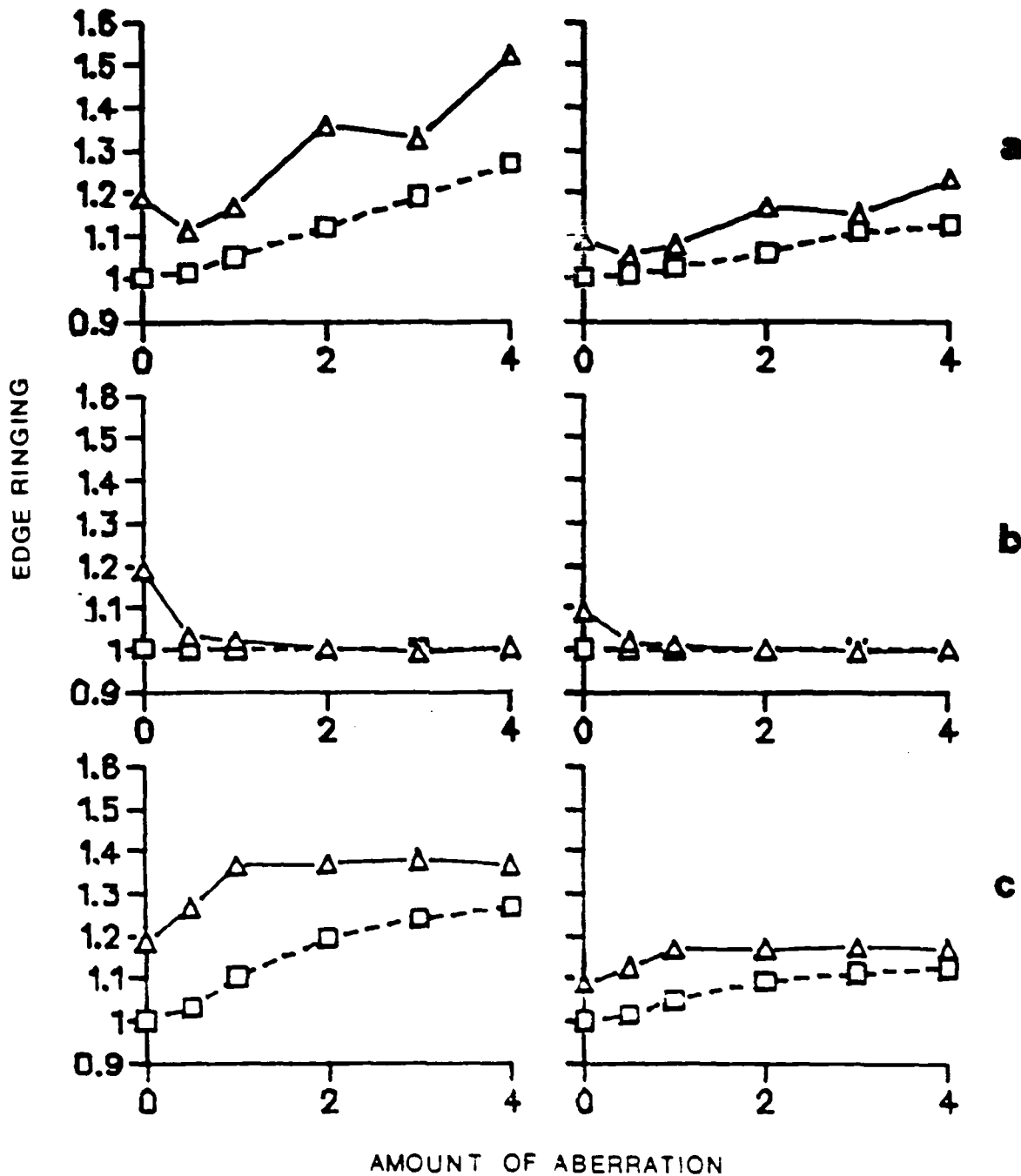
Fig. 4.5 The amount of edge ringing is shown for various amounts of the aberrations of (a) spherical, (b) y-axis coma, and (c) defocus. Edge ringing is defined as the ratio of the peak closest to the edge to unity. The plots in the left column are calculated from the edge image irradiance while the others are from the square root of the edge image irradiance. The solid curves are for the unapodised cases while the dashed curves are for the apodised cases.

also illustrated in this figure. As expected, the amount of edge ringing is reduced in these cases. Although, as a consequence of taking the square root of the irradiance, the ringing on the dark side of the edge has increased.

4.1.2 Edge Shift

The edge shift is the distance from the theoretical position of the geometric edge to the edge defined by the real image. The location of the imaged edge is defined here as the position where the irradiance is half the value of the first peak. The dependence of edge shift on the amount and type of aberration as well as the presence or absence of apodisation is illustrated in Fig. 4.6 (a - c). As seen in this figure, the edge shift is not a strong function of the presence or absence of the apodiser. In general, the application of the apodiser increases the amount of edge shift. However, in the case of y-axis coma, the edge shift is reduced when the apodiser is used.

The amount of edge shift is a function of how the edge is defined. A common choice (one not made here however) for the location of the edge is the point where the irradiance is equal to 0.5, when the value of the irradiance far from the edge on the illuminated side is equal to 1.0. If this choice is made and the square root of the irradiance is taken then there will be no edge shift for the aberrations which are symmetric about the optical axis, e.g., astigmatism, defocus, and spherical. The presence of coma will still cause the edge to shift(see Fig. 4.3). The problem with this choice is that experimentally it is often difficult if not impossible to determine the value of the the bright side of the edge at a great enough distance from the edge. The presence of noise and other edges in the system very often precludes this.

It is for these reasons that the edge is defined here as the point where the irradiance is half of the value of the irradiance at the maximum of the peak closest to the
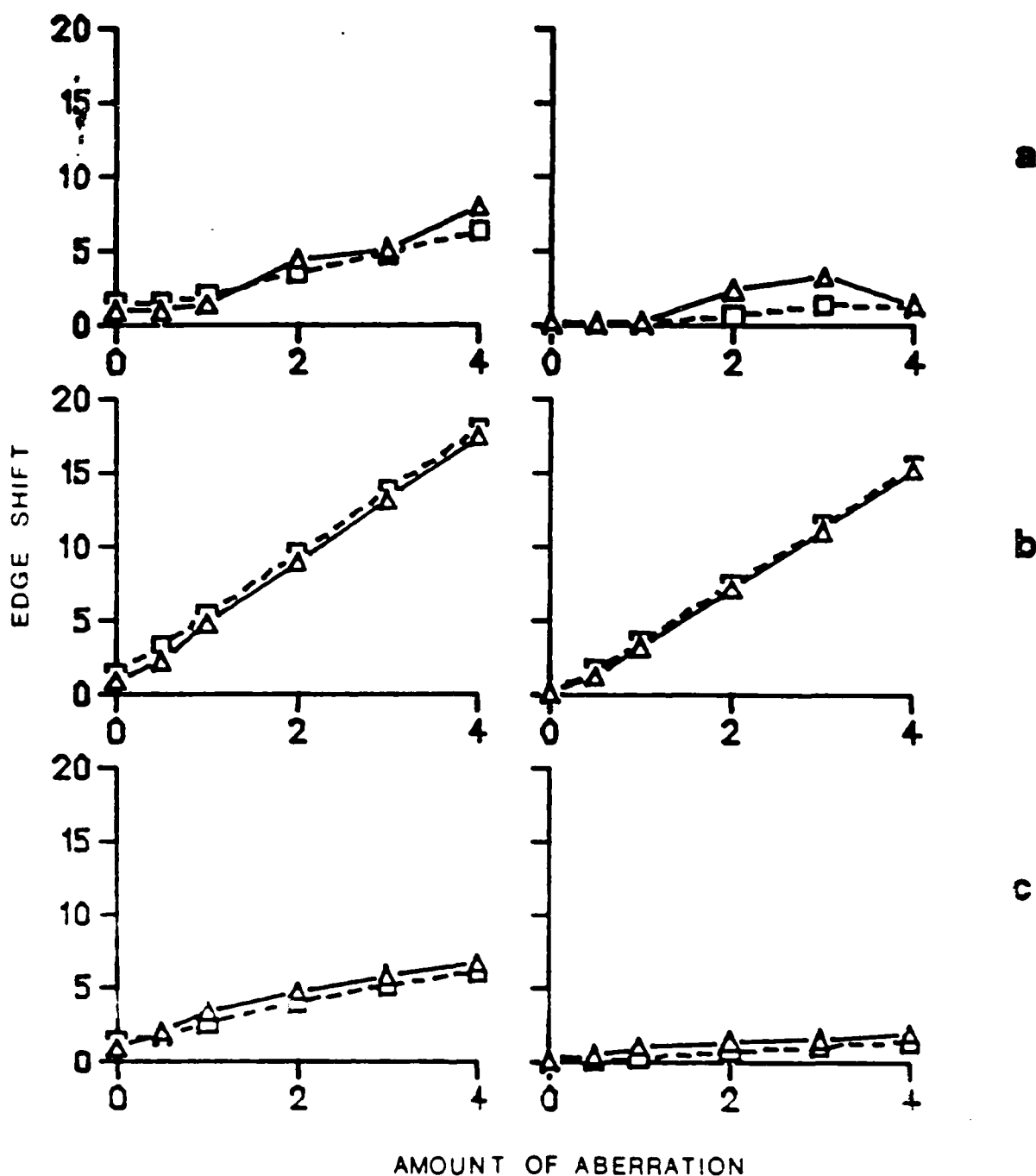
Fig 4.6 The amount of edge shift is shown for various amounts of the aberrations of (a)
spherical, (b) y-axis coma, and (c) defocus. The solid curves are for the
unapodised cases while the dashed curves are for the apodised cases. The edge
shift is defined as the distance of the half peak irradiance point from the
geometric edge. The plots in the left column are calculated from the edge image
irradiance while the others are from the square root of the edge image
irradiance.

edge. The edge is similarly defined when the square root of the irradiance is considered. The advantage of this definition of the edge is that it is always possible to find the first peak.

4.1.3 Edge Acutance

Acutance is a measure of the the slope of the edge. Specifically, as a definition, acutance is defined here as the slope of the irradiance (or square root of irradiance) at the location of the edge. The behavior of the acutance as a function of the amount and type of aberration as well as the presence or absence of apodisation is shown in Fig. 4.7 (a - c). In each case, acutance decreases with both an increase of the amount of aberration and the application of apodisation.

Using the square root of the irradiance distribution seems to have some advantages in the analysis of edge objects. Relative to the use of the irradiance distribution, the edge ringing and shift are reduced and the acutance is not affected significantly. The edge shift should approach zero if it is possible to find the limiting value of irradiance (or square root of irradiance) on the bright side of the edge image, except for axially unsymmetric aberrations like coma. The major disadvantage of using the square root is that the apparent ringing on the dark side of the edge image is enhanced.

Overall, it can be concluded that apodisation is effective in improving the performance of an aberrated coherent optical system for edge objects. Specifically, edge ringing is greatly reduced, while the edge is not significantly shifted relative to the unapodised situation. The major drawbacks of apodisation are that the total flux in the image plane is reduced, as is the acutance of the edge.
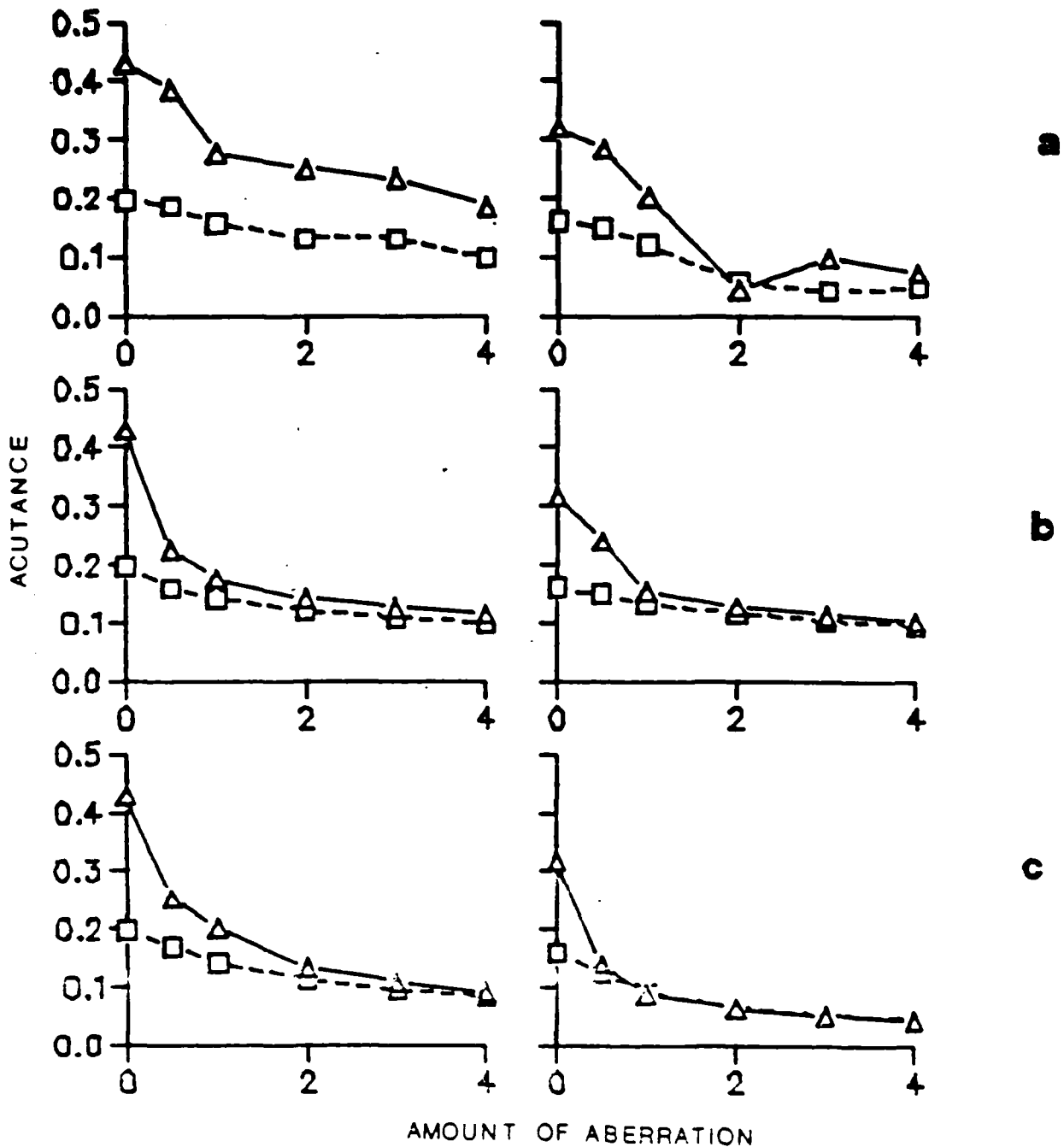
Fig.4.7 The acutance of the edge is shown for various amounts of the aberrations of (a).
spherical, (b) y-axis coma, and (c) defocus. The solid curves are for the
unapodised cases while the dashed curves are for the apodised cases. The plots in
the left column are calculated from the edge image irradiance while the others
are from the square root of the edge image irradiance.

4.2 SLIT OBJECTS

A slit in the object plane can be described by

$$s\left(x_o, y_o\right) = rect\left(\frac{y_o}{a}\right) = \begin{cases} 1 & \text{if } -a \leq y_o \leq a \\ 0 & \text{otherwise} \end{cases} , \tag{4.7}$$

where a is the half-width of the slit. Following (2.28), the inverse Fourier transform of (4 7) is first obtained, then multiplied by the scaled exit pupil function (4.5), and finally, Fourier-transformed to yield the amplitude of the coherent image. The image irradiance is then found as the product of the amplitude times its complex conjugate.

A program called SLIT.FOR was written in FORTRAN on the DEC10 computer of the University of Rochester. An annotated copy of this program is contained in Appendix 1.

Typical results are shown in Figs. 4.8 through 4.13. Figures 4.8, 4.10, and 4.12 display the irradiance of a slice through the image of a slit when the optical system has various amounts (0 0, 0.5, and 1.0 waves) of defocus, y-axis coma, or spherical aberration. Figures 4 9, 4 1', and 4 13 give the same information, respectively, in terms of the square root of the image irradiance. Once again separate plots of astigmatism are not shown because, in one dimension, astigmatism has the same functional form as defocus. The top plot in each figure is for an unapodised optical system, while the bottom plot is for a system having a Gaussian apodiser with an amplitude transmittance described by (4.6). In each plot the ordinate is in terms of the relative irradiance and the abscissa is in terms of the normalized distance u. For reference, the position of the geometrically-imaged slit is indicated in each plot as a line of short dashes.

As can be seen from these figures, the image of a slit, like the image of an edge, exhibits the phenomenon of edge ringing. Since a slit is composed of two edges, this is
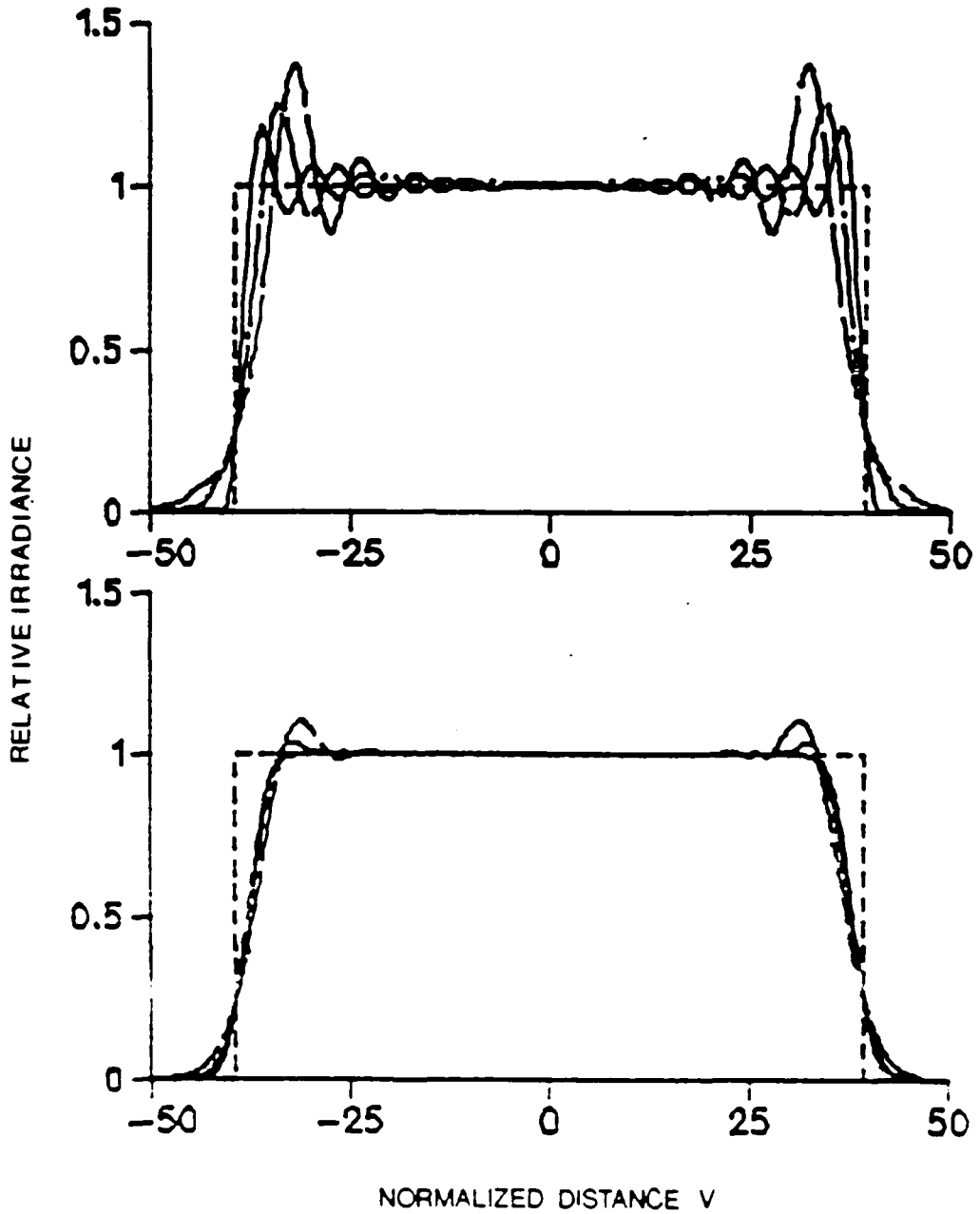
Fig.4.8 The coherent image of a slit through an optical system having 0.0, 0.5, and 1.0 waves of defocus. The top plot is for an unapodised optical system while the bottom plot is for a system having a Gaussian apodiser. Legend:
_____ unaberrated. ___ ___ ___ 0.5 waves. ___ _ _ _ _ 1.0 waves.
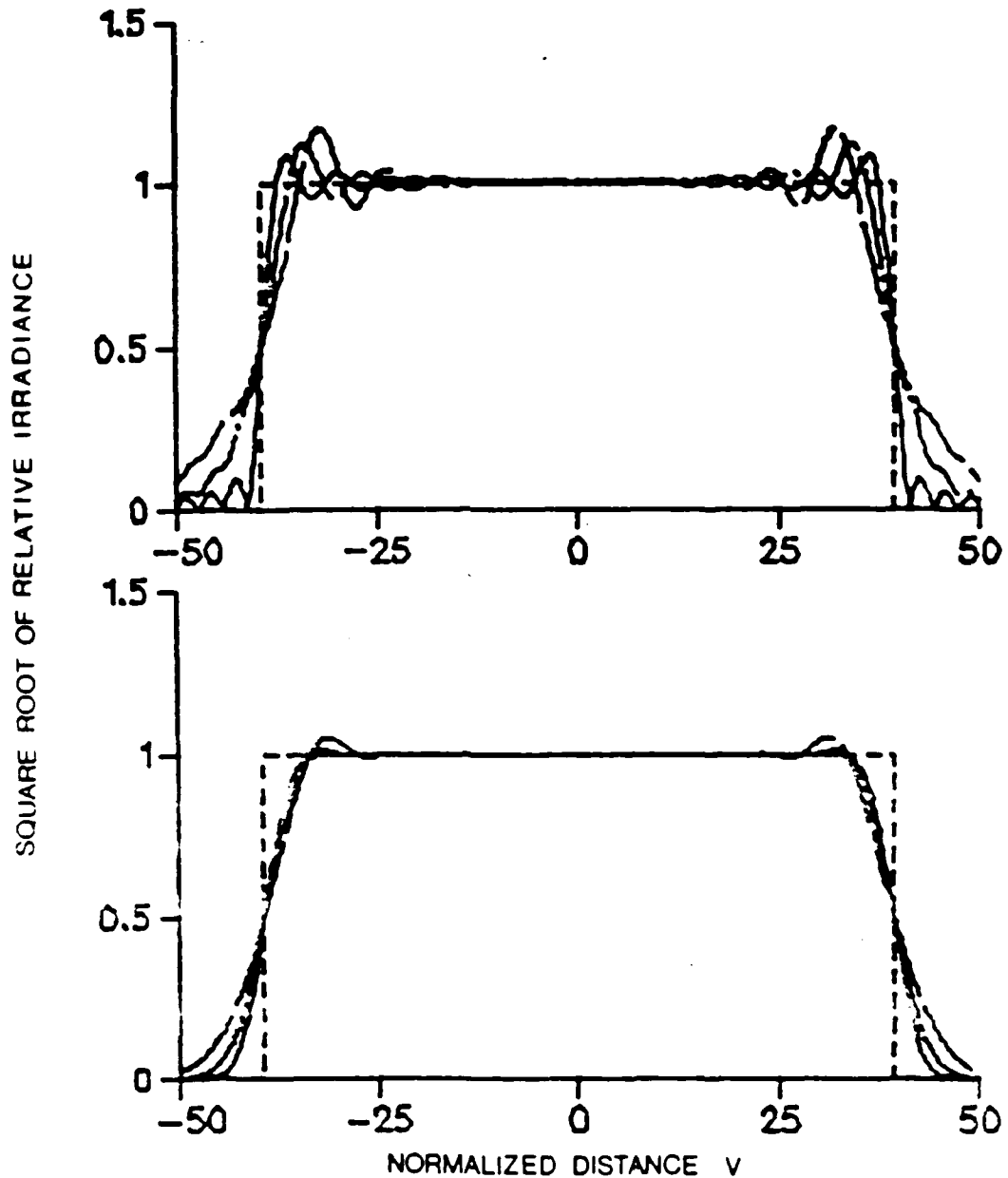
Fig.4.9 The square root of the irradiance of the coherent image of a slit through an optical system having 0.0, 0.5, and 1.0 waves of defocus. The top plot is for an unapodised optical system while the bottom plot is for a system having a Gaussian apodiser. Legend:

_____ unaberrated, ___ ___ ___ 0.5 waves, ___ _ .. ___ 1.0 waves.
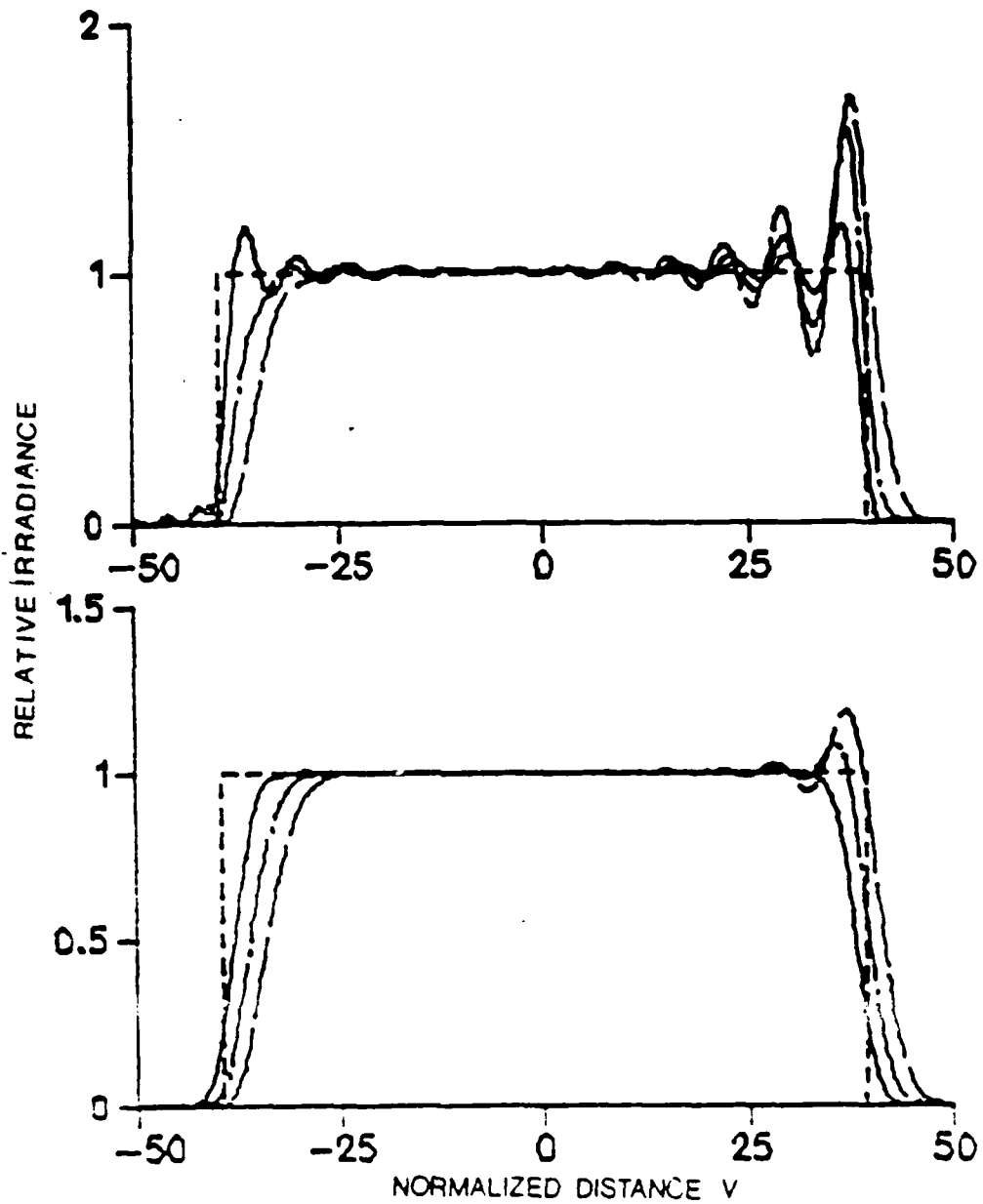
Fig.4.10 The coherent image of a slit through an optical system having 0.0, 0.5, and 1.0 waves of y-axis coma. The top plot is for an unapodised optical system while the bottom plot is for a system having a Gaussian apodiser. Legend: _____unaberrated, ___ ___ ___0.5 waves, ___ _ _ _ ___ 1.0 waves.
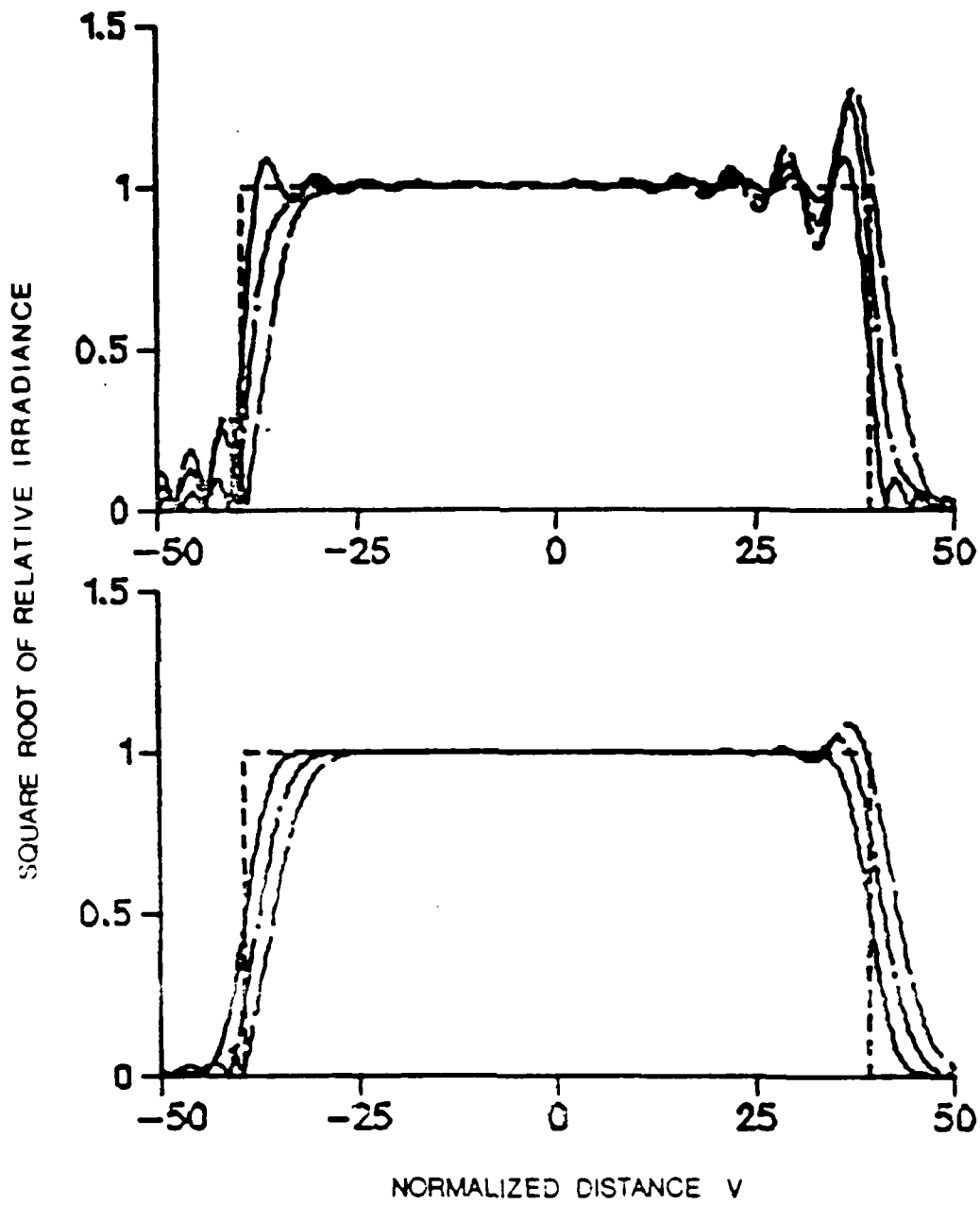
Fig 4.11   The square root of the irradiance of the coherent image of a slit through an optical system having 0.0, 0.5, and 1.0 waves of y-axis coma. The top plot is for an unapodised optical system while the bottom plot is for a system having a Gaussian apodiser. Legend:
_____unaberrated, ____ ____ ____ 0.5 waves, ____ _ .. ____ 1.0 waves.
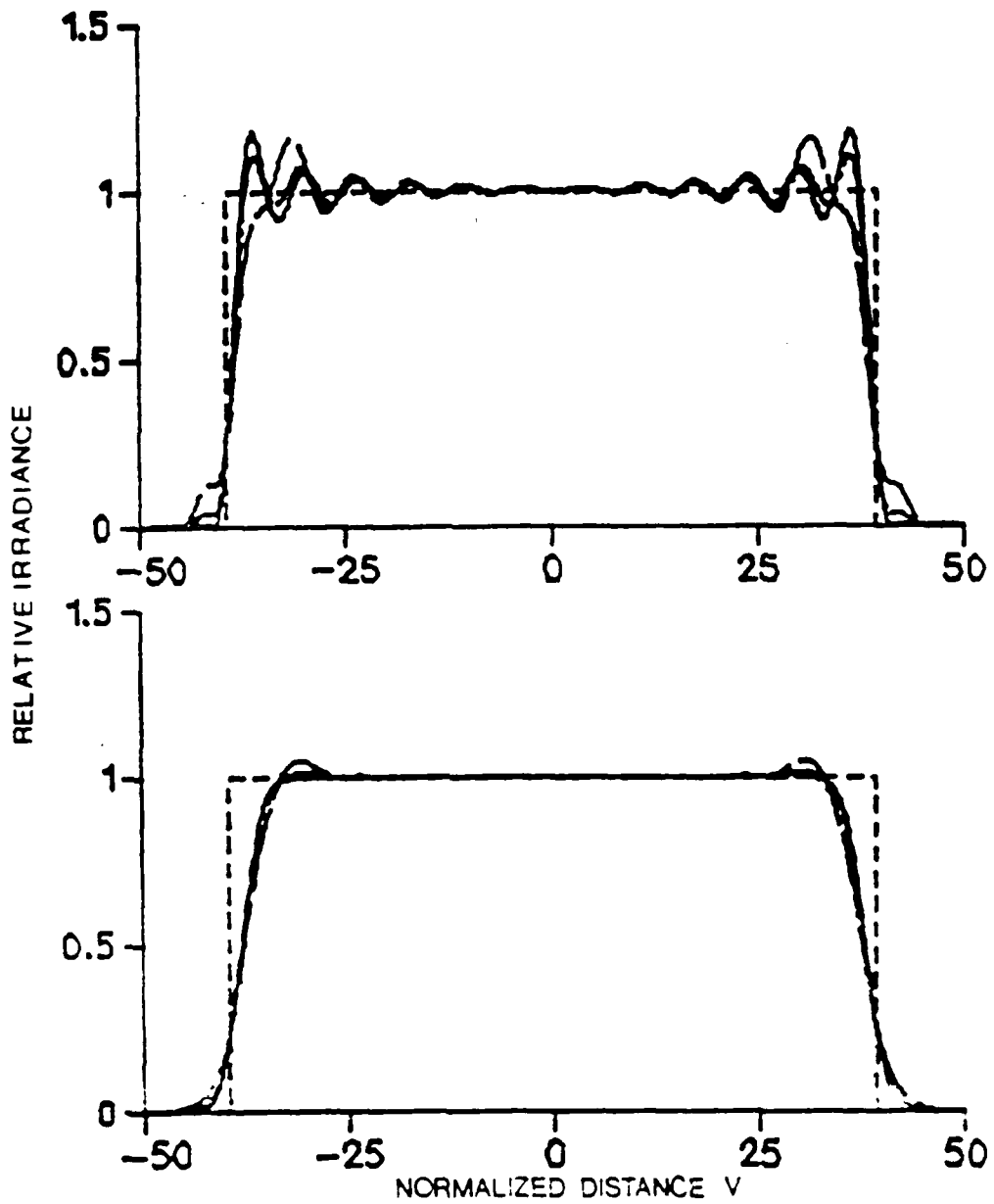
Fig.4.12   The coherent image of a slit through an optical system having 0.0, 0.5, and
1.0 waves of spherical. The top plot is for an unapodised optical system while
the bottom plot is for a system having a Gaussian apodiser. Legend:
_____ unaberrated, ___ ___ ___ 0.5 waves, ___ _ _ _ ___ 1.0 waves.
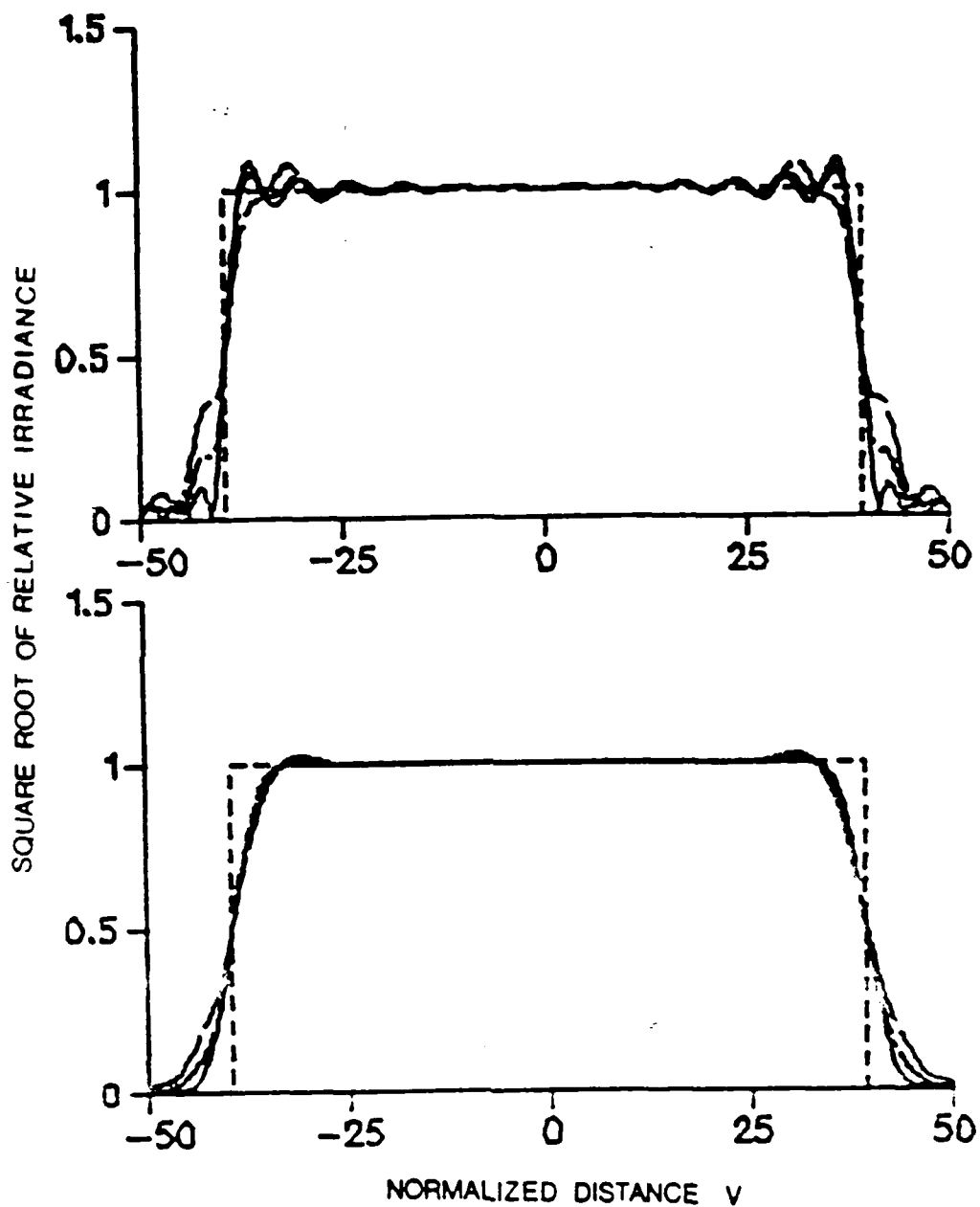
Fig.4.13   The square root of the irradiance of the coherent image of a slit through an optical system having 0.0, 0.5, and 1.0 waves of spherical. The top plot is for an unapodised optical system while the bottom plot is for a system having a Gaussian apodiser. Legend:
_____ unaberrated, ___ ___ ___ 0.5 waves, ___ _ .. ___ 1.0 waves.

not surprising. Also the individual location of each edge in the slit image shifts as a function of the amount of aberration. Likewise, the acutance of each edge varies with the amount of aberration.

The effect of apodisation on the image of a slit is also similar to the case of the edge. The edge ringing is reduced, the edge shift is not affected much, and the actuance is decreased when an apodiser is used.

The only difference between a single edge in a slit image and an isolated edge is the effect of the presence of the second edge. Depending on the width of the slit relative to the width of the impulse response, this effect can be large or small. In the case illustrated here the effect is small. For examples of smaller slits, refer to the experimental results section of Chapter 5, Figs. 5.18 through 5.23.

For the image of a slit, there are two other important measures of performance: the width of the slit image and the translation of the slit image as a whole.

The width of the slit image is defined as the separation of the two individual edges of the slit image (images here were in terms of irradiance). The behavior of the width of the irradiance of the slit image, both with and without apodisation , is shown in Fig. 4.14 (a - c) for the three different aberrations. The image of the slit ideally would have a width of 80 in units of the dimensionless variable v. It can be seen from this figure that in all cases the measured width is less than ideal. Additionally, the width of the slit image decreases as the amount of aberration increases. If the width were calculated from the image in terms of the square root of image irradiance, the width in all cases would be very close to the expected value.
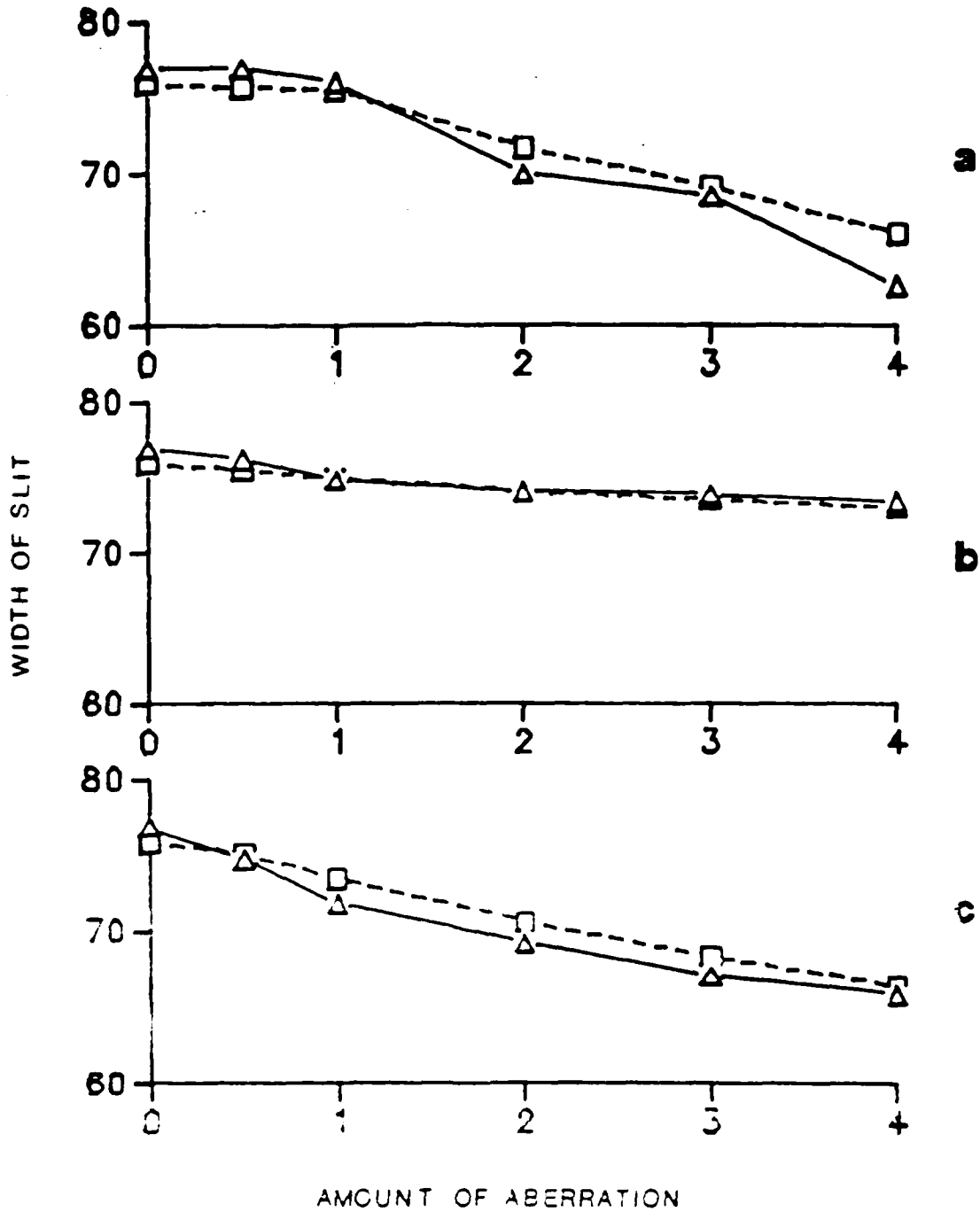
Fig 4.14 The width of the irradiance distribution of the image of a coherently illuminated slit is shown for various amounts of the aberrations of (a) spherical, (b) y-axis coma, and (c) defocus. The solid curves are for the unapodised cases while the dashed curves are for the apodised cases. Only slit images that were in terms of the square root of irradiance were considered.

With the application of the Gaussian apodiser, the width of the slit image will also decrease with increasing amounts of aberration. However, for the cases of spherical aberration, defocus, and astigmatism, the presence of the apodiser results in more accurate width when the amount of aberration exceeds about one wave. For the case of y-axis coma, the presence of the apodiser doesn't affect the width of the image significantly.

The position of the slit image in the image plane, besides being a function of the system's transverse magnification, depends on the type and magnitude of aberration present. An examination of Figs. 4.9, 4.11, and 4.13 confirms that for the symmetric aberrations (defocus, astigmatism, and spherical) the position of the slit is correct (square root of irradiance considered); while for the unsymmetric aberration of coma the center of the slit image is a function of the amount of aberration present. This is in agreement with the definition of coma; i.e., the aberration of coma is a variation of transverse magnification with radial zone of the exit pupil.

As in the case of an edge, the use of apodisation is beneficial when imaging through an optical system which has third-order aberrations. The amount of edge-ringing is reduced and the width is not greatly affected when the apodiser is applied. As before, the drawbacks are a loss of total flux through the image plane and a decrease in the acutance of the edges.

4.3 TWO-POINT OBJECTS

Two-point sources in the object plane can be described by

$$t\left(x_o, y_o\right) = \delta\left(y_o - b\right) + \delta\left(y_o + b\right),$$ (4.8)

where δ is the Dirac delta function and b is the displacement of each point source from the optical axis. Once again, (2.28) is employed. The inverse Fourier transform of (4.8) is

$$F^{-1}\left[t\left(x_o, y_o\right)\right] = 2\cos\left(2\pi bg\right),$$ (4.9)

where $g = \eta/\lambda f_o$. The image field amplitude is then, according to (2.28),

$$U_i\left(x_i, y_i\right) = F\left[k\left(\eta\right) 2 \cos\left(\frac{2\pi b\eta}{\lambda f_o}\right)\right].$$ (4.10)

A program labeled TPNT.FOR, which is a derivation of PSF.FOR, was used to calculate the irradiance distribution associated with (4.10). An annotated copy of TPNT.FOR is in Appendix 1.

Typical results from this program are displayed in Figs. 4.15 and 4.16. These figures display the irradiance distribution of the coherent image of two point sources through an unaberrated optical system. In each figure the two points are separated by (a) $2b$ = 20, (b) $2b$ = 30, and (c) $2b$ = 40. Fig. 4.15 shows the results when the system is unapodised and Fig. 4.16 shows the results when the system has the Gaussian apodiser of (4.5).

In the top plot of each figure the two points are unresolved, while for greater separations in the other plots, they are resolved. Comparing the middle plots of the two figures, it can be seen that the limit of resolution, by the Sparrow limit of resolution is greater for the unapodised case and than for the apodised case. It follows that the apodised case should have a larger Sparrow limit of resolution because the apodised impulse response is wider than the unapodised one. The limit of resolution by the
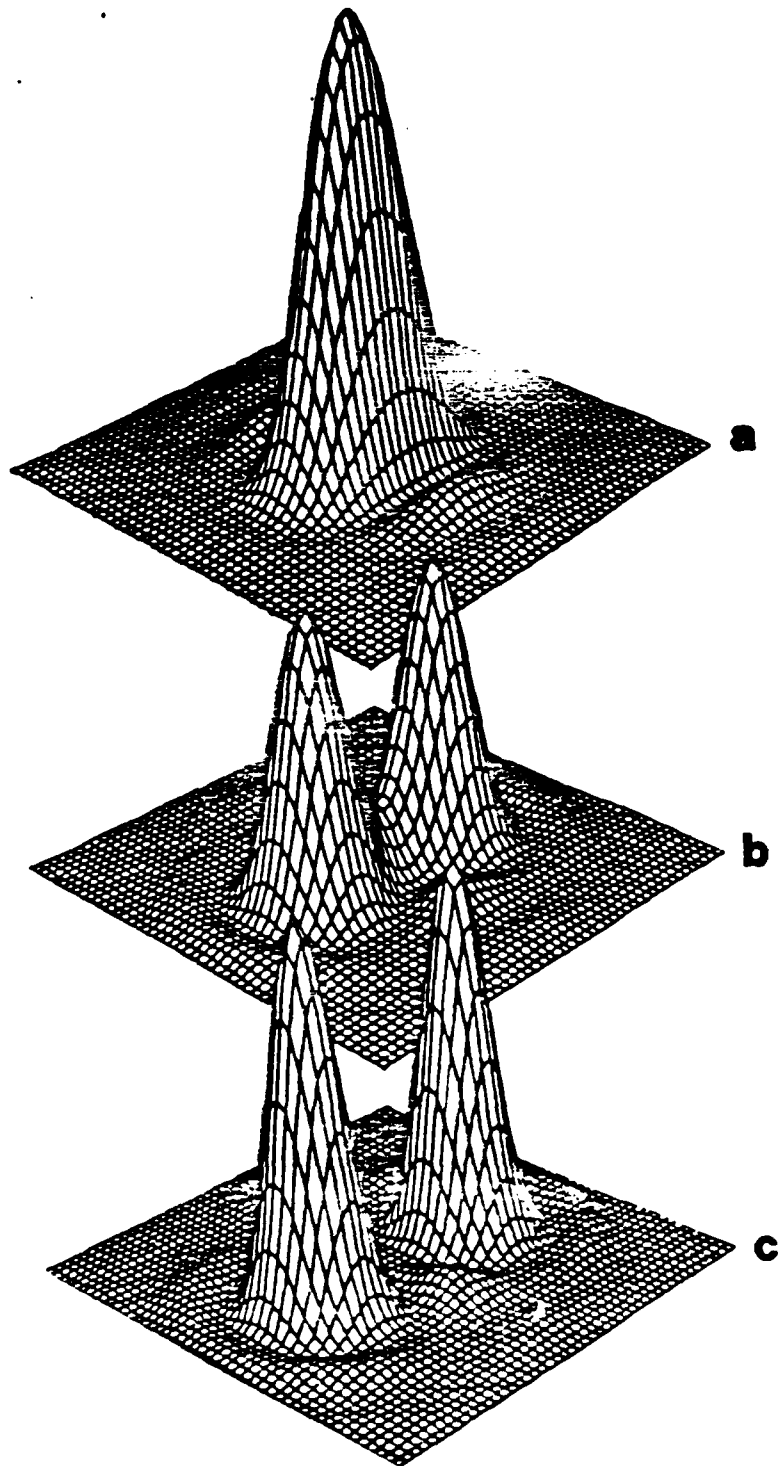
Fig.4.15   The irradiance distribution in the image of two point sources separated in the object plane by (a) $2b = 20$, (b) $2b = 30$), and (c) $2b = 40$. The optical system is unaberrated and unapodised. The vertical axes are scaled in the same relative units of irradiance, while the horizontal axes are scaled in the same relative units of dimensionless distance coordinates.
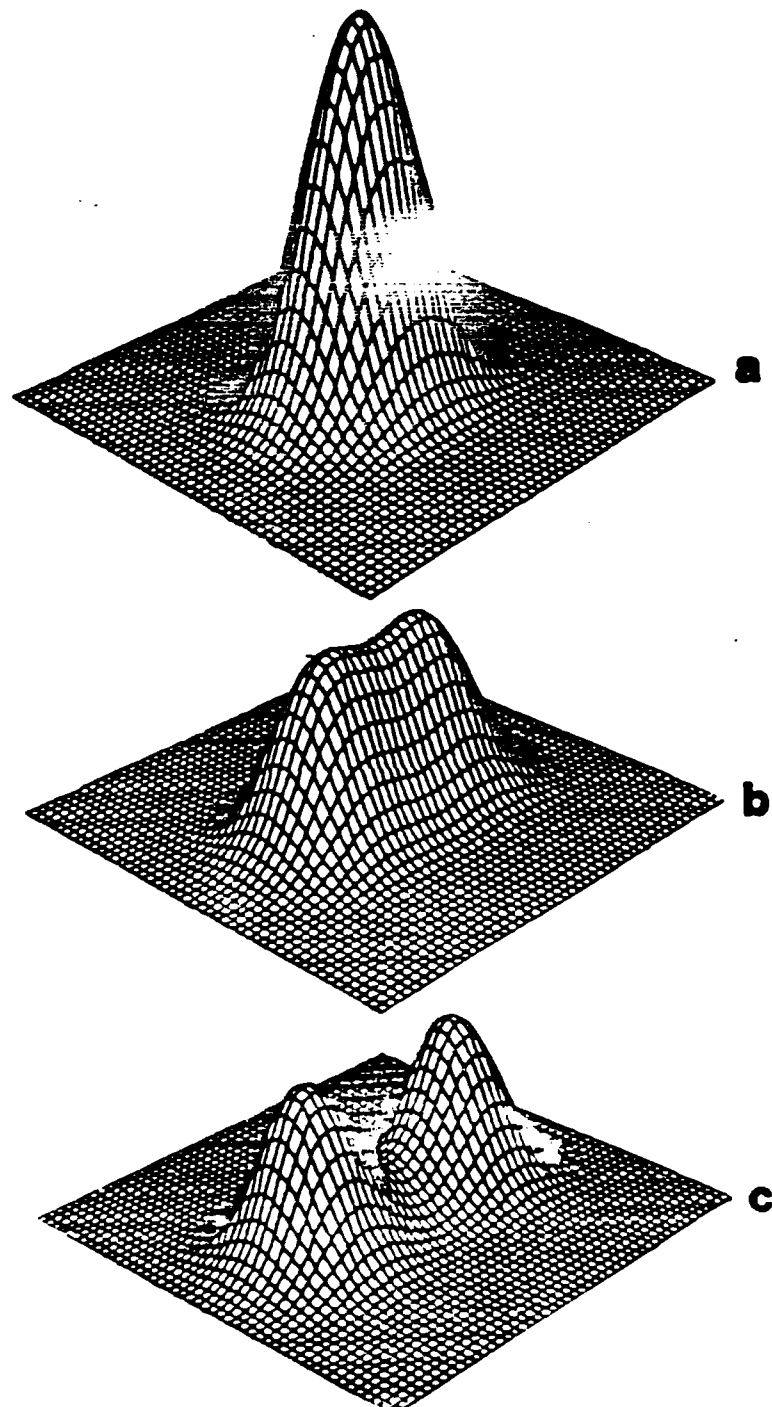
Fig.4.16   The irradiance distribution in the image of two point sources separated in the
object plane by (a) 2b = 20, (b) 2b = 30), and (c) 2b = 40. The optical system is
unaberrated and has a Gaussian apodiser. The vertical axes are scaled in the
same relative units of irradiance, while the horizontal axes are scaled in the
same relative units of dimensionless distance coordinates.

Sparrow criterion is charted in Fig. 4.17 for the third-order aberrations and defocus both with and without a Gaussian apodiser. Data points are not included for higher amount of y-axis coma and defocus because the point image is not sharply peaked (see Chapter 3) at these higher values.

In the image of two points, the centers of the point images are not necessarily in the geometrically predicted locations. The difference between their actual separation and their predicted separation is the mensuration error. The mensuration error for the unaberrated case is shown in Fig. 4.18., where for the solid curve no apodiser was used and for the dashed curve the Gaussian apodiser was used. The abscissa of the plot is the expected separation of the two points based on geometric considerations. The scale is in terms of the canoical coordinate v. The ordinate is in terms of the mensuration error which is the difference between the geometrically expected and the measured separations. At low values of image plane separation the points are unresolved, as in Fig. 4.15a; so that the mensuration error is equal to the expected separation. At the point where the curves start to turn up, the points are just resolvable by the Sparrow criterion. The mensuration error then oscillates about the zero value before damping to the steady-state value of zero. It can be seen that the use of apodisation decreases the mensuration error in the regime where the points are well-resolved. However, the limit of resolution has been degraded.

It can be argued that the better resolution in the unapodised case is not meaningful. This is because the mensuration error is much greater for the unapodised case. So even though the resolution of two closely-spaced points is better in the unapodised case, the apparent position of the two points is more likely to be in error.

As an example of what happens when aberrations are present, Fig. 4.19 shows the mensuration error when the optical system has 0.5 waves of third-order spherical
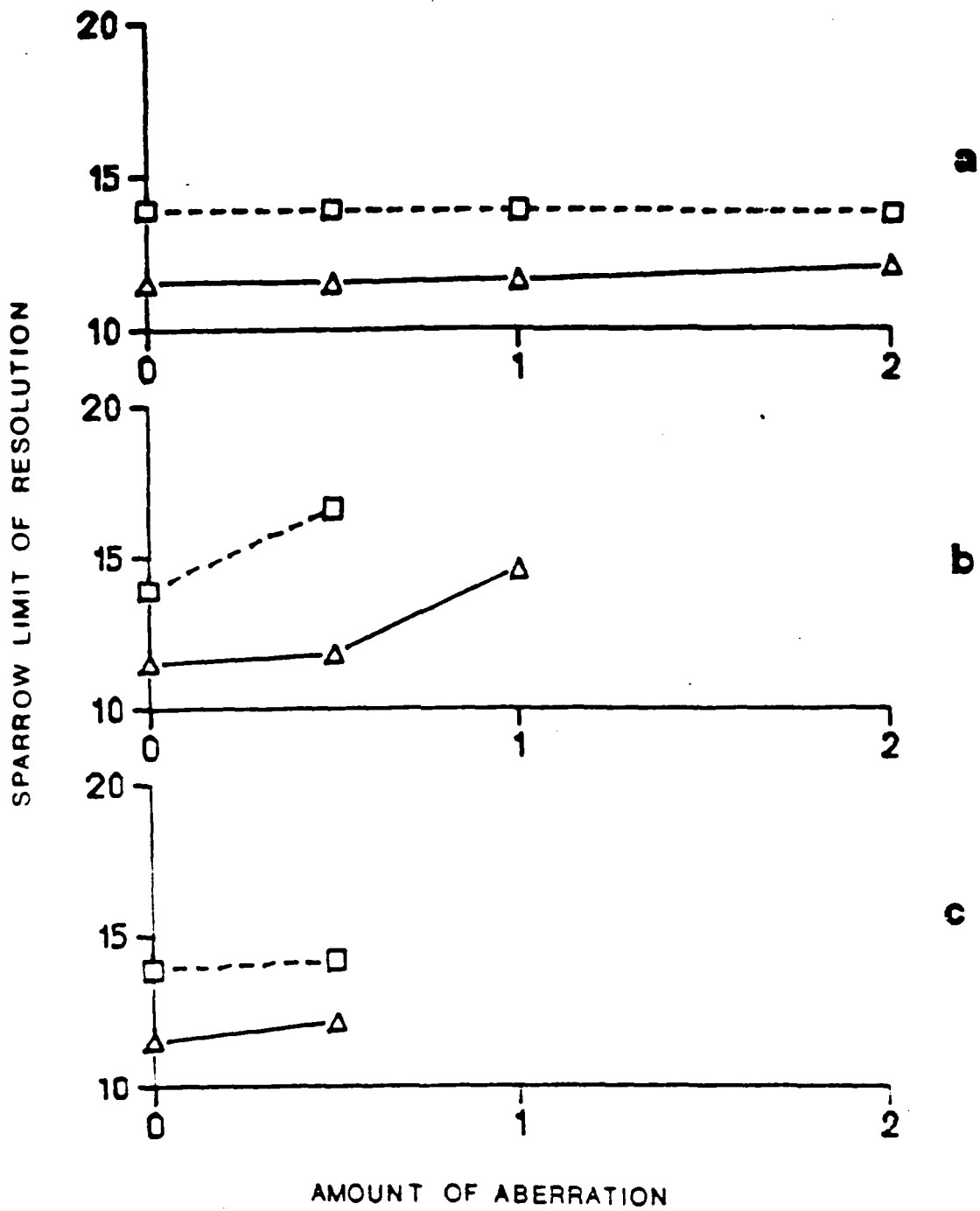
Fig. 4 17   The Sparrow limit of resolution for various values of (a) spherical, (b) y-axis coma, and (c) defocus. Data points are not included for higher amounts of y-axis coma and defocus because the point image is not sharply peaked at these higher values.
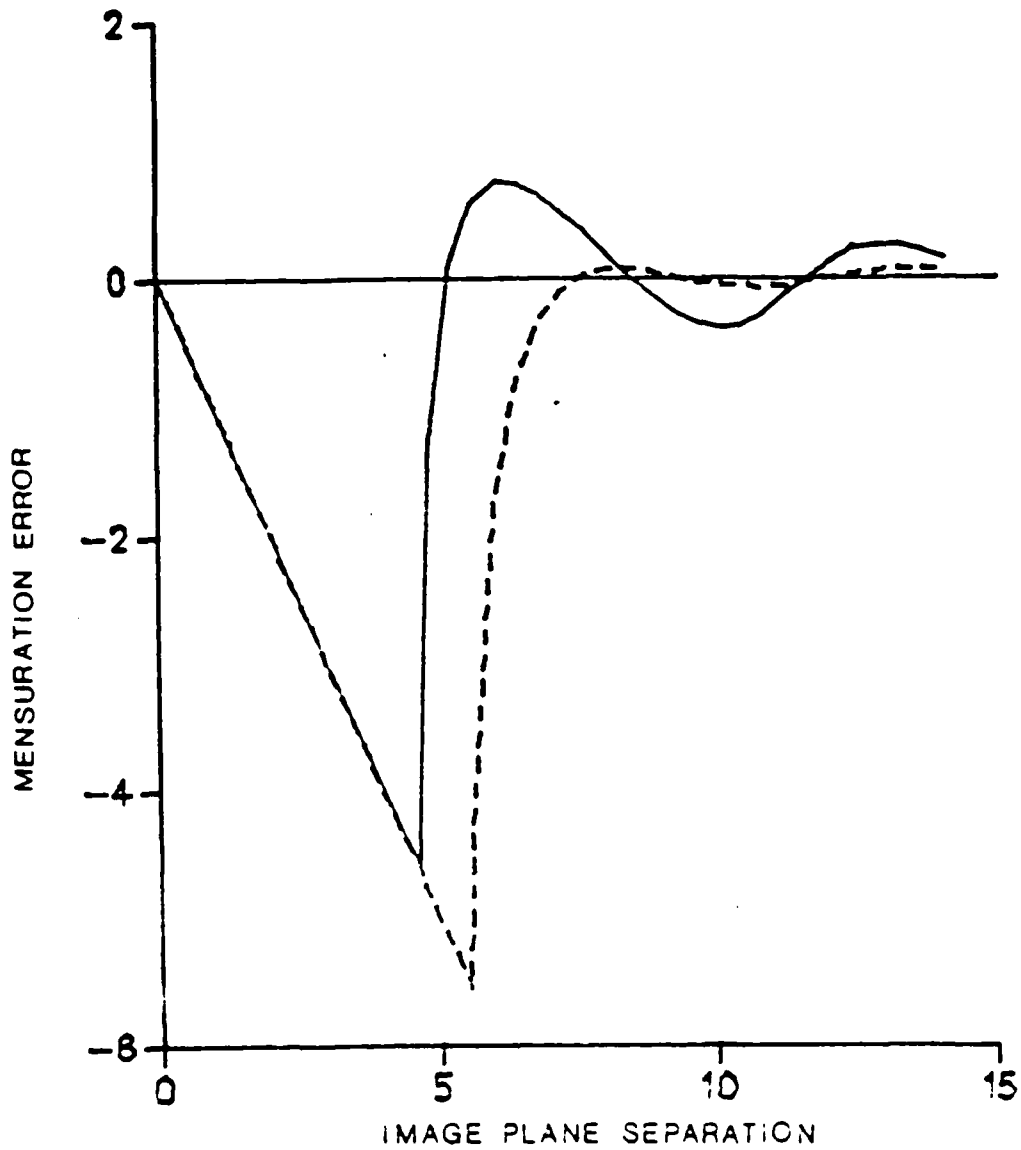
Fig.4.18   The mensuration error for a coherent optical system having no aberrations.
The solid curve is for the unapodised case while the dashed curve is for the
apodised cases. The mensuration error is the measured separation of the two
points minus the expected separation of the Gaussian image points.
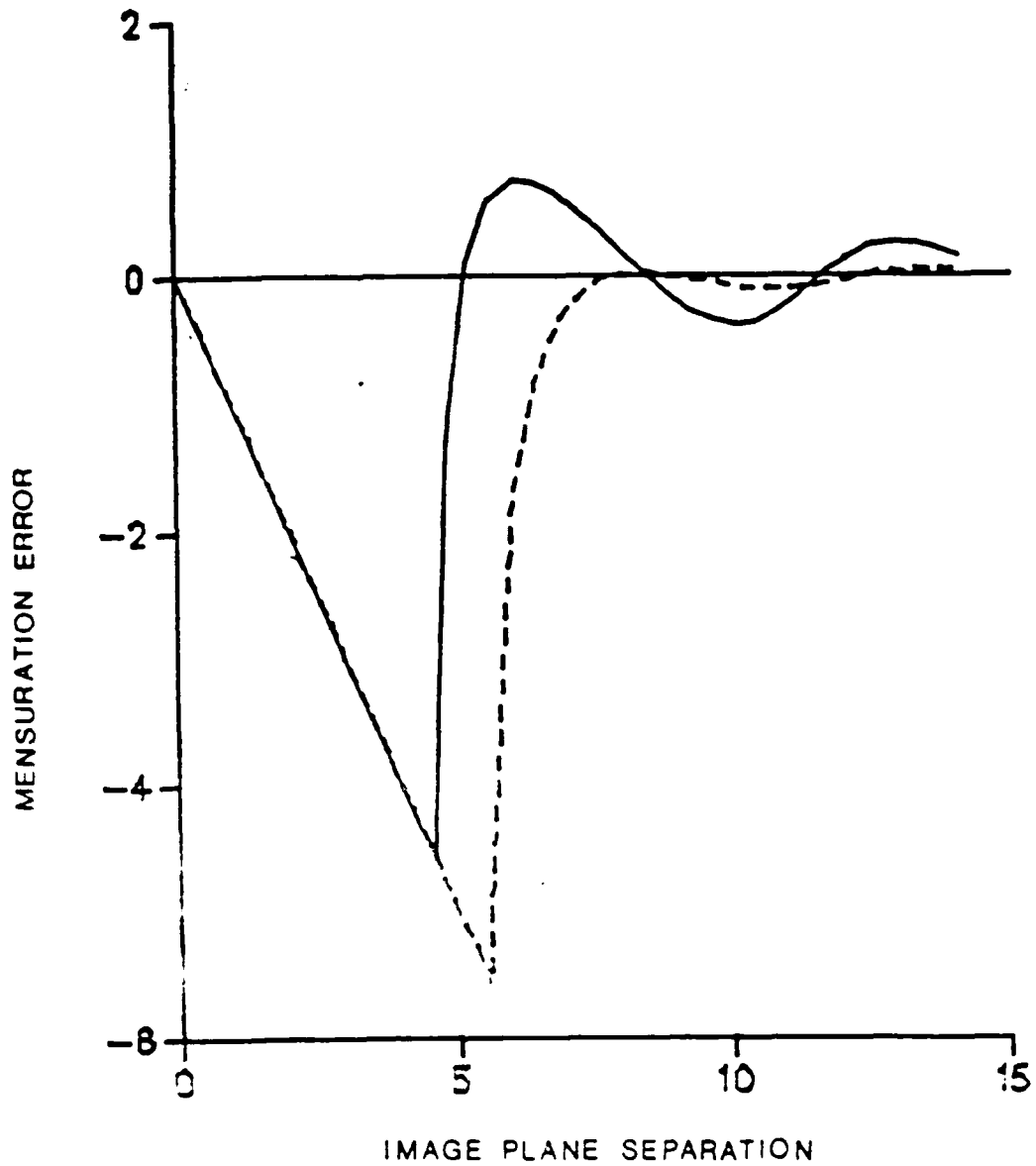
Fig.4.19   The mensuration error for a coherent optical system having 0.5 waves of spherical aberration. The solid curve is for the unapodised case while the dashed curve is for the apodised case. The mensuration error is the measured separation of the two points minus the expected separation of the Gaussian image points.

aberration. Both cases of apodisation are shown; the two sets of curves of Figs. 4.18 and 4.19 are nearly identical. This lack of difference is because the effect of small amounts of spherical aberration on the amplitude impulse response is to transfer energy from the central lobe to the first side lobe while leaving the position of the first dark ring unchanged (see for instance Fig. 3.15). In this case, the aberration in the optical system has not affected the general shape of the curves very much. However, apodisation has the same general effect as in Fig. 1.14. It decreases the mensuration error where the points are resolved, but degrades the limit of resolution.

4.4 IMAGING THEORY CONCLUSIONS

The utility of apodisation in improving the imaging performance of an aberrated coherent optical system has been investigated. The imaging performance has been evaluated in terms of the properties of the images of simple objects.

The image of an edge was evaluated in terms of the edge ringing, shift, and acutance. In general, as the amount of a particular aberration increased the edge ringing increased, the edge shift increased, and the edge acutance decreased. The apodiser was very effective in decreasing the amount of edge ringing in the aberrated image of an edge. The ringing could be suppressed entirely however only when the optical system was free from aberrations.

The evaluation criteria for the image of a slit were ringing on the individual edges of the slit, the apparent width of the slit, and the amount the slit appeared to be shifted. The ringing behavior of the edges in the slit was quite similar to the ringing in the single edge. This is to be expected since the edge separation in the slit considered is much larger than the period of the ringing. The width is a function of the individual shifts of the two edges. The location of the slit image is correct for the symmetrical aberrations

and is shifted for the unsymmetrical ones like coma. The effect of the apodiser is very similar to the effect seen in the case of the edge.

When the image of two closely-spaced points is evaluated, the important parameter is the mensuration error. The mensuration error for an unaberrated system is an oscillatory function which decreases to zero as the point objects are separated in the object space. The addition of spherical aberration to the system did not significantly affect this behavior. The apodiser was quite effective in damping the oscillatory nature of the mensuration error. The resolution limit however suffered as a consequence.

It was not intended that this chapter contain an exhaustive catalog of theoretical results. The intention was to present enough data to gain an understanding of the physical processes. It was not known previously that apodisation would be as effective in improving the performance of aberrated systems as it was in improving unaberrated ones. Now however, in light of the model developed and the results presented, it can be concluded that the apodiser is effective in improving the imaging performance of aberrated coherent optical systems. The reason for this is that the apodiser attenuates by absorption those regions of the exit pupil where the aberrations most affect the phase of the transmitted wavefront.

The results presented here were generated from a theoretical model which has many assumptions and approximations. Therefore, the model which generated them needs to be tested experimentally before they can be fully accepted.

CHAPTER 5 EXPERIMENTS

The purpose of conducting these experiments was to test the theory developed in Chapter 2 and applied in Chapters 3 and 4. The experimental setup and the data acquisition procedure is fully described below before the results are given. The results are given in two separate sections which parallel the subject matter of Chapters 3 and 4. That is, the data sections deal separately with the impulse response and the imaging of simple objects.

5.1 EXPERIMENTAL DESIGN AND DATA ACQUISITION

The basic experimental configuration is shown in Fig. 5.1. This configuration was designed to measure the irradiance impulse response of the optical system formed by lens LI, the apodiser, the iris, and lens L2. Simple modifications of this setup made it possible to measure the image irradiance distribution of simple objects. The specifications of the equipment used in these configurations are in Table 5.1

5.1.1 The Impulse Response Configuration

In the basic optical system of Fig. 5.1, coherent illumination originated from a 0.5 mW, linearly polarized HeNe laser. The laser beam was in the lowest order transverse mode (TEM_{00}) and in, at most, three longitudinal modes with a center wavelength of 0.6328 microns. The beam had a diameter, between the $1/e^2$ irradiance points, of 0.64 mm and a divergence of 1.3 mrad.
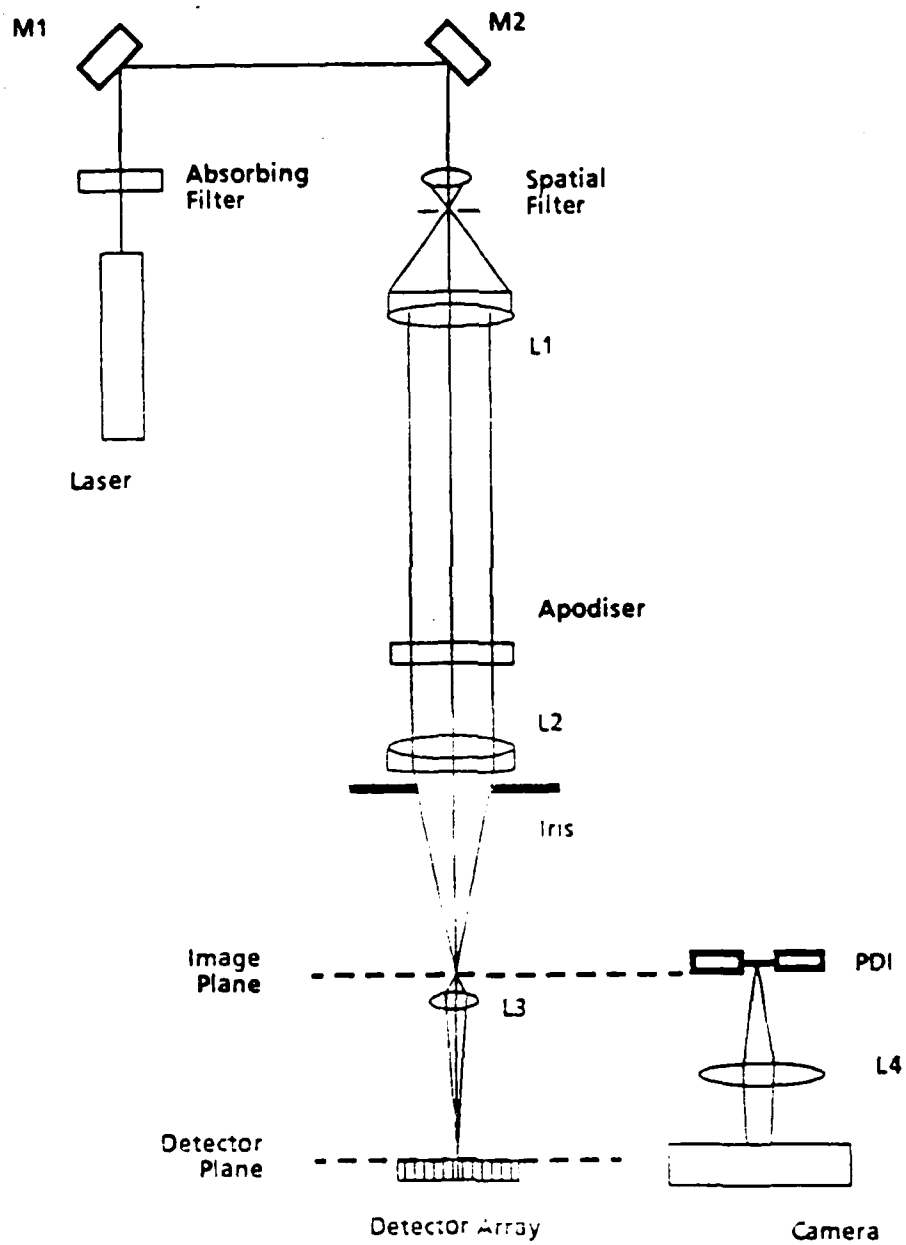
Fig.5.1 The experimental configuration used to measure the irradiance impulse
response of the optical system formed by L1,L2, the iris, and the apodiser

Designation	Source	ID	Description
Laser	Hughes	H3022P	5 mW, linearly polarized
Absorbing filter			Wratten neutral density, various values
M1, M2	Newport	10D10	1" dia. pyrex 1st surface mirrors, $\lambda/10$
Spatial filter	Jodon	LPSF-100	10X microscope objective, 10µm pinhole
L1	Jaegers		Telescope doublet, various focal lengths
Apodiser	See App. 3	52,6	Gaussian amplitude apodiser
Iris	Newport	ID-1.5	18 curved leaves
L2			Depended on particular test configuration
L3	J.E.A.	780094	20X, 0.40 N.A. microscope objective
Detector Array	Fairchild	I-SCAN	256-element CCD linear array with electronics
PDI	Ealing		Point Diffraction Interferometer, f/12 pinhole
Camera	Pentax	K1000	Body used without lens

Table 5.1 The equipment used in the experiment.

The first optical element the beam encountered was the absorbing filter. This filter was actually one or several Wratten neutral density filters of various values. The filters was used to adjust the irradiance level in the plane of the detector array.

Two first-surface mirrors, M1 and M2, directed the beam into the spatial filter. The mirrors had a surface flatness of λ/10. The spatial filter was formed by a 10X, 0.25 N.A. microscope objective and a 10 micron diameter pinhole.

The pinhole acted as a point source for the optical imaging system formed by L1, the apodiser, the iris, and L2. The image of the point source through this system was the irradiance impulse response of the system. Lens L1 was a telescope objective with a diameter of 78.7 mm and a focal length of 495 mm. This iris, while adjustable, was used with a nominal diameter of 25mm. If L1 was used to focus a plane wave limited by the iris at the nominal diameter, the diameter of the resulting Airy spot would be approximately 30 microns. Thus, it is clear that the 10 micron pinhole was indeed acting as a point source for this system. Furthermore, a simple calculation reveals that the irradiance of the wavefront from the pinhole at the lens L1 varied by no more than 2 percent over a central circular region of 25 mm in diameter. Lens L1 was a high quality telescope objective purchased from Jaeger Optical Company. When used at this reduced aperture the lens would be expected to be essentially aberration-free. A measurement of the wavefront after the lens L1 confirmed this expectation.

The apodiser was one of several whose amplitude transmittance was nominally Gaussian. The design, construction, and characterization of these apodisers is detailed in Appendix 2.

Lens L2 was the final element in the optical imaging system. During the experiments different lenses were used in this position. The particular lens used depended upon the aberrations desired.

The image of the point source was formed in the image plane. Two different configurations were used to characterize this image.

The first is shown on the optical axis below the image plane in Fig. 5.1. It consisted of a 20X microscope objective (L3) and a linear detector array. The microscope objective acted as a magnifier. Magnification was needed because the scale of the image of the point in the image plane was too small to be adequately sampled by the detector array. Lens L2 generally had a focal length of about 300 mm. Thus, the diameter of the Airy spot in the image plane was approximately 19 μm. The detector array was a Fairchild CCD111 linear array of charge coupled detectors (CCD), each of area 17 x 13 μm, on 13 μm centers. Hence the magnification provided by the microscope objective L3 was needed. The array was part of a card of electronics marketed by Fairchild under the name I-SCAN. The data flowing from this array was collected by a microcomputer. Appendix 3 contains a complete description of the data collection equipment. This configuration resulted in a linear array of samples of the irradiance through the center of the image of the point source.

The second configuration used to measure the image is shown shifted to the right of the first configuration in Fig. 5.1. It consisted of a point-diffraction interferometer[78] (PDI), lens L4, and a camera back. The PDI is a partially transmitting plate with a totally transmitting circular region in its center. The circular region was on the order of the size of the Airy spot generated by L2. When the PDI was placed in the image plane, the wavefront from L2 passed through the PDI and was split into two wavefronts. One was a replica of the incident wavefront with reduced irradiance, while the other was a diverging spherical wavefront generated by the small circular region. These two wavefronts interfered and the resultant interference pattern contained information about the aberrations in the optical system. Lens L4 was adjusted so that the exit pupil

was imaged onto the film plane in the camera. Thus the recorded interferogram contained information about the aberrations in the exit pupil.

5.1.2 The Imaging Configurations

For the experiments involving the image of two point sources, the configuration of Fig. 5.1 was used with little modification. However, when imaging an extended object such as an edge or a slit this configuration had to be extensively modified as shown in Fig. 5.2.

5.1.2.1 Imaging of Two-point Objects

A set of five double pinholes was purchased for use in the two-point imaging experiments. They were placed, one at a time, in the plane of the pinhole of the spatial filter of the configuration of Fig. 5.1. The double pinholes were mounted on the same type of circular magnetic holders used for the spatial filter. The spatial filter lens was moved longitudinally away from the filter location so that each pinhole was illuminated uniformly The detector array was centered on the resulting image irradiance pattern The separation of the peaks in the image was determined by counting the number of pixels between the peaks.

The double pinholes were manufactured by burning two closely-spaced small holes with a focussed laser beam. The holes were specified to be 10 microns in diameter The spacings were specified to be 42,35,28,21, and 14 microns. The actual diameters and spacings were determined experimentally.

The diameters of the individual holes were determined by observing the far-field diffraction pattern when the hole was illuminated from behind. Essentially, each hole
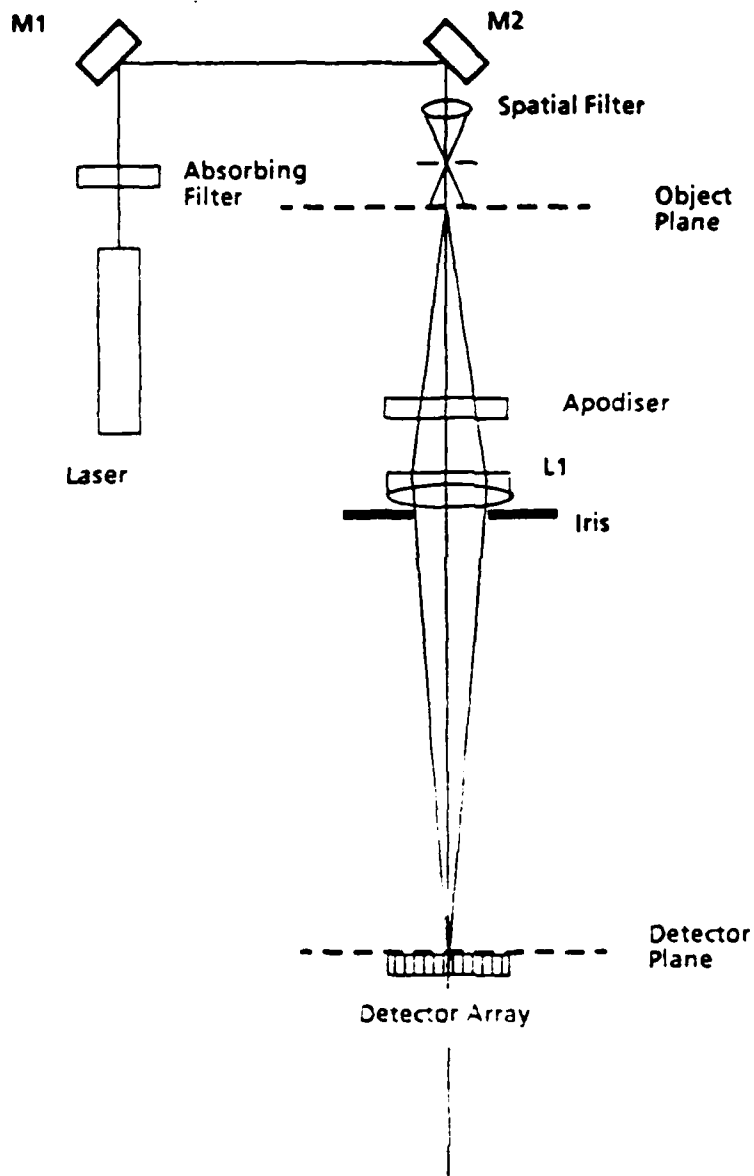
Fig.5.2 The experimental configuration used to measure the image irradiance
distribution of edge and slit objects through the optical system formed by L1 L2
the iris, and the apodiser.

was set up as a slightly defocused spatial frequency filter. The incident wavefront was approximately flat in phase and uniform in irradiance. The far-field pattern was then an Airy diffraction pattern. The width of the first dark ring (diameter of the Airy spot) was measured and the width of the diffracting aperture (pinhole) was inferred using Fourier optics techniques. The pinhole diameters were found to be 9.5 ± 0.5 μm.

The separations were found in a similar manner. For this measurement, both holes of each double pinhole were illuminated by a beam which was approximately uniform in phase and modulus. The resulting far-field pattern was a system of Young's interference fringes. The spacings of these fringes were related to the separation of the holes. Assuming that one pinhole separation was known, the others could be determined by the ratios of the fringe spacings in the various Young's interference patterns.

The separation of the two holes in the double pinhole with the largest labeled separation was measured using a powerful optical microscope. For this purpose, a Leitz Ortholux microscope was used. It had a 50X objective (N.A. = 0.65) and a 10X eyepiece for an overall visual magnification of 500. The smallest resolvable linear dimension in the object plane, by the Rayleigh criterion was $z = 0.61\lambda/N.A.$; with $\lambda = 0.5$ microns this gives $z = 0.47$ microns. The measured separation of the two holes in this case was 42 ± 1 micron. Notice that the measured separation is much greater than the resolution limit so that the mensuration error discussed in Chapters 2 and 4 was negligible.

5.1.2.2 Imaging of Edge and Slit Objects

The configuration of Fig. 5.2 was needed for the imaging of the edge and slit objects because of the presence of speckle. Speckle is the random irradiance fluctuations seen in the image irradiance distribution. It is caused by random variations in the

nominal surface shapes of mirrors and lenses, as well as dust particles on these surfaces. Speckle was reduced in this experiment primarily by using fewer optical elements, one lens instead of three, between the object and the image planes. Thus there were fewer sources of speckle.

The effects of speckle were also controlled by carefully choosing the placement of the iris. The characteristic size of the speckle pattern was determined by the limiting aperture in that part of the system which followed the source of the speckle. For instance, if the source of the speckle was in the object plane of Fig. 5.2, the iris would be the limiting aperture and the characteristic size of the speckle in the image plane would be the Airy spot diameter of the system. In the present case however, the object was one or a pair of razor blades (no source of speckle except perhaps along the edges), and the incident wavefront had just been spatially filtered so it was relatively, if not completely, free from random phase flucuations. This then left as a major source of speckle, the lens L1. But the iris was not the aperture stop for the optical sytem following the lens. The system following the lens was simply a free-space propagation system. Thus the characteristic size of the speckle from sources in or on the lens L1 was much larger than the speckle size from object sources. The effect was a reduction of the speckle which interfered harmfully with the desired images. The speckle in the image plane while not completely removed, was considerably reduced by this technique.

5.1.3 Alignment

The proper alignment of the various experimental configurations was crucial to the success of the experiment. A misaligned system would have unwanted aberrations.

The alignment procedure was based on a technique developed by Taylor and Thompson[79] The essence of the idea was to first establish unambiguously an optical axis

and then align each element to that axis. The procedure outlined here is, for clarity, specific to Fig. 5.1. However, the techniques are perfectly general and were used to align all of the experimental configurations.

Initially, the optical axis was established with the laser, the turning mirrors M1 and M2, and a target placed in the detector plane (see Fig. 5.1). The target was a black cross inked on a white card. The card was mounted so as to be perpendicular to the optical table surface. The center of the cross was 4.44 inches above the surface. Placing the cross in front of the laser, the output aperture of the laser was adjusted to be 4.44 inches above the surface. Then the cross was moved to a position in front of M1 and the laser was tilted, about the output aperture, to center the laser beam on the cross. Next, the target was moved just in front of M2 and then M1 was rotationally adjusted to the center of the laser beam on the cross. Then the target was moved to the detector plane and M2 similarly adjusted.

Next a white painted sheet of metal with an aperture that was smaller than the laser beam was placed between M1 and the spatial filter location. The small hole was centered on the beam by observing and centering the circular diffraction pattern from the hole on the cross. This hole was used as a reference for aligning the lens in the spatial filter

Before the spatial filter was aligned, a crosshair formed by two thin metal wires was placed between the position of the spatial filter and position of lens L1. The crosshair was centered on the optical axis by observing and centering the shadow of the crosshair on the target cross. The center of the hole in the metal sheet and the crosshairs then defined the optical axis.

The spatial filter was modified so that the lens and the pinhole were separately adjustable. After mounting the spatial filter lens in its approximate location it was

adjusted in tilt by observing the reflected light as it impinged upon the white-painted metal. The reflected light formed a circular interference pattern which was centered on the hole by adjusting the tilt of the lens. Simultaneously, the transmitted beam which again cast a shadow of the metal crosshairs onto the target was aligned to the target cross by adjusting the lens in translation. When the reflected circular diffraction pattern was aligned on the hole and, at the same time, the shadow of the crosshair was aligned on the target cross, the alignment of the spatial filter lens was complete.

The spatial filter pinhole was then put in place and aligned in the usual manner by maximizing the power throughput while minimizing the transmission of higher spatial frequencies. When done correctly, the shadow cast by the metal crosshairs remained centered on the target cross. The metal sheet with the small hole was then removed. At this point the optical axis was defined by the pinhole and the metal crosshairs

Next, the main elements of the optical system were put in place and aligned. These elements were lenses L1 and L2, the iris and the apodiser.

First, L2 was put in place. It was adjusted in translation by observing and centering the shadow of the metal crosshairs on the target cross. The rotational alignment was accomplished by using the Boys points. Boys points are images of the spatial filter pinhole formed by reflections from the surfaces of the lens. These points occur both before and after the lens. The position of these points which occur before the lens are particularly sensitive to rotational adjustment.[?] To aid in aligning these points a fine metal mesh screen was interposed between the lens L2 and the pinhole. This screen was placed in the plane of one of the reflected Boys points. Thus, a small bright spot appeared on the screen. The shadow of the metal crosshair also appeared on the screen. The lens was properly aligned, in a rotational sense, when the Boys point was centered

on the shadow of the crosshair and simultaneously the transmitted shadow of the crosshair was centered on the target cross..

Lens L1 was then put in place and aligned in an analogous manner. Additionally, lens L2 was adjusted along the optical axis so that it was exactly its focal length away from the pinhole. This was done by placing a shear plate between lens L1 and L2 and observing the reflected interference pattern. The lens was adjusted correctly in a longitudinal sense when the interference fringes were completely fluffed out.

Next the iris was put in place quite close to lens L2. It was aligned in translation by observing its shadow cast on the target. The apodiser, when used, was aligned similarly and was placed as close as possible to the iris.

At this point the optical system was completely aligned. Depending on the particular need, either L3 and the detector array or the PDI, L4, and camera was then aligned to the optical axis.

As a test of the accuracy and repeatability of alignment, the same optical system was aligned from scratch several times. Each time the aberrations were measured. The optical system (see Fig. 5.1) consisted of a Jaegers #1158 lens (f = 495 mm) as L1, a Jaegers # 358 lens (f = 390 mm) as L2, and an iris with a diameter of 0.525 inches. The measured third order aberrations, in terms of Siedel aberration coefficients, for each of these tests are tabulated in Table 5.2. Two conclusions can be drawn from the data in this table. First, because of the low magnitude of each aberration, it can be concluded that the lenses were of high quality and the system was aligned well each time. Second, because the different alignments produced very similar results, it can be concluded that the alignment procedure was repeatable.

	1	2	3
Astigmatism	0.0	0.0	0.0
Coma	0.1	0.1	0.1
Spherical	-0.1	-0.0	-0.1

Table 5.2   The measured third-order Seidel aberrration coefficients after several aligments of the same optical system. The units of the tabulated values are wavelengths ($\lambda = 0.6328$ microns).

5.1.4 Data Acquisition

After a particular optical system had been set up and aligned the data acquisition process could proceed. The raw data were in two forms, photographic and electro-optic. These will be discussed separately. To clarify this process, a particular optical system will be analyzed as an example. For this purpose, the optical system of Fig. 5.1 was constructed where L1 was a Jaeger's # 1158 lens (f = 495 mm), L2 was a Jaeger's # 958 lens (f = 390 mm), and the apodiser was #6. These components were selected and oriented to achieve a system having small amounts of aberrations which would result in an Airy diffraction pattern in the detector plane.

5.1.4.1 Electro-optic Data

Electro-optic data were generated by operating the linear CCD detector array when that array was in the plane of the diffraction pattern of interest. The detector

array and the associated 20X microscope objective were installed and aligned as described in section 5.1.1 and 5.1.3.

The data were in the form of 256 eight-bit words; one word for each element in the detector array. Such a grouping was called a frame of data. Eight frames of data were taken each time data was collected.

A single frame of data from a test of the example system is shown in Fig. 5.3a. The optical configuration was that of the example system. The vertical axis is relative irradiance plotted logarithmically and the horizontal axis is normalized distance v. The scales are the same for all the plots in Fig. 5.3.

The digitized nature of the data is evident from Fig. 5.3a. There are 256 (2^8) possible values of relative irradiance because the word size is eight bits. Thus, the minimum resolvable signal difference is 1/256 = 0.0039 relative to a maximum signal value of 1.0. This minimum resolution is seen as discrete steps in the data of Fig. 5.3a. The steps are of different vertical size because the vertical axis was plotted logarithmically.

When eight consecutive frames of data were averaged the result was the curve in Fig. 5.3b. The integration time for each frame was 4.2 msec. The data after this averaging process were considerably smoother.

In Fig. 5.3c, the averaged data (plotted as triangles) are shown relative to an Airy pattern. The difference between the data and the Airy pattern never exceeds the minimum resolution of the system.

In Fig 5.3d, the averaged data are shown relative to a central slice of the irradiance impulse response of an optical system having the aberrations measured using the PDI. The theoretical plot was generated using the model described in Chapter 3.

NORMALIZED DISTANCE V
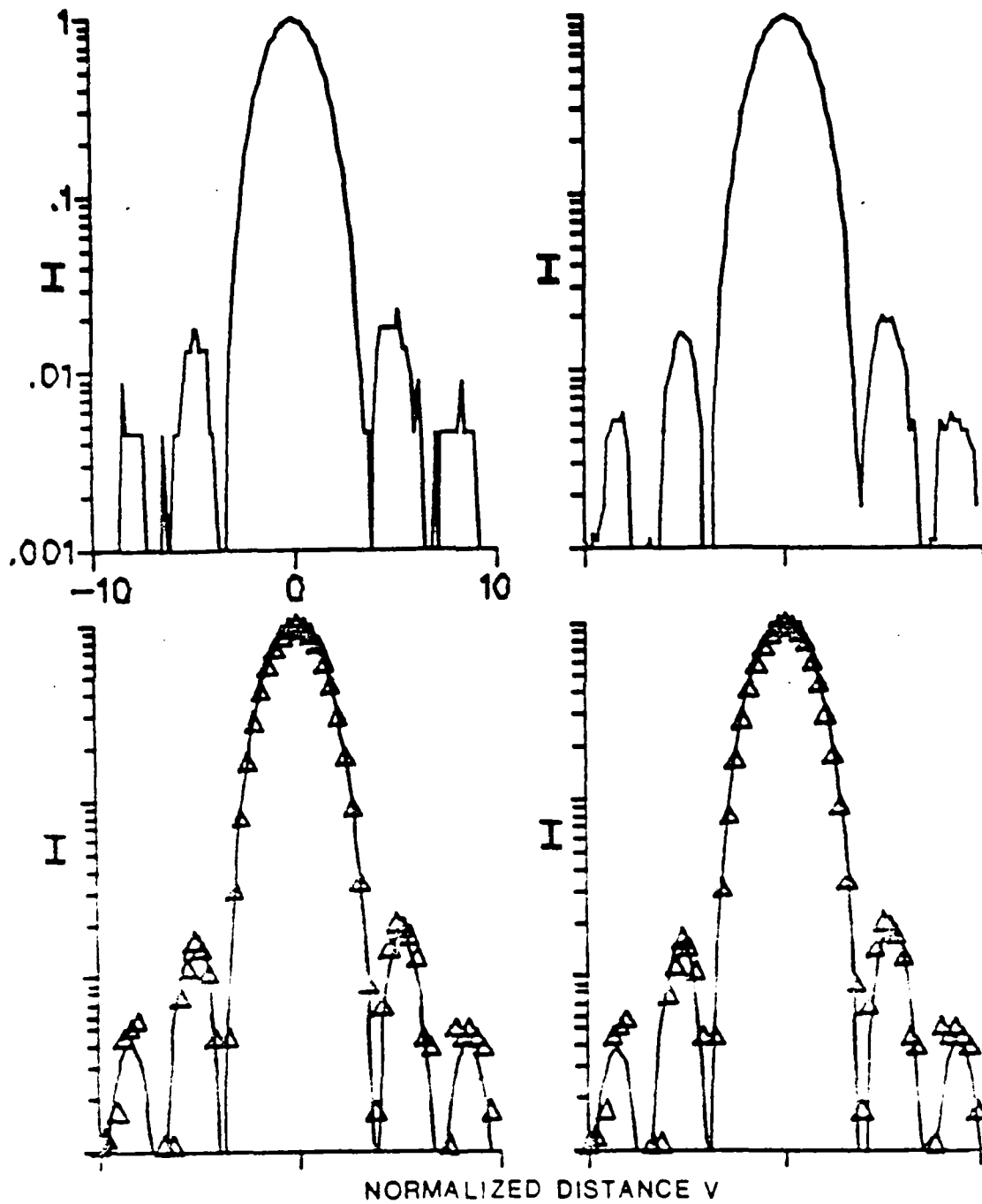
Fig.5.3 A comparison of theoretical and experimental results. (a) A single frame of data.
(b) The average of eight frames of data. (c) A comparison of the data in (b) to an
Airy pattern. (d) A comparison of the data in (b) to a central slice through the
impulse response predicted using the measured aberrations. The vertical axis for
each plot is relative irradiance(I) plotted on a logarithmic scale. The horizontal
axis for each plot is normalized distance v. The scales are the same on all of the
plots.

A photograph of the irradiance impulse response through this optical system is shown in the top of Fig. 5.4. In this case there was no apodiser and essentially no aberrations (only those of column 3 of Table 5.2). The photograph should be and is approximately an Airy diffraction pattern. The plot in the bottom of this figure is the calculated modulus of the amplitude impulse response with the above aberrations and no apodiser. The plot was generated by the model described in Chapter 3 (PSF.FOR) with the measured aberrations as inputs.

Two different apodisers were used at different times during these experiments. When they were put into the system, the impulse response was significantly modified. Experimental data in the form of a central slice through the impulse response for one of these apodisers (#6) is shown in Fig. 5.5. The broken curves represent the experimental data from two data collections when the detector array was rotated about the optical axis by 90° for one of the collections relative to the other. The theoretically predicted irradiance impulse response is shown as a solid line in this figure. The predictions were generated by the model described in Chapter 3 with the aberrations measured with the PDi and with the apodiser parameter described by (4.6). The apodiser can be described by the function $T(\eta) = \exp(-G\eta^2)$, where, when $G = 3$, the apodiser described by this function was in place in the system and, when $G = 0$, there was no apodiser in place. This shorthand notation will be used in future references to the existence of an apodiser. For these data the iris diameter was set to be 0.525 inches. Details about how the apodisers were designed, constructed, and tested are contained in Appendix 2.

A photograph of an apodised ($G = 3$) and essentially unaberrated irradiance impulse response is shown in Fig. 5.6. The optical system had the third-order aberrations
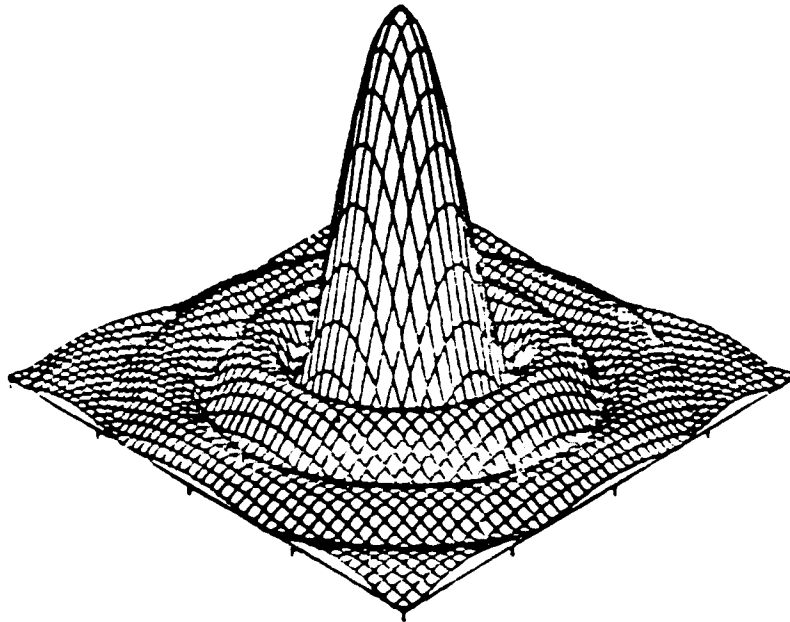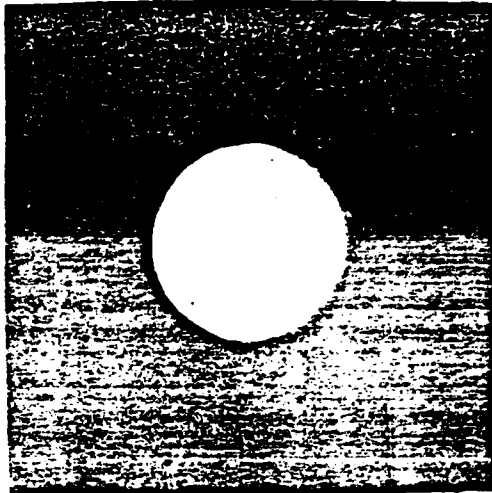
Fig 5.4 The photograph in the top of this figure is of the irradiance impulse response of an unapodised and essentially unaberrated optical system. The aberrations of this system are listed in column 3 of Table 6.2. The plot on the bottom of this figure is the calculated modulus (vertical axis) of the impulse response through the same optical system. The horizontal axes have the same units of normalized distance.
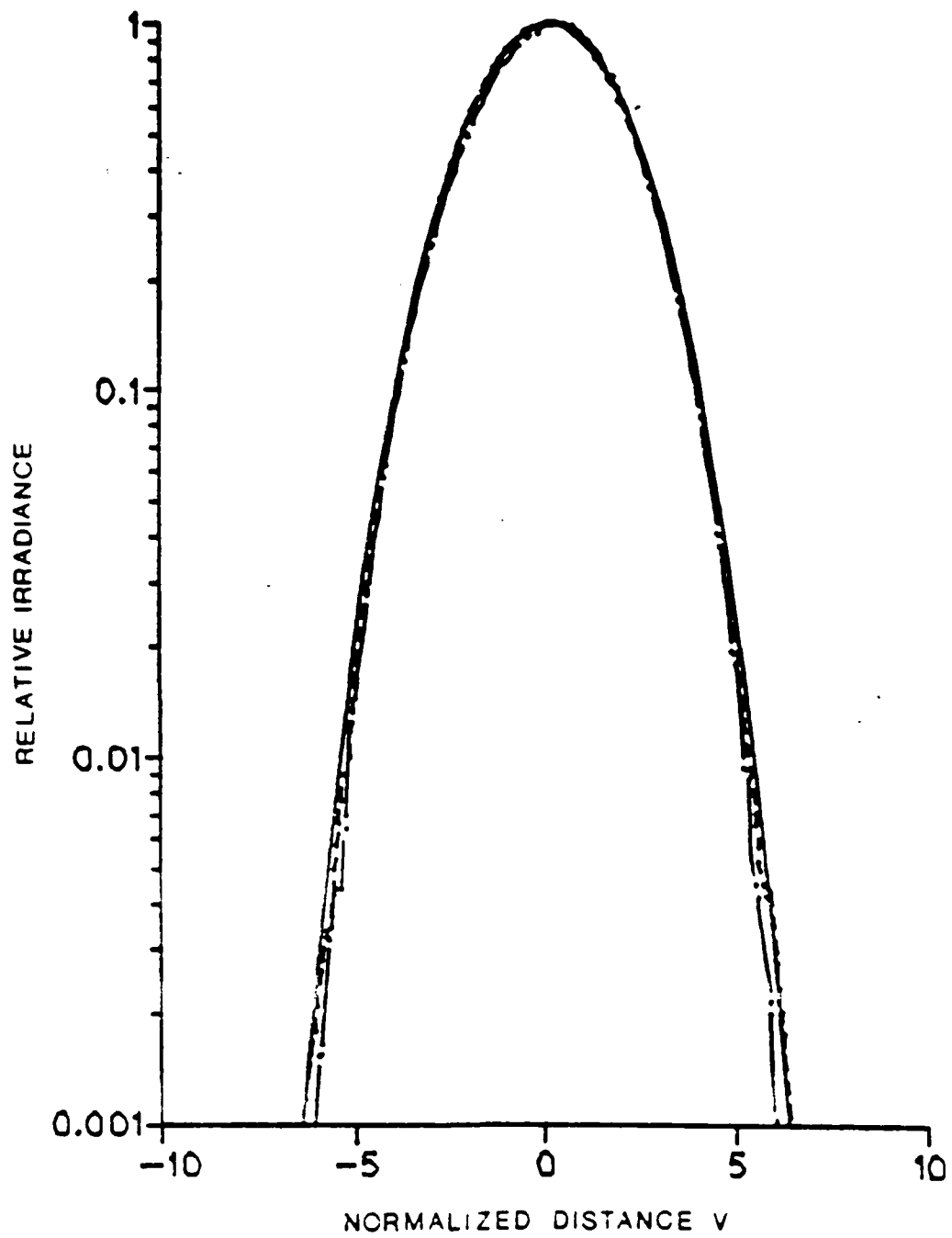
Fig.5.5 Theoretical (solid curve) and experimental (broken curves) plots of central slices of the irradiance impulse response for an apodised (G = 3) and unaberrated optical system.
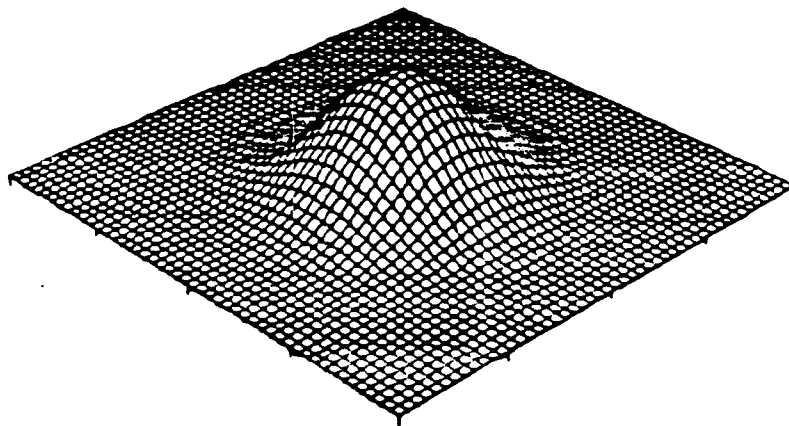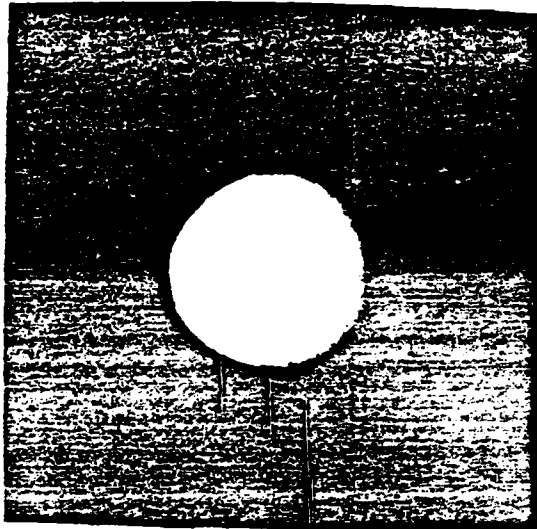
Fig.5.6 The photograph in the top of this figure is of the irradiance impulse response of an apodised (G = 3) and essentially unaberrated optical system. The aberrations of this system are listed in column 3 of Table 6.2. The apodiser is described by (4.6) and shown in Fig. 3.9. The plot on the bottom of this figure is the calculated modulus (vertical axes) of the impulse response through the same optical system. The horizontal axes have the same units of normalized distance.

listed in column 3 of Table 5.2. The apodiser was #6 and the iris diameter was 0.525 inches. The plot in the bottom of this figure was generated with the same aberrations and apodisation by the computer model PSF.FOR.

At this point, it is clear that the experimental apparatus was capable of making measurements which were fine enough to measure the important details of the diffraction patterns produced by these optical systems. The measurements were accurate, precise, and replicable. The measured patterns agreed well with the predicted patterns.

5.1.4.2 Photographic Data

The data recorded by photographic means were the interference patterns generated from the point-diffraction interferometer (PDI) and analog data from the I-SCAN detector displayed on the oscilloscope and photographed.

The PDI was used to measure the aberrations in the optical system. The PDI, lens L4, and the camera back were installed and aligned as described in the previous sections This was done on every data run. The interference pattern was recorded on Kodak Plus-X Pan 35 mm film, which was developed according to the manufacturer s instructions. The resulting negative was used to print a positive image onto an 8" x 10" sheet of Kodak Polycontrast RC II film, which also was developed according to the manufacturer's instructions.

An interferogram from the example system is displayed in Fig. 5.7. These data were collected with the iris diameter set to be 0.525 inches. The shape of the fringes and their spacing are related to the aberrations in the optical system. These aberrations were
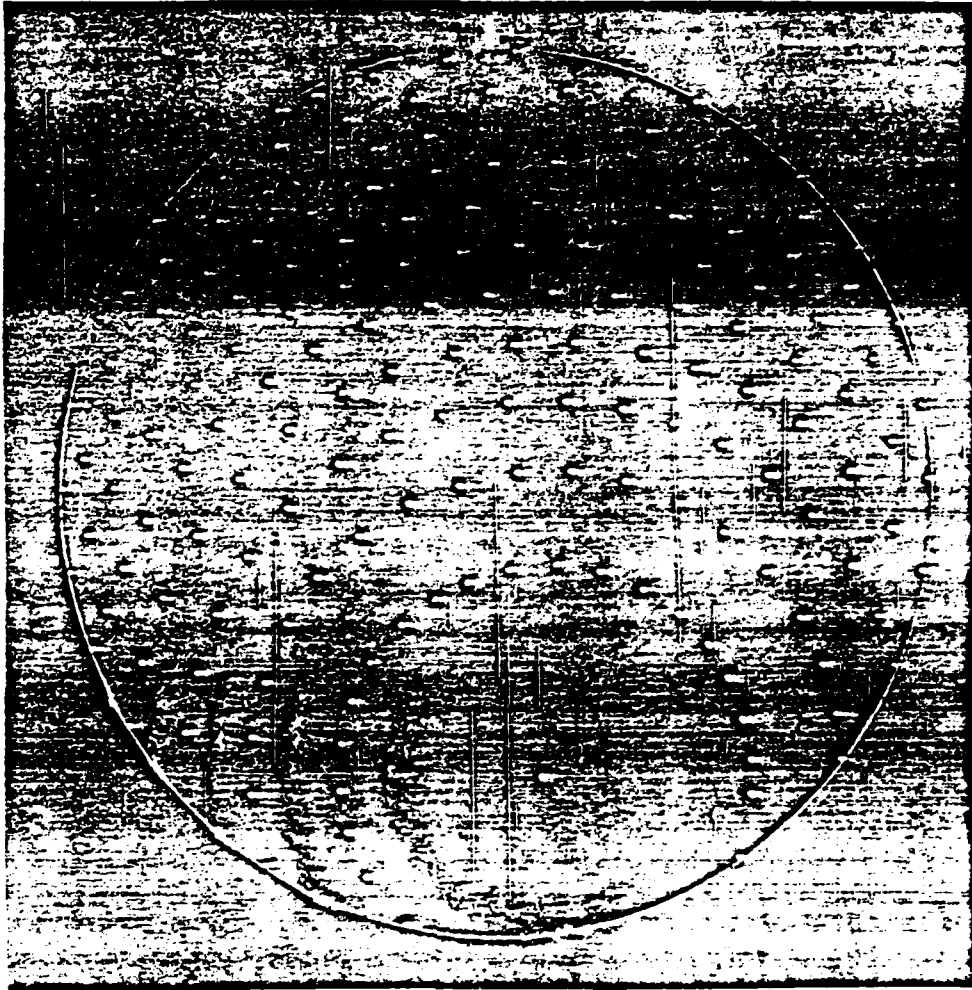
Fig 5.7 An interferogram of the example optical system generated by the point-diffraction interferometer. The white dots are the points which were digitized and entered into the interferogram analysis program WISP.

found by digitizing the coordinates of central points along the fringes. The interferogram as well as the digitized points for this example are shown on the in Fig. 5.7. The digitized points were the input data to a fringe analysis program written by Professor James Wyant of the University of Arizona. One of the outputs of the program is the aberration values in terms of the Zernike as well as Siedel coefficients. The third order Siedel coefficients for the interferogram of Fig. 5.7 are listed in column 3 of Table 5 2

At times, instead of collecting the I-SCAN data, digitizing it, and processing it with the microcomputer, the analog data from the I-SCAN detector was displayed on the oscilloscope where it was photographed. This analog data was then compared to the theoretical predictions. This method of data collection was considerably more simple to accomplish than the totally electro-optic method of section 5.1.4.1.

5.2 EXPERIMENTAL EVIDENCE

As stated in the beginning of this chapter, the purpose of the present experiments was to adequately test the theory developed in Chapters 2, 3, and 4. The development of that theory involved several assumptions and approximations. Extensive predictions about the behavior of aberrated coherent imaging systems and the utility of apodisation were made based on this theoretical development. Thus it was necessary to perform credible experiments to establish the validity of the model used to make those predictions.

In the previous sections some experimental results were presented. The experimental data on the irradiance impulse response of the nearly unaberrated system agreed very well with the theoretical predictions.

In the following sections, the theory will be tested under a wider range of conditions. Aberrations will be introduced into the optical system and imaging of a point, two closely-spaced points, an edge, and a slit will be performed. It will be seen that in these cases also the theory is sufficient.

5.2.1 Aberrated Impulse Response Data

Aberrations were introduced by a number of methods. Spherical aberration was introduced, for instance, by reversing the orientation of lens L2 in the configurations of Figs. 5.1 and 5.2. The lens L2 was usually a well-corrected telescope doublet. Such elements are designed assuming that one of the conjugates is at infinity. This results in the surface of the doublet having the largest curvature being on the infinite conjugate side. For example, the lenses in Fig. 5.1 are drawn with the infinite conjugate sides towards each other. In this orientation the system will have a minimum amount of spherical aberration. This is indeed how the system was oriented when the data tabulated in Table 5.2 were gathered. If the orientation of lens L2 were reversed so that

the infinite conjugate side faced the image plane, it could be expected that the dominant aberration in the system would be third order spherical.

This is indeed the case for the data in Figs. 5.8 through 5.11. The data in these figures were collected using the configuration of Fig. 5.1, where different lenses, oriented for maximum spherical aberration, were used as L2.

In Figs. 5.8 and 5.9, photographs of the irradiance impulse response of an aberrated system are displayed along with calculated 3-D plots of the modulus of the amplitude impulse response generated by the model PSF.FOR using the measured aberrations of the photographed system. Fig. 5.8 is for an unapodised system and Fig. 5.9 is for an apodised (G = 3) system. The measured third order Seidel coefficients were astigmatism = 0.1λ, coma = 0.1λ, and spherical = -0.8λ. There were negligible amounts of higher order aberrations. In the theoretical plots shown just below the photographs, the modulus is used instead of the irradiance to emphasize the ring structure.

The agreement between the experimental and theoretical data is qualitatively very good. In the case of the unapodised impulse response (Fig. 5.8), the magnitude of the first ring grew while the magnitudes of the central peak and the second ring decreased relative to the unaberrated case (compare Fig. 5.8 to Fig. 5.4). This behavior was predicted in Figs. 3.11 and 3.15. As seen in Fig. 5.9, the apodiser was quite effective in removing the ring structure. The impulse response has been considerably smoothed which is in agreement with theory. This smoothing implies that the apodiser will be effective in reducing the ringing in the image of an edge or a slit, as well as reducing the mensuration error in the image of two closely-spaced points. Data from these types of images through a system with the present impulse response will be displayed in the next section.
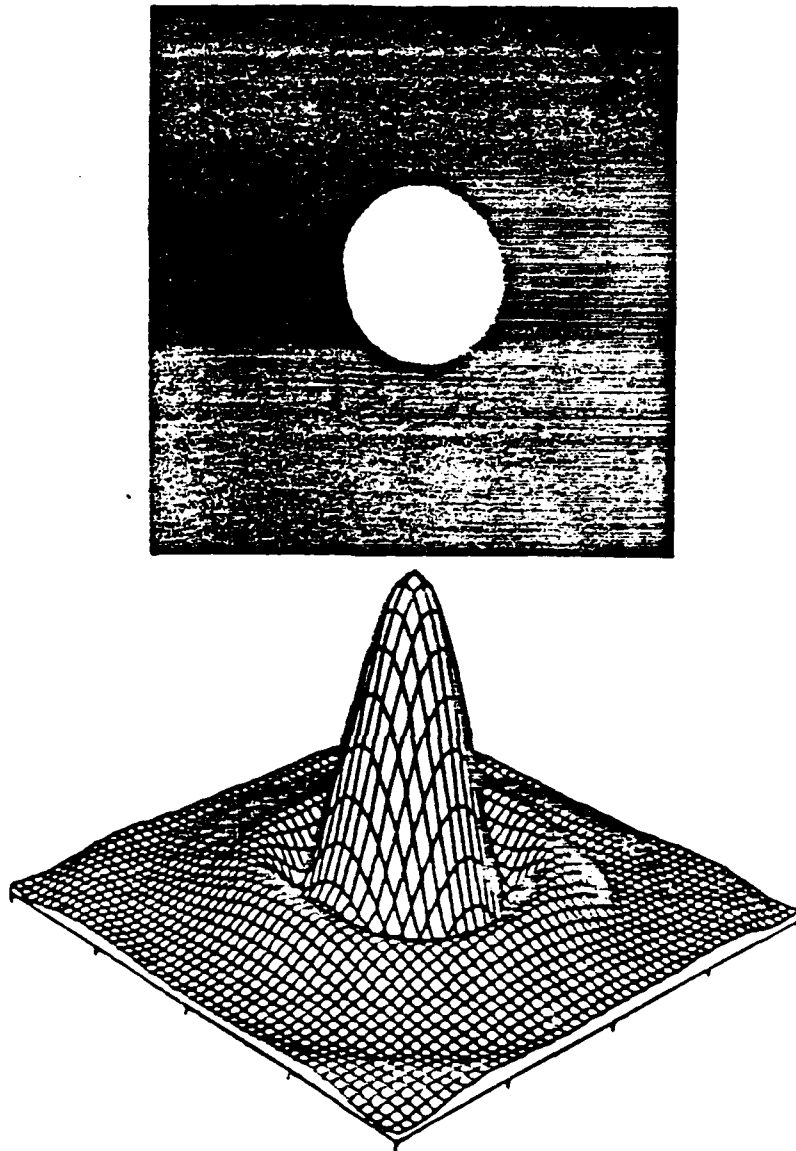
Fig. 5.8 The photograph is of the irradiance impulses response of an unapodised optical system with the aberrations of astigmatism = 0.1λ, coma = 0.1λ, and spherical = -0.8λ. The 3-D plot is the theoretically predicted modulus (vertical axis) based on these aberrations. The horizontal axes are in the same units of normalized distance.
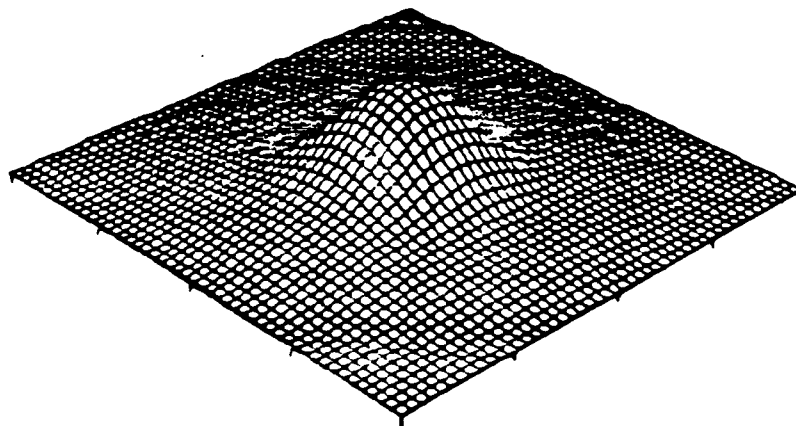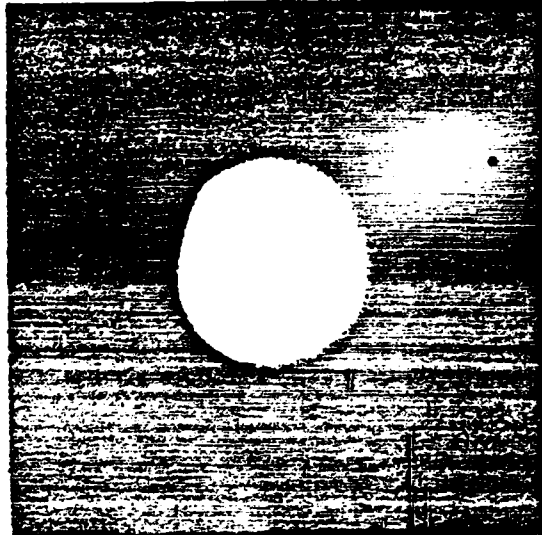
Fig 5.9   The photograph is of the irradiance impulses response of an apodised (G = 3)
           optical system with the aberrations of astigmatism = 0.1λ, coma = 0.1λ, and
           spherical = -0.8λ. The 3-D plot is the theoretically predicted modulus
           (vertical axis) based on these aberrations. The horizontal axes are in the same
           units of normalized distance.

When other lenses of various focal lengths and orientations were substituted for L2, different impulse responses were obtained. Data collected by the electro-optic technique of Section 5.1.4.1 are shown in Figs. 5.10 and 5.11. In each figure the theoretical data are plotted as solid lines and the experimental data are plotted as dashed lines. The unapodised (G = 0) cases are on the left side of each figure and the apodised (G = 3) cases are on the right. The measured amounts of third order spherical aberration for the four cases was -0.2λ, -0.6λ, -1.2λ, and -1.9λ for Figs. 5.10a, 5.10b, 5.11a, and 5.11b respectively. Smaller amounts of the other third order aberrations were present and are noted in the figure captions. Higher order aberrations were negligible.

These data show quantitatively the same effects seen qualitatively in Figs. 5.8 and 5.9. There is, first of all, good agreement between the experimental and theoretical data in each of the figures. The only exception is that the theoretical and experimental data differ by about 10% in some portions of Fig. 5.11b.

Aberrations other than spherical could be generated by misaligning an originally unaberrated system. For instance, the optical system of Fig. 5.1 with the elements oriented for minimum spherical aberration was deliberately misaligned until the impulse response in the top of Fig. 5.12 was obtained. The aberrations were measured and found to be: astigmatism $= 0.2\lambda$, coma $= 0.2\lambda$, and spherical $= -0.1\lambda$. The 3-D plot in the bottom of this figure is the calculated modulus of the amplitude impulse response of a system having the measured aberrations and no apodiser. Similar data for the same system with an apodiser (G = 3) as part of the system is shown in Fig. 5.13.

130
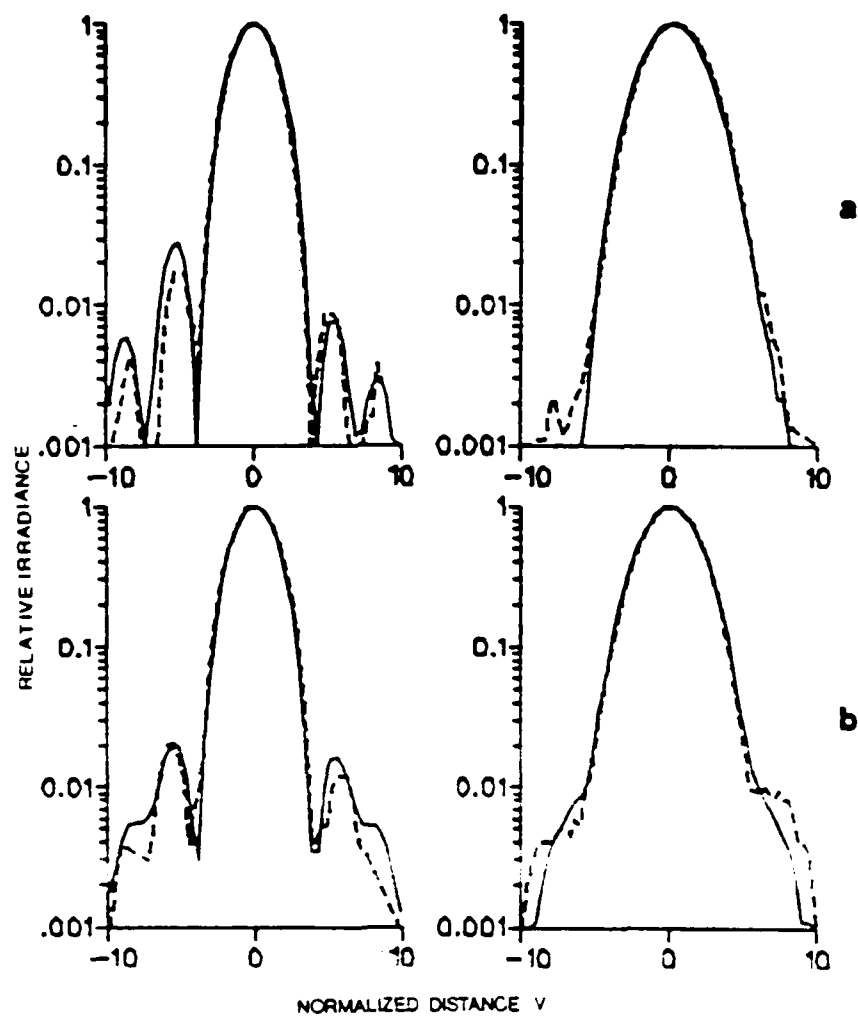
Fig 5.10 Theoretical (solid lines) and experimental (dashed lines) results are compared for two systems. In the first system (a) astigmatism = 0.1λ, coma = 0.1λ, and spherical = -0.2λ; and in the second system (b) astigmatism = 0.1λ, coma = 0.1λ, spherical = -0.5λ. The plots on the left are for the unapodised case while the others are for the apodised (G = 3) case.
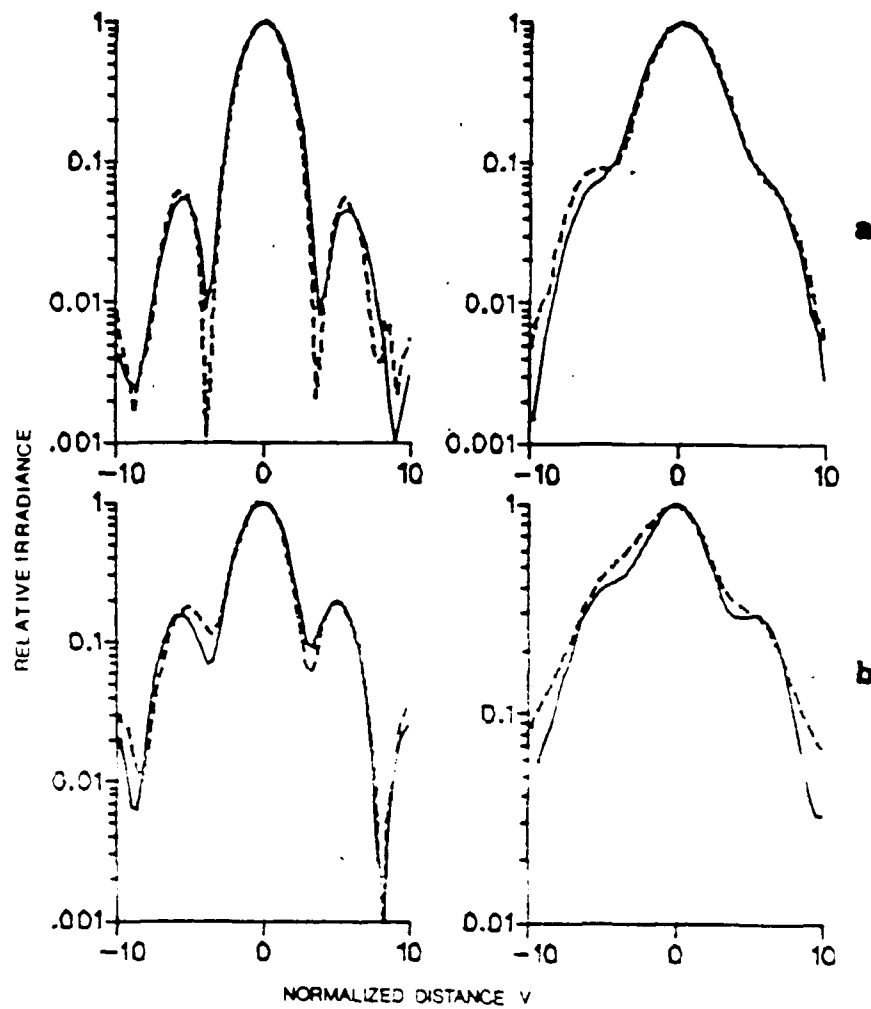
Fig. 5.11   Theoretical (solid lines) and experimental (dashed lines) results are compared for two systems. In the first system (a) astigmatism = 0.0λ, coma = 0.1λ, and spherical = -1.2λ; and in the second system (b) astigmatism = 0.2λ, coma = 0.3λ, spherical = -1.3λ. The plots on the left are for the unapodised case while the others are for the apodised (G = 3) case.

Fig. 5.12   The pnotograpn is of the irradiance impulses response of an unapoaised
optical system witht he aberrations of astigmatism = 0.2λ, coma = 0.2λ, and
spherical = -0.1λ. The 3-D plot is the theoretically predicted modulus
(vertical axis) based on these aberrations. The horizontal axes are in the same
units of normalized distance.

Fig. 5.13 The photograph is of the irradiance impulses response of an apodised (G = 3) optical system witht he aberrations of astigmatism = 0.2λ, coma = 0.2λ, and spherical = -0.1λ. The 3-D plot is the theoretically predicted modulus (vertical axis) based on these aberrations. The norizontal axes are in the same units of normalized distance.

A quantitative comparison between theory and experiment for the impulse responses of Figs. 5.12 and 5.13 is provided by the data shown in Figs. 5.14 and 5 15. The data in Fig. 5.14 were generated by placing the I-SCAN linear detector array in the center of the impulse response. The orientation of the linear array corresponds to a horizontal line through the center of the photographs of Fig. 5.12 and 5.13, with the sense of left and right reversed. The analog output of the I-SCAN detector array was displayed on the CRT of an oscilloscope where it was photographed.

These photographs are displayed in Fig. 5.14. The horizontal axes are the same for both photographs and correspond to a linear distance in the plane of the impulse response. The veritcal axes, respresenting image irradiance, also have the same units, except that for the top photograph a neutral density filter (ND = 0.7) was inserted into the system.

The data of Fig. 5.14 are displayed as black dots in the plots of Fig. 5.15. The solid curves in this figure are theoretical plots of the irradiance along a line through the center of the impulse response for a system having the measured aberrations of Fig. 5.12. The top plots in both Fig 5.14 and 5.15 are for an unapodised system, while the bottom plots are for an apodised (G = 3) system.

From the several different impulse responses considered in this section it is clear that the model is accurate in predicting the experimental results. The largest error is about 10% in the case where the spherical aberration equaled 1 9λ. In the other cases, involving aberration with magnitudes less than this, the agreement between theory and experiment was less than 5%.
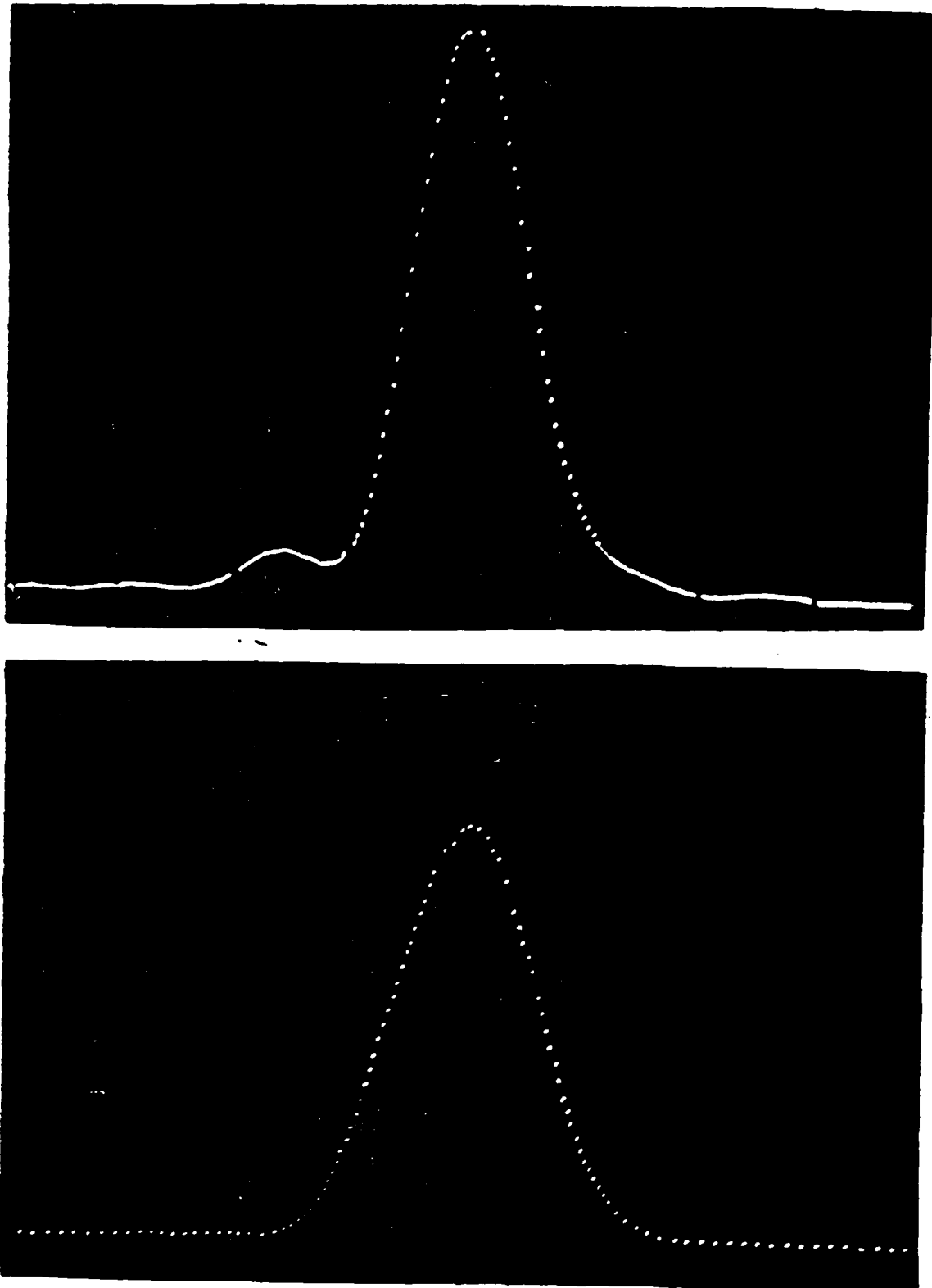
Fig. 5.14 Experimental data through the center of the unapodised (top) and apodised (bottom) irradiance impulse response of a system with astigmatism = 0.2λ, coma = 0.2λ, and spherical = -0.1λ. The apodiser had a value of G = 3.
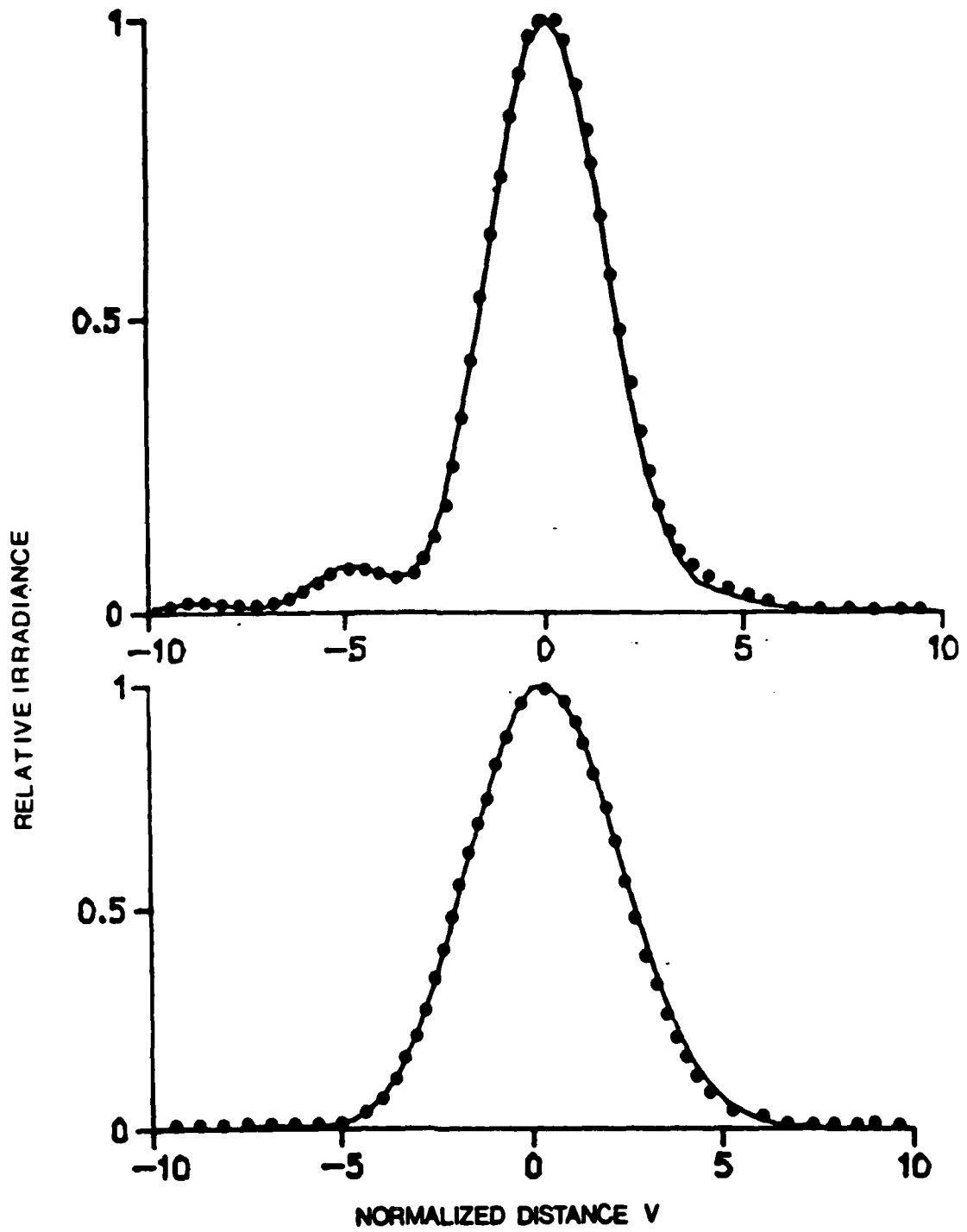
Fig. 5.15 Experimental (dots) and theoretical (solid lines) data are compared for the experimental conditions described in Fig. 5.13.

5.2.2 Aberrated Imaging Data

Imaging experiments were performed where the objects were an edge, a slit, and a set of two closely-spaced points. The experimental configuration is shown in Fig. 5.2. The specific optical system used here was the one which generated the impulse response data of Figs. 5.8 and 5.9. That is, the measured aberrations were: astigmatism = 0.1λ, coma = 0.1λ, and spherical = -0.8λ.

5.2.2.1 Edge and Slit Images

After the aberrations were measured and the impulse data were taken, the pinhole in the spatial filter was replaced with the edge object. Both the pinhole and the edge object were on identical magnetic mounts so that the edge object went into the system at the same axial location formerly occupied by the pinhole. The 10X microscope objective was moved axially back from the pinhole so as to provide a relatively uniform illumination at the edge object. The 10 micron pinhole was reinserted at the focal point of the laser beam after the objective. This was done to spatially filter out the high frequency noise on the beam. The edge was a section of a razor blade.

Data were collected by placing the I-SCAN detector array in the image plane with the axis of the detector array perpendicular to the edge image. The analog output from the detector array was connected to an oscilloscope and photographs were taken of the patterns displayed on the CRT.

Data obtained in this manner are shown in Fig. 5.16 where the coherent image of an edge with no apodisation is displayed in the top photograph and the same image with an apodiser (G = 3) in the system is displayed below it.

These data (in the form of black dots) are shown superimposed on theoretical curves (solid lines) in the plots of Fig. 5.17. Two conclusions can be drawn from these
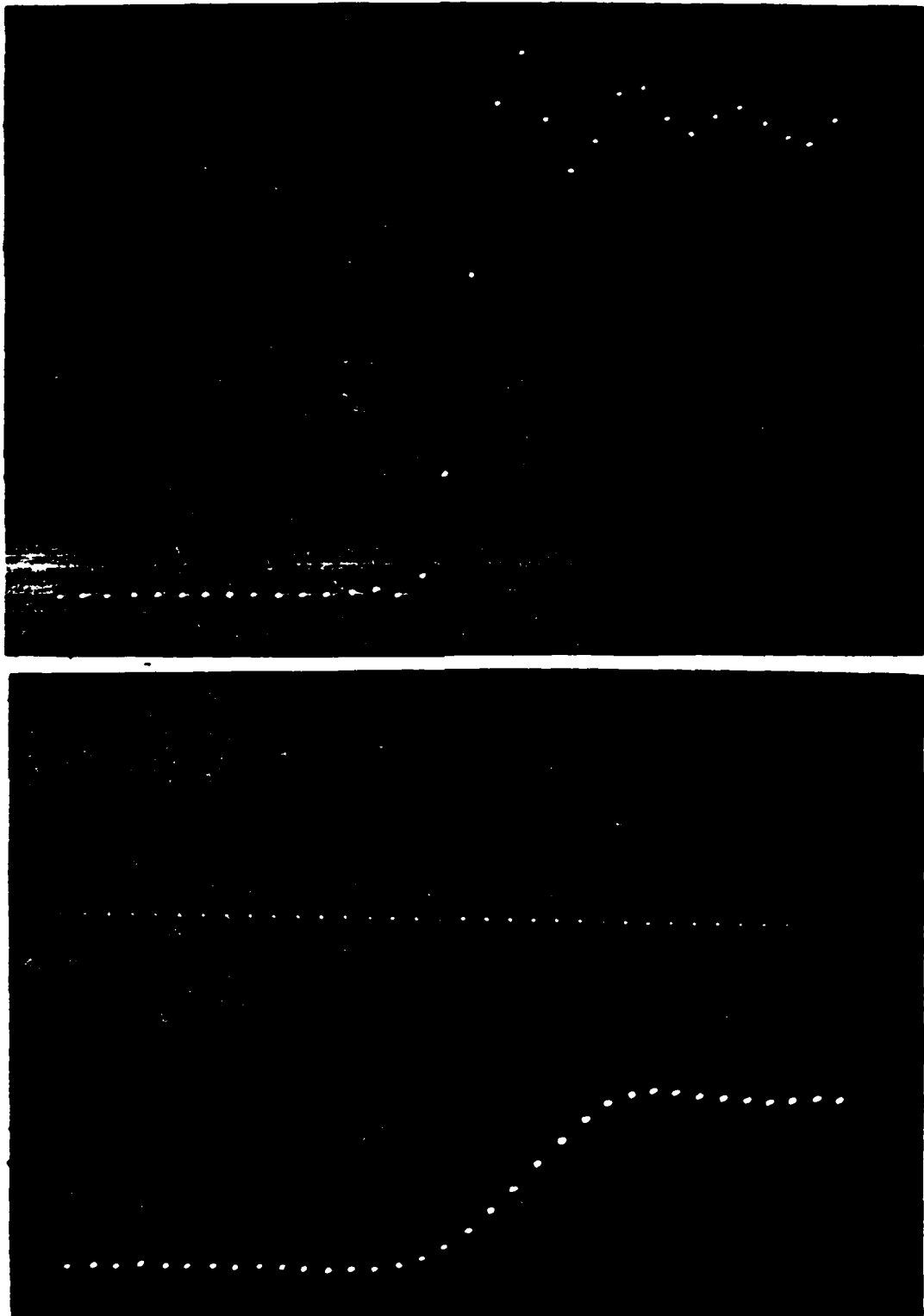
Fig. 5.16   Experimental data from the analog output of the I-SCAN linear detector
oriented perpendicular to the edge image through an unapodised (top plot)
and apodised (bottom plot, G = 3) optical system with measured third order
aberrations: astigmatism = 0.1λ, coma = 0.1λ, and spherical = -0.8λ.
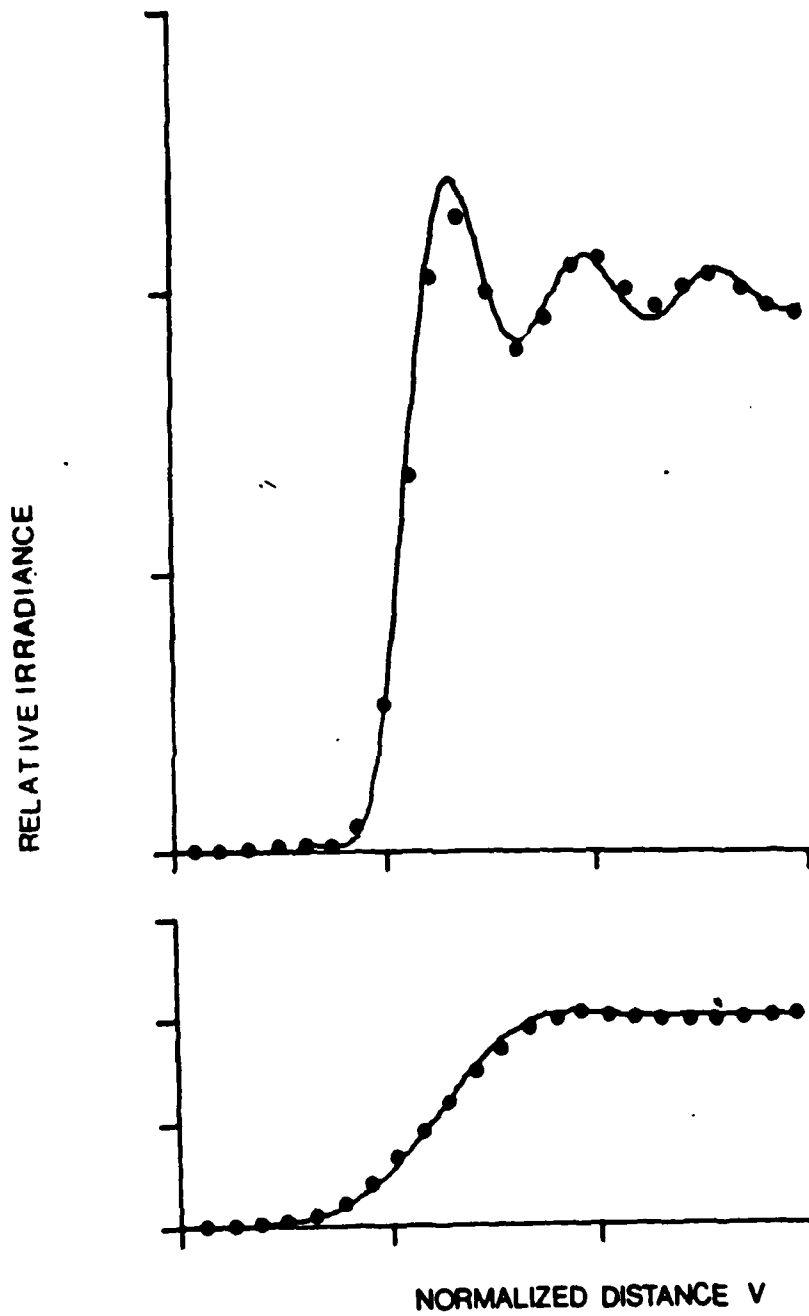
Fig. 5.17 Experimental (dots) and theoretical (solid lines) data are compared for the experimental conditions described in Fig. 5.16.

data. First, the apodiser has been effective in removing the edge ringing in the image of the edge through this aberrated system. This behavior is a direct result of the smoothing of the impulse response seen when comparing Figs. 5.8 and 5.9. The second conclusion that can be drawn is that the theoretical model is quite accurate in predicting the experimentally observed behavior.

When the object was two razor blade edges instead of one, a slit was formed. The width of the slit was varied and image data were collected in the same manner as with the edge. The photographic data for three different slit widths are shown in Figs. 5.18, 5.20, and 5.22. These data (in the form of black dots) are shown relative to theoretical predictions in Figs. 5.19, 5.21, and 5.23 respectively. The predictions were based on the measured system aberrations (same as for the edge).

The same conclusions that were drawn for the edge can be drawn here. Namely, the apodiser is effective in removing the edge ringing and the theoretical model does a good job in predicting the experimental outcome.

The small deviations between theory and experiment in the top plots of Figs. 5.19 and 5.20 are caused by speckle. It is interesting to note that the apodiser has diminished this difference (compare the top and bottom plots of Figs. 5.19 and 5.20).
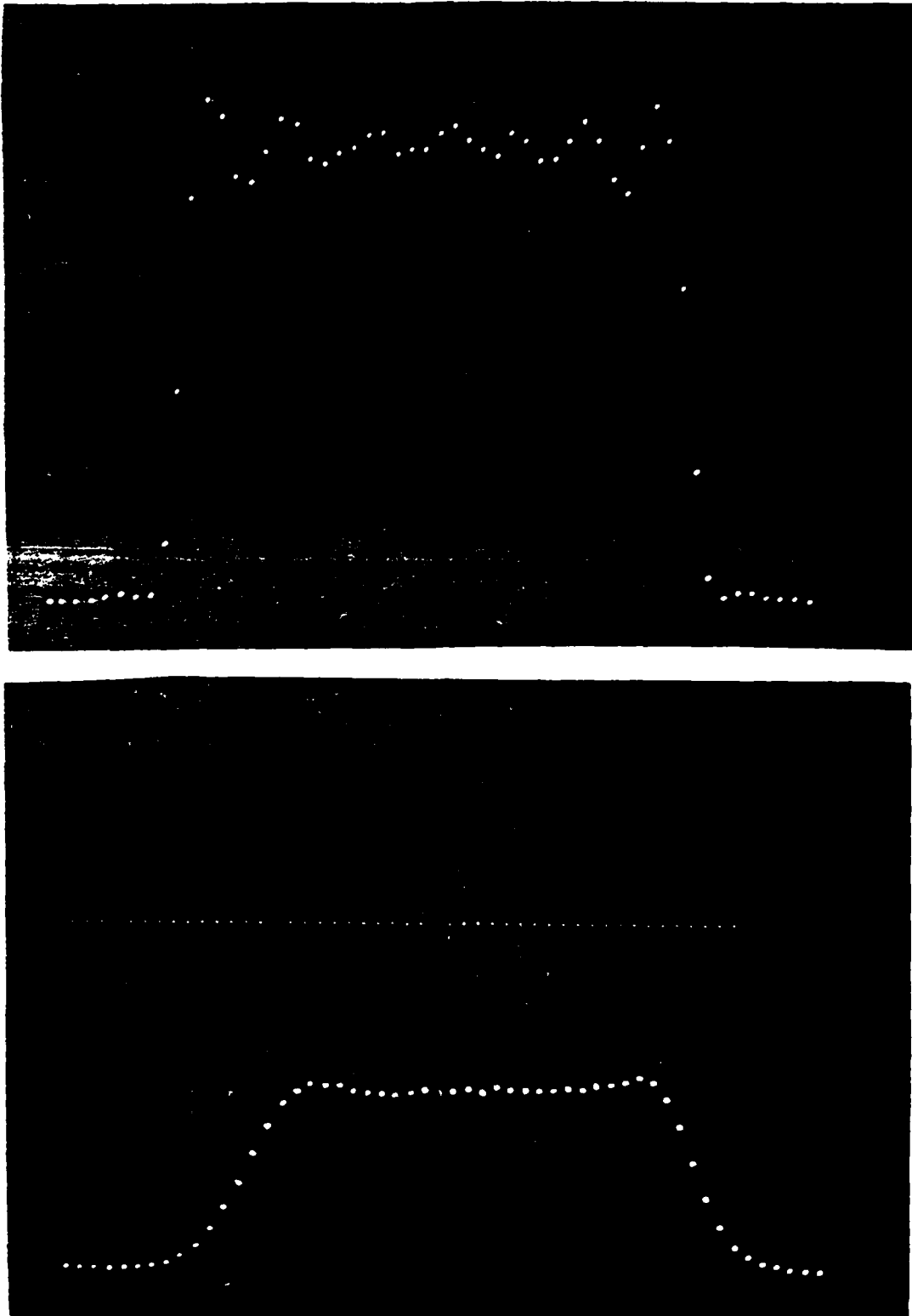
Fig. 5.18   Experimental data from the analog output of the I-SCAN linear detector
oriented perpendicular to the slit image through an unapodised (top plot)
and apodised (bottom plot, G = 3) optical system with measured third order
aberrations: astigmatism = 0.1λ, coma = 0.1λ, and spherical = -0.8λ.
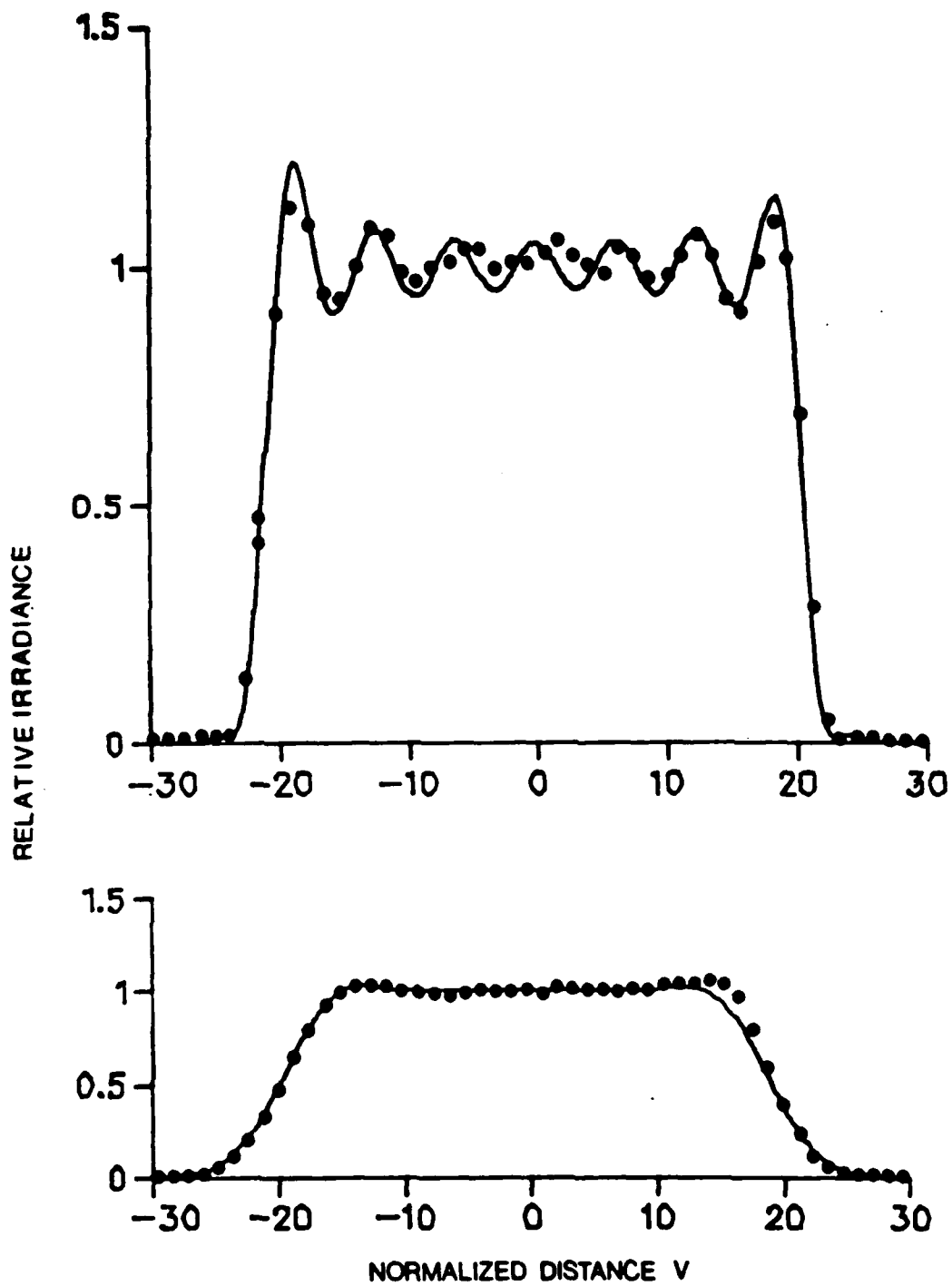
Fig. 5.19   Experimental (dots) and theoretical (solid lines) data are compared for the experimental conditions described in Fig. 5.18.
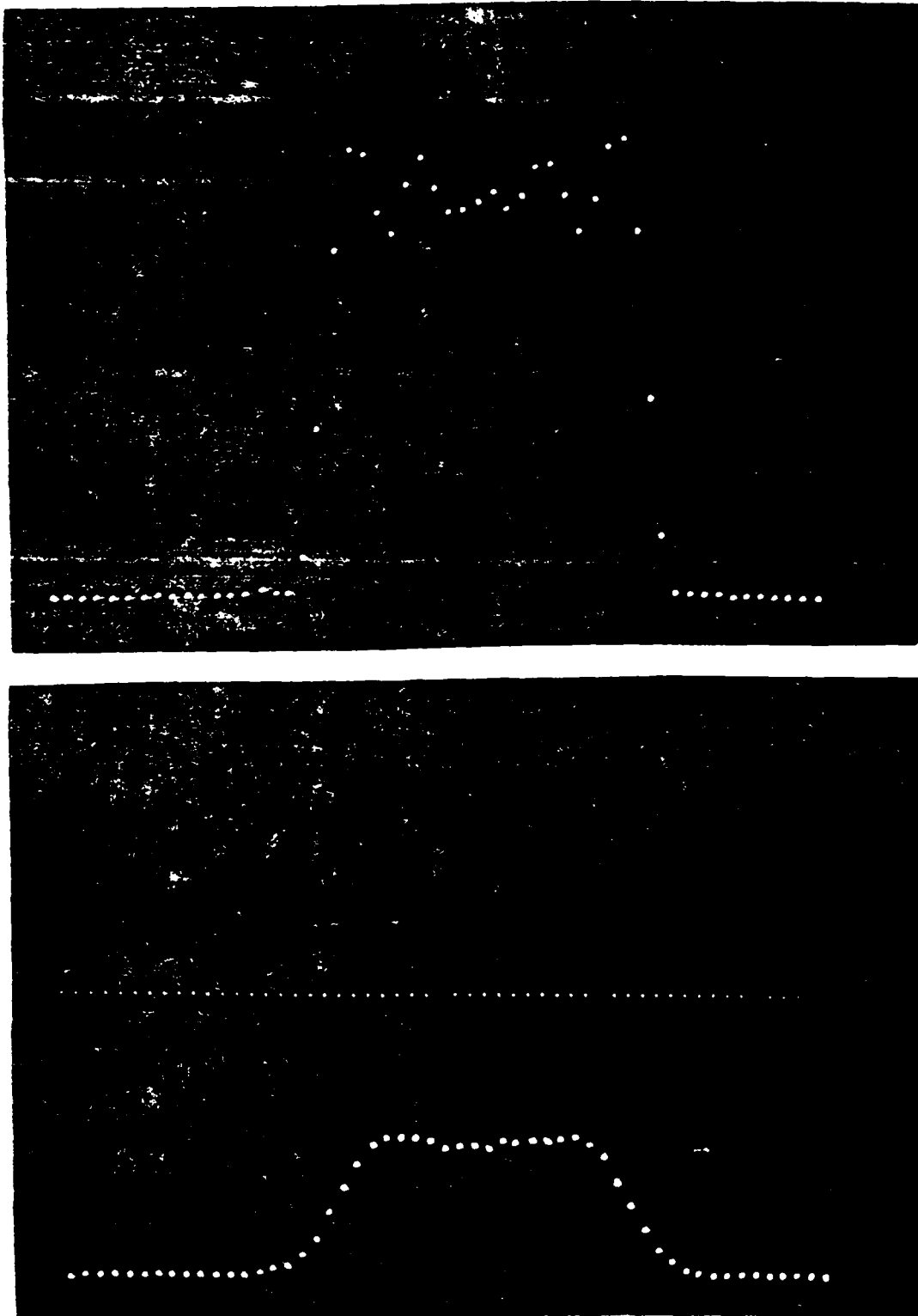
Fig. 5.20 Experimental data from the analog output of the I-SCAN linear detector oriented perpendicular to the slit image through an unapodised (top plot) and apodised (bottom plot, G = 3) optical system with measured third order aberrations: astigmatism = 0.1λ, coma = 0.1λ, and spherical = -0.8λ.
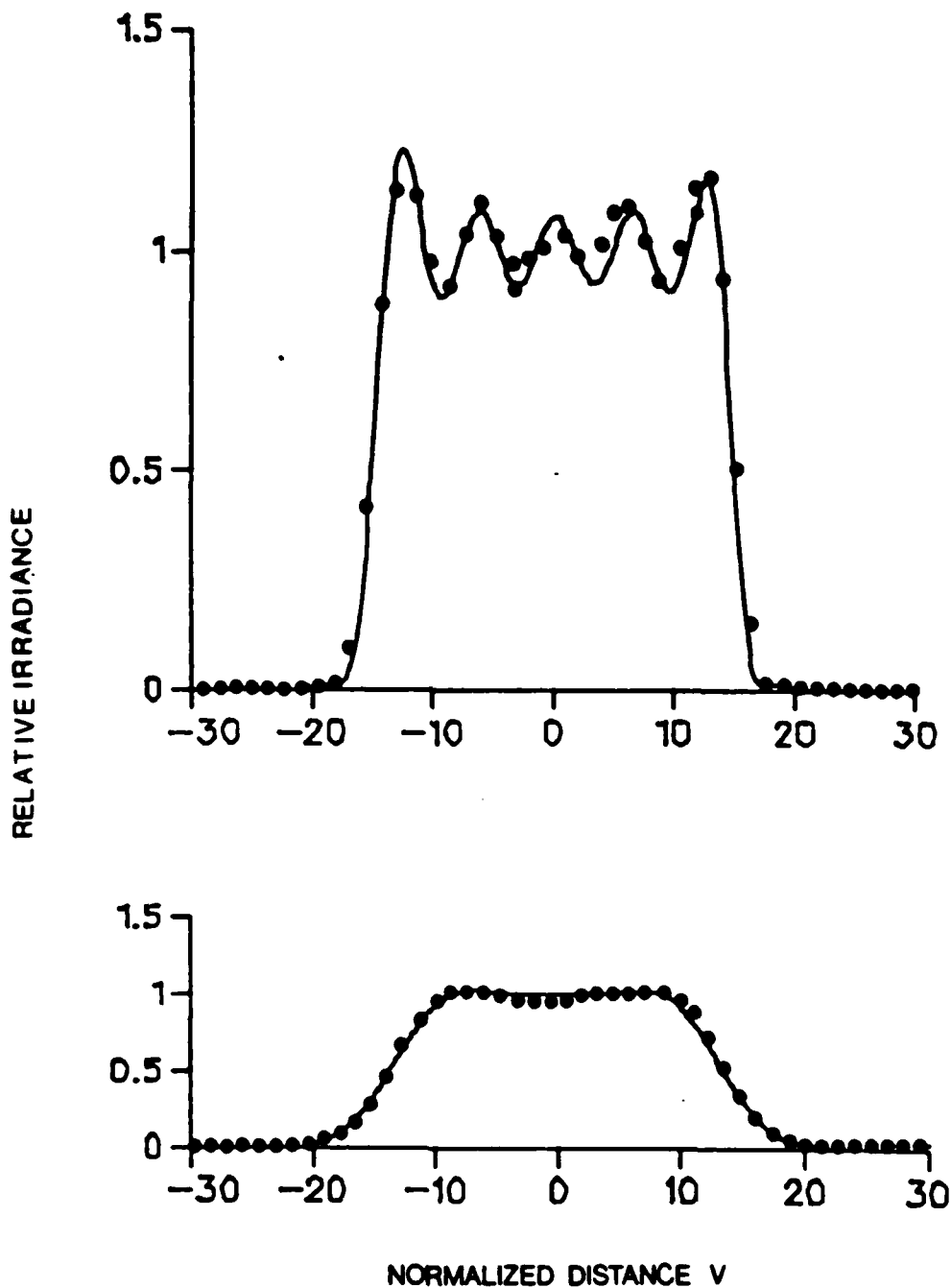
Fig. 5.21 Experimental (dots) and theoretical (solid lines) data are compared for the experimental conditions described in Fig. 5.20.
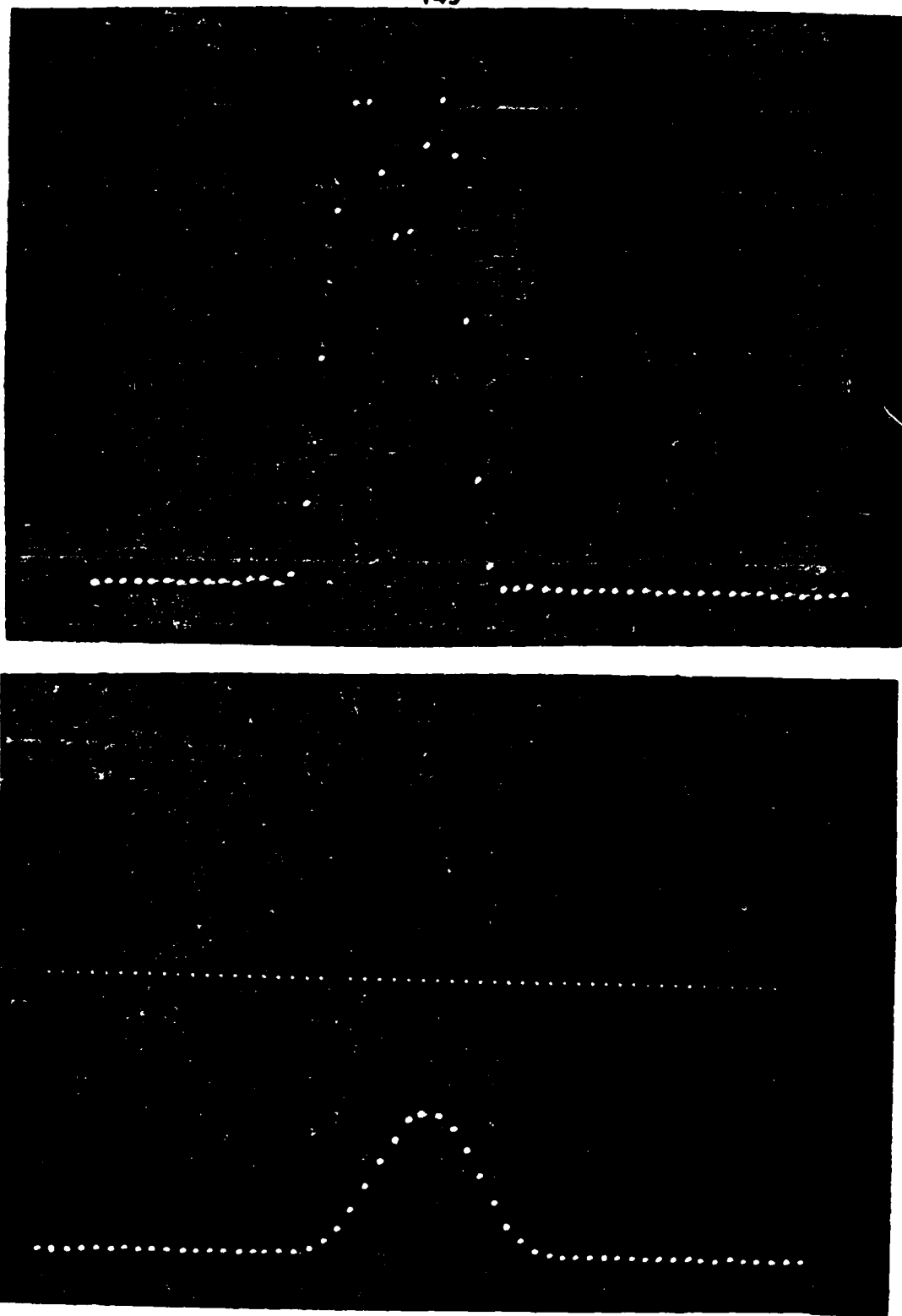
Fig. 5.22   Experimental data from the analog output of the I-SCAN linear detector oriented perpendicular to the slit image through an unapodised (top plot) and apodised (bottom plot, G = 3) optical system with measured third order aberrations: astigmatism = 0.1λ, coma = 0.1λ, and spherical = -0.8λ.
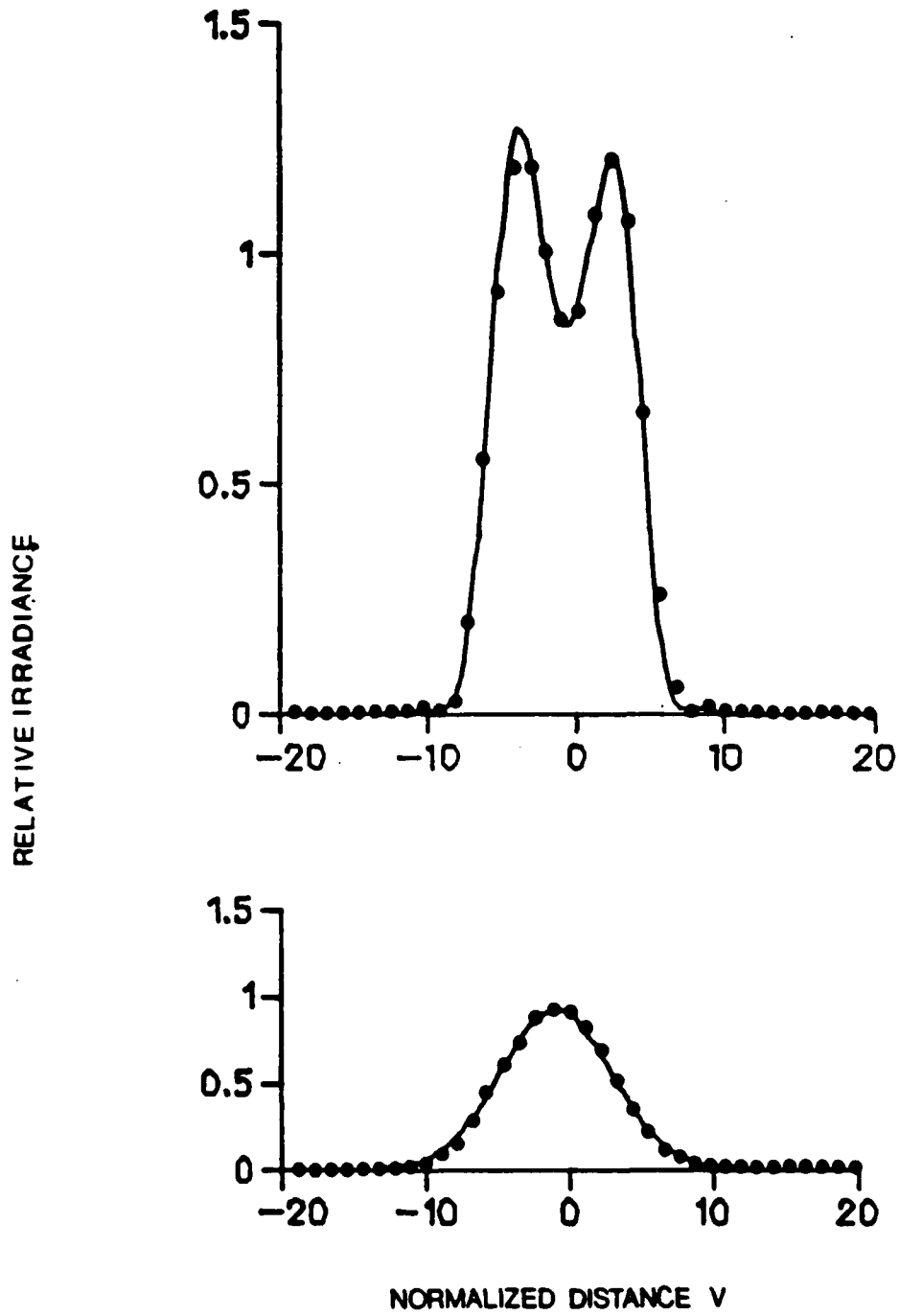
Fig. 5.23   Experimental (black dots) and theoretical (solid lines) data are compared for the experimental conditions described in Fig. 5.22.

5.2.2.2 Two-point Images

The data collected in the two-point imaging experiments were from two different optical configurations. The first configuration (Fig. 5.1 was used) was designed to have small amounts of aberrations. A measurement of the aberrations after this design was configured gave: astigmatism = 0.1λ, coma = 0.0λ, and spherical = 0.0λ.

The five double-pinholes described in Section 5.1.2.1 were individually inserted into the system and the resulting image plane separation of peaks was measured. An example of the data obtained from this process is shown in Fig. 5.24. In this case the object was the double pinhole with a pinhole separation of 42 microns. In the top plot of this figure, the experimental data with no apodiser was drawn as a dashed line. The theoretically predicted image irradiance distribution for the same condition was drawn as a solid line. When the apodiser (G = 3) was added to the system the curves in the bottom plot of Fig. 5.24 are obtained. The geometrically expected locations of the pinhole images are indicated by vertical dashed lines.

This procedure was repeated for the other double pinholes as well as for all five double pinholes in an essentially unaberrated system having twice the magnification. All of these data are combined into Fig. 5.25. The horizontal axis in this figure is the geometrically expected image point separation while the vertical axis is the mensuration error. The mensuration error is the difference between the expected and the actual separation. The theoretically predicted mensuration error is shown as a solid line for the unapodised case and as a dashed line for the apodised (G = 3) case. The experimental data points are shown as boxes for the unapodised situation and as X's for the apodised (G = 3) situation.

A similar set of data is displayed in Fig. 5.26. In this case the optical system was modeled after Fig. 5.2 and the measured aberrations were astigmatism = 0.1λ, coma =
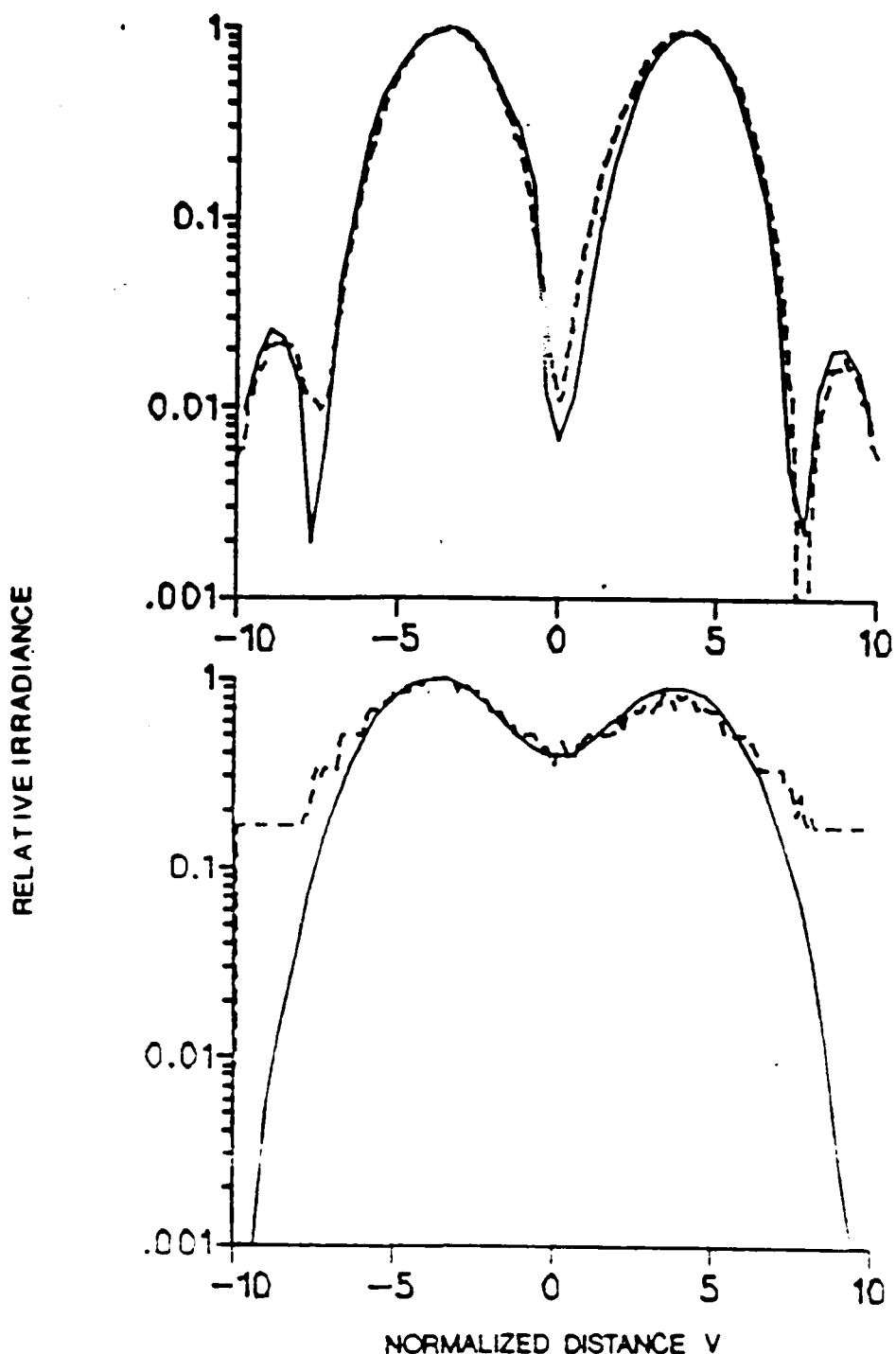
Fig. 5.24   The irradiance distribution in the image of a two-point object through an essentially unaberrated system which is unapodised in the top plot and apodised (G = 3) in the bottom plot. In each plot, the solid curve represents a theoretical prediction and the broken curve represents experimental data.
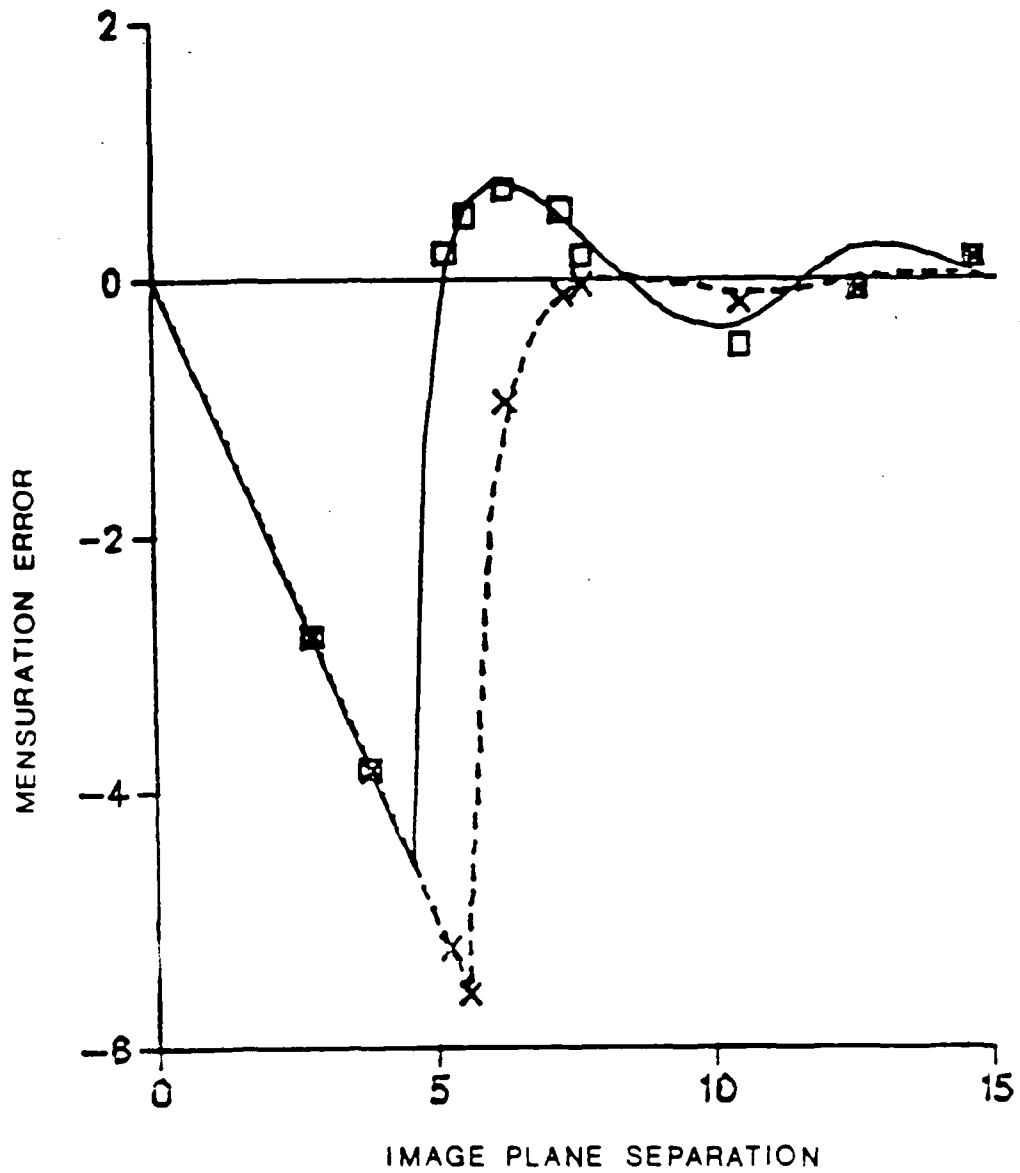
Fig 5.25   The mensuration error is plotted relative to the geometrically expected
image point separation for a system which is essentially unaberrated and is
unapodised (solid curve) or has a Gaussian apodiser (broken curve).
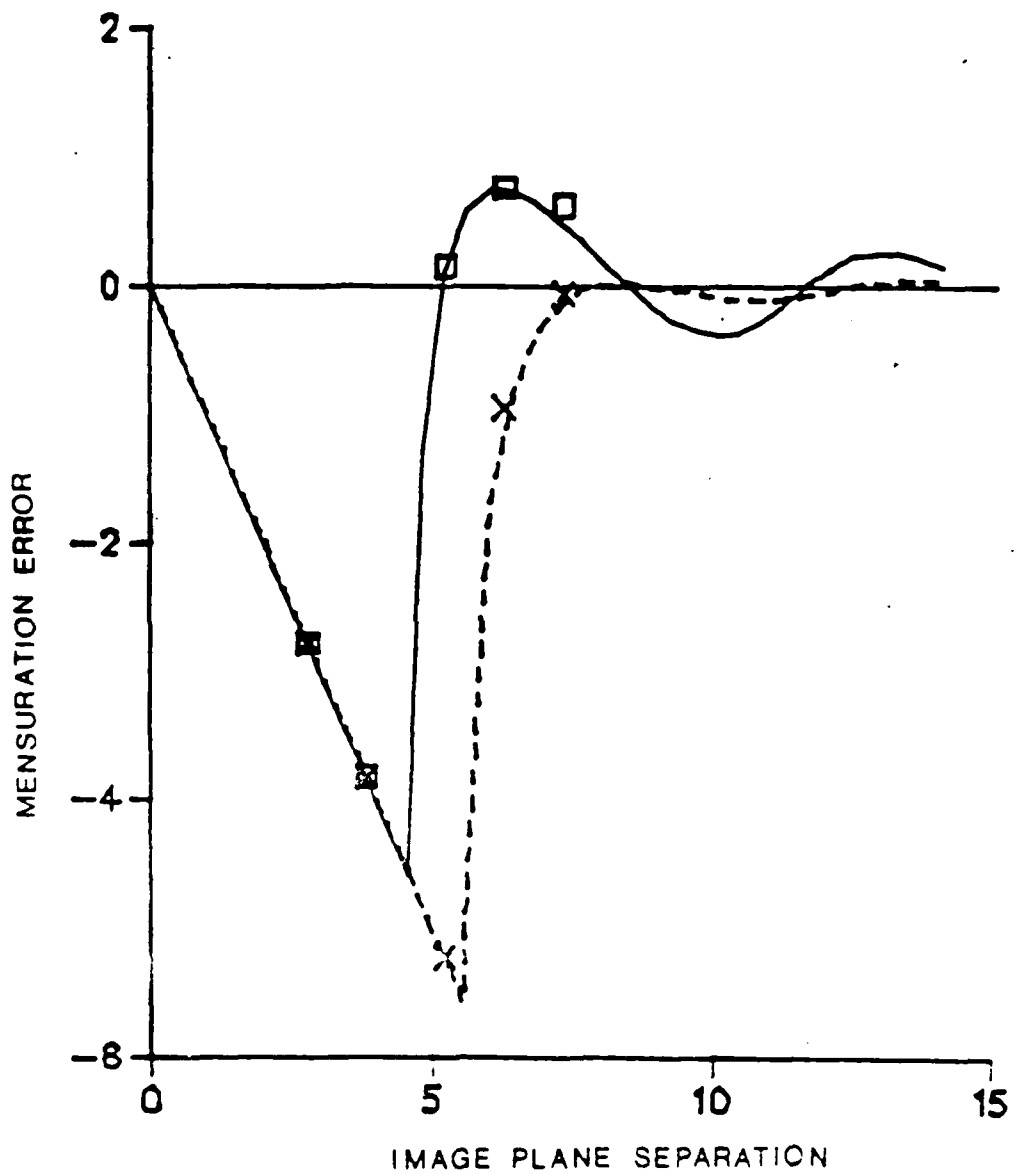
Fig. 5.26   The mensuration error is plotted relative to the geometrically expected image point separation for an unapodised (solid curve) and Gaussian apodised (broken curve). The measured aberrations were astigmatism = 0.1λ, coma = 0.1λ, and spherical = -0.3λ.

0.1λ, and spherical $= -0.8\lambda$.

In both Figs. 5.25 and 5.26 the data show that a mensuration error exists when the separation is close to the limit of resolution. This is true for both cases of apodisation and for both figures. However, the data also reveal that the mensuration error when the points are resolved is less when the sytem is apodised. The unapodised case has a better resolution limit, but this is misleading because the mensuration error is greatest in the region between the resolution limits for the two cases of apodisation. This conclusion applies equally to the unaberrated and aberrated situations.

5.3 EXPERIMENTAL SUMMARY

Experiments were performed involving the imaging of simple objects through coherent optical systems having various amounts of optical aberrations. The effect on imaging performance of adding a Gaussian $(G = 3)$ apodiser to the optical system was determined. The objects were a point, two closely-spaced points, an edge, and a slit.

The goal of these experiments was to adequately test the theory developed in Chapters 2, 3, and 4. These chapters contain a large amount of theoretical data. The experiments were not intended to test each individual theoretical result; rather representative theoretical results were tested. The experimental results were very close to the theoretical predictions for those cases which were tested. The experiments confirm that the theory is valid at least under the range of conditions tested.

CHAPTER 6 CONCLUSIONS

This study was performed to investigate both theoretically and experimentally the effects of aberrations on the performance of coherent imaging systems, and the utility of apodisation in improving that performance. It has been established by other workers that apodisation is useful in improving the performance of unaberrated coherent imaging systems. Any real optical system, of course, has some amount of residual aberrations. So this study, by considering the reality of aberrations, has extended the body of knowledge in the field of apodisation.

It is worth emphasizing the ubiquity of aberrations in optical systems. There are a few optical systems which are essentially free of aberrations; for example, the projection system used to make masks for the semiconductor industry. Such systems are extremely expensive however. It is more likely that an optical system will be considered well corrected if it meets the Rayleigh quarter wavelength rule. This rule of thumb states that an element is well corrected if the absolute value of its dominant aberration does not exceed a quarter of a wavelength. In buying optical elements for this experiment, optics of this quality were found to be the norm. Initially in the experimental phase it was very difficult to acheive a system having low amounts of aberrations (say less than 0.1 waves of each of the third order aberrations.) The problem was that each of the individual elements just met the quarter wavelength rule. Eventually high quality, large $f/\#$ telescope objectives were employed to acheive a low aberration system. But even a system like this could have several tenths of a wave of aberration unless the elements were aligned with great care. The lesson here is that it is very difficult to acheive an effectively unaberrated system. This difficulty translates into extra weight, size, and expense in any practical optical system.

152

In the theoretical development of Chapter 2 and its application to specific imaging situations in Chapters 3 and 4, several simplifying assumptions were made. These were clearly noted when made but for convenience are assembled as a group here. The major assumptions are the following.

1. Scalar Fresnel-Kirchoff diffraction theory (see for example Born and Wolf[5]) is adequate to describe the systems investigated here.

2. The system parameters are limited such that the complex amplitude U_o in the (x_o, y_o) plane is related to the complex amplitude in the (x_i, y_i) plane by the Fresnel propagation formula

$$U_i\left(x_i, y_i\right) = \frac{e^{i\frac{2\pi}{\lambda}z}}{i\lambda z} e^{i\frac{\pi}{\lambda z}\left(x_i^2 + y_i^2\right)} \int \int_{-\infty}^{\infty} U_0\left(x_o, y_o\right) e^{i\frac{\pi}{\lambda z}\left(x_o^2 + y_o^2\right)} e^{-\frac{i2\pi}{\lambda z}\left(x_o x_i + y_o y_i\right)} dx_o dy_o, \quad (2.6)$$

where λ wavelength of light and z is the distance between planes. This equation will be valid if the largest aperture dimension is much greater than λ and less than $z/10$.

3. The light source is monochromatic and produces a field in the first plane of interest which is completely spatially coherent.

4. The imaging process for the magnitude of aberrations considered and the size of the objects is isoplanatic. There are aberrations in the optical systems considered in this study, so the form of the impulse response changes as an object point explores the object plane. However, for the small region of the objects considered here it was assumed that the form of the impulse response changes negligibly. In this case, the imaging process was expressed as the convolution integral

$$U\left(x_i, y_i\right) = \int \int_{-\infty}^{\infty} U_j\left(x_j, y_j\right) K\left(x_i - x_j, y_i - y_j\right) dx_o dy_o, \quad (2.21)$$

where K is the amplitude impulse response of the system.

The assumption of isoplanitism for the systems considered in this study were checked and found to be valid. The largest object considered was a slit which had an image width of $v = 80$. This corresponds to an object width of approximately 300 microns for the imag... ...n of Fig. 5.2. Theoretical imaging calculations were performed using this object size through an optical system having as much as four waves of defocus or one of the third order aberrations.

The isoplanatic assumption implies that an off-axis amplitude impulse response in the vicinity of the edge of the largest slit differs only slightly from an on-axis impulse response. These two amplitude impulse response functions were calculated using the program PSF.FOR described in Chapter 3. The off-axis amplitude impulse response was then translated until i peak was aligned with the peak of the on-axis impulse response. The difference in the complex values of the two patterns was obtained and the intensity of this difference was found. The area under the resulting intensity pattern was calculated and compared to the area under the on-axis intensity impulse response. The comparison was in the form of a ratio. If this ratio was less than 0.01 then the assumption of isoplanatism was considered justified.

This calculation was performed for the off-axis point being 150 microns from the axis and with 4 0 waves of one of the aberrations (defocus, astigmatism, coma, and spherical) A different calculation for each aberraton was performed. The effect of apodisation was also determined. In each case, the ratio was much less than 0.01

Since the agreement between the experiments and the theory is so good, the assumptions outlined here clearly are valid for the optical systems considered in this thesis. In that case, certain general conclusions can be drawn First of all, the presence of aberrations in a coherent imaging system degrades the imaging performance of that system in a predictable way and apodisation is effective in improving selected aspects of

system performance. The experiments conducted on both the unapodised and apodised systems agree well with the theoretical predictions. This agreement implies that the other theoretical predictions of Chapters 3 and 4 are valid as well.

It can also be concluded that the use of apodisation is beneficial in improving certain aspects of system performance. Specifically, apodisation of aberrated coherent imaging systems reduces the mensuration error in the image of two closely-spaced points and reduces the edge ringing in the images of both an edge and a slit.

It appears that expressing the images in terms of the square root of irradiance is beneficial. This effectively removes the nonlinearity associated with the detection process. As a result, the edge ringing and shift are reduced. If the asymptotic value of the irradiance on the bright side of the edge can be determined, then the edge shift can be reduced to zero, except when unsymmetrical aberrations are present.

Finally, this research has indicated that there is still some work to be done in order to fully understand the effect of apodisation on aberrated coherent optical systems Specifically, the effect of aberrations and the utility of apodisation on beam propagation systems should be studied. The theoretical effect of various apodisers on aberration-free beam propagation systems has been studied, but the benefit of using apodisation n aberrated beam propagation systems has not been investigated.

BIBLIOGRAPHY

1. Thompson,.B.J.,(1984),"Droplet characteristics with conventional and holographic imaging techniques', *Liquid Particle Size Measurement Techniques*, Ed. by J.M. Tishkoff, et. al., American Society for Testing and Materials Special Technical Publication, 848, 111.

2. Goodman, J.W.,(1968), *Introduction to Fourier Optics*, McGraw-Hill.

3. Duffieux, P.M.,(1946),*L'Intégrale de Fourier et ses Applications à l'Optique*, Rennes, English version: (1983) *The Fourier Transform and it Application to Optics*, 2nd Edition, Wiley, New York.

4. Duffieux, P.M. and Lansraux, G.,(1945), "Les facteurs de transmission et la lumière diffractée, Rev. d'Optique 24,65,151,215.

5. Born, M. and Wolf, E.,(1975), *Principles of Optics*, 5th Edition, Pergamon Press.

6. Lord Rayleigh, (1902), *Collected Papers*, Cambridge University Press, 384.

7. Airy, G.B.,(1835),"On the diffraction of an object-glass with circular aperture", Trans. Camb. Phil. Soc.5,283.

8. Barakat, R.,(1962),"Application of apodization to increase two-point resolution by the Sparrow criterion. I. Coherent illumination", J. Opt. Soc. Am. 52, 276.

9. Sparrow, G.,(1916), "On Spectroscopic Resolving Power", Astrophysical J. 44, 76.

10. Grimes,D.N. and Thompson,B.J.,(1967),"Two-point resolution with partially coherent light", J Opt. Soc. Am. 57, 1330.

11. Rojak,F.,(1961), M.S. Thesis, Lowell Technological Institute.

12. Hopkins, H.H.,(1953),"On the diffraction theory of optical images", Proc. Roy. Soc. A 217, 408.

13. Steel, W.H.,(1957),"Effects of small aberrations on the images of partially coherent objects", J. Opt. Soc. Am. 47,405.

14. Canals-Frau, D. and Rousseau,M., (1958),"Influence de l'eclairage partiellement coherent sur la formation des images de quelques objets etendure opaques", Optica Acta 5, 15.

15. Kinzly, R.E .(1965),"Investigations of the influence of the degree of coherence upon images of edge objects ',J Opt. Soc. Am. 55,1002.

16. Skinner, T.J.,(1963),"Surface texture effects in coherent imaging", J. Opt. Soc. Am. 53,1350A.

17. Skinner, T.J.,(1964), Thesis, Boston Univ.

18. Considine, P.S.,(1966),"Effects of coherence on imaging systems", J. Opt. Soc. Am. 56,1001.

19. Thompson, B.J.,(1969), "Image Formation with Partially Coherent Light", *Progress in Optics, Vol VII*, Ed. by E. Wolf, North-Holland, Amsterdam, 171.

20. Avizonis,P.V.,O'Neil,B.D. and Hedin,V.A.,(1978),"Intensity mapping optical aberrations",Appl. Opt. **17**, 1527.

21 Zernike, F.,(1934),"Beugungstheorie des schneidenverfahrens und seiner verbesserten form, der phasenkontrastmethode", Physica 1, 689.

22. Lord Rayleigh,(1872), Monthly Not. Roy. Soc. 33, 59 [reprinted in Sci. Papers 1,164(1964)].

23. Straubel, R.,(1902), "Zusammenhang Zwischen Absorption and Auflögen", Phys. Z. 4, 74.

24. Toraldo di Francia, G., (1952), "Super-Gain Antennas and Optical Resolving Power",Suppltemento Al Vol.IX, Series IX Del Nuovo Cimento, 426.

25. Luneberg, R.K.,(1944), *Mathematical Theory of Optics*, Brown University,Providence, Rhode Island, 390.

26. Wolf, E.,(1951),"The diffraction theory of aberrations", *Rep. Prog. Phys. 14*, 95.

27. Jacquinot, P. and Roizen-Dossier, B.,(1964), "Apodisation", *Progress in Optics, Vol III*, Ed. by E. Wolf, North-Holland, Amsterdam.

28. Tikhomirova,M.G.,(1978),"The apodization method of increasing the accuracy of sighting", Radio Eng. and Electron. Phys.(USA) **23**, 30.

29 Mondal,P K., Rao,K.P. and Ch A. Dev Ravalu, K.P (1979),"Encircled energy in the diffraction pattern of circular apertures with parabolic filters", Nat. Acad Sci Letters 2, 147.

30 Ch A. Dev Rayaiu, K.P and Mondal,K P (1979),"Encircled energy in the diffraction pattern of shaded circular apertures", Nat. Acad. Sci. Letters 2, 349

31 Mints,M. Ya., and Prilepskii,E.D.,(1980),"Apodization of a passive axially symmetric optical system", Opt. Spectrosc.(USSR) **48**, 543.

32. Barakat, R., (1963),"Application of apodization to increase two-point resolution by the Sparrow criterion. II. Incoherent illumination", J. Opt. Soc. Am. **53**, 274.

33. Barakat, R.,(1962),"Solution of the Luneberg apodization problems", J. Opt. Soc. Am 52, 264

34. McKechnie,T.S.,(1972),"The effect of condenser obstruction on the two-point resolution of a microscope", Optica Acta 19, 729.

35. Nayyar,V.P. and Verma, N.K.,(1976),"Two point resolution limit with partially coherent light", Optica Pura Y Aplicada 9, 165.

36. Magiera, A. and Pietraszkiewicz, K.,(1981),"Two-point resolution with phase and anti-phase partially coherent illumination in apodized systems", Optica Applicata 11, 311.

37. Nayyar, V.P. and Verma, N.K.,(1978),"Two-point resolution of Gaussian aperture operating in partially coherent light using various resolution criteria", Appl. Optics 17, 2176.

38. Mehta, B.L.,(1975),"Effect of non-uniform illumination on critical resolution by a circular aperture using partially coherent light", Atti. Fond. Ronchi 30, 17.

39. Mehta,B.L.,(1973),"Effect of non-uniform illumination on the critical resolution in partially coherent light", Optics Commun. 9, 364.

40. Kintner, E.C. and Sillitto, R.M.,(1977),"Edge-ringing in partially coherent imaging", Optica Acta 24, 591.

41. Som,S.C. and Biswas,S.C.,(1971),"Performance of the optimum apodisers in partially coherent light", Optica Acta 18, 939.

42. Asakura,T. and Araki,T.,(1976),"Apodization in coherent image formation", Optik 46, 365.

43. Araki,T. and Asakura,T.,(1977),"Coherent Apodisation Problems", Optics Commun 20, 373.

44 Rao, K.P., Mondal, P.K., and Seshagiri Rao, T.,(1978),"Coherent imagery of straight edges with Straubel appodisation filters", Optik 50, 73.

45 Rao, K P, Chiranjivi,T., Mondal,P.K., and Deb,K.K.,(1980),"Coherent images of straight edges with raised cosine apodising pupils", Atti. Fond. Ronchi 35, 751

46 Smith, R.W.,(1973),"Apodisation for coherent imagery of extended objects - a second class of apodisation functions", Optics Comm. 9, 61.

47 Leaver, F G and Smith, R.W.,(1975),"Apodisation to produce a monotonically-decreasing radially symmetric, point-spread function", Optics Comm. 15, 374

48. Thompson, B.J. and Krisl, M.E.,(1977),"Evaluation of conerent optical systems", Photo. Sci. and Eng. 21, 109.

49 Leaver, F G.,(1975),"Apodisation to produce a monotonically-decreasing coherent line-spread function", Optics Comm. 15, 370

50. Prabhakar Rao, K., Chiranjivi, T., and Mondal, P. K.,(1980),"On coherent imagery of extended objects", Atti. Fond. Ronchi **35**, 31.

51. Thompson,B.J.,(1965),"Diffraction by semitransparent and phase annuli", J. Opt. Soc. Am. **55**, 145.

52. Wilkins, J.E.,(1977),"Apodization for maximum Strehl criterion and specified Sparrow limit of resolution for coherent illumination", J. Opt. Soc. Am. **67**, 553.

53. Clements,A.M. and Wilkins, J.E.,(1974),"Apodisation for maximum encircled energy ratio and specified Rayleigh limit", J. Opt. Soc. Am. **64**, 23.

54. Hazra,L.N.,(1977),"A new class of optimum amplitude filters", Optics Commun. **21**, 232.

55. Rao,K.P., Mondal,P.K. and Rao,T.S.,(1976),"Diffracted field characteristics of Straubel class of apodisation filters", Pramana **1**, 389.

56. Hadley,G.R.,(1974),"Diffraction by apodized apertures", IEEE J. of Quantum Elec. QE-10, 603.

57. Tsujiuchi, J.,(1963),"Correction of optical images by compensation of aberrations and by spatial frequency filtering", *Progress in Optics, Vol. II*, Ed. by E. Wolf, North-Holland, Amsterdam.

58. Biswas, S.C. and Boivin, A.,(1976),"Influence of spherical aberration on the performance of optimum apodizers", Optica Acta **23**, 569.

59. Biswas,S.C. and Boivin,A.,(1975),"Influence of primary astigmatism on the performance of optimum apodizers",J. Optics **4**,

60. Hazra, L.N., Purkait, P.K., and De, M.,(1979),"Apodisation of aberrated pupils", Can. J. Phys. **57**, 1340

61. Yzuel, M.J. and Calvo, F.,(1979)," A study of the possibility of image optimization by apodization filters in optical systems with residual aberrations", Optica Acta **26**, 1397

62. Mints, M. Ya. and Prilepskii, E.D.,(1982),"Apodisation of a passive optical system with aberrations", Opt. Spectrosc.(USSR) **52**, 538.

63. Magiera, A., Magiera, L., and Pluta, M.,(1979),"Apodization for minimizing the second moment of the intensity diffraction pattern in optical systems with aberrations (!)", Optik **53**, 343.

64. Magiera, A., Magiera, L., and Pluta, M.,(1980)," Numerical examination of apodising filters which minimize the second moment of the point spread function", Optik **56**, 413.

65. Asakura, T. and Ueno, T.,(1977),"Apodization for minimizing the second moment of the intensity distribution in the Fraunnofer pattern(III),J. Optics **8**, 89.

66. Magiera, L. and Pluta, M.,(1981),"Image quality criteria of the apidized optical systems with spherical aberrations for one- and two-point imaging", Optica Applicata **11**, 231.

67. Gupta, A.K. and Singh, K.,(1980),"Effect of a quadratic phase factor on the partially coherent far-field diffraction in the presence of primary astigmatism", Optica Applicata **10**, 381.

68. Barakat, R.,(1969),"Diffraction images of coherently illuminated objects in the presence of aberrations",Optica Acta **16**, 205.

69. Holmes,D.A., Korka,J.E. and Avizonis, P.V.,(1972),"Parametric study of apertured focused gaussian beams", Appl. Opt. **11**, 565.

70. Lowenthal,D.D.,(1975),"Far-field diffraction patterns for gaussian beams in the presence of small spherical aberrations", J. Opt. Soc. Am. **65**, 853.

71. Lowenthal,D.D.,(1974),"Maréchal intensity criteria modified for gaussian beams", Appl. Opt. **13**, 2126.

72. Malacara, D. (Ed.),(1978),*Optical Shop Testing*, John Wiley and Sons,New York, 493.

73. Brigham,E.O.,(1974), *The Fast Fourier Transform*. Prentice-Hall,Inc.

74. IMSL Library, Version 9, (1979).

75. Nijboer, B.R.A.,(1942), Thesis, Univ. of Groningen.

76. Nijboer, B.R.A.,(1947),"The diffraction theory of optical aberrations. Part 2: Diffraction patterns in the presence of small aberrations", Physica **13**, 605.

77. Gaskill, J. D.,(1978), *Linear Systems, Fourier Transforms, and Optics*, John Wiley and Sons, New York.

78. Smartt, R.N. and Steel, W.H.,(1974),"Theory and application of point-diffraction interferometers",Japan J. Appl. Physics,**14**,Suppl.14-1,351.

79. Weller,L., 983),Thesis,University of Rochester.

79. Taylor, C.A. and Thompson, B.J.,(1957),"Some improvements in the operation of the optical diffractometer",J. of Scientific Instruments, **43**, 439

80. Hee, E.W S.,(1975),"Fabrication of Apodized apertures for laser beam attenuation", Optics and Laser Tech., **7**,75

81. Kay, D.,(1976), Ph.D. Thesis, University of Rochester.

82. Krisl, E.,(1979), Ph.D. Thesis, University of Rochester.

83. Morris, G.M.,(1984), Private communication.

84. Boas,R.P. and Kac, M.,(1945),"Inequalities for Fourier transforms of positive functions',Duke Math. J. 12,189.

85. Lukosz,W.,(1962),"Ubertragung nicht-negativer signale durch lineare filter',Optica Acta 9,335.

APPENDIX 1 COMPUTER PROGRAMS

The computer programs which are documented in this appendix were developed to perform the calculations leading to the various theoretical results of Chapters 3 and 4. The program PSF.FOR is the parent program; all the others are derived from it.

The program PSF.FOR calculates the modulus, phase, and irradiance of the point spread function of an optical system. The inputs to the program are the size of the array representing the exit pupil, the third order aberrations in terms of Zernike coefficients, and the radial width factor of the Gaussian apodiser. The point spread function is found by performing a fast Fourier transform of the exit pupil array.

The program TPNT.FOR calculates the irradiance in the image of two point sources. The point sources are of equal amplitude and have zero relative phase. TPNT.FOR is an only slightly modified version of PSF.FOR. The modification is an additional multiplicative term in the exit pupil:

$$ARG2 = F\left\{\delta\left(x-b\right)+\delta\left(x+b\right)\right\} = 2\ \cos\left(\frac{2\pi by}{\lambda f}\right).\tag{A: 1}$$

where b is the separation of each object point from the optical axis, y is the linear dimension of the exit pupil parallel to a line joining the two points, λ is the wavelength of the illumination, and f is the distance from the object plane to the entrance pupil. The modification occurs in the section of the program labeled "Circular Aperture." Much of the program after that point is not included because it is identical to PSF.FOR

The programs EDGE.FOR and SLIT.FOR are also modifications of PSF.FOR. Both programs have been specialized to one dimension because of the inherent one-dimensional nature of the edge and slit objects.

```
          PROGRAM PSF
C
C
C    THIS PROGRAM CALCULATES THE PHASE, MODULUS AND
C    INTENSITY OF THE TWO-DIMENSIONAL IMAGE OF AN
C    ON-AXIS POINT SOURCE THROUGH AN OPTICAL
C    SYSTEM WITH ARBITRARY ABERRATIONS AND
C    APODISATION
C
C
          INTEGER IWK(2000),IA1,IA2,N1,N2,N3,IJOB
          REAL RWK(2000)
          REAL P(48,48),M(48,48),E(48),INT(48,48)
          COMPLEX A(256,256),CWK(256),B(48,48),C(48)
          COMPLEX D(48)
C
OPEN(UNIT=22,STATUS='NEW',FILE='PH.DAT')
OPEN(UNIT=23,STATUS='NEW',FILE='MOD.DAT')
OPEN(UNIT=24,STATUS='NEW',FILE='INT.DAT')
OPEN(UNIT=25,STATUS='NEW',FILE='BB.DAT')
C
C    READ PARAMETER VALUES FROM MIC FILE
C
          READ(5,20)N
          READ(5,40)A20
          READ(5,40)A21
          READ(5,40)A22
          READ(5,40)A31
          READ(5,40)A32
          READ(5,40)A42
          READ(5,40)GG
     20 FORMAT(I4)
     40 FORMAT(F10.4)
41FORMAT(I3,3X,I3,3X,F10.4,3X,F10.4)
42FORMAT(I3,3X,I3,3X,F10.4)
43FORMAT(3(2X,I3),5(3X,F8.4))
44FORMAT(I3,3X,F10.4,3X,F10.4)
C
C       N=NUMBER OF SAMPLE POINTS IN ONE DIMENSION
C    A20=45 deg ASTIGMATISM
C    A21=FOCAL SHIFT
C    A22=0 deg ASTIGMATISM
C    A31=X COMA
C    A32=Y COMA
C    A42=SPHERICAL
C     GG=WIDTH OF GAUSSIAN
PI=3.1415927
Q1=3.*PI/4.
DL=3.*PI/2.
```

```
C
C   CIRCULAR APERTURE WITH VARIABLE TRANSMITTANCE
C   AND ABERRATIONS
C
      DO 220 I=1,N
      DO 200 J=1,N
      RAD=SQRT((I-(18.+0.5))**2+(J-(18.+0.5))**2)
      X=(I-(18.+0.5))/17.0
      Y=(J-(18.+0.5))/17.0
C   CALCULATE CONTRIBUTIONS OF THIRD ORDER
C   ABERRATIONS
C   USING ZERNIKE MONOMIAL REPRESENTATION
      ARG20=A20*2.*X*Y
      ARG21=A21*(-1.+2.*Y*Y+2.*X*X)/2.
      ARG22=A22*(Y*Y-X*X)
      ARG31=A31*(-2.*X+3.*X*Y*Y+3.*X**3)/3.
      ARG32=A32*(-2.*Y+3.*Y**3+3.*X*X*Y)/3.
      ARG42A=A42*(1.-6.*Y*Y-6.*X*X+6.*Y**4)
      ARG42=ARG42A+(12.*X*X*Y*Y+6.*X**4)*A42
      ARG42=ARG42/6.
      ARG1=(ARG20+ARG21+ARG22+ARG31+ARG32+ARG42)*2.*PI
C   CALCULATE CONTRIBUTIONS OF VARIOUS APODISERS
C   GAUSSIAN APODISER
C      TT=EXP(-GG*RAD*RAD/17.0/17.0)
C   SUPERGAUSSIAN APODISER
F=1.
TT=EXP(-(GG*RAD*RAD/17./17.)**F)
IF(RAD.LT.16.5)GO TO 60
IF(RAD.GT.17.5)GO TO 100
SC=-RAD+17.5
GO TO 80
   60 A(I,J)=CMPLX(TT*COS(ARG1),TT*SIN(ARG1))
      GO TO 120
   80 A(I,J)=CMPLX(SC*TT*COS(ARG1),SC*TT*SIN(ARG1))
      GO TO 120
  100 A(I,J)=(0.,0.)
  120 CONTINUE
  200 CONTINUE
  220 CONTINUE
DO 230 I=1,48
DO 225 J=1,48
M(I,J)=CABS(A(I,J))
CWRITE(24,42)I,J,M(I,J)
225CONTINUE
230CONTINUE
```

```
C
C   PERFORM FAST FOURIER TRANSFORM USING IMSL
C
  240 IA1=N
      IA2=N
      N1=N
      N2=N
      N3=1
      IJOB=-1
      CALL FFT3D (A,IA1,IA2,N1,N2,N3,IJOB,IWK,RWK,CWK)
DO 242 J=1,N
I=1
CWRITE(22,41)I,J,A(I,J)
242CONTINUE
C
C   REDUCE SIZE OF ARRAY
C
DO 250 I=1,24
DO 245 J=1,24
B(I,J)=A(I,J)
B(I,24+J)=A(I,N-24+J)
B(24+I,J)=A(N-24+I,J)
B(24+I,24+J)=A(N-24+I,N-24+J)
245CONTINUE
250CONTINUE
DO 252 I=1,48
DO 251 J=1,48
CWRITE(23,41)I,J,B(I,J)
251CONTINUE
252CONTINUE
C
C   SHIFT ZERO FREQUENCY TO ARRAY CENTER
C
DO 260 I=1,48
DO 255 J=1,24
A(I,J)=B(I,25-J)
A(I,24+J)=B(I,49-J)
255CONTINUE
260CONTINUE
DO 270 I=1,24
DO 265 J=1,48
B(I,J)=A(25-I,J)
B(24+I,J)=A(49-I,J)
265CONTINUE
270CONTINUE
DO 274 J=1,48
DO 272 I=1,48
C TYPE 41,I,J,B(I,J)
272CONTINUE
274CONTINUE
```

```
C
C   FIND PHASE OF ARRAY
C
  248 DO 360 I=1,48
      DO 340 J=1,48
      AA=AIMAG(B(I,J))
      BB=REAL(B(I,J))
IF (BB.EQ.0.00000000)BB=0.000001
      P(I,J)=ATAN2(AA,BB)
C         WRITE(25,42)I,J,P(I,J)
  340 CONTINUE
  360 CONTINUE
C
C   FIND MODULUS AND INTENSITY OF ARRAY
C
      DO 400 I=1,48
      DO 380 J=1,48
      M(I,J)=CABS(B(I,J))/.0139
INT(I,J)=M(I,J)**2.
  380 CONTINUE
  400 CONTINUE
DO 404 I=1,48
DO 402 J=1,48
C         WRITE(23,42)I,J,M(I,J)
  WRITE(24,42)I,J,INT(I,J)
402CONTINUE
404CONTINUE
C   WRITE CENTRAL SLICE OF INTENSITY
DO 415 I=1,48
CWRITE(23,44)I,M(I,24)
WRITE(25,44)I,INT(1,24)
415CONTINUE
C
C   REMOVE TILT FROM EACH ROW
C
DO 420 I=1,48
DC 410 J=2,48
P(I,J)=P(I,J)-(J-1)*.4295
C         WRITE(23,42)I,J,P(I,J)
410CONTINUE
420CONTINUE
C
```

```
C   HANDLE PHASE JUMPS ON EACH ROW
C
DO 500 I=1,48
DEL=0.
ICNT=0
DO 490 J=1,48
ICNT=ICNT+1
P(I,J)=P(I,J)+DEL
F1=P(I,J)
      G1=P(I,J+1)+DEL
H1=ABS(G1-F1)
CWRITE(22,43)I,J,ICNT,DEL,F1,G1,H1
IF(H1.LE.Q1)GO TO 490
IF((H1.GE.DL).AND.(G1.GT.F1))GO TO 450
IF((H1.GE.DL).AND.(G1.LT.F1))GO TO 460
IF(ICNT.LT.5)GO TO 411
ICNT=4
C   DO LINEAR FIT TO LAST ICNT POINTS(B1=SLOPE)
411IF(ICNT.EQ.1)GO TO 431
    SXY=0.
SX=0.
SY=0.
SX2=0.
DO 421 K=1,ICNT
X=ICNT+1-K
SXY=SXY+X*P(I,J+1-K)
SX=SX+K
SY=SY+P(I,J+1-K)
SX2=SX2+K**2.
421CONTINUE
B1=(SXY-SX*SY/ICNT)/(SX2-SX*SX/ICNT)
GO TO 429
431B1=P(I,J+2)-P(I,J+1)
429IF((B1.LE.0.).AND.(G1.GT.F1))GO TO 430
IF((B1.GT.0.).AND.(G1.LT.F1))GO TO 440
ICNT=0
GO TO 490
430INCT=0
GO TO 450
440ICNT=0
GO TO 460
450DEL=DEL-2.*PI
GO TO 490
460DEL=DEL+2.*PI
490CONTINUE
500CONTINUE
DO 850 I=1,48
DO 849 J=1,48
C               WRITE(24,42)I,J,P(I,J)
849CONTINUE
850CONTINUE
```

```
C
C   CORRECT PHASE ON ENTIRE ROWS RELATIVE TO ROW I=1
C
DO 1160 I=1,48
J=24
C     WRITE(25,42)I,J,P(I,J)
1160CONTINUE
C   REMOVE TILT BETWEEN ROWS
DO 1200 I=2,48
DO 1150 J=1,48
P(I,J)=P(I,J)-(I-1)*.4295
1150CONTINUE
1200CONTINUE
DO 1210 I=1,48
J=24
C       WRITE(22,42)I,J,P(I,J)
1210CONTINUE
C
C   HANDLE PHASE JUMPS BETWEEN EACH ROW
C
DEL=0.
ICNT=0
DO 1500 I=1,48
ICNT=ICNT+1
DO 1510 J=1,48
P(I,J)=P(I,J)+DEL
1510CONTINUE
J=24
F1=P(I,J)
G1=P(I+1,J)+DEL
H1=ABS(G1-F1)
CWRITE(24,43)I,J,ICNT,DEL,F1,G1,H1
IF(H1.LE.Q1)GO TO 1500
IF((H1.GE.DL).AND.(G1.GT.F1))GO TO 1450
IF((H1.GE.DL).AND.(G1.LT.F1))GO TO 1460
IF(ICNT.LT.4)GO TO 1411
ICNT=3
C   DO LINEAR FIT TO LAST ICNT POINTS
1411IF(ICNT.EQ.1)GO TO 1426
    SXY=0.
SX=0.
SY=0.
SX2=0.
DO 1421 N=1,ICNT
X=ICNT+1-N
```

```
      SXY=SXY+X*P(I+1-K,J)
      SX=SX+K
      SY=SY+P(I+1-K,J)
      SX2=SX2+K**2.
1421  CONTINUE
      B1=(SXY-SX*SY/ICNT)/(SX2-SX*SX/ICNT)
      GO TO 1427
1426  B1=P(I+2,J    ,I+1,J)
1427     IF((B1.LE.0.).AND.(G1.GT.F1))GO TO 1430
      IF((B1.GT.0.).AND.(G1.LT.F1))GO TO 1440
      ICNT=0
      GO TO 1500
1430  ICNT=0
      GO TO 1450
1440  ICNT=0
      GO TO 1460
1450  DEL=DEL-2.*PI
      GO TO 1500
1460  DEL=DEL+2.*PI
1500  CONTINUE
      DO 2470 J=1,48
      I=24
C        WRITE(25,42)I,J,P(I,J)
2470  CONTINUE
C   CENTER PHASE AROUND ZERO VALUE
      DO 2501 I=1,48
      DO 2491 J=1,48
      P(I,J)=P(I,J)-9.
C                WRITE(22,42)I,J,P(I,J)
2491  CONTINUE
2501  CONTINUE


C
C   WRITE CENTRAL SLICES OF MODULUS AND PHASE
C
      I=24
      DO 2550 J=1,48
C        WRITE(22,44)J,P(I,J)
c     WRITE(23,44)J,M(I,J)
2550  CONTINUE
      CLOSE(UNIT=22)
      CLOSE(UNIT=23)
      CLOSE(UNIT=24)
      CLOSE(UNIT=25)
1100      STOP
          END
C   IMSL ROUTINE NAME    - FFT3D
```

```
      PROGRAM TPNT
C
C
C     THIS PROGRAM CALCULATES THE PHASE, MODULUS AND
C     INTENSITY OF THE TWO-DIMENSIONAL IMAGE OF TWO
C     POINT SOURCES THROUGH AN OPTICAL SYSTEM WITH
C     ARBITRARY ABERRATIONS AND APODISATION
C
C
      INTEGER IWK(2000),IA1,IA2,N1,N2,N3,IJOB
      REAL RWK(2000)
      REAL P(48,48),M(48,48),E(48),INT(48,48)
      COMPLEX A(256,256),CWK(256),B(48,48),C(48)
      COMPLEX D(48)
C
OPEN(UNIT=22,STATUS='NEW',FILE='PH.DAT')
OPEN(UNIT=23,STATUS='NEW',FILE='MOD.DAT')
OPEN(UNIT=24,STATUS='NEW',FILE='INT.DAT')
OPEN(UNIT=25,STATUS='NEW',FILE='BB.DAT')
C
C   READ PARAMETER VALUES FROM MIC FILE
C
      READ(5,20)N
      READ(5,40)A20
      READ(5,40)A21
      READ(5,40)A22
      READ(5,40)A31
      READ(5,40)A32
      READ(5,40)A42
      READ(5,40)GG
READ(5,40)BBB
READ(5,40)FF
   20 FORMAT(I4)
   40 FORMAT(F10.4)
41FORMAT(I3,3X,I3,3X,F10.4,3X,F10.4)
42FORMAT(I3,3X,I3,3X,F10.4)
43FORMAT(3(2X,I3),5(3X,F8.4))
44FORMAT(I3,3X,F10.6,3X,F10.4)
C
C        N=NUMBER OF SAMPLE POINTS IN ONE DIMENSION
C     A20=45 des ASTIGMATISM
C     A21=FOCAL SHIFT
C     A22=0 des ASTIGMATISM
C     A31=X COMA
C     A32=Y COMA
C     A42=SPHERICAL
C      GG=WIDTH OF GAUSSIAN
C     BBB=OFF-AXIS DISTANCE OF ONE POINT
C      FF=FOCAL LENGTH OF FIRST LENS
PI=3.1415927
Q1=3.*PI/4.
DL=3.*PI/2.
```

```
C
C   CIRCULAR APERTURE WITH VARIABLE TRANSMITTANCE
C   AND ABERRATIONS
C
      DO 220 I=1,N
      DO 200 J=1,N
      RAD=SQRT((I-(18.+0.5))**2+(J-(18.+0.5))**2)
      X=(1-(18.+0.5))/17.0
      Y=(J-(18.+0.5))/17.0
C    CALCULATE CONTRIBUTIONS OF THIRD ORDER
C    ABERRATIONS
C    USING ZERNIKE MONOMIAL REPRESENTATION
      ARG20=A20*2.*X*Y
      ARG21=A21*(-1.+2.*Y*Y+2.*X*X)/2.
      ARG22=A22*(Y*Y-X*X)
      ARG31=A31*(-2.*X+3.*X*Y*Y+3.*X**3)/3.
      ARG32=A32*(-2.*Y+3.*Y**3+3.*X*X*Y)/3.
      ARG42A=A42*(1.-6.*Y*Y-6.*X*X+6.*Y**4)
      ARG42=ARG42A+A42*(12.*X*X*Y*Y+6.*X**4)
      ARG42=ARG42/6.
      ARG1=(ARG20+ARG21+ARG22+ARG31+ARG32+ARG42)*2.*PI
ARG2=2.*PI*BBB*Y/FF/.6328
C    CALCULATE CONTRIBUTIONS OF VARIOUS APODISERS
C      GAUSSIAN APODISER
C       TT=EXP(-GG*RAD*RAD/17.0/17.0)
C      SUPERGAUSSIAN APODISER
F=1.
TT=EXP(-(GG*RAD*RAD/17./17.)**F)
IF(RAD.LT.16.5)GO TO 60
IF(RAD.GT.17.5)GO TO 100
SC=-RAD+17.5
GO TO 80
   60 A(I,J)=CMPLX(TT*COS(ARG1)*2.*COS(ARG2),TT*SIN(ARG1))
      GO TO 120
   80 A(I,J)=CMPLX(SC*TT*COS(ARG1)*2.*COS(ARG2),SC*TT*SIN(ARG1))
      GO TO 120
  100 A(I,J)=(0.,0.)
  120 CONTINUE
  200 CONTINUE
  220 CONTINUE
DO 230 I=1,48
DO 225 J=1,48
M(I,J)=CABS(A(I,J))
CWRITE(24,42)I,J,M(I,J)
225CONTINUE
230CONTINUE
C
C   PERFORM FAST FOURIER TRANSFORM USING IMSL
C
```

```
            PROGRAM EDGE
C
C
C   THIS PROGRAM CALCULATES THE INTENSITY IN THE
C   COHERENT IMAGE OF AN EDGE THROUGH AN
C   ABERRATED AND APODISED SYSTEM
C
C
      INTEGER IWK(25000)
      REAL WK(25000),H(4096),INT(2048),E(200)
         COMPLEX G(2048),F(4096)
         OPEN(UNIT=22,DEVICE='DSK',ACCESS='SEQOUT',
     +   FILE='PH.DAT')
         OPEN(UNIT=23,DEVICE='DSK',ACCESS='SEQOUT',
     +   FILE='MOD.DAT')
         OPEN(UNIT=24,DEVICE='DSK',ACCESS='SEQOUT',
     +   FILE='E.DAT')
         OPEN(UNIT=25,DEVICE='DSK',ACCESS='SEQOUT',
     1   FILE='BB.DAT')
C
C   READ PARAMETER VALUES FROM MIC FILE
C
      READ(5,20)N
      READ(5,40)A20
      READ(5,40)A21
      READ(5,40)A22
      READ(5,40)A31
      READ(5,40)A32
      READ(5,40)A42
      READ(5,40)GG
   20 FORMAT(I4)
   40 FORMAT(F10.4)
   41    FORMAT(F10.4,3X,F10.4)
   42    FORMAT(I3,3X,I3,3X,F10.4)
   43    FORMAT(3(2X,I3).5(3X,F8.4))
   44    FORMAT(I5,3X,F10.4)
   45    FORMAT(12X,F10.6,3X,F10.6)
   46    FORMAT(I4,3X,F10.4,3X,F10.4)
C
C      N=NUMBER OF SAMPLE POINTS IN ONE DIMENSION
C   A20=45 deg ASTIGMATISM
C   A21=FOCAL SHIFT
C   A22=0 deg ASTIGMATISM
C   A31=X COMA
C   A32=Y COMA
C   A42=SPHERICAL
C    GG=WIDTH OF GAUSSIAN
         PI=3.1415927
```

```
C
C    INPUT FUNCTION - AN EDGE
C
        DO 6C I=1,1024
        G(I)=CMPLX(1.,0.)
6C      CONTINUE
        DO 70 I=1025,2048
        G(I)=CMPLX(0.,C.)
70      CONTINUE
C
C    PERFORM FIRST FOURIER TRANSFORM
C
        CALL FFTCC(G,N,IWK,WK)
        DO 9C I=1,2048
C       WRITE(23,46)I,G(I)
9C      CONTINUE
C
C    MOVE ZERO SPATIAL FREQ TO CENTER OF APERTURE
C
        G(255)=G(128)
        DO 1CC I=1,127
        G(127+I)=G(I)
        G(I)=G(1921+I)
1CC     CONTINUE
        DO 11C I=1,2048
C       WRITE(22,46)I,G(I)
11C     CONTINUE
C
C    1-D APERTURE WITH VARIABLE TRANSMITTANCE AND
C    ABERRATIONS
C
        DO 2CC I=1,255
        Y=(I-128)/127.
        ARG21=A21*(-1.+2.*Y*Y)/2.
        ARG22=A22*(Y*Y)
        ARG32=A32*(-2.*Y+3.*Y**3)/3.
        ARG42=A42*(1.-6.*Y*Y+6.*Y**4)/6.
        ARG1=(ARG21+ARG22+ARG32+ARG42)*2.*PI
C    GAUSSIAN APODISER
        A=EXP(-(GG*Y*Y))
        F(I)=CMPLX(A*COS(ARG1),A*SIN(ARG1))*G(I)
2CC     CONTINUE
        DO 22C I=256,4096
        F(I)=CMPLX(C.,C.)
22C     CONTINUE
        DO 23C I=1,4096
C       WRITE(24,46)I,F(I)
23C     CONTINUE
```

MICROCOPY RESOLUTION TEST CHART

```
C
C   PERFORM SECOND FAST FOURIER TRANSFORM
C
        M=4096
      CALL FFTCC (F,M,IWK,WK)
        DO 240 I=1,4096
C       WRITE(25,46)I,F(I)
240     CONTINUE
C
C   CALCULATE INTENSITY : USED TO NORMALIZE
C
        DO 244 I=2000,2150
        H(I)=((CABS(F(I))/1E+3)**2.)*.2384
        X=(I-2050)*18.85/96
        WRITE(24,41)X,H(I)
244     CONTINUE

C
C   GEOMETRIC EDGE
C
        DO 260 I=2000,2050
        E(I)=0.
260     CONTINUE
        DO 270 I=2051,2150
        E(I)=1.
270     CONTINUE
        DO 280 I=2000,2150
        X=(I-2050)*18.85/96.
        WRITE(25,41)X,E(I)
280     CONTINUE
        CLOSE(UNIT=22)
        CLOSE(UNIT=23)
        CLOSE(UNIT=24)
        CLOSE(UNIT=25)
1100    STOP
        END
```

```
          PROGRAM SLIT
C
C
C   THIS PROGRAM CALCULATES THE INTENSITY IN THE
C   COHERENT IMAGE OF A SLIT THROUGH AN ABERRATED
C   AND APODISED SYSTEM
C
C
      INTEGER IWK(25000)
      REAL WK(25000),H(4096),INT(2048),E(700),X(500)
        REAL V(700)
        COMPLEX G(2048),F(4096)
        OPEN(UNIT=22,DEVICE='DSK',ACCESS='SEQOUT',
     +  FILE='PH.DAT')
        OPEN(UNIT=23,DEVICE='DSK',ACCESS='SEQOUT',
     +  FILE='MOD.DAT')
        OPEN(UNIT=24,DEVICE='DSK',ACCESS='SEQOUT',
     +  FILE='B.DAT')
        OPEN(UNIT=25,DEVICE='DSK',ACCESS='SEQOUT',
     +  FILE='BB.DAT')
C
C   READ PARAMETER VALUES FROM MIC FILE
C
      READ(5,20)N
      READ(5,40)A20
      READ(5,40)A21
      READ(5,40)A22
      READ(5,40)A31
      READ(5,40)A32
      READ(5,40)A42
      READ(5,40)GG
   20 FORMAT(I4)
   40 FORMAT(F10.4)
   41     FORMAT(F10.4,3X,F10.4)
   42     FORMAT(I3,3X,I3,3X,F10.4)
   43     FORMAT(3(2X,I3),5(3X,F8.4))
   44     FORMAT(I5,3X,F10.4)
   45     FORMAT(12X,F10.6,3X,F10.6)
   46     FORMAT(I4,3X,F10.4,3X,F10.4,3X,F10.4)
C
C      N=NUMBER OF SAMPLE POINTS IN ONE DIMENSION
C     A20=45 deg ASTIGMATISM
C     A21=FOCAL SHIFT
C     A22=0 deg ASTIGMATISM
C     A31=X COMA
C     A32=Y COMA
C     A42=SPHERICAL
C      GG=WIDTH OF GAUSSIAN
          PI=3.1415927
```

```fortran
C
C   INPUT FUNCTION - A SLIT
C
        DO 6C I=1,2CC
        G(I)=CMPLX(1.,C.)
60      CONTINUE
        DO 70 I=201,2048
        G(I)=CMPLX(0.,C.)
7C      CONTINUE
C
C   PERFORM FIRST FOURIER TRANSFORM
C
        CALL FFTCC(G,N,IWK,WK)
        DO 90 I=1,2C48
        H(I)=(CABS(G(I)))**2.
C       WRITE(23,46)I,H(I)
9C      CONTINUE
C       GO TO 231
C
C   MOVE ZERO SPATIAL FREQ TO CENTER OF APERTURE
C
        G(255)=G(128)
        DO 100 I=1,127
        G(127+I)=G(I)
        G(I)=G(1921+I)
1CC     CONTINUE
        DO 11C I=1,2048
C       WRITE(22,46)I,G(I)
11C     CONTINUE
C
C   1-D APERTURE WITH VARIABLE TRANSMITTANCE AND
C   ABERRATIONS
C
        DO 2CC I=1,255
        Y=(I-128)/127.
        ARG21=A21*(-1.+2.*Y*Y)/2.
        ARG22=A22*(Y*Y)
        ARG32=A32*(-2.*Y+3.*Y**3)/3.
        ARG42=A42*(1.-6.*Y*Y+6.*Y**4)/6.
        ARG1=(ARG21+ARG22+ARG32+ARG42)*2.*PI
C   GAUSSIAN APODISER
        A=EXP(-(GG*Y*Y))
        F(I)=CMPLX(A*COS(ARG1),A*SIN(ARG1))*G(I)
2CC     CONTINUE
        DO 22C I=256,2C48
        F(I)=CMPLX(C.,C.)
220     CONTINUE
        DO 23C I=1,2C48
C       WRITE(24,46)I,F(I)
23C     CONTINUE
```

```
C
C   PERFORM SECOND FAST FOURIER TRANSFORM
C
          N=4096
231       CALL FFTCC (F,N,IWK,WK)
          DO 240 I=1,4096
          H(I)=((CABS(F(I))/1E+3)**2.)/4.0933
C         WRITE(25,46)I,H(I)
240       CONTINUE
C
C   CALCULATE INTENSITY : USED TO NORMALIZE
C
          DO 244 I=1,120
          H(I+499)=((CABS(F(I))/1E+3)**2.)/4.192C
244       CONTINUE
          DO 246 I=1,499
          H(I)=((CABS(F(3597+I))/1E+3)**2.)/4.192C
246       CONTINUE
          DO 248 I=1,602
          V(I)=(I-301)*PI/16.
          WRITE(24,41)V(I),H(I)
248       CONTINUE

C         GO TO 333
C
C   GEOMETRIC SLIT
C
          DO 260 I=1,607
          E(I)=0.
260       CONTINUE
          DO 270 I=97,511
          E(I)=1.
270       CONTINUE
          DO 280 I=1,602
          V(I)=(I-301)*PI/16.
C         WRITE(6,41)V(I),E(I)
C         WRITE(22,41)V(I),E(I)
280       CONTINUE
333       CLOSE(UNIT=22)
          CLOSE(UNIT=23)
          CLOSE(UNIT=24)
          CLOSE(UNIT=25)
100       STOP
          END
```

APPENDIX 2 THE FABRICATION OF GAUSSIAN AMPLITUDE APODISERS

The Gaussian apodisers used in this experiment were produced using a photographic method perfected by Weller[79]. The method was originated in 1964, by P. Jacquinot and B. Roizen-Dossier[27] and refined by Hee[80] (1974), Kay[81] (1976), and Krisl[82] (1978). The essence of the method was the imaging of a rotating mask onto a photographic plate. The mask is mostly black with a generally wedge-shaped region in white (see Fig. A2.1). The tip of the wedge was at the center of rotation and the angular extent of the wedge, θ, varied with radial distance, r, from the center. Thus the exposure of the photographic plate varied radially. If the shape of the wedge was chosen appropriately the exposure would be Gaussian. By working in the linear region of the film, the developed plate had an amplitude Gaussian transmittance.

While this method proved satisfatory, it should be noted that other methods of achieving a Gaussian apodiser are possible. A method suggested by G.M. Morris[83] involves illuminating a film plate with a laser beam directly. If the laser is operating in the lowest order transverse mode, the illumination would have had a Gaussian profile. Another method uses a digital film plotter such as the Photowrite P-1500 by Optronics International, Inc. This device can focus a light-emitting diode light source onto a 12.5 micron diameter spot on unexposed film. The light can be modulated (256 energy levels) and the spot moved to any location on a 10-inch by 10-inch area. By properly tailoring the write instructions to this device, almost any desired transmittance, including a Gaussian, can be achieved.

The Procedure for Making the Gaussian Filter

The objective was to make a transmitting filter which had an amplitude transmittance of the form

$$T_A\left(r\right) = e^{-\left(\frac{r}{a}\right)^2},$$ (A2.1)

where r was the radial distance, a is a constant which controls the width of the Gaussian, and the subscript A refers to the amplitude transmittance of the filter. In making the mask, a was chosen so that $T_A(r) = 0.05$, where $r = 1.0$ inch. When a was evaluated and substituted into (A2.1) the result was

$$T_A\left(r\right) = e^{-\left(\frac{r}{0.58}\right)^2}.$$ (A2.2)

The intensity transmittance of the filter was

$$T_I\left(r\right) = T_A\left(r\right) T_A\left(r\right)^* = e^{-\frac{r^2}{0.17}},$$ (A2.3)

where the subscript I refers to the intensity transmittance of the filter

In the linear region of the film, the intensity transmittance will be proportional to the exposure. Thus the opening angle θ which controls the exposure of the film varied as

$$\theta\left(r\right) = B\left[1 - e^{-\frac{r^2}{0.17}}\right],$$ (A2.4)

where B was chosen such that $\theta(1) = \pi/2$. Choosing this value of θ insured that the mask variation occurs only in the first quadrant. The other quadrants of the mask were entirely black. Upon evaluating B, (A2.4) yielded

$$\theta\left(r\right)=1.58\left[1-e^{-\frac{r^2}{0.17}}\right] . \tag{A2.5}$$

Using the Euler relationships

$$x=r \sin \theta \quad and \quad y=r \cos \theta . \tag{A2.6}$$

the x-y coordinates of the outline of the mask were determined.

The mask profile was calculated on a DEC10 computer and plotted on a Tektronix 4662 plotter. The profile was then transferred to a diffusely reflecting white paper; standard computer paper worked well. The mask shape in the first quadrant was cut carefully with a razor blade and mounted with paper cement to a very black piece of paper. The resultant mask is shown in Fig. A2.1

The mask was then centered on a turntable which had been centered underneath a camera. The setup as well as the exposure and development times are the same as those used by Weller[78]. The process which initially appeared straightforward was, in fact, time-consuming and produced results which were quite variable. Nevertheless, several satisfactory filters were produced

Two filters (Nos. 6 and 52) were characterized by measuring the diffraction pattern produced by them The optical configuration is shown in Fig. 5.1 Initially the apodiser was not in the optical system. The lens L1 was a Jaegers #1158 telescope doublet and lens L2 was a Jaegers #958. The iris had an aperture diameter of 0.4 inches for apodiser # 52 and 0.525 inches for apodiser # 6. In these cases, the system was essentailly unaberrated. The aberrations were measured with a point diffraction interferometer as explained in Chapter 5 and found to be on the order of 0.1 waves for third order astigmatism, coma, and spherical, and much less for the higher order aberrations

The results when these filters were used in the system are displayed in Figs. A2.2 and A2.3 for filters #6 and #52, respectively. In each figure the photographs are of the impulse response of the system both unapodised(on the left) and apodised(on the right). In each case the ringing nature of the unapodised impulse response was suppressed by the use of the apodiser. In the other half of each figure, theoretical and experimental data are displayed. The solid lines are the predicted values of a central slice of the irradiance impulse response with the measured aberrations. The experimental data are shown as dashed curves on these same plots. The experimental data are from the I-SCAN device which was centered on the impulse response. The apodised impulse response was measured in two orthogonal directions.

The agreement between theory and experiment is within 1% for these data. This agreement indicates that the filters are indeed Gaussian in transmittance and are effective in removing the ringing structure from the irradiance impulse response in the presence of a small amount of aberration.
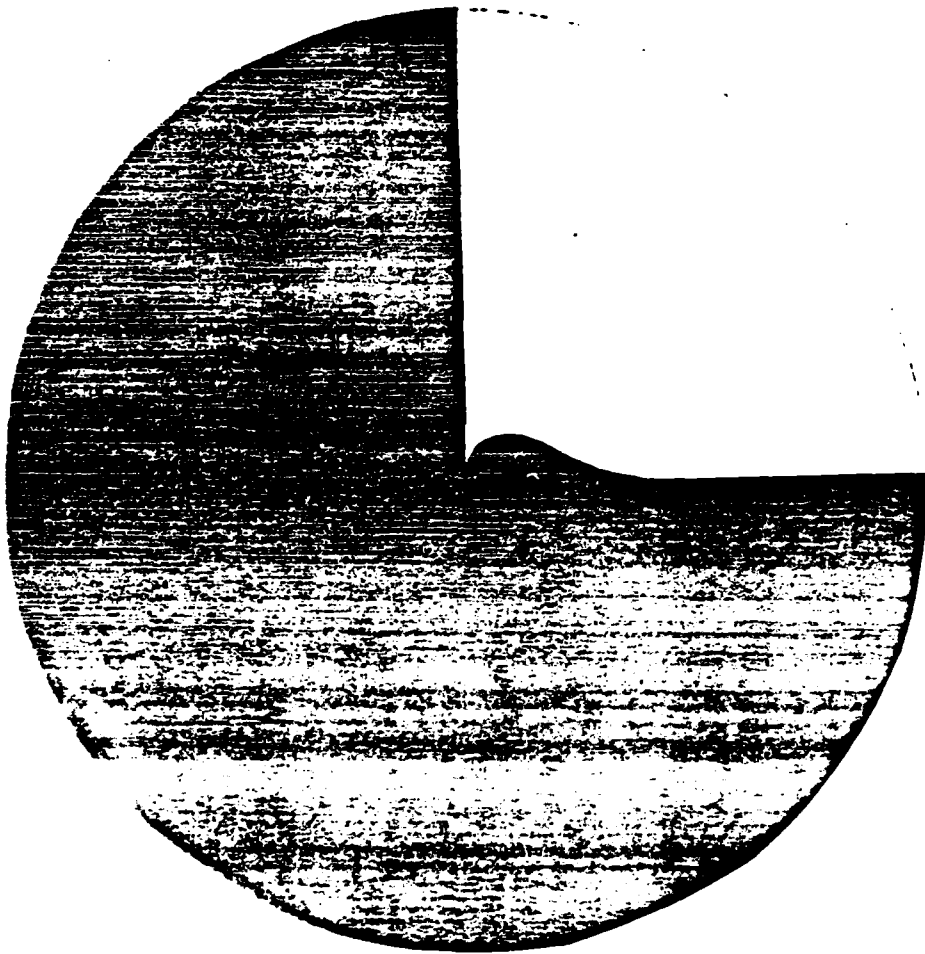
Fig. A2.1 The mask used to make the Gaussian filters used in this experiment.
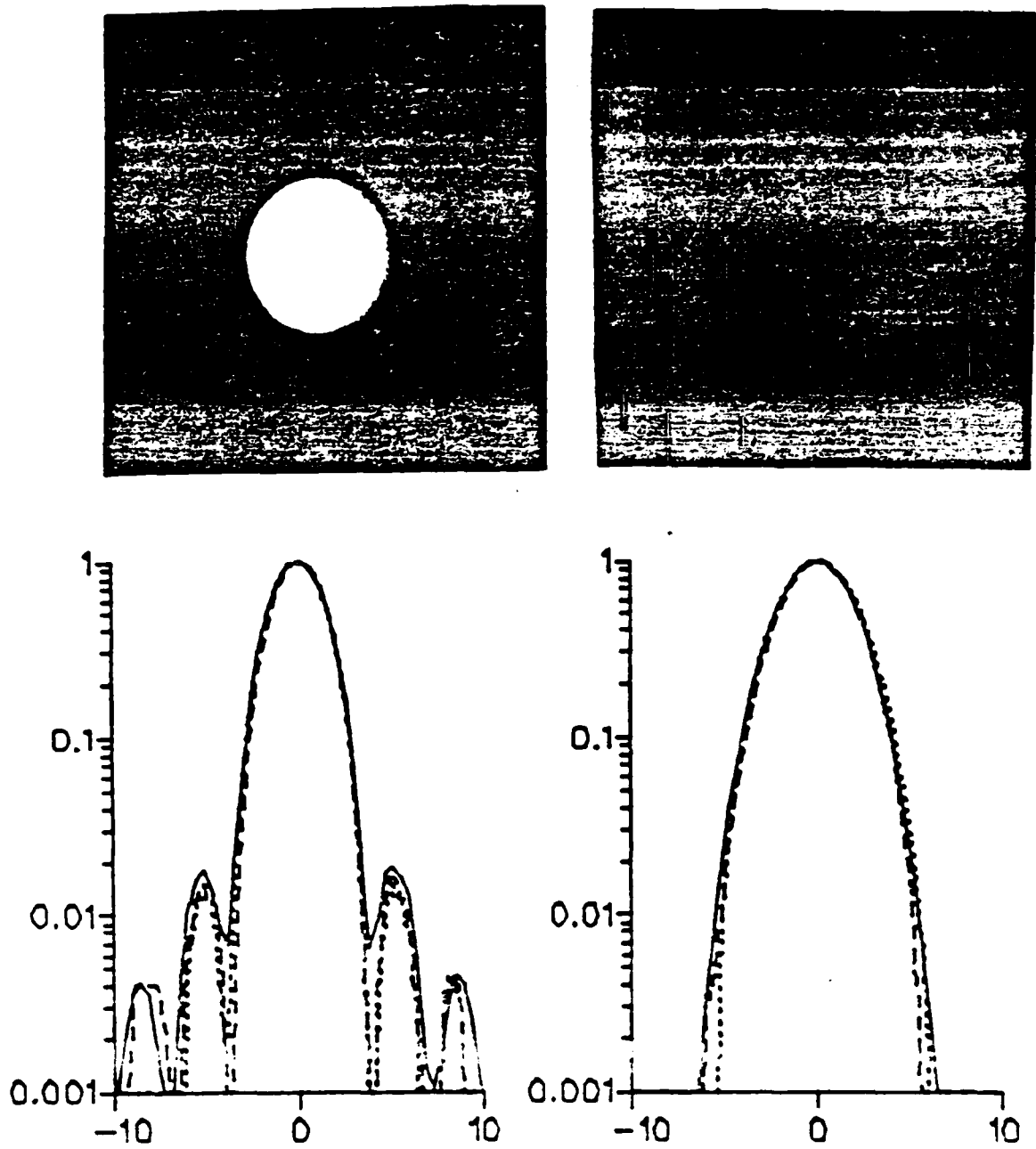
Fig.A2.2   The characterization of filter #6.   The photographs are of the
unapodised(upper left) and apodised impulse responses of the test system.
Below each photograph are plots of the corresponding theoretical(solid
curve) and experimental plots of irradiance along a line through the center of
the impulse responses. Experimental data are from two orthogonal slices.
The ordinate of each plot is in terms of the logarithm of relative irradiance (I)
and the abscissa is in terms of the normalized distance v.
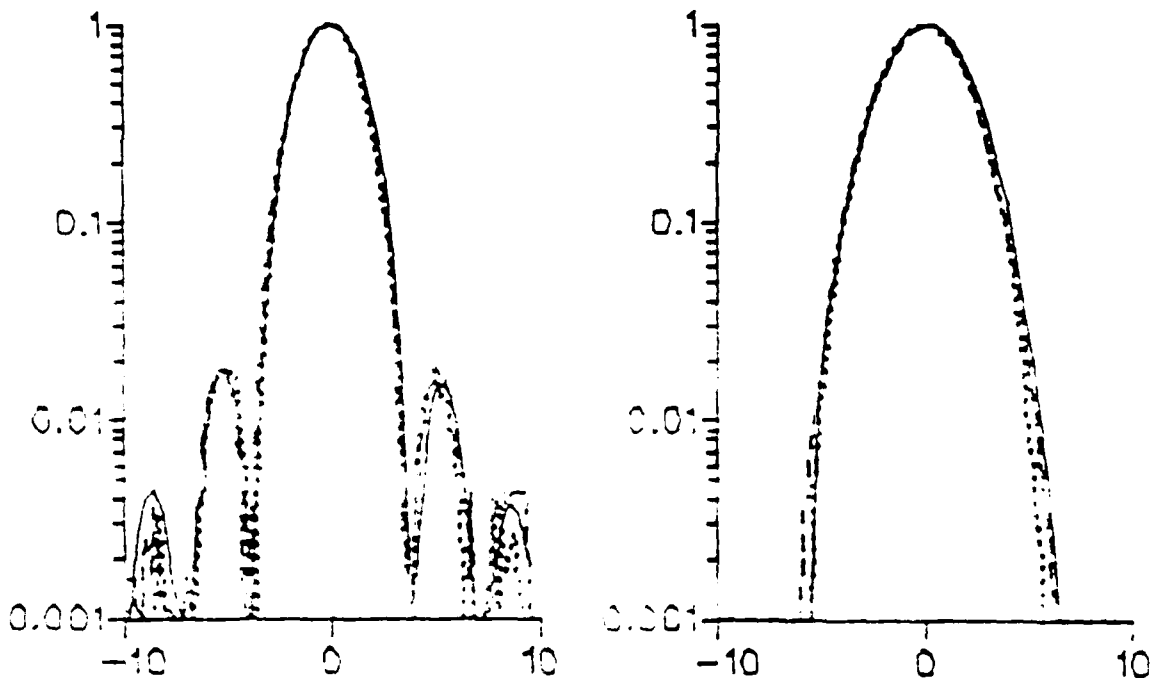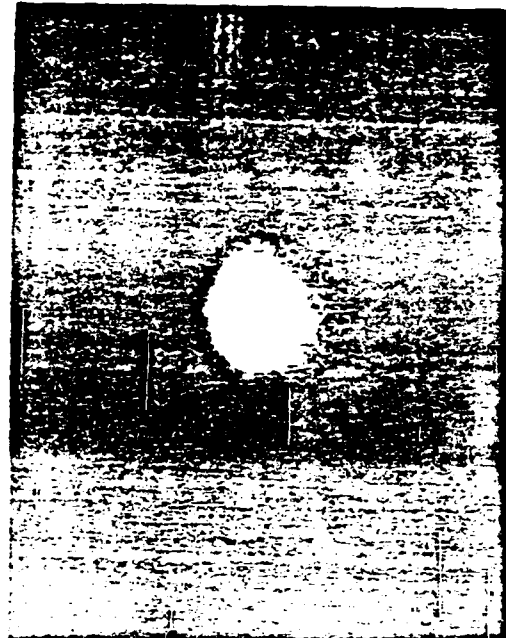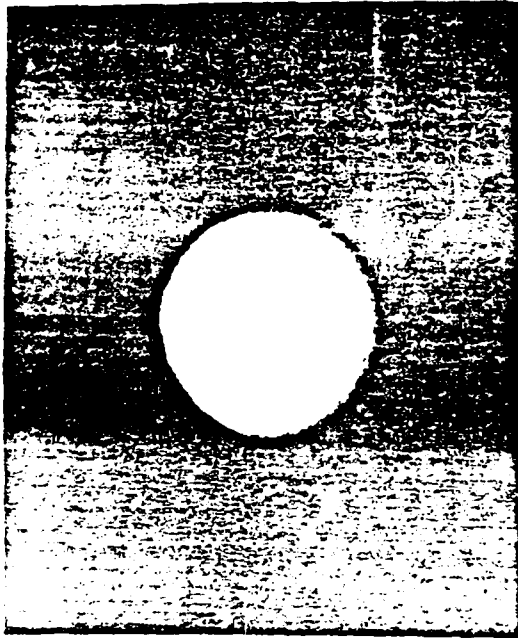
Fig A2 3   The characterization of filter # 52. The photographs are of the
unapodised(upper left) and apod sed impulse responses of the test system
Below each photograph are plots of the corresponding theoretical(solid
curve) and experimental plots of irradiance along a line through the center of
the impulse response5. Experimental data are from two orthogonal slices.
The ordinate of each plot is in terms of the logarithm of relative irradiance (I)
and the abscissa is in terms of the normalized distance u.

APPENDIX 3 DATA COLLECTION SYSTEM

The data collection system consisted of three main units, as shown in Fig. A3.1. The first unit was the I-SCAN card which contained a 256-element linear CCD array and some supporting electronics. The sec: s the data acquisition unit which converted the analog output from the I-SCAN into an 8-bit digital format and stored it in temporary memory. The last unit was the microcomputer, which controlled the data collection process and transfered the data from the temporary location to an internal floppy disk The microcomputer performed some simple preprocessing on the collected data as well and transferred of the data to a large mainframe computer for a more detailed analysis.
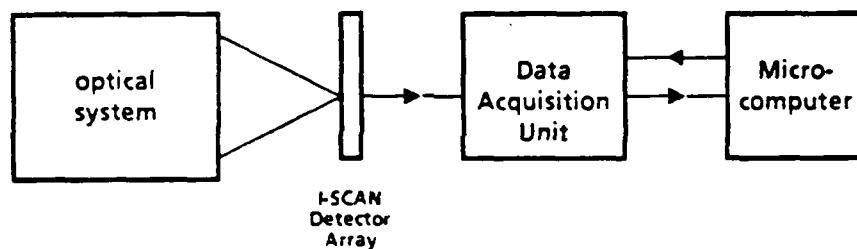
Fig. A3.1 Block diagram of the data collection system.

The I-SCAN consisted of a Fairchild CCD111 256-element line scan sensor mounted on a printed circuit card that contained all the necessary CCD111 operating electronics. The data were available on one of the output pins of the card edge connector in the form of a 0.5-2.0 MHz analog (Video) data stream Also available was a compensation (COMP) signal which was identical to the video signal except for the lack of input optical information The other two signals used were a 0.5-2.0 MHz clock, (MC/2) and an exposure sync (ES). These four signals as well as power and ground were connected to the data acquisition unit.

The purpose of the data acquisition unit was to condition the video signal, convert it to 8-bit digital words and to temporarily store it in a memory chip. The temporary storage was necessary because the data flowed from the I-SCAN at a rate which was much faster than the m̄   ːʊter could handle. Additionally, this card contained several logical circuits to control these processes.

The schematic for the data acquisition unit is shown in Fig. A3.2. The interconnections to the I-SCAN card are shown in the upper left-hand corner. Below that the power supply for both the I-SCAN and the data acquisition card is shown. The power supply was physically located within the data acquisition unit.

The video and compensation signals were connected through 47 ohm resistors R5 and R4 to pins 6 and 5, respectively, of the Analog Devices ADLH0032CG operational amplifier. With these connections the operational amplifier acted as a differential amplifier. Feedback resistors R3, R6, and R7 controlled the gain of the op amp. The gain was set to provide a 0.0 to -5.0 volt signal on the input (pin 19) of the Analog Devices MAH-0801-1 analog-to-digital (A/D) converter.

The A/D converter, when triggered by the encode command pulse, (input on pin 3), converted the analog signal into an eight-bit digital word. When the data ready signal (pin 1 of the A/D) went low a valid data word existed on the output pins 5 through 8 and 11 through 14.

A two-stage pulse shaping circuit (U2A and U2B) generated the encode command pulse in response to the applied MC/2 signal. The MC/2 signal was at the same data rate as the video. The first stage, U2A, created a long pulse which was adjustable in length through resistor R1. The second state, U2B, generated the encode command pulse which was approximately 100 nsec long. The encode command occurred in time just after the

start of the data pulse on pin 19 of the A/D converter. Resistor R1 of the first stage was used to insure this coincidence.

The digital data generated by the A/D converter was connected to the data bus through the bus transciever U7(74LS245). This chip allowed the data to be transferred to the memory chip U11(TC5517APR) when the read enable signal (from the microcomputer) was low. However, when data was being transferred from the memory chip to the microcomputer, the read enable line was brought high, isolating the A/D converter from the data bus.

The memory chip required several time-coincident signals to function properly in its read and write modes. During the write mode, data from the A/D converter was stored into the chip. When valid data were on the data bus, the read/write signal (R/W) on pin 21 was held low for approximately 500 nsec. This negative pulse was generated by U6A in response to the data-ready signal.

The particular address within the memory chip where each data word was stored was controlled by the address counters U8, U9, and U10. These binary counters (93L16) sequentially counted from binary zero to binary 2048 in response to the data-ready transitions. The first address (zero) was set by the master reset (MR) signal from the microcomputer before data acquisition started. Then, after each memory write operation, a pulse from U6B stepped the memory counters to the next address. U6B was triggered by the data-ready transition

The MR signal not only reset the memory address counters to zero, but it also reset the three-input logical switch U4. When U4 was reset the output on pin 10 was held low. This pin was connected to one of the inputs of the AND gate U3A; thus when it was low the encode command pulse could not reach the A/D converter and data were not converted.

The data collection process was initiated by a MR followed by a carriage return (CR) signal from the microcomputer. The latter signal set U4 so that the next exposure sync (ES) signal from the I-SCAN brought the output (pin 10) of U4 high. These ES pulses occurred in time just before a serial stream of analog data. The ES pulses were about 1 msec apart and the data stream was about 500 nsec long (for an 0.5 MHz data rate).

The data collection process up to this point can be summarized in the following series of steps.

1. A MR from the microcomputer reset the three-input switch U4 and zeroed the memory address counter.

2. A CR set U4.

3. The next ES forced pin 10 of U4 high, allowing the encode commands to pass through the AND gate U3A.

4. Each encode command initiated an A/D conversion which was stored in the memory chip.

5. The data-ready transition generated two pulses The first signalled the memory chip to store the data currently on the data bus. After the data word was stored, the second pulse incremented the memory address for the next data word

There were 256 (2^8) detector elements on the CCD111 line scan detector This constituted one frame of data. When the last address of a frame was reached the memory address counters generated a terminal count (TC) signal which was used to terminate the data collection process for that frame The memory chip could hold eight frames so the process was repeated seven times. The TC acted as a memory reset for U4 but did not reset the memory address counters Instead, a software clock signal from the microcomputer incremented the address counters by one address. Then a CR initiated

another frame of data. The microcomputer monitored the TC signal and after the eighth one was sensed, the data collection process was terminated.

Next, the data were transferred to the microcomputer. The first signal in this process was a MR which set the memory address to binary zero. Next, read enable was brought high isolating the A/D converter and forcing the memory chip, through the signal on pin 20, into the data-read mode. At this time, the contents of the first memory location were on the data bus. When the microcomputer had stored that data, it issued a software clock pulse. This pulse incremented the memory address thus placing the next word of data on the data bus. This process continued until all 2048 memory locations were read and stored in the microcomputer.

The microcomputer was a Healthkit H89 with 64K (8-bit) internal memory and two 100K single-density, single-sided disk drives. Once all eight frames of data were within the microcomputer, a software program on the microcomputer performed some simple preprocessing. First, the eight frames of data were averaged, on a pixel by pixel basis. Then the data was displayed in a x-y graphic format on the microprocessor CRT screen. Finally, the average frame was stored in a file on disk. Additional software allowed one frame of data to be subtracted from another (SUB.DAT) and the data to be transferred to a DEC10 computer (via MODEM7) The data collection process was initiated by entering 'DATA FILE.DAT' into the microprocessor The data was stored in the file named FILE.DAT. The software used in this data acquisition process was developed by Mr Lee Butler.
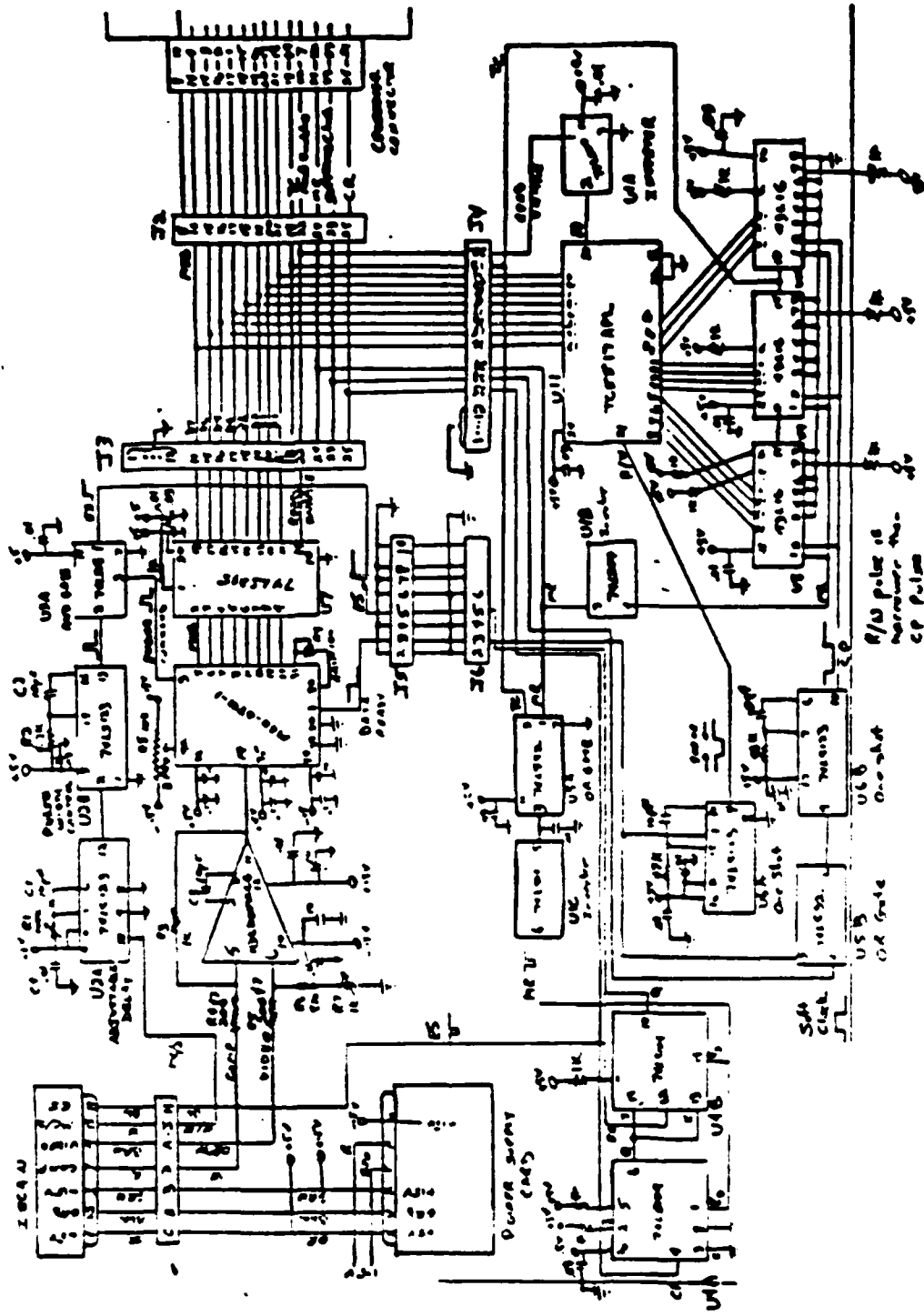
Fig.A3.2   The circuit diagram of the Data Aquisition Unit.

END
FILMED

4-86

DTIC